NASA/CR—2008-215440/PART3

Hydrogen Research for Spaceport and Space-Based Applications

Hydrogen Production, Storage, and Transport

Tim Anderson and Canan Balaban
University of Florida, Gainesville, Florida

November 2008

NASA STI Program . . . in Profile

Since its founding, NASA has been dedicated to the advancement of aeronautics and space science. The NASA Scientific and Technical Information (STI) program plays a key part in helping NASA maintain this important role.

The NASA STI Program operates under the auspices of the Agency Chief Information Officer. It collects, organizes, provides for archiving, and disseminates NASA's STI. The NASA STI program provides access to the NASA Aeronautics and Space Database and its public interface, the NASA Technical Reports Server, thus providing one of the largest collections of aeronautical and space science STI in the world. Results are published in both non-NASA channels and by NASA in the NASA STI Report Series, which includes the following report types:

- TECHNICAL PUBLICATION. Reports of completed research or a major significant phase of research that present the results of NASA programs and include extensive data or theoretical analysis. Includes compilations of significant scientific and technical data and information deemed to be of continuing reference value. NASA counterpart of peer-reviewed formal professional papers but has less stringent limitations on manuscript length and extent of graphic presentations.

- TECHNICAL MEMORANDUM. Scientific and technical findings that are preliminary or of specialized interest, e.g., quick release reports, working papers, and bibliographies that contain minimal annotation. Does not contain extensive analysis.

- CONTRACTOR REPORT. Scientific and technical findings by NASA-sponsored contractors and grantees.

- CONFERENCE PUBLICATION. Collected papers from scientific and technical conferences, symposia, seminars, or other meetings sponsored or cosponsored by NASA.

- SPECIAL PUBLICATION. Scientific, technical, or historical information from NASA programs, projects, and missions, often concerned with subjects having substantial public interest.

- TECHNICAL TRANSLATION. English-language translations of foreign scientific and technical material pertinent to NASA's mission.

Specialized services also include creating custom thesauri, building customized databases, organizing and publishing research results.

For more information about the NASA STI program, see the following:

- Access the NASA STI program home page at *http://www.sti.nasa.gov*

- E-mail your question via the Internet to *help@sti.nasa.gov*

- Fax your question to the NASA STI Help Desk at 301–621–0134

- Telephone the NASA STI Help Desk at 301–621–0390

- Write to:
  NASA Center for AeroSpace Information (CASI)
  7115 Standard Drive
  Hanover, MD 21076–1320

NASA/CR—2008-215440/PART3

Hydrogen Research for Spaceport and Space-Based Applications

Hydrogen Production, Storage, and Transport

Tim Anderson and Canan Balaban
University of Florida, Gainesville, Florida

Prepared under Grant NAG3–2930

National Aeronautics and
Space Administration

Glenn Research Center
Cleveland, Ohio 44135

November 2008

This work was sponsored by the Fundamental Aeronautics Program at the NASA Glenn Research Center.

Level of Review: This material has been technically reviewed by NASA technical management.

Available from

NASA Center for Aerospace Information
7115 Standard Drive
Hanover, MD 21076–1320

National Technical Information Service
5285 Port Royal Road
Springfield, VA 22161

Available electronically at http://gltrs.grc.nasa.gov

CONTENTS

Hydrogen Research for Spaceport and Space-Based Applications

Hydrogen Production, Storage, and Transport

Tim Anderson and Canan Balaban
University of Florida
Gainesville, Florida 32611

Abstract

The activities presented are a broad based approach to advancing key hydrogen related technologies in areas such as fuel cells, hydrogen production, and distributed sensors for hydrogen-leak detection, laser instrumentation for hydrogen-leak detection, and cryogenic transport and storage. Presented are the results from research projects, education and outreach activities, system, and trade studies. The work will aid in advancing the state-of-the-art for several critical technologies related to the implementation of a hydrogen infrastructure. Activities conducted are relevant to a number of propulsion and power systems for terrestrial, aeronautics and aerospace applications.

Hydrogen storage and in-space hydrogen transport research focused on developing and verifying design concepts for efficient, safe, lightweight liquid hydrogen cryogenic storage systems. Research into hydrogen production had a specific goal of further advancing proton conducting membrane technology in the laboratory at a larger scale. System and process trade studies evaluated the proton conducting membrane technology, specifically, scale-up issues.

1. Hydrogen Production Using Advanced Protonic Conductor

Task PI: Dr. Eric Wachsman, Material Science & Engineering

Gradute Students: Dr. Heesung Yoon (Post doc), Ta keun Oh, and Jianlin Li, Material Science & Engineering

Research Period: August 3, 2004 to March 31, 2008

Abstract

A ceramic hydrogen (H_2) permeation cell was developed based on the advanced protonic conductor: europium-doped strontium cerate ($SrCe_{1-x}Eu_xO_{3-\delta}$). The permeation cell is has a tubular design (with one end capped) to alleviate gas leakage issues common in planar designs. To maximize hydrogen permeation flux the basic cell architecture consists of a dense thin film $SrCe_{1-x}Eu_xO_{3-\delta}$ membrane (for the actual hydrogen permeation) supported by a porous (for unimpeded gas flow) Ni-$SrCeO_3$ composite to provide mechanical strength to the thin film membrane and catalytic activity to the feed gases (from the Ni component). With this membrane cell a maximum hydrogen flux of 6.9 cm^3/min was achieved.

To optimize the performance of the membrane, the transport phenomena of $SrCe_{1-x}Eu_xO_{3-\delta}$ was investigated, in dry and wet hydrogen atmospheres, as a function of temperature. To wit, the optimal europium dopant concentration in $SrCe_{1-x}Eu_xO_{3-\delta}$ for maximum hydrogen permeation was determined from measurements of ambipolar conductivity, total conductivity and open circuit potential. Of the compositions of $SrCe_{1-x}Eu_xO_{3-\delta}$ ($x = 0.1$, 0.15, and 0.2) studied, $SrCe_{0.9}Eu_{0.1}O_{3-\delta}$ showed highest total conductivity between 500 °C and 900 °C under both dry and wet hydrogen conditions. However, the highest ambipolar conductivity was obtained over the compositional range from $SrCe_{0.85}Eu_{0.15}O_{3-\delta}$ to $SrCe_{0.8}Eu_{0.2}O_{3-\delta}$, depending on temperature. Therefore, since H_2 flux is proportional to ambipolar conductivity these compositions were characterized for H_2 permeation efficiency.

Finally, the use of the permeation cell to enhance hydrogen production from both water-gas shift (WGS) reaction and steam reforming (SR) was explored. Our $SrCe_{1-x}Eu_xO_{3-\delta}$-based permeation cell was employed to continuously remove the H_2 produced by the WGS or SR reactions from either reaction stream. The CO conversion (for WGS) and the methane conversion (for SR) as well as the total hydrogen production (for both WGS and SR) were considerably improved. Moreover, the use of the H_2 permeation cell allows the WGS reaction to be operated with low H_2O/CO ratios, without the thermodynamic constraint.

This technology will dramatically improve H_2 production technology from a broad array of conventional (natural gas, coal) and renewable (biomass) fuels. Moreover, it is a compact efficient technology that can be used to produce pure H_2 for aerospace transportation applications (jet fuel/JP8) once sulfur issues are dealt with. Finally, as this is a transition project it directly lends itself to technology transfer and commercialization.

Introduction

Background

Hydrogen is the most abundant chemical-energy resource in the world. Historically, hydrogen has been produced from fossil fuels, and for the foreseeable future, will continue to be so. The major source of H_2 is steam reformation of natural gas. Therefore, improvements in the efficiency and cost of H_2 production from natural gas are necessary in the near future. Gas separation membranes and membrane reactors, based on ion conducting ceramics, may provide the technological advance necessary to increase the efficiency and reduce the cost of H_2 production from natural gas. However, other sources of H_2 must be developed for the envisioned hydrogen economy, and coal provides the greatest U.S. domestic resource-based option. The U.S. DOE is developing a FutureGen plant based on coal gasification, solid oxide fuel cells (SOFCs), biomass resources and ion conducting membranes that will produce H_2 and electricity with zero emissions and carbon sequestration; thereby, not contributing to global warming.

Membrane reactor technology holds the promise to circumvent thermodynamic equilibrium limitations by *in situ* removal of product species, resulting in improved chemical yields. Mixed-conducting oxide-membrane technology presents the possibility for a dramatic reduction in the cost of converting petroleum and coal derived feed stocks to hydrogen and other value-added hydrocarbons. The membranes are based on metal oxides (e.g., $SrCe_{1-x}M_xO_{3-\delta}$, where M is a metal dopant, e.g., Eu) that exhibit both ionic and electronic (mixed) conductivity. Because of their significant electronic conductivity, these mixed ionic-electronic conductors (MIECs) have an internal electrical short and the ionic species selectively permeates through a dense film of the material under a differential partial pressure, as shown conceptually for H_2 permeation. The potential permeation flux rates of these materials are extremely high.

High-temperature proton conducting ceramics are promising materials for many applications, including solid-oxide fuel cells, solid-state gas sensors, and membranes for hydrogen gas separation, etc. [1-3]. Recently, a series of high-temperature proton conducting ceramics, typically doped with multivalent cations, have been studied, based on $BaCeO_{3-\delta}$ [4-6], $SrCeO_{3-\delta}$ [7-9], and complex perovskites in the form of $A_2B'B''O_6$ and $A_3B'B''_2O_9$ [10-12]. $BaCeO_{3-\delta}$ based oxides exhibit oxygen ion conductivity comparable to their proton conductivity and thus are not desirable for hydrogen separation applications where oxygen is present [13, 14]. According to previous reports by Knight and Bonanos *et al.*, distorted orthorhombic structure of $SrCeO_{3-\delta}$ inhibits oxygen ion conduction, thereby enabling high transference number for proton conduction [15, 16]. Therefore, $SrCeO_3$ based oxides have promise for selective hydrogen separation if their electronic conductivity can be improved by proper doping.

The advancement of hydrogen separation technology has become important in energy applications for production of petrochemicals and hydrogen for fuel cells [2]. High temperature proton conductors based on perovskite-structured oxides have received increasing attention for hydrogen separation technologies. The separation process of protonic conductors is purely ionic transport, and results in nearly 100% pure hydrogen. Recently, our group studied Eu-doped $SrCeO_3$ for use as hydrogen separation membranes due to its mixed protonic-electronic conductivity [7, 8, 17-21]. Eu-doped $SrCeO_3$ is especially promising since it provides high selectivity to protons. Also, T. Norby and Y. Larring showed the flux of each carrier is inversely proportional to membrane thickness [22]. Therefore, our research has been directed towards the development of thin film hydrogen membranes using tubular-type porous supports for increasing the hydrogen production by reducing the thickness of the membrane. Figure 1 illustrates the basic design for producing pure hydrogen through the methane steam reforming process using thin film proton conducting membranes. For a hydrogen production cell, a hydrogen permeable thin film is coated on the inner-side of a catalytic tubular-type porous support. A methane and steam mixture is flowed on the outer side of a reactor cell. At operating temperatures, CO, CO_2, and H_2 are formed, and due to the hydrogen partial pressure gradient, H_2 permeates through the hydrogen permeable thin film.

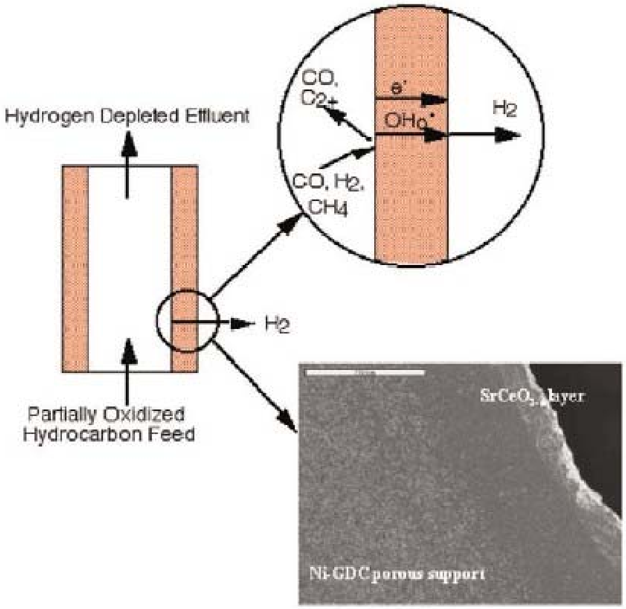

Figure 1. Integration of proton transport membranes (including SEM of membrane) in conversion of hydrocarbon fuels to H_2.

Membrane reactors can be used to produce hydrogen from hydrocarbon feed-stocks, from natural gas to coal to a variety of hydrocarbon containing waste streams such as landfill gas and swamp gas. The overall objective of this project is to demonstrate the feasibility of producing hydrogen from hydrocarbon based fuels using advanced proton conducting membranes. The objectives of this phase are to develop thin film proton conducting membranes on porous supports and to advance our fundamental understanding of these materials. The anticipated result is demonstration of high hydrogen fluxes through these thin supported membranes.

Technical Approach

The objectives of this report are to optimize electrical properties, to improve the stability of $SrCeO_3$, and to fabricate and demonstrate a membrane reactor that produces hydrogen from hydrocarbon based fuels (natural gas, jet fuel, coal gas, or biomass) using advanced proton conducting membrane materials.

Optimization of electrical properties for hydrogen permeation-To find optimized dopant concentration in $SrCeO_3$, we conducted a study of the electrical properties of $SrCe_{1-x}Eu_xO_{3-\delta}$ ($x = 0.1$, 0.15, and 0.2) in various oxygen and hydrogen atmosphere. The protonic conductivity was determined by impedance spectroscopy which allows one to extract bulk resistance from complex impedance as a function of frequency.

Improvement of chemical stability of $SrCeO_3$-Zirconates, such as $SrZrO_3$, show good chemical stability and mechanical strength and they are more stable against carbon dioxide gas, which reacts with cerate materials below 800 °C [23, 24], though the conductivity of zirconates is lower than that of the cerates [25]. However, it is possible to achieve a compromise between the proton conductivity and chemical stability using a mixed solid solution of $SrCeO_3$ and $SrZrO_3$.

Fabrication and performance of membrane reactor-Hydrogen separation membranes were fabricated by tape casting and rolling end-capped tubular supports (Ni-$SrCeO_3$ or Ni-$SrCe_{0.8}Zr_{0.2}O_3$) and by slurry-coating to form dense $SrCe_{0.9}Eu_{0.1}O_{3-\delta}$ (10ESC) hydrogen permeable membrane thin films on the inner-side of tubular-type supports. In this work, the $SrZr_{0.2}Ce_{0.7}Eu_{0.1}O_{3-\delta}$ tubular membrane, with Ni-$SrCe_{0.8}Zr_{0.2}O_{3-\delta}$ porous support, was also investigated for the chemical stability improvement. Steam reforming and WGS reaction were carried out with this membrane. The theoretical CO conversion and hydrogen production were calculated using thermodynamic data. The significant effect of the membrane reactor on the steam reforming and WGS reaction is discussed.

Experimental

Fabrication and Characterization

Powder Synthesis and Characterization

Polycrystalline $SrCe_{1-x}Eu_xO_{3-\delta}$ (x = 0.1, 0.15, and 0.2) samples were prepared by solid-state reaction. $SrCO_3$ (99.99%, Alfa Aesar), CeO_2 (99.99%, Alfa Aesar), and Eu_2O_3 (99.99%, Alfa Aesar) in the desired stoichiometric ratio were ball-milled for at least 24 h and then calcined for 10 h at 1573 K in air. The calcined oxides were pressed into pellets and cold-isostatic-pressed. The pellets were sintered at 1723 K for 5 h in air and X-ray diffraction was used to confirm a single phase with the orthorhombic perovskite structure.

Conductivity

Pt electrodes were applied on the 10 mm diameter x 2 mm thickness dense disk pellets using Pt-paste (Engelhard 6926) and heated to 1273 K for 1 h for electrical measurement. Conductivity measurements were performed with a Solartron 1260 Impedance Analyzer in the frequency range of 0.1 Hz to 1 MHz and temperature range of 773 to 1173 K under dry/wet pure hydrogen atmosphere. Water vapor was obtained by bubbling the hydrogen gas through de-ionized water at room temperature.

Open circuit voltage (OCV) measurements were performed on dense disks 24 mm diameter x 1.7 mm thickness. Each disk was sintered at 1723 K for 5 h with 2 °C/min ramp rate. The planar surface of each disk was connected with two platinum lead wires to measure OCV. The samples were sealed to the alumina tube with a glass sealant.

The gas inlets in the set-up were positioned as close as possible to the test sample. A constant 40 sccm H_2/Ar mixture was controlled by BOC Edwards 825 mass flow controllers on both gas inlets. Water vapor was obtained by controlling the bubbler temperature and gas tubes were wrapped using heating tape to prevent water vapor condensation. OCV was measured using a multimeter (Keithley 2000-20).

Hydrogen Membrane Cell

Ni-$SrCeO_3$ tubular-type supports for 10ESC hydrogen membrane thin film was prepared by tape casting as shown in Figure 2 and rolling techniques. Using tape casting and slurry coating, $SrCeO_3$ powder for a tubular-type support material was prepared by a conventional solid state reaction method from $SrCO_3$ (99.9%, Alfa-Aesar) and CeO_2 powder (99.9%, Alfa- Aesar) as starting materials. The $SrCe_{0.9}Eu_{0.1}O_3$ powder was synthesized by a citrate process using 1 to 2 molar ratios of the total metal nitrates to citric acid in order to prevent second phase formation and to decrease the calcining temperature [26].

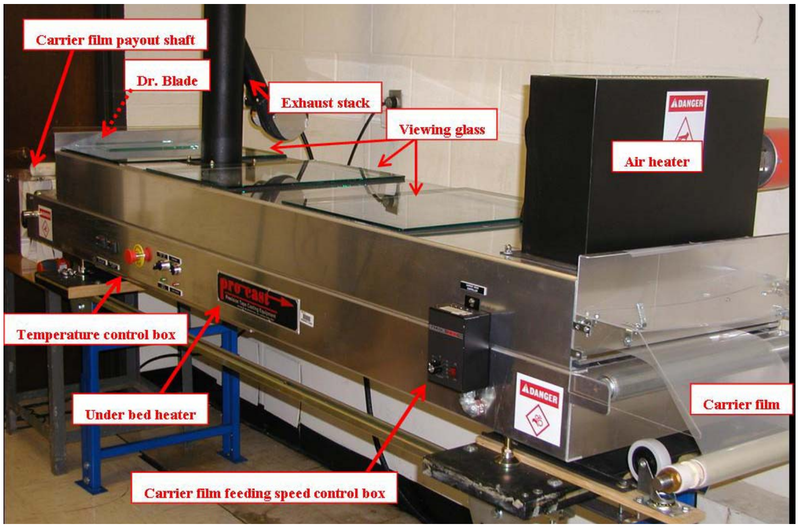

Figure 2. Tape caster for making ceramic green tape.

Figure 3. Pictures of (a) tubular hydrogen membrane cells and (b) 10 mol% Eu-doped $SrCeO_3$ membrane coated on the inner side of NiO(Ni)-$SrCeO_3$ tubular support at each processing step.

Figure 3(a) shows the 15 cm long end capped tubular-type hydrogen membrane cell. The preparation of the ESC hydrogen membrane on NiO (or Ni)-SC tubular support consists of four steps; and the pictures of a six-inch unit cell thus prepared at each preparation step are shown in Figure 3(b).

Hydrogen Permeation Experimental Setup

The $SrCe_{0.9}Eu_{0.1}O_{3-\delta}/Ni\text{-}SrCeO_3$ tubular-type membrane cell was installed in a hydrogen production reactor to confirm the cell was leak free. In order to make sure the leakage level and hydrogen permeation for the tubular-type hydrogen membrane cells, H_2 balanced with Ar was flowed to the feed side and He was flowed to the inner side of the cell to sweep permeated H_2 and leaked Ar through the hydrogen membrane cell. The components of permeated gases on the sweep side were measured by the mass-spectrometer (Q100MS Dycor QuadLink). For the hydrogen permeation measurement, tubular-type hydrogen membrane cells were installed in a high temperature reactor apparatus as shown in Figure 4. One side of the membrane cell (feed) was exposed to H_2 (99.999%) diluted to the desired.

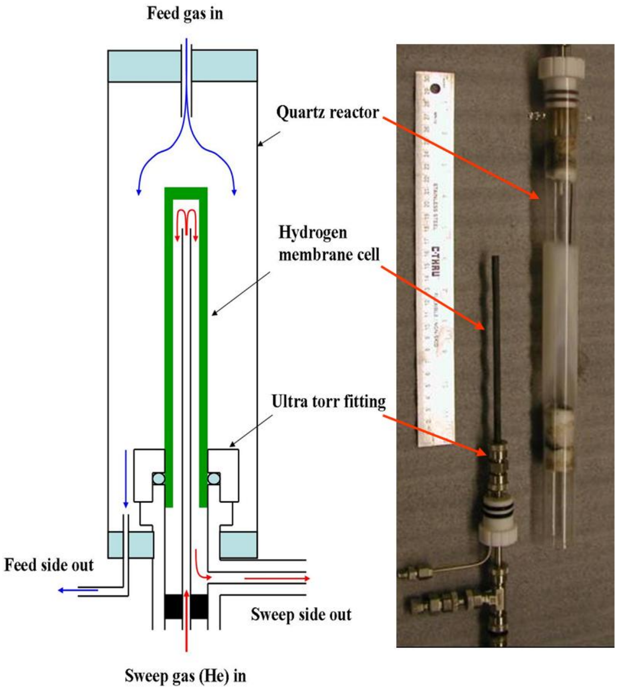

Figure 4. Configuration of the hydrogen permeation reactor using a 15 cm long one-end-closed tubular-type hydrogen membrane cell.

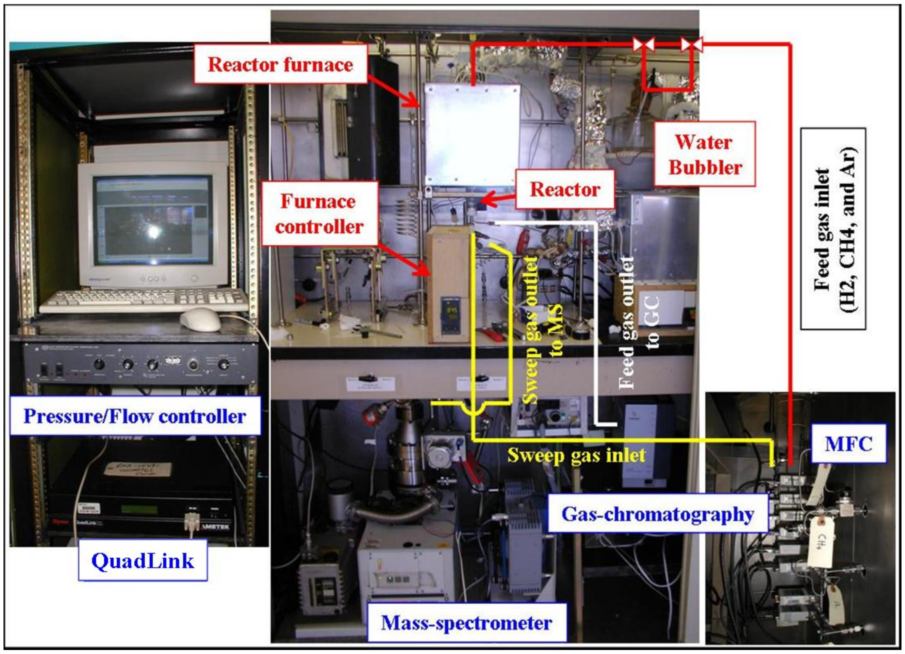

Figure 5. Experimental set-up for hydrogen permeation test.

concentration using He (99.999%) with 20~30 cm^3/min total flow rate. For the wet gas flow, the feed gas was flow through a water bubbler at 25 °C to pick up 3 vol% water vapor. The other side (sweep) was swept with He at 20 cm^3/min. Permeation was measured using a mass spectrometer (Dycor QuadLink IPS Quadrupole Gas Analyzer). The actual experimental set-up is shown in Figure 5. Permeated hydrogen was measured by a mass-spectrometer which was connected with the sweep gas outlet. Gas-chromatography was installed for measuring the product gases, while CH_4 gas was used as a feed gas.

Results and Discussion

Conductivity in $SrCe_{1-x}EuxO_{3-\delta}$

Electrical Properties of $SrCe_{1-x}Eu_xO_{3-\delta\delta}$

X-ray diffraction was used to determine the phase purity of $SrCe_{1-x}Eu_xO_{3-\delta}$ (x = 0.05 to 0.2). Single-phase with orthorhombic perovskite structure was achieved for each dopant concentration. The electrical conductivity of $SrCe_{1-x}Eu_xO_3$ (x = 0.1, 0.15, and 0.2), under various hydrogen atmospheres, was also investigated. In Figure 6, a plot of the electrical conductivity against $P_{H_2}^{1/4}$ in dry hydrogen atmospheres shows a linear relationship between σ_{tot} and $P_{H_2}^{1/4}$, which is consistent with Kosacki et al. for Yb-$SrCeO_3$ [27].

The hydrogen dependence of the conductivity can be explained if we assume that n-type conduction occurs because of the formation of electrons, as shown here

$$H_2(g) + 2O_O^x \leftrightarrow 2OH_O^\bullet + 2e'; \; K_1 = \frac{[OH_O^\bullet]^2 n^2}{P_{H_2}} = \frac{K_2}{K_3K_4} \quad (1)$$

$$H_2(g) + O_O^x \leftrightarrow H_2O(g) + V_O^{\bullet\bullet} + 2e'; \; K_2 = \frac{P_{H_2O}[V_O^{\bullet\bullet}]\; n^2}{P_{H_2}} \quad (2)$$

$$2OH_O^{\bullet} + \frac{1}{2}O_2(g) \leftrightarrow H_2O(g) + 2h^{\bullet} + 2O_O^{x};\ K_3 = \frac{P_{H_2O}p^2}{[OH_O^{\bullet}]^2 P_{O_2}^{\frac{1}{2}}} \qquad (3)$$

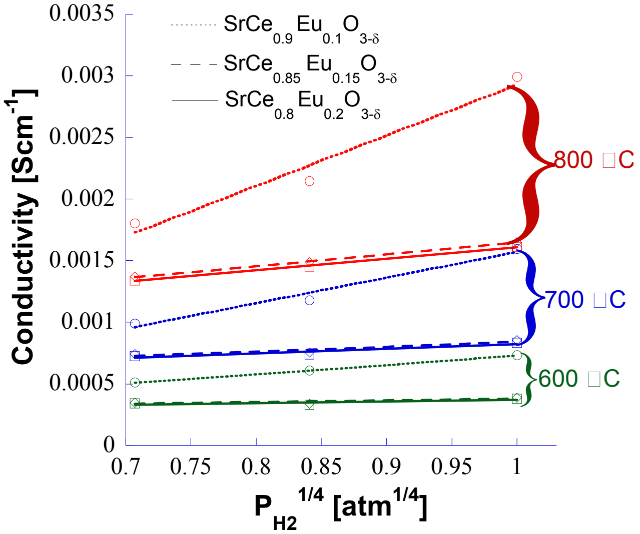

Figure 6. Total conductivity of $SrCe_{1-x}Eu_xO_{3-\delta}$ (x = 0.1, 0.15, and 0.2) as a function of P_{H2}.

The total conductivity of $SrCe_{0.9}Eu_{0.1}O_{3-\delta}$ was higher than that of $SrCe_{0.85}Eu_{0.15}O_{3-\delta}$ and $SrCe_{0.8}Eu_{0.2}O_{3-\delta}$, which are similar in value. Also, $SrCe_{0.9}Eu_{0.1}O_{3-\delta}$ varied more with P_{H2} than other formulations. This behavior may be attributed to protons being the predominant charge carrying species in $SrCe_{0.9}Eu_{0.1}O_{3-\delta}$, whereas $SrCe_{0.85}Eu_{0.15}O_{3-\delta}$ and $SrCe_{0.8}Eu_{0.2}O_{3-\delta}$ show non-negligible electronic conduction.

Protonic, Electronic and Ambipolar Conductivity of $SrCe_{1-x}Eu_xO_3$

Figures 7 and 8 show proton and electron conductivity as a function of dopant level (i.e., x in $SrCe_{1-x}Eu_xO_{3-\delta}$) and temperature for strontium cerate in dry and wet H_2, respectively. In both figures, proton conductivity decreases with increasing dopant concentration due to reduction of proton mobility and entropic destabilization of proton defects [29]. In contrast, electron conductivity increases with increasing Eu dopant. However, there is a slight decrease for x>0.15 in $SrCe_{1-x}Eu_xO_{3-\delta}$ at low temperature due to the increased activation energy for electron conduction. Still, the decrease of electron conductivity in wet H_2 (Figure 8) was greater than that in dry H_2 (Figure 7) due to the higher Po_2 of wet H_2.

Generally, hydrogen permeation flux across the oxide membrane can be calculated using the Wagner equation (equation 4), assuming that bulk diffusion is the rate-limiting step. If oxygen conduction is negligible, then the proton flux, $J_{OH_O^{\bullet}}$, is given by

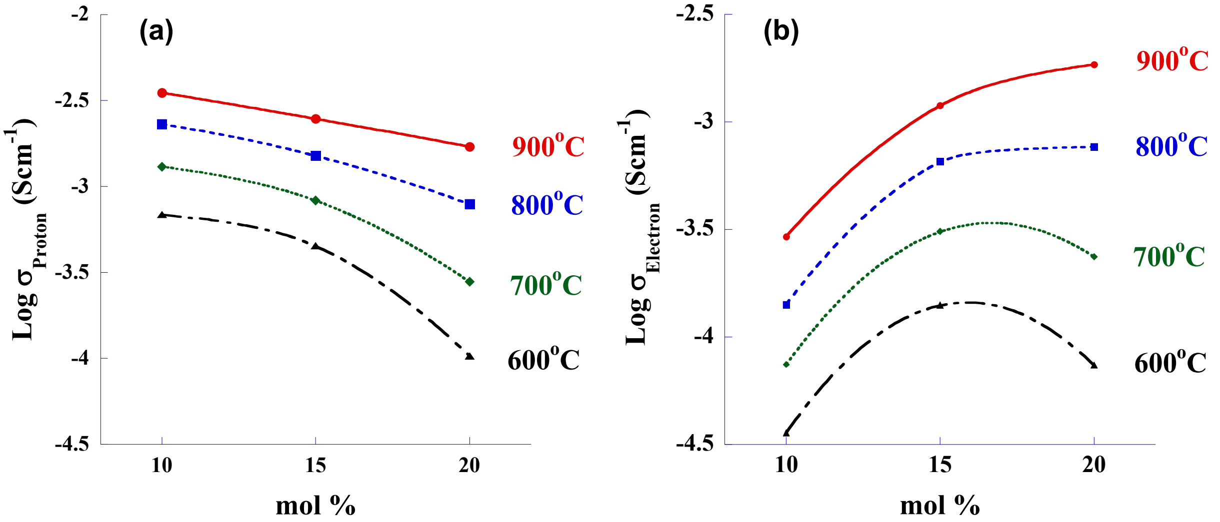

Figure 7. Proton and electron conductivity behavior of $SrCe_{1-x}Eu_xO_{3-\delta}$ (x = 0.1, 0.15, and 0.2) with different temperatures under dry hydrogen atmosphere.

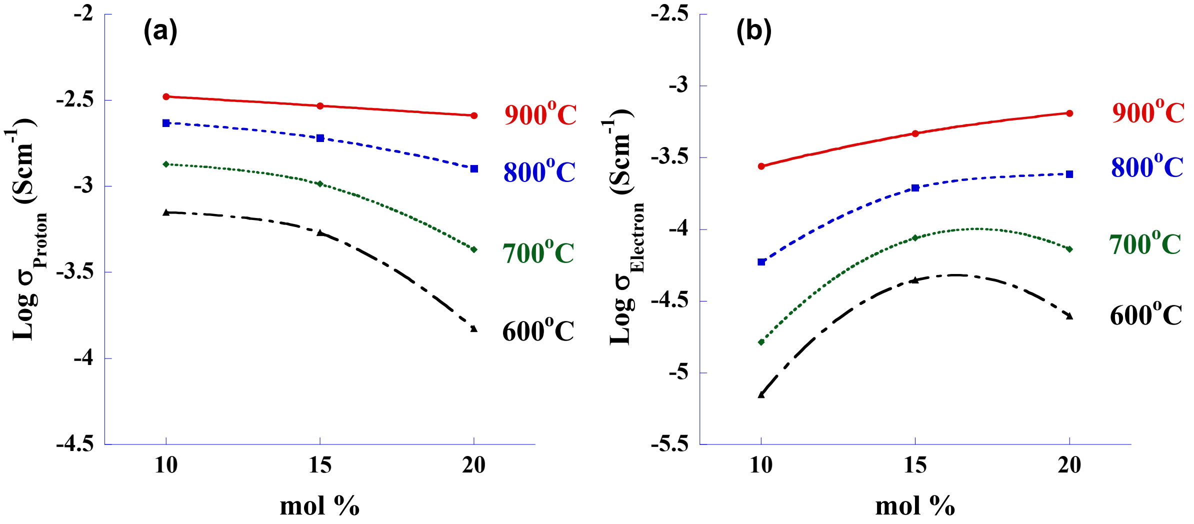

Figure 8. (a) Proton and (b) electron conductivity behavior of $SrCe_{1-x}Eu_xO_{3-\delta}$ (x = 0.1, 0.15, and 0.2) with different temperatures under hydrogen/water vapor atmosphere.

$$J_{OH_O^\bullet} = -\frac{1}{L}\left[\frac{RT}{2F^2}\int_{P'_{H_2}}^{P''_{H_2}} \frac{\sigma_{OH_O^\bullet}\sigma_{e'}}{\sigma_{OH_O^\bullet}+\sigma_{e'}}\, d\,\mathbf{ln}P_{H_2}\right] \rightarrow J_{OH_O^\bullet} \propto \sigma_{amb} = \frac{\sigma_{OH_O^\bullet}\sigma_{e'}}{\sigma_{OH_O^\bullet}+\sigma_{e'}} \qquad (4)$$

where σ_{amb} is the ambipolar conductivity, R is the gas constant, F is Faradays constant, σ is conductivity and L is membrane thickness [20].

Equation 4 shows that hydrogen permeation is proportional to the ambipolar conductivity. Figure 9 shows the ambipolar conductivity dependence on dopant concentration in dry hydrogen atmosphere and hydrogen/water vapor atmosphere. The maximum ambipolar conductivity increases with temperature and Eu dopant concentration in dry hydrogen atmospheres. Therefore, the optimal dopant concentration for maximum ambipolar conductivity is obtained from 15 mol% Eu-doped strontium cerate at 600 °C to 20 mol% Eu-doped strontium cerate at 900 °C. Ambipolar conductivity values in hydrogen/water vapor atmosphere were lower than that in dry hydrogen atmosphere, and the maximum ambipolar conductivity was observed on 20 mol% Eu-doped strontium cerate in the range of investigated temperature. Therefore, maximum hydrogen flux can be achieved by controlling Po_2, dopant concentration, and temperature.

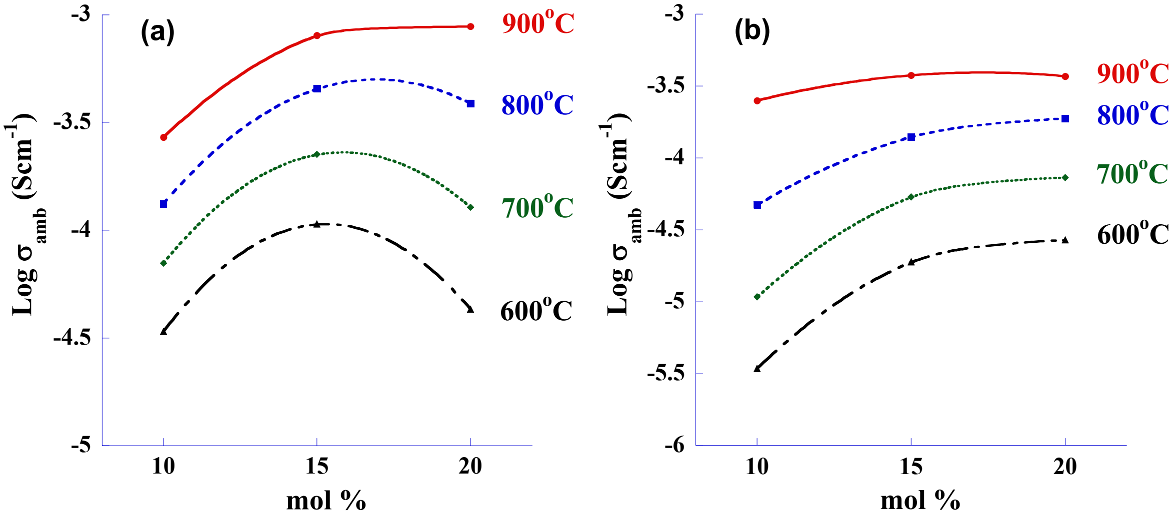

Figure 9. The ambipolar conductivity behavior depends on the dopant concentration under (a) dry hydrogen and (b) hydrogen/water vapor atmospheres.

Stability During Tube Fabrication of Hydrogen Membrane Cell

Evaluation of Supporting Materials: NiO-SC

Undoped strontium cerate was investigated as a support material. The main complication using $SrCeO_3$ as the support material is the reaction between $SrCeO_3$ and NiO at 1450 °C. Thus, NiO-$SrCeO_3$ tapes prepared at temperatures below 1450 °C were characterized. Observed shrinkage behavior of uniaxially-pressed $SrCe_{1-x}Eu_xO_{3-\delta}$, $SrCeO_3$ and tape-casted $SrCeO_3$-NiO shows that $SrCe_{1-x}Eu_xO_{3-\delta}$ sinters more easily than $SrCeO_3$ below 1450 °C and that $SrCe_{1-x}Eu_xO_{3-\delta}$ and NiO-$SrCeO_3$ have comparable shrinkage rates, which is necessary for dense thin film preparation. Moreover, the low sinterability of $SrCeO_3$ should improve the porosity of the support tube. Also, the samples with higher europium concentration demonstrate similar shrinkage rates.

The thermal expansion of $SrCe_{1-x}Eu_xO_{3-\delta}$ and 30 wt% NiO-$SrCeO_3$ must be similar in both air and in hydrogen to avoid failure of the $SrCe_{1-x}Eu_xO_{3-\delta}$ film since the samples are sintered in air and tested in hydrogen. The expansion of $SrCe_{1-x}Eu_xO_{3-\delta}$ is very similar to that of 30 wt% NiO-$SrCeO_3$ in air as shown by Figure 10(a) and the $SrCe_{1-x}Eu_xO_{3-\delta}$ films do not crack after sintering which is confirmed by the SEM micrograph. In hydrogen, the thermal expansion coefficient (TEC) of the 30 wt% NiO-$SrCeO_3$ is approximately 13% higher than the TEC of $SrCe_{1-x}Eu_xO_{3-\delta}$. As shown by Figure 10(b), this expansion difference is not significant enough to result in cracking of the $SrCe_{1-x}Eu_xO_{3-\delta}$ film.

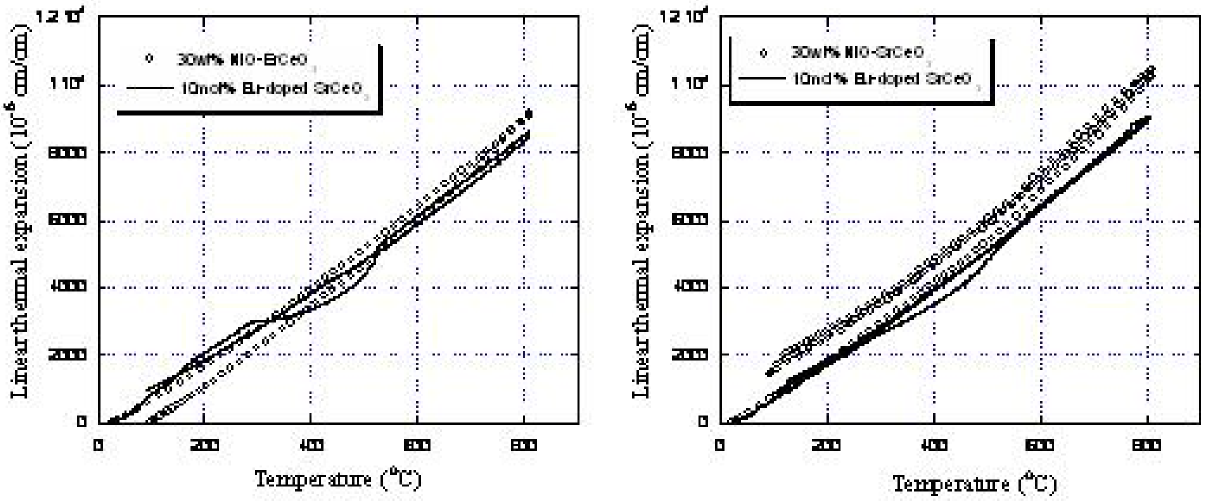

(a) (b)

Figure 10. Thermal expansion behavior of $SrCe_{1-x}Eu_xO_{3-\delta}$ and NiO- $SrCeO_3$ in (a) air and (b) H_2.

Sintering Temperature of ESC film on NiO-SC Support

The tubular-type hydrogen membrane cell is composed of a dense $SrCe_{0.9}Eu_{0.1}O_{3-\delta}$ film and a Ni-$SrCeO_3$ catalytic support. To preserve the integrity of the tube, the shrinkage rates between the $SrCe_{0.9}Eu_{0.1}O_{3-\delta}$ film and the support need to be matched so that cracking does not occur on $SrCe_{0.9}Eu_{0.1}O_{3-\delta}$ film. Figure 11 shows the linear shrinkage rates for NiO-$SrCeO_3$ support, which was prepared by tape casting and Eu_2O_3 doped and un-doped $SrCeO_3$ which were prepared by uniaxial pressing according to the firing temperature.

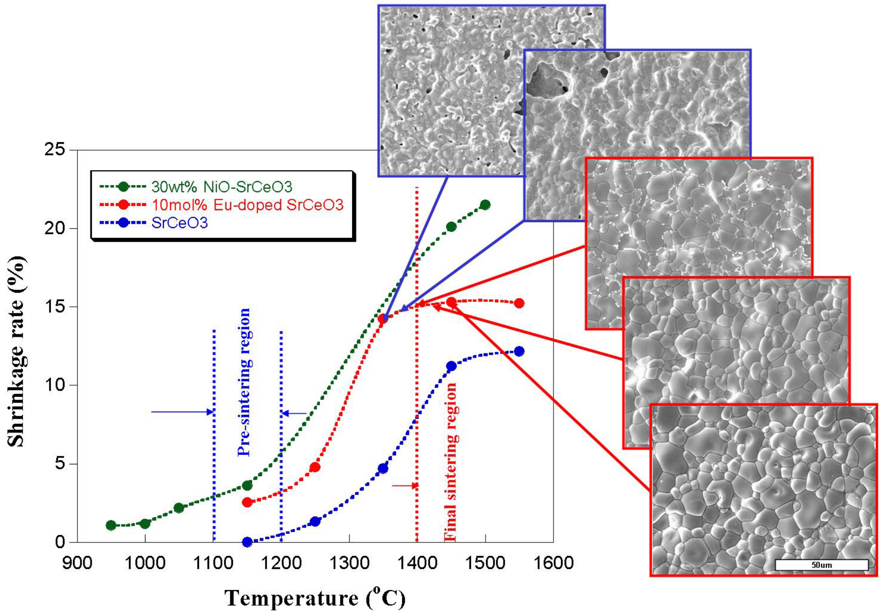

Figure 11. Shrinkage rates for 10 mol% Eu-doped and undoped SrCeO3 and SrCeO3 with 30 wt% NiO green tape. Microstructural images are shown for 10 mol% Eu-doped SrCeO3 thin films on NiO-SrCeO3 supports.

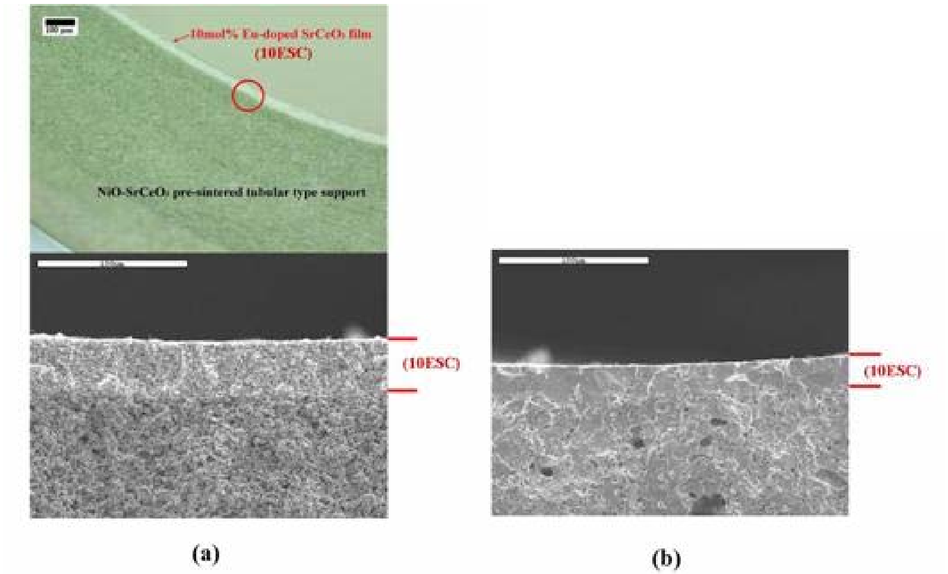

Figure 12. Cross-sectional view of (a) coated $SrCe_{0.9}Eu_{0.1}O_{3-\delta}$ film on partially sintered NiO-$SrCeO_3$ and (b) dense $SrCe_{0.9}Eu_{0.1}O_{3-\delta}$ film on a Ni-$SrCeO_3$ support after sintering and reduction in H_2 atmosphere.

By doping with Eu_2O_3, the $SrCeO_3$ system was easily densified, and the shrinkage rate for $SrCeO_3$ was increased. For the NiO-$SrCeO_3$ tubular-type support, the shrinkage rate of the support was higher than that of the $SrCeO_3$ thin films due to the high concentration of organic vehicles. In order to increase the compatibility of the linear shrinkage of $SrCe_{0.9}Eu_{0.1}O_{3-\delta}$ film and the support, the NiO-$SrCeO_3$ support was initially partially sintered at 1100 to 1200 °C for 4 h. The $SrCe_{0.9}Eu_{0.1}O_{3-\delta}$ hydrogen membrane film which and the partially sintered NiO-$SrCeO_3$ support were then sintered between 1350 to 1450 °C. The microstructures of $SrCe_{0.9}Eu_{0.1}O_{3-\delta}$ film on NiO-$SrCeO_3$ supports according to sintering temperature are shown in Figure 11. From the SEM results, the $SrCe_{0.9}Eu_{0.1}O_{3-\delta}$ film was fully densified above 1400 °C. Also, Figure 12 shows the cross-sectional view of the as-coated $SrCe_{0.9}Eu_{0.1}O_{3-\delta}$ layer on the inner side of the partially sintered NiO-$SrCeO_3$ tubular-type support and the fully densified $SrCe_{0.9}Eu_{0.1}O_{3-\delta}$, with apparent thickness of 30 μm, on the Ni-$SrCeO_3$ support after sintering at 1450 °C and reducing in a hydrogen atmosphere at 900 °C. The porous substrate was achieved by reduction of the NiO-$SrCeO_3$ at 900 °C.

From our investigation, the final sintering temperature should be below 1450 °C to prevent reactions between NiO and strontium cerate, and above 1400 °C to obtain dense films of Eu-doped strontium cerate. In addition, to obtain compatible shrinkage rates between NiO- $SrCeO_3$ and $SrCe_{1-x}Eu_xO_{3-\delta}$ film during sintering, pre-sintering temperatures for the NiO-$SrCeO_3$ support should be in the range 1150 to 1200 °C. Cracks were observed in the NiO-$SrCeO_3$ support when it was pre-sintered at temperatures below 1150 °C; optimal pre-sintering and sintering temperature ranges are given in Figure 11.

Hydrogen Permeation

Hydrogen Permeation Properties at Dry/Wet Hydrogen Atmosphere

The presence of water vapor reduces the concentration of oxygen vacancies and increases that of proton defects. However, hydrogen permeability in humid hydrogen atmosphere is lower due to lower electron concentration resulting from the higher P_{O2} of the humid atmosphere. Figure 13 shows the hydrogen permeation flux for H_2 (P_{H2}=0.03 atm) with and without water vapor in the feeding Ar gas (total 22 cc/min of flow rate) obtained from the hydrogen permeation reactor. As shown in this figure, hydrogen permeation in wet H_2 is slightly lower than that in dry H_2. After reduction in H_2, protons and electrons are the dominating defects. Under this condition, the hydrogen flux is expected to be proportional to $[P_{H2}]^{1/4}$ according to Norby and Larring [22].

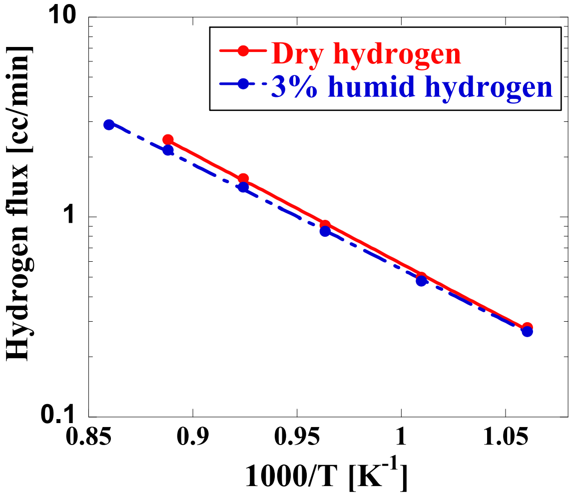

Figure 13. Hydrogen flux in dry/humid hydrogen as a function of temperature.

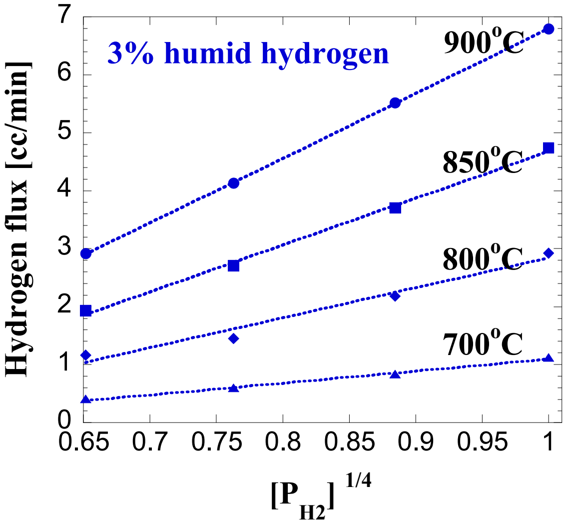

Figure 14. Hydrogen flux as function of P_{H2} and temperature.

The water vapor flux increased with increasing hydrogen partial pressure. In low oxygen partial pressures, oxides can be reduced, releasing oxygen which will form water vapor in the presence of H_2. If the water vapor comes from the reaction of the permeated H_2 and oxygen ions in $SrCe_{1-x}Eu_xO_{3-\delta}$ lattice, then the H_2 permeation should be decreased as a result.

When the hydrogen permeation membrane is exposed to a wet hydrogen atmosphere, protons and electrons are the dominating defects and the hydrogen flux through the membrane is proportional to $[P_{H2}]^{1/4}$ as shown in Figure 14.

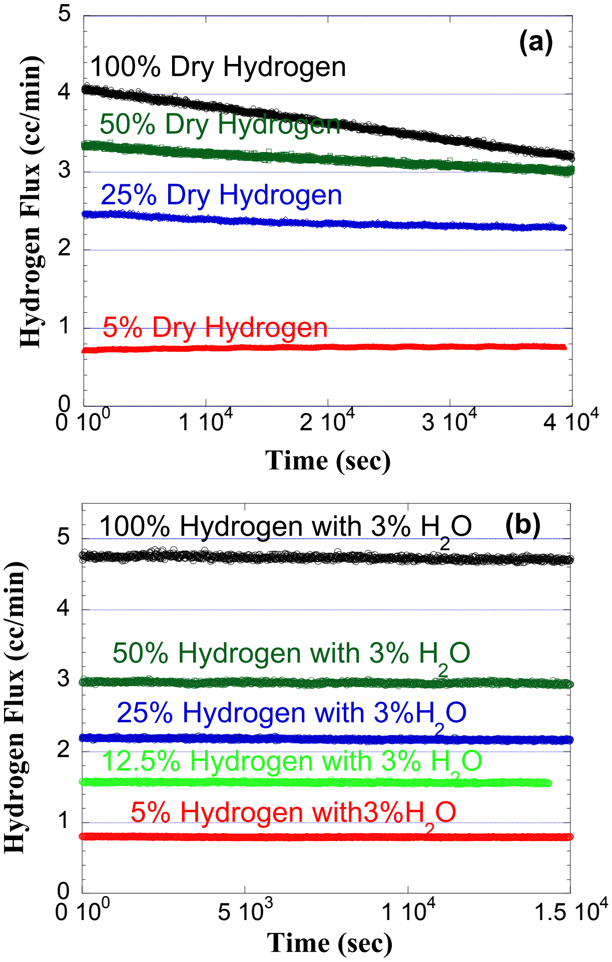

Figure 15. Time dependence of Hydrogen flux according to the P_{H2} with (a) Dry and (b) Wet H_2.

Figure 15 shows dry and wet hydrogen permeation flux on $SrCe_{0.9}Eu_{0.1}O_{3-\delta}$,. The permeability of $SrCe_{0.9}Eu_{0.1}O_{3-\delta}$ under dry hydrogen atmosphere is higher than under wet hydrogen atmosphere. Under dry hydrogen atmosphere, hydrogen permeation flux through $SrCe_{0.9}Eu_{0.1}O_{3-\delta}$ degraded with time and this degradation was more severe under high hydrogen partial pressure on the feed side. On the contrary, the $SrCe_{0.9}Eu_{0.1}O_{3-\delta}$, under wet hydrogen atmosphere, shows stable hydrogen permeation flux with time. This degraded hydrogen permeation under dry hydrogen atmosphere may be interpreted as evidence for the secondary CeO_2 phase formation by decomposition.

Hydrogen Permeation Properties from CH_4 Steam Reforming

We have evaluated the hydrogen permeability for the $SrCe_{1-x}Eu_xO_{3-\delta}$ tubular-type hydrogen membrane cell in a H_2 atmosphere on the feed side. The overall goal of the $SrCe_{1-x}Eu_xO_{3-\delta}$ hydrogen membrane cell is pure hydrogen production from hydrocarbon fuels. Figure 16 shows hydrogen flux for CH_4 on the feed side.

In order to use steam reforming of methane for hydrogen production using a hydrogen membrane cell, we have to consider methane conversion rates, partial pressure of product hydrogen, and solid state carbon formation rates. Using thermodynamic data for CH_4 and H_2O, we calculated the conversion rate of methane, H_2 partial pressure after methane conversion, and the amount of carbon formation according to the ratio of methane to steam. When the steam ratio is increased, the conversion rate of methane and the hydrogen partial pressure are increased. As shown in Figure 18, the hydrogen flux through the $SrCe_{1-x}Eu_xO_{3-\delta}$ membrane for methane was higher than when pure H_2 was introduced. This is due to the increase of hydrogen partial pressure after methane was converted to CO, CO_2, and H_2 by the steam reforming process.

Nevertheless, the issue of coking needs to be considered when was using the hydrogen membrane cells on Ni-based porous support materials for the steam reforming of the methane process. Coking can cause degradation of hydrogen permeability and crack formation in the hydrogen permeation cells. As the steam ratio for methane increases, the formation of carbon decreases and the hydrogen permeation through the $SrCe_{1-x}Eu_xO_{3-\delta}$ membrane increases. For the steam reforming of methane, the methane to steam ratio should be below 0.6 to avoid coking and to increase the production of pure hydrogen.

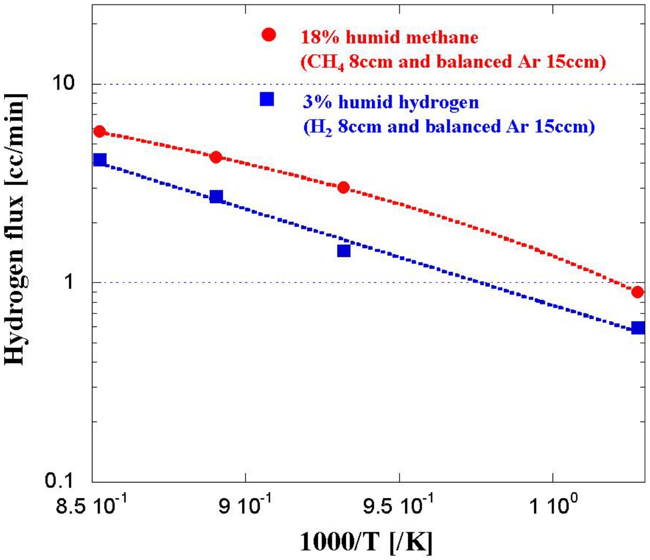

Figure 16. Temperature dependence of H_2 flux in humid hydrogen/methane.

Figure 17 shows the $SrCe_{0.9}Eu_{0.1}O_{3-\delta}$/Ni-$SrCeO_3$ and $SrCe_{0.9}Eu_{0.1}O_{3-\delta}$/Ni-$SrCe_{0.8}Zr_{0.2}O_3$ hydrogen membrane cells after exposed in methane with 8% steam. In the case of $SrCe_{0.9}Eu_{0.1}O_{3-\delta}$/Ni-$SrCeO_3$ cell, the crack occurred at around the 700 °C region. However, there were no cracks on the $SrCe_{0.9}Eu_{0.1}O_{3-\delta}$/Ni-$SrCe_{0.8}Zr_{0.2}O_3$ hydrogen membrane cell. The crack is possibly caused by the phase change of $SrCeO_3$ in CO/CO_2 atmosphere and/or the coking in methane steam reforming that is above 0.6 ratio of CH_4/H_2O. Substitution of Zr onto Ce-site enhances the structural stability of $SrCeO_3$ and hence decreases the probability of cracking for the hydrogen membrane cell. Thus, the fabrication process for the tubular-type hydrogen membrane cells was modified accordingly.

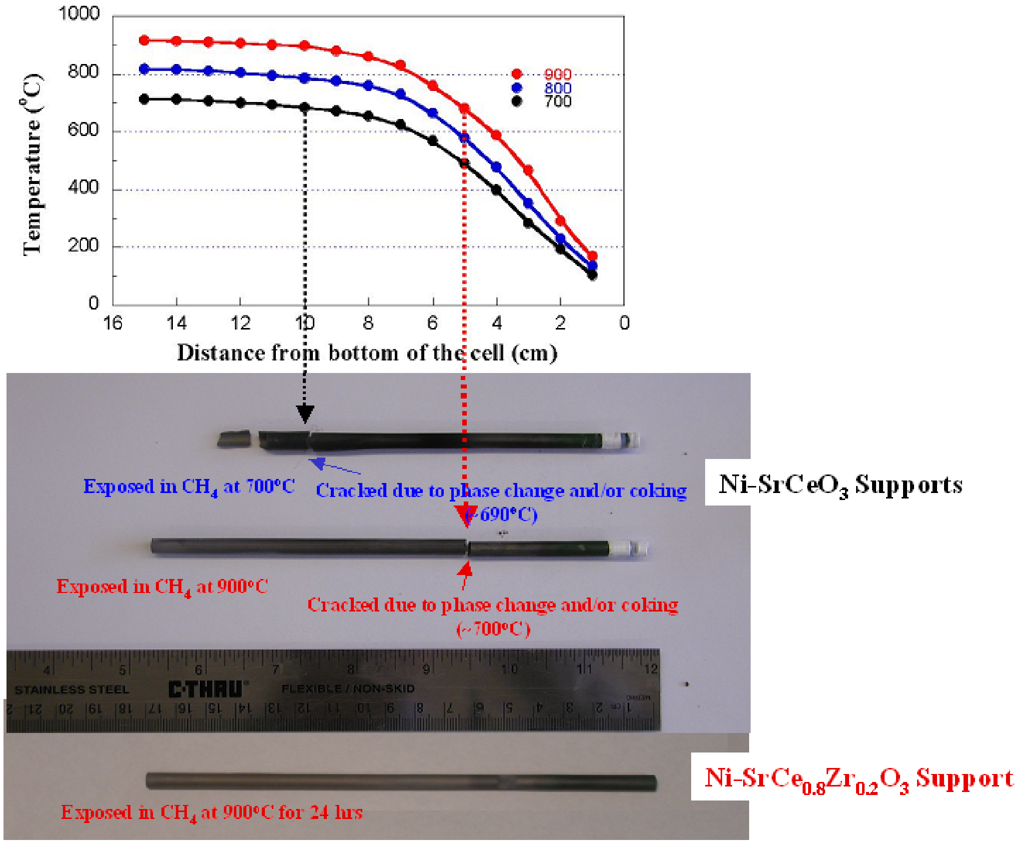

Figure 17. Photograph of the $SrCe_{0.9}Eu_{0.1}O_{3-\delta}$/Ni-$SrCeO_3$ and 10ESC/Ni-$SrCe_{0.8}Zr_{0.2}O_3$ hydrogen membrane cells after exposed in methane with 8% steam.

10ESC/Ni-$SrCeO_3$/Ni-$SrCe_{0.8}Zr0_{0.2}O_3$ Tubular-type Hydrogen Membrane Cells

In order to prevent the reaction due to Zr-ion diffusion to $SrCe_{0.9}Eu_{0.1}O_{3-\delta}$ layer, the Ni-$SrCeO_3$ buffer layer was placed between $SrCe_{0.9}Eu_{0.1}O_{3-\delta}$ and Ni-$SrCe_{0.8}Zr0_{0.2}O_3$ layer as shown in Figure 18. However, the Ni-$SrCeO_3$ buffer layer looks dense after sintering the hydrogen membrane cell. The hydrogen flux for $SrCe_{0.9}Eu_{0.1}O_{3-\delta}$/Ni-$SrCeO_3$/Ni-$SrCe_{0.8}Zr0_{0.2}O_3$ hydrogen membrane cell was higher than that of the cell without the Ni-$SrCeO_3$ buffer layer, Figure 19, but the flux level was still lower than that of the $SrCe_{0.9}Eu_{0.1}O_{3-\delta}$/Ni-$SrCeO_3$ cell. To increase the hydrogen flux through the $SrCe_{0.9}Eu_{0.1}O_{3-\delta}$/Ni-$SrCe_{0.8}Zr0_{0.2}O_3$ hydrogen membrane cell, it is necessary to increase the porosity of Ni-10ESC buffer layer, thereby increasing the gas flow to the $SrCe_{0.9}Eu_{0.1}O_{3-\delta}$ layer.

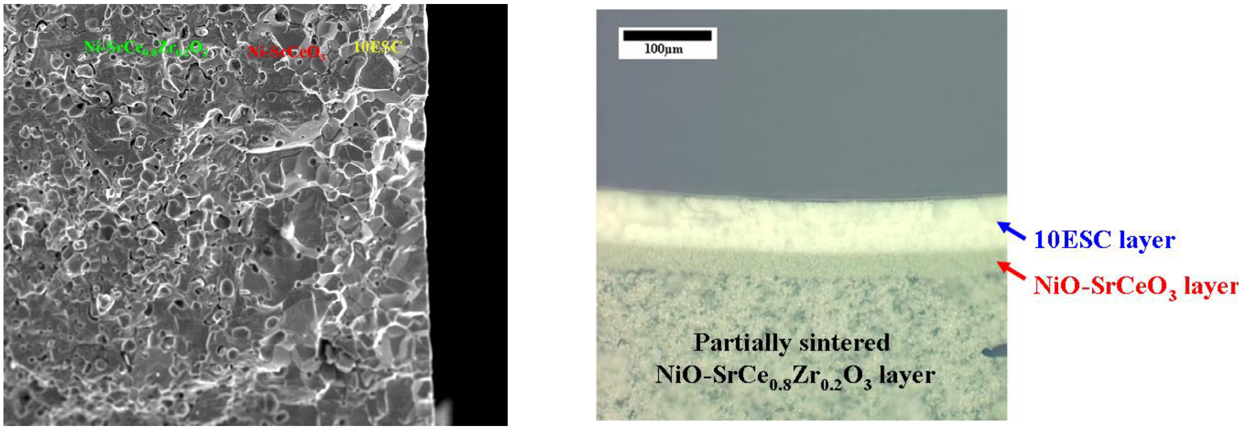

(a) (b)

Figure 18. (a) FESEM image and (b) photograph of 10ESC/Ni-$SrCeO_3$/Ni-$SrCe_{0.8}Zr0_{0.2}O_3$ hydrogen membrane cell.

Ni-$SrCe_{0.8}Zr0_{0.2}O_3$ Tubular-type Supports

To determine the phase stability of the cell supports in CO/CO_2 produced by methane steam reforming, the Ni-$SrCe_{0.8}Zr0_{0.2}O_3$ system was used instead of the previous Ni-$SrCeO_3$ systems. Figure 19 shows the hydrogen flux through the $SrCe_{0.9}Eu_{0.1}O_{3-\delta}$ /Ni-$SrCe_{0.8}Zr0_{0.2}O_3$ hydrogen membrane cell. However, the flux level is much lower than that of $SrCe_{0.9}Eu_{0.1}O_{3-\delta}$/Ni-$SrCeO_3$ cell. The SEM images show the grains of $SrCe_{0.9}Eu_{0.1}O_{3-\delta}$ close to the interface of $SrCe_{0.9}Eu_{0.1}O_{3-\delta}$ and Ni-$SrCe_{0.8}Zr0_{0.2}O_3$ are larger than those close to the top of $SrCe_{0.9}Eu_{0.1}O_{3-\delta}$ layer. We supposed that the Zr ions reacted at the interface between the support and $SrCe_{0.9}Eu_{0.1}O_{3-\delta}$ layer.

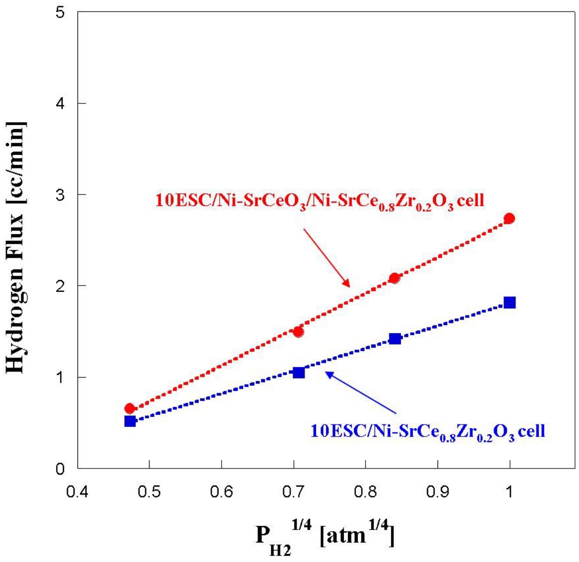

Figure 19. Comparison of hydrogen flux for the $SrCe_{0.9}Eu_{0.1}O_{3-\delta}$/Ni-$SrCe_{0.8}Zr0_{0.2}O_3$ H_2 membrane cells with or without Ni-$SrCeO_3$ buffer layer as a function of $P_{H2}^{1/4}$ in humid hydrogen at 900 °C.

10ESZC or 15ESZC / Ni-SrCe$_{0.8}$Zr0$_{0.2}$O$_3$ Tubular-type Hydrogen Membrane Cells

Inevitable Zr ion diffusion into the membrane material resulted on Zr substituted ESC membrane materials. Though permeation flux could decrease by Zr substitution, continuous stable hydrogen permeation flux and chemical stability under CO/CO$_2$ condition can be achieved. SrZr$_{0.2}$Ce$_{0.7}$Eu$_{0.1}$O$_{3-\delta}$ and SrZr$_{0.2}$Ce$_{0.65}$Eu$_{0.15}$O$_{3-\delta}$ hydrogen membranes show increased hydrogen flux with temperature and hydrogen partial pressure. They also show $[P_{H2}]^{1/4}$ dependence of hydrogen permeation as in Norby and Larring's model. Both hydrogen permeation show linear dependence with membrane thickness which means bulk diffusion is the rate-limiting factor for permeation.

Water vapor can be formed from the reaction with permeated hydrogen gas and oxygen gas which comes from oxide lattice under reduced atmosphere. This water vapor formation may reduce the permeated hydrogen pressure. The permeated hydrogen from the both proton membrane (SrZr$_{0.2}$Ce$_{0.7}$Eu$_{0.1}$O$_{3-\delta}$ & SrZr$_{0.2}$Ce$_{0.65}$Eu$_{0.15}$O$_{3-\delta}$) with counting on the hydrogen from water formation on the permeated side are shown in Figures 20(a) and 20(b), respectively. Increased hydrogen permeation with Eu dopant concentration in membrane material was observed.

Figure 21 shows the hydrogen flux versus time at 5% CO and 3% H$_2$O at 900 °C. It decreased with time and an 8% drop was observed in 8 h for SrCe$_{0.9}$Eu$_{0.1}$O$_{3-\delta}$ membrane. The hydrogen flux was stable for the SrZr$_{0.2}$Ce$_{0.7}$Eu$_{0.1}$O$_{3-\delta}$ membrane, which verifies the stability enhancement by zirconium dopant.

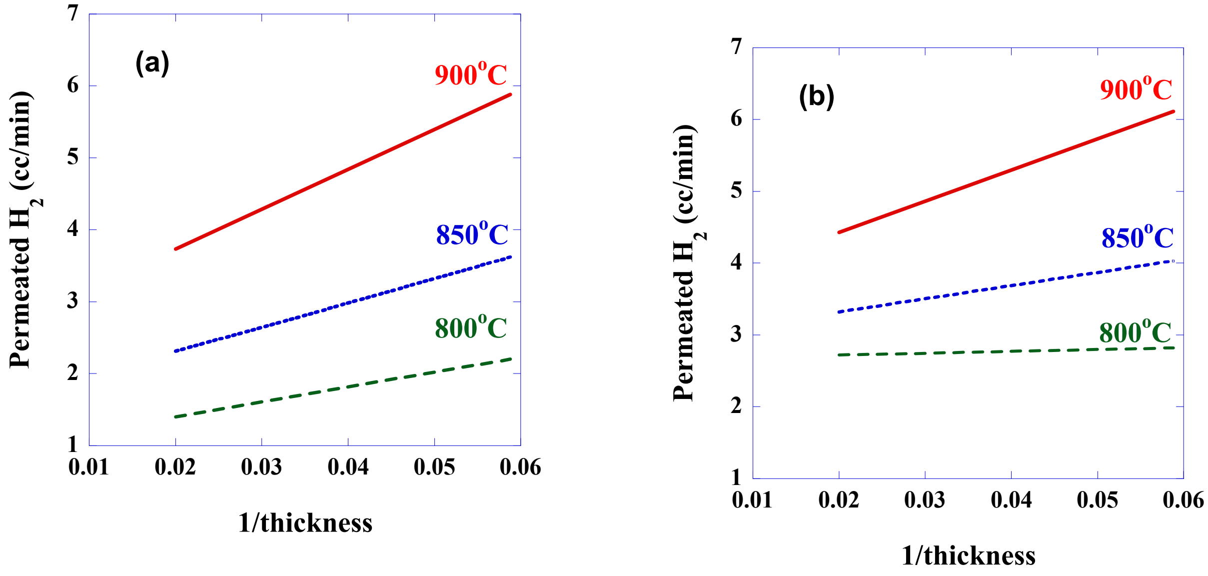

Figure 20. Permeated hydrogen from A) SrZr$_{0.2}$Ce$_{0.7}$Eu$_{0.1}$O$_{3-\delta}$ and B) SrZr$_{0.2}$Ce$_{0.65}$Eu$_{0.15}$O$_{3-\delta}$ with counting hydrogen from water formation.

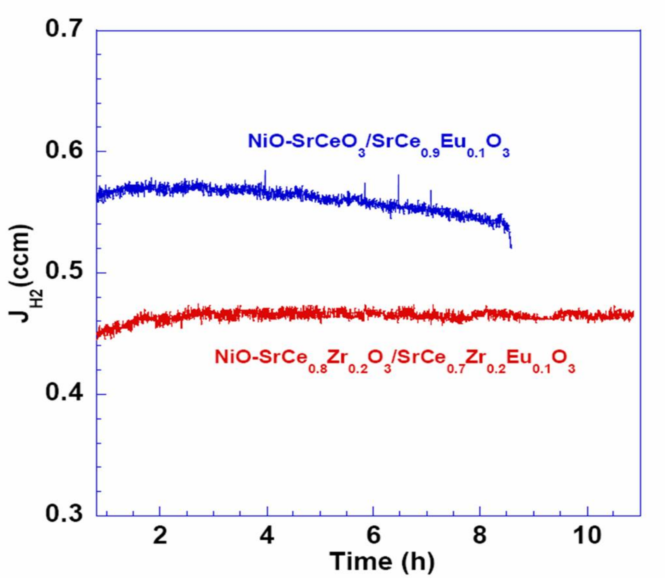

Figure 21. Hydrogen flux as a function of time under WGS reaction atmosphere.

$SrCeO_3$-based Hydrogen Transport under Water Gas Shift Reaction

After the supported hydrogen membrane was synthesized, a WGS reactor was fabricated by installing the hydrogen membrane to a quartz reactor and connecting it to the gas line by O-rings. The WGS reactor was put into a furnace vertically. The reactants (CO and steam) were flown from the top of the reactor to the outside of the hydrogen membrane. The retained gases were analyzed by gas chromatography (Varian CP 4900). A sweeping gas was flown to the inside of the hydrogen membrane. The outlet of sweeping gas was connected to a mass spectrometer so that the permeated hydrogen can be analyzed by the mass spectrometer (Q100MS Dycor, Quadlink). Gas flow rates were controlled by mass flow controllers. To investigate the effect of the WGS reactor on the hydrogen production and separation, three experiments were carried out with constant flow rates and concentrations of the reactants:

(1) WGS reaction without hydrogen membrane: CO and H_2O were fed into the quartz reactor without installing the hydrogen membrane.
(2) WGS reaction with hydrogen membrane, functioning solely as a catalyst: CO and H_2O were fed to the outside of the hydrogen membrane with the sweep side of the membrane blocked to prevent hydrogen removal by permeation.
(3) WGS reaction with the hydrogen membrane and in-situ hydrogen removal: CO and H_2O were fed to the outside of the hydrogen membrane. A sweeping gas was flown to the inner side of the membrane and the permeated hydrogen was carried out by the sweeping gas and analyzed by the mass spectrometer.

The CO conversion and hydrogen selectivity is calculated as:

$$X_{CO}\% = \frac{C^{out}_{CO_2}}{C^{out}_{CO} + C^{out}_{CO_2}} \times 100\% \tag{5}$$

$$X_{H_2}\% = \frac{F^S \times C^P_{H_2}}{F^R \times C^{out}_{H_2} + F^S \times C^P_{H_2}} \times 100\% \tag{6}$$

where C_{CO}^{out}, $C_{CO_2}^{out}$ and $C_{H_2}^{out}$ are the concentrations of CO, CO_2, and H_2 at the reactant outlet analyzed by the gas chromatography, respectively. $C_{H_2}^{P}$ is the concentration of permeated H_2 analyzed by the mass spectrometer. F^s and F^R are the total flow rates of the sweeping gas and reactant gas outlet. In all three modes, two different gas compositions were applied: 3% CO +3% H_2O and 3% CO +6% H_2O, while maintaining a constant flow rate balanced by Ar. Gas flow rates were controlled by mass flow controllers.

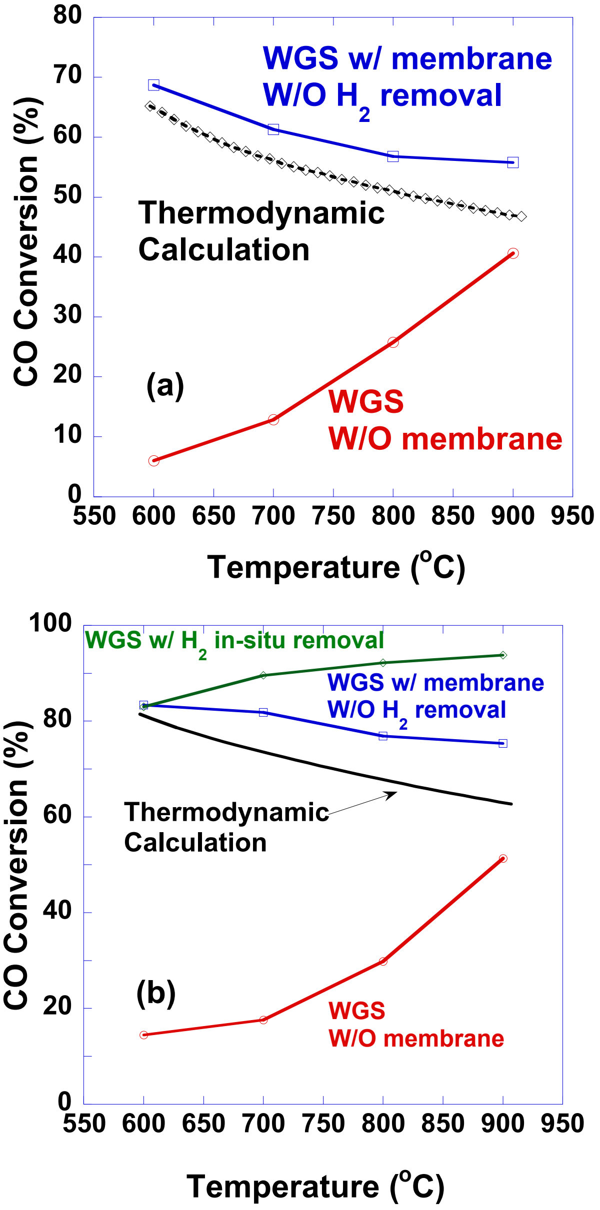

Figure 22. CO conversion versus temperature with (a) CO/H_2O=1:1 and (b) CO/H_2O=1:2.

Figure 22 shows the temperature dependence on CO conversion at three conditions with CO/H_2O ratio of 1:1 and 1:2, respectively. For the WGS without hydrogen membrane, CO conversion was lower than the thermodynamically calculated value, but increased with rising temperature for both CO/H_2O=1:1 and 1:2. The reaction rate may be quite slow without catalyst. The dwell time for CO and H_2O in the reactor was very short. Equilibrium could not be reached before the gases exited the reactor, so the CO conversion was lower than the equilibrium value. On the other hand, the reaction rate increased with increasing temperature. Hence, a higher temperature resulted in higher reaction rate and higher CO conversion. With the catalyst, the CO conversion was slightly higher than the calculation value and decreased with increasing temperature.

The WGS reaction consisted of a series of reactions, and the thermodynamic calculation was based on the assumption that all those reactions were in equilibrium. However, equilibrium may not have been achieved in such a short dwell time, even in the presence of Ni catalyst, which affected the CO conversion. Due to the exothermic nature of WGS reaction, CO conversion was more favorable at lower temperature. Figure 22(b) shows the CO conversion increased with increasing temperature with hydrogen in-situ removal and was higher than that with the catalyst. Timely in-situ removal of hydrogen, through the hydrogen membrane, reduced the hydrogen concentration on the product side and moved the reaction forward toward product side, resulting in a higher CO conversion.

The hydrogen permeability of $SrCe_{0.9}Eu_{0.1}O_{3-\delta}$ increases with increasing temperature due to higher protonic and electronic conductivity [30]. A larger amount of H_2 permeated through $SrCe_{0.9}Eu_{0.1}O_{3-\delta}$ at higher temperature, leading to a larger improvement of CO conversion compared to that with the catalyst.

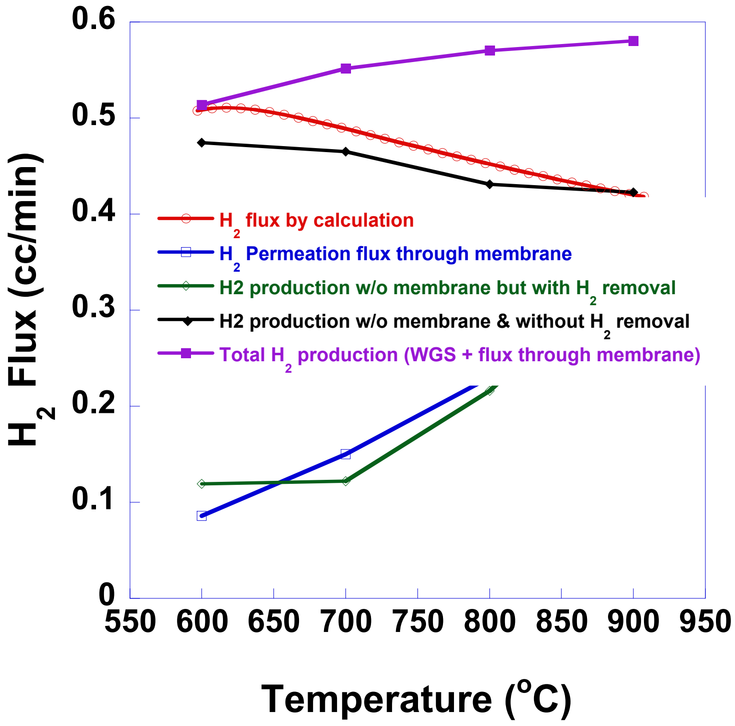

Figure 23. H_2 flux versus temperature with a total flow rate of 20 ccm.

Figure 23 shows, for the thermodynamic calculation, that hydrogen flux decreases with increasing temperature, in accordance with the CO conversion in Figure 22(a). The plot also shows the hydrogen production for WGS in the absence of a hydrogen membrane, increases with increasing temperature, a similar trend with the CO conversion, which can be explained by the kinetic reaction rate. However, without hydrogen removal hydrogen production decreased with increasing temperature, in agreement with (though slightly lower than) the trend of the calculated data. The difference was possibly caused by the by-reactions, such as the formation of methane, consuming some of the produced hydrogen.

Finally, Figure 23 shows the hydrogen permeation flux increased with temperature due to higher ambipolar conductivity at higher temperature. Likewise, the total hydrogen production increased with increasing temperature, in agreement with the trend of the CO conversion. At 900 °C, there was 39% improvement in hydrogen production compared to the equilibrium value.

Conclusion

The total conductivity of $SrCe_{1-x}Eu_xO_{3-\delta}$ (x = 0.1 to 0.2) was measured by impedance spectroscopy, and ambipolar conductivity was calculated with proton and electron transference numbers. In the temperature range studied, $SrCe_{0.9}Eu_{0.1}O_{3-\delta}$ showed the highest total conductivity in both conditions. However, the proton transference number decreases with increasing europium dopant concentration, and electron transference number increases with increasing dopant concentration due to increasing n-type electronic conduction. In other words, proton conductivity decreases with increasing dopant concentration, while electron conductivity increases. A slight decrease in electronic conductivity for $x>0.15$, at low temperature, is observed due to the increased activation energy for electron conduction. The highest ambipolar conductivity was obtained from $SrCe_{0.85}Eu_{0.15}O_{3-\delta}$ to $SrCe_{0.8}Eu_{0.2}O_{3-\delta}$ between 600 °C and 900 °C under dry hydrogen atmosphere and $SrCe_{0.8}Eu_{0.2}O_{3-\delta}$ under hydrogen/water vapor atmosphere.

$NiO-SrCeO_3$ tubular-type supports for thin film hydrogen separation membranes were prepared by tape casting and rolling after the optimized slurry for tape casting was achieved. $SrCe_{0.9}Eu_{0.1}O_{3-\delta}$ thin film hydrogen separation membranes on the inner side of the partially sintered $NiO-SrCeO_3$ tubular supports were obtained by the colloidal coating method. Leak-free, 15 cm long, end-capped, tubular $SrCe_{0.9}Eu_{0.1}O_{3-\delta}/Ni-SrCeO_3$ hydrogen production cells were prepared by adjusting pre-sintering and final sintering temperatures. Hydrogen separation using the $SrCe_{0.9}Eu_{0.1}O_{3-\delta}/Ni-SrCeO_3$ hydrogen membrane cell was successfully performed without leakage.

Hydrogen production was improved significantly by incorporating the $SrCe_{0.9}Eu_{0.1}O_{3-\delta}/Ni-SrCeO_3$ hydrogen separation cell for both the water-gas shift reaction and steam reforming. For the WGS reaction an improvement of 39% in hydrogen production compared to the equilibrium value was achieved at 900 °C.

Publications

1. “Determination of Optimal Eu dopant Concentration in $SrCe_{1-x}Eu_xO_{3-\delta}$ for Hydrogen Permeation,” T. Oh, H. Yoon and E. Wachsman, to be submitted.

2 “Transport Phenomena of $SrCe_{1-x}Eu_xO_{3-\delta}$ under Hydrogen atmosphere,” T. Oh, H. Yoon and E. Wachsman, to be submitted.

3. “Stability of $SrCe_{0.9}Eu_{0.1}O_{3-\delta}$ and $SrZr_{0.2}Ce_{0.7}Eu_{0.1}O_{3-\delta}$ under dry/wet H2 and CO atmosphere,” T. Oh, J. Li, H. Yoon and E. Wachsman, to be submitted.

4. “Tubular-type Proton Conducting Membrane Process and Permeability of $SrCe_{1-x}Eu_xO_{3-\delta}$,” T. Oh, H. Yoon and E. Wachsman, to be submitted.

5. “Stability improvement of $SrCeO_3$ using zirconium dopant under CO/H_2O atmosphere,” J. Li, H. Yoon, T. Oh and E. Wachsman, to be submitted to *J. Am. Cera. Soc.*

6. “Non-galvanic Hydrogen Production Using High Steam Pressure Gradients,” Sun-Ju Song and Eric D. Wachsman, Chemistry Letters Vol.35, No.9 (2006).

7. “Hydrogen Permeability and Microstructure Effect on Mixed Protonic-Electronic Conducting Eu-doped Strontium Cerate,” S.-J. Song, E.D. Wachsman, J.M. Rhodes, H.-S. Yoon, G. Zhang, K.-H. Lee, S.E. Dorris and U. Balachandran, Journal of Materials Science, **40**, 4061-4066 (2005).

8. “Hydrogen Production from Fossil Fuels with High Temperature Ion Conducting Ceramics,” E. D. Wachsman and M.C. Williams, *Interface*, 13-3, 32-37 (2004).

9. “Hydrogen Permeability of $SrCe_{0.95}Eu_{0.05}O_{3-\delta}$ (x = 0.05, M = Eu, Sm)”, S. J. Song, E. D. Wachsman, J. Rhodes, S. E. Dorris and U. Balachandran, *Solid State Ionics*, **167**, 99-105 (2004).

10. “Numerical Modeling of Hydrogen Permeation in Chemical Potential Gradients,” S. J. Song, E. D. Wachsman, J. Rhodes, S. E. Dorris and U. Balachandran, *Solid State Ionics*, **164**, 107-116 (2003).

11. “Defect Structure and n-Type Electrical Properties of $SrCe_{0.95}Eu_{0.05}O_{3-\delta}$”, S. J. Song, E. D. Wachsman, S. E. Dorris and U. Balachandran, *Journal of the Electrochemical Society*, **150**, A1484 (2003).

12. “Electrical Properties of p-Type Electronic Defects in the Protonic Conductor $SrCe_{0.95}Eu_{0.05}O_{3-\delta}$”, S. J. Song, E. D. Wachsman, S. E. Dorris and U. Balachandran, *Journal of the Electrochemical Society*, **150**, A790 (2003).

13. “Defect Structure and n-Type Electrical Properties of $SrCe_{0.95}Eu_{0.05}O_{3-\delta}$”, S. Song, E.D. Wachsman, S.E. Dorris and U. Balachandran, *Solid State Ionic Devices III*, Electrochem. Soc., E.D. Wachsman, K.S. Lyons, M. Carolyn, F. Garzon, M. Liu and J. Stetter, Ed., **2002-26**, 456-470 (2003).

Presentations

1. “Eu Dopant Contents Optimization for Maximum Hydrogen Production on $SrCeO_{3-\delta}$,” T. Oh, H. Yoon and E. Wachsman, presented in the Symposium "Hydrogen Production, Transport, and Storage 2," of the 211th Meeting of the Electrochemical Society which held in Chicago, Illinois from May 6 - May 10, 2007.

2. “Phase Stability and Hydrogen Permeation Properties of SrCeO3 for Methane Steam Reforming,” H. Yoon, T. Oh, J. Li, E.D. Wachsman, *31st International Cocoa Beach*

Conference Exposition on Advanced Ceramics & Composites in Daytona Beach, Florida (2007).

3. “Determination of Optimal Eu dopant Concentration in $SrCe_{1-x}Eu_xO_{3-\delta}$ for Hydrogen Permeation,” T. Oh, H. Yoon, E. D. Wachsman, *31st International Cocoa Beach Conference Exposition on Advanced Ceramics & Composites in Daytona Beach, Florida (2007).*

4. “Hydrogen Transport Water Gas Shift Membrane Reactor,” J. Li, H. Yoon, T. Oh, E. D. Wachsman, *31st International Cocoa Beach Conference Exposition on Advanced Ceramics & Composites in Daytona Beach, Florida* (2007).

5. “Electrochemical Studies of Mixed Protonic Electronic Conduction in Eu-doped $SrCeO_3$,” T. Oh, H. Yoon, E. Wachsman, *209th ECS meeting in Denver, Colorado* (2006).

6. “Hydrogen Permeation through Dense $SrCe_{0.9}Eu_{0.1}O_{3-\delta}$ Membrane on Ni-$SrCeO_3$ Tubular Supports,” E. Wachsman, H. Yoon, *209th ECS meeting in Denver, Colorado* (2006).

7. “Fabrication of Thin Film Eu-doped $SrCeO_3$ Hydrogen Membrane on Ni-$SrCeO_3$ support,” H. Yoon, T. Oh, E. Wachsman, *209th ECS meeting in Denver, Colorado* (2006).

8. “Fabrication and Hydrogen permeation properties of Dense Eu-doped $SrCeO_3$ Membrane on Ni-$SrCeO_3$ Support,” H. Yoon, T. Oh, and E. Wachsman, *208th ECS meeting in Los Angeles*, (2005).

9. *“*The Stability and Permeation properties of $SrCe_{0.9}Eu_{0.1}O_3$*,”* T. Oh, H. Yoon, and E. Wachsman, *208th ECS meeting in Los Angeles*, (2005).

10. “Fabrication of Dense Eu-doped $SrCeO_{3-\delta}$ Membrane on Ni-$SrCeO_3$ Tubular-type Support”, H.-S. Yoon, E.D. Wachsman and J.M. Rhodes, 29th International Cocoa Beach Conference and Exposition on Advanced Ceramics and Composites, Cocoa Beach, January 2005.

11. “Preparation of Thin Film Inorganic Hydrogen Separation Membranes on Ni-GDC Tubular-type Supporters Using Tape Casting Process”, H.-S. Yoon, S.-J. Song, E.D. Wachsman and J.-H. Lee, 28th International Cocoa Beach Conference and Exposition on Advanced Ceramics and Composites, Cocoa Beach, January 2004.

12. “Hydrogen Permeability of Mixed Protonic-Electronic Conducting Multivalent Cation Doped Strontium Cerate”, S.-J. Song, E.D. Wachsman, J. Rhodes, H.-S. Yoon and G. Zhang, 204th Meeting of The Electrochemical Society, Orlando, October 2003.

13. “Preparation of Dense Barium Cerate Film on Planar Porous Substrate for Hydrogen Seperation Membranes”, R. Bagul, H.-S. Yoon, S.-J. Song and E.D. Wachsman, 204th Meeting of The Electrochemical Society, Orlando, October 2003.

Post Doctoral Associate

Dr. Heesung Yoon

Students from Research

Former-Graduate Students:
Sun-Ju Song, Ph.D.
Dissertation: “Mixed Protonic-Electronic Conductors for Hydrogen Separation Membrane”

J.M. Rhodes, Ph.D.
Dissertation: “Effect of B-Site Europium Doping the Hydrogen Transport Properties of Barium Cerate”

G. Zhang, Ph.D.
Dissertation: “Synthesis and Characterization of a New Proton Conducting Material and Its Use as Hydrogen Separation Membrane”

Tak-keun Oh,
Dissertation: “Optimization of Eu doped SrCeO3 Mixed Conducting Ceramic Membrane for Maximum Hydrogen Production”

Current-Graduate Students:
Jianlin Li

References

1. J. Guan, S.E. Dorris, U. Balachandran and M. Liu, *Solid State Ionics* **100** (1997) (1-2), p. 45.
2. H. Iwahara, T. Esaka, H. Uchida and N. Maeda, *Solid State Ionics* **3-4** (1981) (Aug), p. 359.
3. T. Tsuji and T. Nagano, *Solid State Ionics* **136-137** (2000), p. 179.
4. H. Iwahara, H. Uchida, K. Ogaki and H. Nagato, *J Electrochem Soc* **138** (1991) (1), p. 295.
5. H. Iwahara, *Solid State Ionics* **52** (1992) (1-3), p. 99.
6. J.M. Rhodes and E.D. Wachsman, ***Solid State Ionics Devices II-Ceramic Sensors***, In: E.D. Wachsman, W. Weppner, E. Traversa, M. Liu, P. Vanysek and N. Yamazoe, Editors, *The Electrochemical Society Proceedings Series*, Pennington, NJ (2001), p. 137.
7. S.J. Song, E.D. Wachsman, S.E. Dorris and U. Balachandran, *J Electrochem Soc* **150** (2003) (11), p. A1484.
8. S.J. Song, E.D. Wachsman, S.E. Dorris and U. Balachandranb, *J Electrochem Soc* **150** (2003) (6), p. A790.
9. S. Hamakawa, L. Li, A. Li and E. Iglesia, *Solid State Ionics* **148** (2002) (1-2), p. 71.
10. A.S. Nowick and Y. Du, *Solid State Ionics* **77** (1995), p. 137.
11. T. Schober, *Solid State Ionics* **109** (1998) (1-2), p. 1.
12. Y. Du and A.S. Nowick, *J Am Ceram Soc* **78** (1995) (11), p. 3033.
13. H. Iwahara, T. Mori and T. Hibino, *Solid State Ionics* **79** (1995), p. 177.
14. N. Bonanos, B. Ellis and M.N. Mahmood, *Solid State Ionics* **44** (1991) (3-4), p. 305.
15. K.S. Knight and N. Bonanos, *Mater Res Bull* **30** (1995) (3), p. 347.
16. N. Bonanos, K.S. Knight and B. Ellis, *Solid State Ionics* **79** (1995), p. 161.
17. S. Stotz and C. Wagner, *Berich Bunsen Gesell* **70** (1966) (8), p. 781.
18. S.J. Song, E.D. Wachsman, S.E. Dorris and U. Balachandran, *Solid State Ionics* **149** (2002) (1-2), p. 1.
19. S.J. Song, E.D. Wachsman, J. Rhodes, S.E. Dorris and U. Balachandran, *Solid State Ionics* **164** (2003) (1-2), p. 107.
20. S.J. Song, E.D. Wachsman, J. Rhodes, S.E. Dorris and U. Balachandran, *Solid State Ionics* **167** (2004) (1-2), p. 99.
21. S.J. Song, E.D. Wachsman, J. Rhodes, H.S. Yoon, K.H. Lee, G. Zhang, S.E. Dorris and U. Balachandran, *J Mater Sci* **40** (2005) (15), p. 4061.
22. T. Norby and Y. Larring, *Solid State Ionics* **136** (2000), p. 139.
23. T. Yajima, H. Kazeoka, T. Yogo and H. Iwahara, *Solid State Ionics* **47** (1991) (3-4), p. 271.
24. T. Yajima, H. Suzuki, T. Yogo and H. Iwahara, *Solid State Ionics* **51** (1992) (1-2), p. 101.
25. T. Matzke and M. Cappadonia, *Solid State Ionics* **86-8** (1996), p. 659.

26. R.J. Phillips, N. Bonanos, F.W. Poulsen and E.O. Ahlgren, *Solid State Ionics* **125** (1999) (1-4), p. 389.
27. I. Kosacki and H.L. Tuller, *Solid State Ionics* **80** (1995) (3-4), p. 223.
28. K.D. Kreuer, *Solid State Ionics* **125** (1999) (1-4), p. 285.
29. K.D. Kreuer, *Annu Rev Mater Res* **33** (2003), p. 333.
30. T.K. Oh, H.S. Yoon and E.D. Wachsman, Electrochemical studies of mixed protonic electronic conduction in Eu-doped $SrCeO_3$, *209th ECS Meeting*, Denver (2006).

31. Report Date: May 15, 2008

2. Lightweight Composite Tanks for Liquid Hydrogen Storage

Task PI: Dr. Bhavani Sankar, Mechanical & Aerospace Engineering (sankar@ufl.edu)
Graduate Students: Jianlong Xu, James Van Pelt

Research Period: August 3, 2004 to March 31, 2007

Abstract

Gas permeability in composite laminates is investigated based on Darcy's law for porous materials. The permeability is derived in terms of transverse crack densities in each ply, delamination intersection area and a material constant to be determined from experiments. The permeability in cross-ply laminates is investigated first. A three-dimensional finite element model based on strain energy release rate is used to determine the crack densities in each ply of the laminate. Then the three-dimensional model with delaminations is used to obtain the crack intersection area. Parametric studies were performed and it has been found that the permeability is related not only to the resultant forces and thermal loads but also to length and shape of the delamination, stacking sequence and temperature dependent material properties. Finally, the progressive permeability in cross-ply laminate is predicted as a function of applied loads.

Permeability tests were performed on various composite laminates including textile composites. The gas permeability, in general, increased with cryo-cycling. The increase was significantly higher in thin laminates. Textile composites showed remarkable damage tolerance in that the permeability remained al most constant after several cryo-cycles. The use of textile composites such as woven composites for cryogenic storage tanks warrants further investigation.

Background

High strength/weight and stiffness/weight ratio makes graphite/epoxy composite materials much more favorable to other conventional materials in aerospace industry. Reduction of structural weight of space vehicle is a critical issue to reduce the cost of sending payload to space. It is estimated that various gas storage tanks account for about 50% of the dry weight of space vehicles. Currently, the cost to transport payload into orbit is $10,000 per pound. NASA initiated the next generation single-stage-to-orbit reusable launch vehicle (RLV) program trying to reduce the cost to $1,000 per pound. One of such vehicle is the Lockheed Martin X-33 (see Fig. 1).

The linear aerospike engines in X-33 operate using hydrogen mixed with an oxidizer, which needs to be stored at cryogenic temperatures. It had been estimated that composite fuel tank would reduce its weight by 40% and the overall weight of the vehicle by 14% compared to conventional metallic fuel tank (Kessler, Matuszeski, and McManus, 2001). The honeycomb sandwich structure was used in liquid hydrogen (LH2) tank in X-33. In November 1999, the outer wall of the sandwich structure explosively debonded when the tank was ground-tested at the NASA Marshall Space Flight Center. The reason for the failure was believed to be the excessive permeation of liquid hydrogen from inner face sheet to honeycomb. When the tank was warmed up, the gas in honeycomb could not escape quickly, and the corresponding pressure increase caused the failure. The failure has caused a setback to further application of composite materials in cryogenic tanks. Hence, understanding the mechanism of gas leakage through composite laminates is very critical to the future application of composite materials in cryogenic storage tanks.

Composite laminate usually include several layers with different fiber orientations. Generally, the cryogenic tank is under high mechanical/thermal loading and also subjected to cyclic loads, which could cause microcracks and delaminations. From experimental observation (Berthelot, 2003), microcracks developed in 90°-ply of cross-ply laminate when the laminate was loaded in 0°-direction. The "microcracks" in the present work refers to those matrix cracks fully developed in thickness direction of the ply and fully extended through the laminate. These microcracks induce local stress concentrations at the crack tip and can cause delaminations between 0°- and 90°-plies (see Fig. 2).

Figure 1: Lockheed Martin X-33
(http://www.makelengineering.com/dir/Company/History/History.htm)

In reality, the composite laminate is under bi-axial cyclic loading as the wall of the cryogen tank. In this case, the matrix microcracks will form in both 90°-plies and 0°-plies of cross-ply laminates. Because of the interlaminar delamination, the microcracks in different plies can be connected by intersection areas (shaded areas) as shown in Fig. 3. The network formed by microcracks and intersection areas provide a pathway for hydrogen to leak through the laminate. Of course, there will be some gas leak due to diffusion mechanism even no microcracks are present. But the amount would be negligibly small compared to the amount leaked through the cracks and delamination. Hence, in the present work, we focus on the gas leakage due to the damage - transverse cracks and delaminations - in the composite laminate.

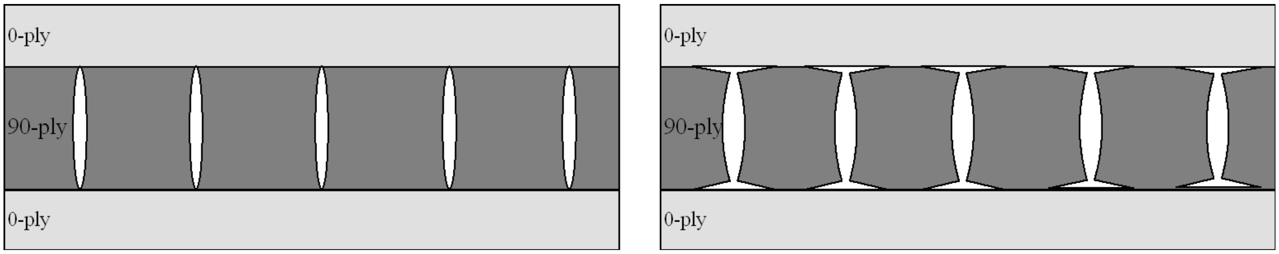

Figure 2: Microcracks in 90° ply and interfacial delaminations between 0°- and 90°- plies generated under thermal/mechanical loading.

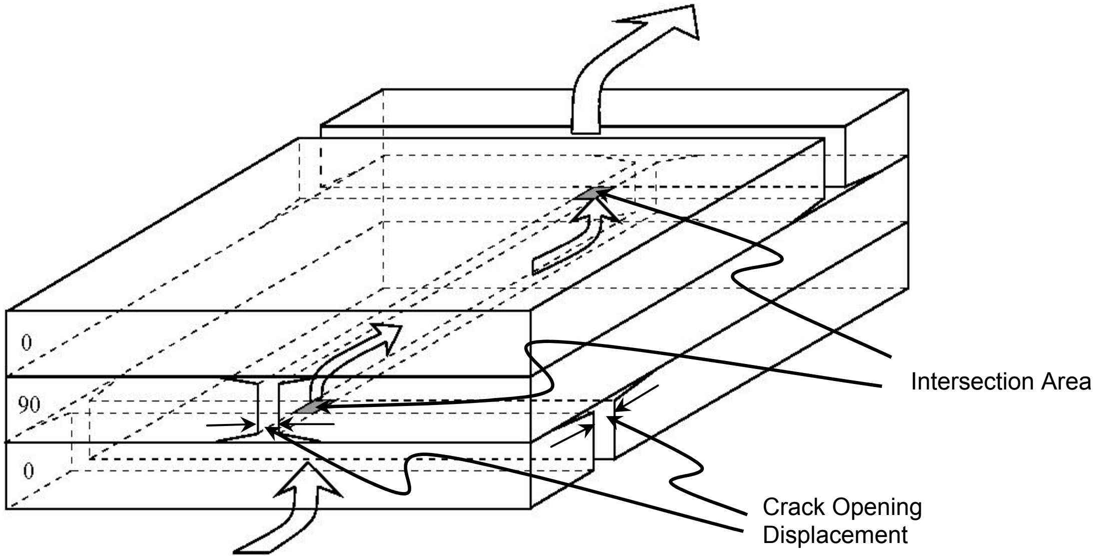

Figure 3: Gas permeation pathway provided by microcracks and delaminations in cross-ply laminates.

Literature Review

There are a number of experimental and analytical investigations on microcracking formation in the literature, e.g., see Nairn (2000) and Berthelot (2003) and references therein. In the current research, we focus on the analytical modeling of microcracking. In conventional stress analysis it is assumed that microcracks form when stress in the 90°-plies reaches the strength of matrix material. This method, however, did a poor job to predict the microcracking process compared to the experimental observation (Nairn, 2000). Nairn presented methods based on fracture mechanics and energy balance to analyze microcracking, which assumed that new microcracks formed if the total energy released due to the formation of the microcracks reached the microcracking fracture toughness G_{mc}. These energy release rate based methods did a good job of predicting microcracking in cross-ply laminates under uniaxial loading. The energy release rate method was then extended by Bapanapalli, Sankar and Primas (2006) to predict crack density evolution in cross-ply laminates under bi-axial and thermal loading using three-dimensional finite element method. This method is used in the current research to predict the crack densities evolution in each ply of composite laminates.

After the failure of the liquid hydrogen tank of X-33 reusable launch vehicle many experimental and analytical works have been done to investigate the permeability in composite laminates. Stokes (2002) performed permeability testing on IM7/BMI laminated composites under bi-axial strains based on ASTM standard (ASTM D1434-82, 1992). The permeability was measured under constant strain at room temperature and it has been found that the permeability is a time dependent property. Nettles (2001) tested permeability of composite laminates after impact testing and found that the flow rate usually had a nonlinear dependence on the applied pressure. McManus, Faust, and Uebelhart (2001) investigated the influence of loading conditions, crack density and ply orientation on the permeability of graphite/epoxy laminates. Choi (2005) performed permeability tests on various composite material systems subjected to certain cryogenic cycles, and found that for the laminates with same thickness the one with grouped lay-up has higher permeability than the one with dispersed lay-up. Among all the specimens, textile composite yields the lowest permeability. Kumazawa, Aoki, and Susuki (2003) investigated Helium gas leakage through composite laminates, and compared the experimental results with the analytical models. In their later work (Kumazawa, Susuki, & Aoki, 2006), they measured the gas leakage rate of cross-ply laminates under biaxial loading and found that besides the amount of damage, the gas permeability is dependent on both load level and biaxial load ratio. Grenoble and Gates (2006) performed permeability tests on composite material IM-7/977-2 after specimen being mechanically cycled at room temperature and found that the leak rate depended on applied mechanical strain, crack density and test temperature. Bechel, Camping, and Kim (2005) measured the evolution of microcrack density in composites due to cryogenic thermal cycling. Bechel and Arnold (2006) investigated the permeability in multi-directional laminates after certain thermal cycling from room temperature to cryogenic temperature and found that the permeability increases significantly as the number of cycling increased.

Besides the experimental measurement of the permeability in composite laminates, efforts were also devoted to develop analytical and numerical models to understand the mechanism of the permeability. As shown in Fig. 3, the matrix microcracking and the interlaminar delaminations form the leakage pathways for cryogenic gas. The intersection areas (the shaded areas shown in Fig. 3) formed by the crack opening in adjacent plies are the neck areas in the leakage pathway. If we treat the damaged composite laminate as a porous medium, then Darcy's law for porous materials can be used in modeling gas permeability (Aoki, Kumazawa, & Susuki, 2002, Kumazawa, et al. 2003, Roy & Benjamin, 2004, and Roy & Nair, 2006). In Darcy's law, the volume flow rate of fluid is proportional to the pressure gradient, and the proportionality constant is given by the ratio of permeability constant to the viscosity of the fluid. The gas permeability constant is determined by the micro-structure of the porous material. In our case, it is determined by crack densities in each ply, ply thicknesses, intersection area and a material constant that can be determined from experiments. For a given laminate, the ply thicknesses and the material constant are fixed. The crack densities can be predicted using the energy release rate method mentioned before or directly measured from experiments. However, the crack opening of the microcracks is hard to measure in experiments. Hence, analytical models are required to predict the intersection area. Kumazawa et al. (2003) only considered microcracking in their model and took mean crack opening displacement computed from two-dimensional shear-lag analysis to get the intersection area. Theoretically, however, microcracking alone cannot form the intersection area; delaminations have to be introduced in the model. Roy and Benjamin (2003) developed a model with delamination and computed crack opening displacement based on first-order shear deformable laminate theory. They compared the analytical results for crack opening displacement with finite element results and investigated the permeability under mechanical loading and thermal loading. Later on, Roy and Nair (2006) extended this model to include the stitch cracks developed in the oblique layers of the laminate by introducing effective spring stiffness. All these models are 2-D models. In the current work, we have found that the intersection areas are largely dependent on the local geometries and a full three-dimensional analysis is required to obtain accurate result (Xu & Sankar, 2007).

Some researchers predicted the gas permeability in composite laminate based on fluid mechanics principles (Noh, Whitcomb, Peddiraju, & Lagoudas, 2004, Peddiraju, Lagoudas, Noh, & Whitcomb, 2004, Peddiraju, Grenoble, Fried, Gates, & Lagoudas, 2005, and Peddiraju, Noh, Whitcomb, Lagoudas, 2007). In their models, the opening due to transverse microcracks and delaminations and the intersection area are first investigated. Then a damage network through laminates with assumed crack opening and delamination was set up and the effective conductance through this network was predicted using a computational fluid dynamics program FLUENT®. In these studies, the effective conductance is related to the ply thickness, the crack density in each ply. Also, the conductance of gas through a representative volume element (RVE) of intersection and microcracks were computed and a simplified model was set up, which agreed well with the previous simulation results. In these models, however, since the damage network was assumed with fixed opening and intersection area, each model can only represent one single loading case because the opening and the intersection area are dependent on the applied loads. Hence these models have difficulties to relate conductance to applied loads.

Most of the analytical models focus on cross-ply laminates, in which transverse matrix cracks are developed in each ply and extended thorough the thickness in both thickness direction and width direction. In general, however, it is good to include angle-plies in composite laminate design to gain better performance. Different from extensive transverse matrix cracks in cross-ply laminates, short cracks (or called stitch cracks) emanated in angle plies in multi-directional laminates. This phenomenon was first identified by Jamison, Schulte, Reifsnider, and Stinchcomb (1984) in the multi-directional laminates under fatigue loading. Lately, the stitch cracks formed in laminates with stacking sequence $[+\theta_n/-\theta_n/90_{2n}]_s$ were systematically investigated by Lavoie and Adolfsson (2001). It has been found that the stitch cracks not only emanated under fatigue loading but also emanated due to monotonic loading and thermal residue stresses. Stitch cracks were also observed in $[0/+45/-45/90]_s$ laminates by Bechel et al. (2005) after certain thermal cycling between room temperature and cryogenic temperature. Yokozeki and his colleagues (Yokozeki, Aoki, Ogasawara, and Ishikawa (2005), Yokozeki & Ishikawa (2005), and Yokozeki, Aoki, & Ishikawa (2005)) performed experiments on laminates of type $[0/\theta_n/90]_s$ under uniaxial loading and they found that whether stitch cracks or developed cracks will emanate in θ^o-ply depends on the value of θ and the thickness of the θ°-ply.

Some of the analytical models mentioned before included stitch cracks in the modeling. As mentioned before, Roy and Nair (2006) introduced an effective spring stiffness to incorporate the stitch crack into their model and still used the first-order shear deformable laminate theory to compute the crack opening displacement of stitch crack. In the damage network, Peddiraju et al. (2005) included the stitch cracks with assumed crack length and crack opening. Note that all these models either eliminated the difference between stitch crack and transverse crack using an effective spring stiffness or assumed damage state of stitch cracks. They were not able to represent the relationship between stitch crack and loads. In reality, the crack densities, the crack length and the opening displacement of stitch cracks are functions of the applied loads.

Objectives

The objectives of the current work are:

- Develop a method based on Darcy's law and three-dimensional finite element analysis to predict the gas permeability in cross-ply composite laminates.
- Extend the method to multi-directional laminates
- Study the effects of ply thickness, delamination length, delamination shape, lay-ups on the permeability
- Perform permeability tests on a variety of composite laminates including textile composites
- Study the effects of cryo-cycling on the permeability

Analytical Model

There are several theories that might be useful in deriving the permeation model for composite laminates: Darcy's Law for porous materials, Poiseuille's Law for capillary and Darcy-Weisbach Equation for pipe pressure loss. In the present work, the permeation model in composite laminate is mainly derived from Darcy's law for porous materials and verified by other laws. The permeability is represented in terms of crack density, crack intersection area and a material constant to be determined from experiments. The derivation of the permeation model is based on the cross-ply laminate, where only 0°-ply and 90°-ply present, but it can be extended to multi-directional-ply laminate as well.

Permeation Model

From experimental observations, matrix transverse micro-cracking in 90°-ply is the first form of damage in cross-ply composite laminates. Due to stress singularity at the crack tip when transverse crack reaches the interface between 90°-ply and 0°-ply, interlaminar delamination may occur at the interface. Theoretically, microcracks alone cannot form a contiguous path for gas leakage since no intersection area is formed. Hence the delamination has to be introduced in the numerical model as shown in Fig. 3. The shaded intersection areas formed by the crack opening displacements (CODs) of adjacent plies connect the micro-cracks, and allow gas to leak out. If the composite laminate with micro-cracks and delaminations were treated as a porous material, Darcy's Law for porous materials can be applied.

Darcy's law for viscous flow of gases through porous media is given as

$$q = -\frac{\kappa}{\mu}\nabla P \tag{1}$$

where q is volume flow rate per unite area, k is permeability tensor, μ is the viscosity and ∇P is pressure gradient vector. If only consider the gas leak in thickness direction of laminate, following one-dimensional Darcy's law can be used:

$$q = -\frac{k}{\mu}\frac{\partial P}{\partial z} \tag{2}$$

where k is overall permeability constant in thickness direction and z is the thickness coordinate. The permeability constant k is dependent on the microstructure of the laminate. Integrating both side of Eq. (2) over laminate thickness gives

$$qh = -\frac{k}{\mu}\left(P_N - P_0\right) \tag{3}$$

or

$$-\left(P_N - P_0\right) = qh\frac{\mu}{k} \tag{4}$$

where h is the laminate thickness, P_N and P_0 are pressure at the top and bottom respectively (see Fig. 4).

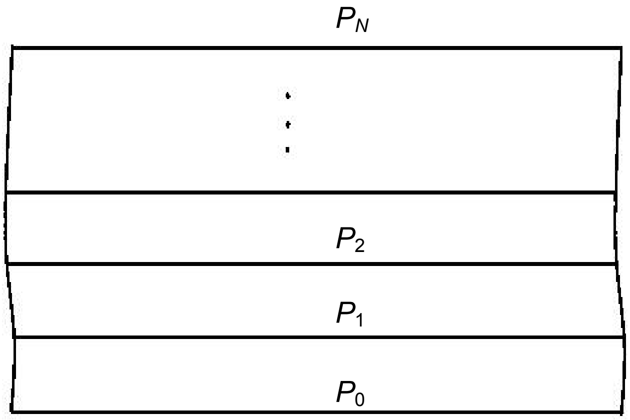

Figure 4: Pressure distribution along thickness direction of laminate.

Also, if the integration is done layer-wisely, we have

$$-\left(P_i - P_{i-1}\right) = q h_i \frac{\mu}{k_i}, \quad i = 1,\ldots,N \tag{5}$$

where h_i and k_i are thickness and permeability for each lamina. Summing Eq. (5) from i = 1 to i = N yields

$$-(P_N - P_0) = q\mu \sum_{i=1}^{N} \frac{h_i}{k_i} \tag{6}$$

Compare Eq. (6) with Eq. (4), it can be seen that

$$\frac{h}{k} = \sum_{i=1}^{N} \frac{h_i}{k_i} \quad \text{or} \quad k = \frac{h}{\sum_{i=1}^{N} h_i / k_i} \tag{7}$$

For each lamina, most of the resistance comes from the intersection area. According to the Poiseuille's Law, the volume flow rate in a rectangular tube (see Fig. 5) for the laminar flow is given by:

$$Q = \frac{d^4}{12\mu L} \Delta P \tag{8}$$

Dividing both sides by the cross-section area of the tube, d^2, gives:

$$q = \frac{d^2}{12\mu} \frac{\Delta P}{L} \tag{9}$$

Comparing Eq. (9) with Eq. (2), it can be seen that the permeability constant k for the rectangular tube is proportional to the cross-section area. Based on this fact, we can assume that the permeability for each lamina is proportional to the total intersection area. This assumption is also confirmed by Peddiraju, et al. (2007) using FLUENT® simulation. Noting that first and last laminas only have one interface with other laminas while others have two interfaces, so the individual permeability is assumed to take following form:

$$\begin{aligned} k_1 &= C\lambda_1\lambda_2 A_{(1,2)} \\ k_i &= C\left(\lambda_{i-1}\lambda_i A_{(i-1,i)} + \lambda_i\lambda_{i+1} A_{(i,i+1)}\right)/2,\ i = 2,\ldots,N-1 \\ k_N &= C\lambda_{N-1}\lambda_N A_{(N-1,N)} \end{aligned} \tag{10}$$

where λ_i is the crack density in i^{th} ply, $A_{(i,i+1)}$ is the individual intersection area between i^{th} and $i+1^{th}$ ply, and C is a material property to be determined by experiments.

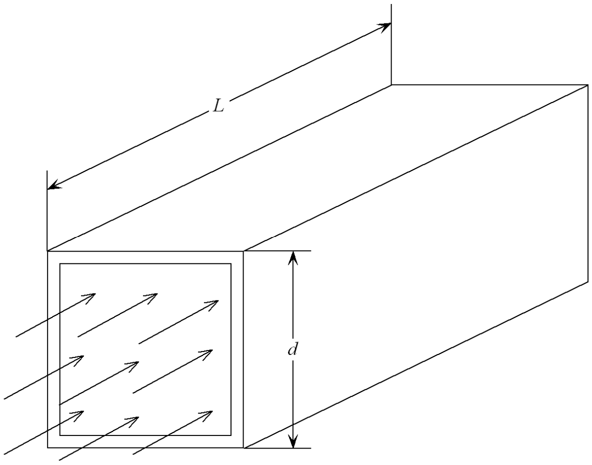

Figure 5: Laminar flow in a rectangle tube.

Substituting k_i back into Eq. (7), the overall permeability of laminate can be written as:

$$k = \frac{Ch}{h_1/\lambda_1\lambda_2 A_{(1,2)} + \sum_{i=2}^{N-1} 2h_i/\left(\lambda_{i-1}\lambda_i A_{(i-1,i)} + \lambda_i\lambda_{i+1} A_{(i,i+1)}\right) + h_N/\lambda_{N-1}\lambda_N A_{(N-1,N)}} \tag{11}$$

It is obvious from Eq. (11) that the permeability is determined by the crack densities λ_i and the intersection areas $A_{(i,j)}$ once the laminate lay-up is given and the material constant C is characterized by experiments. In another word, the overall permeability is determined by the total intersection area in each ply because that the crack densities give the number of intersection area in each ply.

Preliminary Two-Dimensional FE Modeling

Before using a three-dimensional finite element model, two-dimensional FE modeling is presented first to obtain some preliminary results. A three-layer cross-ply laminate is considered in this modeling. Figure 6 shows the representative volume element (RVE) for two different cases of damage scenarios that could occur in cross-ply composite laminates. In the first case, [90/0/90], the delamination emanates from the surface ply of the laminate whereas in the second case, [0/90/0], it emanates from the middle ply. Due to symmetry, only one-fourth of the RVE is considered in the simulation. Eight-node isoparametric elements are used in the simulation and the orthotropic material properties used in the simulation are shown in Table 1. The simulation has been done using the commercial finite element package ABAQUS 6.5®.

From Fig. 6, it can be seen that the RVE can be described by crack spacing (reciprocal of crack density), ply thickness and delamination length. The ply thickness h is taken as 0.33 mm in the current model. First, the variation of strain energy release rate (SERR) at the delamination tip with respect to the delamination length a is investigated. The crack density is taken as 1 cm^{-1}. Even though the individual Mode I and Mode II strain-energy release rates do not exist due to the oscillatory characteristic of stresses and displacements near the crack tip for bi-material interface cracks (Sun & Jih, 1987), the total strain-energy release rate is well defined (Hutchinson & Suo, 1992). Under linear elastic assumption, path independent J-integral is identical to strain energy release rate. Since J-integral is insensitive to the FEM mesh, uniform mesh is accurate enough for this simulation.

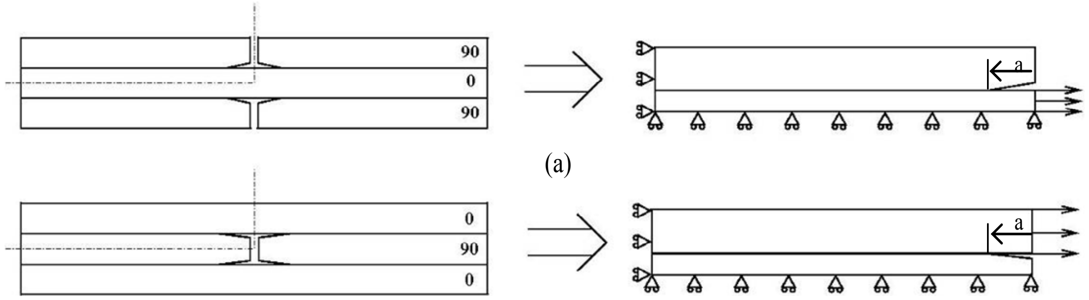

(a)

(b)

Figure 6: Two-dimensional delamination model: (a) Delamination from surface plies [90/0/90]; (b) delamination from middle ply [0/90/0].

Table 1: Orthotropic Material Properties for the Composites. Moduli are in GPa

Properties	E_1	$E_2 = E_3$	$G_{12}=G_{13}$	G_{23}	$\nu_{12}=\nu_{13}$	ν_{23}	α_1	$\alpha_2 = \alpha_3$
Value	169	8.62	5.0	1.22	0.355	0.41	-3.384e^{-9}/°C	28.998e^{-6}/°C

Figure 7 shows the J-integrals with respect to the delamination length a. The delamination length a is normalized by the ply thickness h in Fig. 7. The RVE is under constant displacement loading. It can be seen that the J-integrals reach maximum values when delamination length is about the ply thickness, and then decrease slowly. This implies that the delamination propagate steadily when delamination length exceeds ply thickness under displacement control loading. When the delamination length is too small, less than the ply thickness, the boundary effects are obvious.

From Fig. 7, it seems to be appropriate to take ply thickness as the delamination length since the delamination propagates steadily after its length exceeds ply thickness. Hence, in three-dimensional FE analysis, a length comparable to the ply thickness is taken to be the delamination length and the sensitivity of the intersection area to the delamination length is investigated.

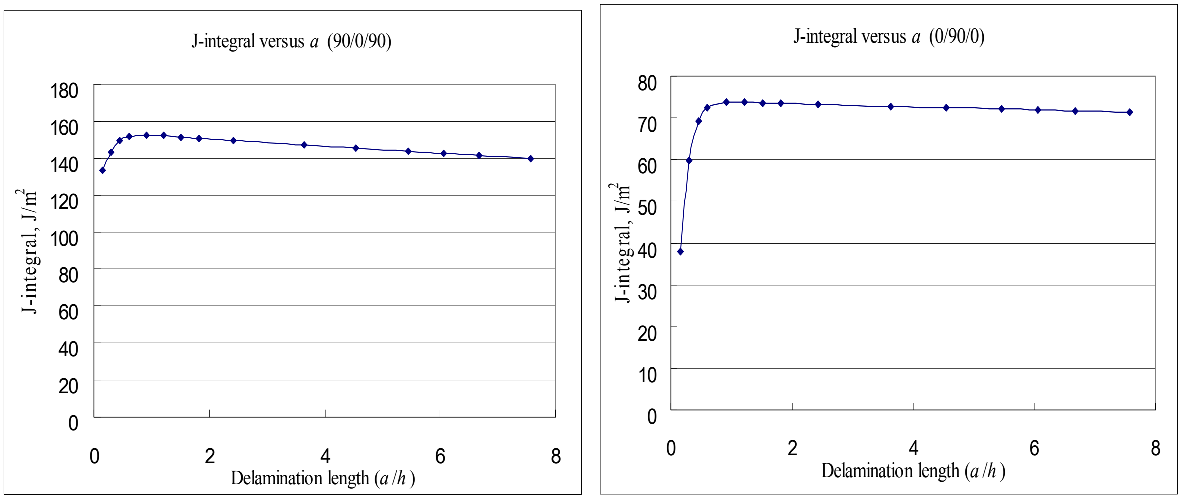

(a) (b)

Figure 7: J-integral variation with respect to delamination length *a*, which is normalized by dividing by ply thickness *h*: (a) [90/0/90] laminate; (b) [0/90/0] laminate.

Next, the crack opening displacements (COD) of microcracks are computed with a fixed delamination length and varied crack density. Even though both crack density and intersection area are functions of applied loads, fortunately, following results show that these two factors can be decoupled since crack density does not have much influence on the COD. Figure 8 shows the computed COD with respect to crack density. The CODs are expressed for unit force by normalizing with respect to the force resultant N_x, which can be computed directly from finite element analysis by volume average method (force resultant equal to the summation of product of stress and element volume and then divided by the laminate thickness). It can be seen from these two figures that the CODs are almost constants for a given force resultant and delamination length.

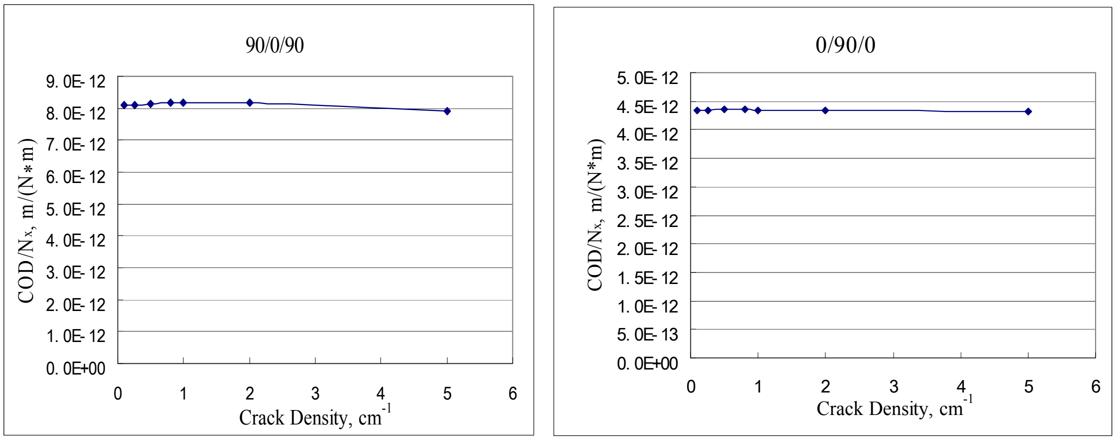

(a) (b)

Figure 8: (a) COD variation with respect to crack density for lay-up [90/0/90]; (b) COD variation with respect to crack density for lay-up [0/90/0].

From the above discussion, we can argue that the crack density does not influence the crack opening displacement much. Hence, the permeability prediction can be decoupled into two parts, first find crack densities for given force resultants and then compute intersection area under these loads. Then, the permeability for a given set of force resultants can be computed using Eq. (11). The crack densities in each ply can be either predicted using analytical methods (Nairn, 2000 and Bapanapalli, et al., 2006) or measured directly from experiments (Nairn, et al., 1993 and Nairn, 2000). However, most of the available experimental data are for laminates under uniaxial loading. In reality, the composite laminate in cryogenic tank is under biaxial loading. Hence, the analytical method developed by Bapanapalli, et al. (2006) will be adopted in the current work to predict crack densities in cross-ply laminate under biaxial loading. The intersection area will be computed using three-dimensional FEM and a parametric investigation will be performed.

Crack Density Prediction

In this chapter, the method developed by Bapanapalli, et al. (2006) is briefly summarized, predicted crack densities under uniaxial loading is compared with experimental result, and then crack densities under biaxial loading are predicted in various cases.

A composite laminate with configuration [0/90/0] is considered in the current work. From experimental observation (Nairn, 1993), two different microcracking scenarios could develop in the laminate when it is subjected to uniaxial loading as seen in Fig. 9. If the laminate is loaded in 0°-direction, microcracks emanated in 90°-ply (middle ply) and next new microcrack usually formed in between two existing cracks (see Fig. 9(a)). On the other hand, if the laminate is loaded in 90°-direction, microcracks emanated in 0°-plies (surface plies). The asymmetric crack pattern shown in Fig. 9(b) has been observed by Nairn (2000). Hence, four new cracks formed to keep the same pattern.

A finite fracture mechanics approach was used by Nairn (2000) to predict new microcrack formation. In this approach, the strain energy release rate due to the formation of new microcracks is expressed as a function of applied load, mechanical properties and crack density. Then, this strain energy release rate is equated to microcracking fracture toughness, G_{mc}, to solve for the required load to form new microcracks. It has been shown that the microcracking fracture toughness G_{mc} is a material property and it can be determined through experimental techniques (Nairn, 2000). The predicted results using this approach matched the experimental results quite well. However, this approach can only predict the crack density of composite laminate subjected to uniaxial loading. Bapanapalli, et al. (2006) extended this approach to predict crack densities in both 0°-ply and 90°-ply at same time when the laminate is subjected to biaxial loading.

In the current work, the extended finite fracture mechanics approach (Bapanapalli, et al., 2006) is used to predict crack densities in each ply of composite laminate. Based on the two scenarios shown in Fig. 9, a three-dimensional unit cell is taken as shown in Fig. 10. In this model, crack surfaces are shown in shaded area. The dimension of the unit cell is determined by the crack densities of surface and middle plies.

The strain energy of the unit cell for load control condition is given by

$$G = \frac{1}{2}\frac{1}{\lambda_x}\frac{1}{\lambda_y}N^T \cdot \overline{A} \cdot N \tag{12}$$

where $\overline{A} = \begin{bmatrix} A_{11} & A_{12} \\ A_{21} & A_{22} \end{bmatrix}^{-1}$ is the inverse of laminate extensional stiffness matrix (or the compliance matrix), $N = \begin{bmatrix} N_x \\ N_y \end{bmatrix}$ is force resultant matrix, and λ_x, λ_y are crack densities in *x*- and y-direction. The formation of new microcracks will cause the degradation of the stiffness matrix of the laminate. Hence, the released strain energy due to the formation of new microcracks is given by

$$G_m = \frac{1}{2}\frac{1}{\lambda_x}\frac{1}{\lambda_y} N^T \cdot \Delta\overline{A} \cdot N \tag{13}$$

where $\Delta\overline{A} = \overline{A}_2 - \overline{A}_1$ is the difference of the compliance matrix before and after the formation of new microcracks.

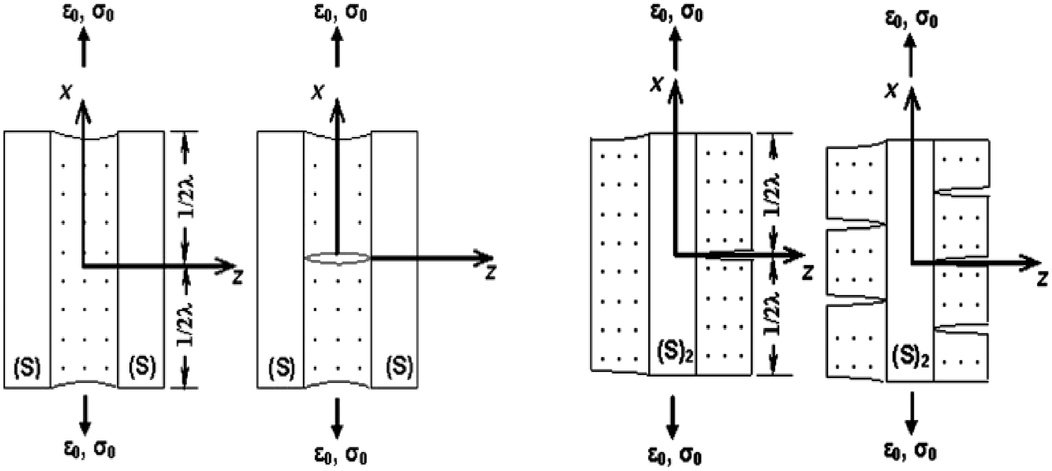

(a) (b)

Figure 9: Two microcracking scenarios in composite laminate [0/90/0] under uniaxial loading. (a) Unit cell for microcracks in middle ply and new crack formation. (b) Unit cell for microcracks in surface ply and new cracks formation. (Courtesy: Bapanapalli, et al., 2006)

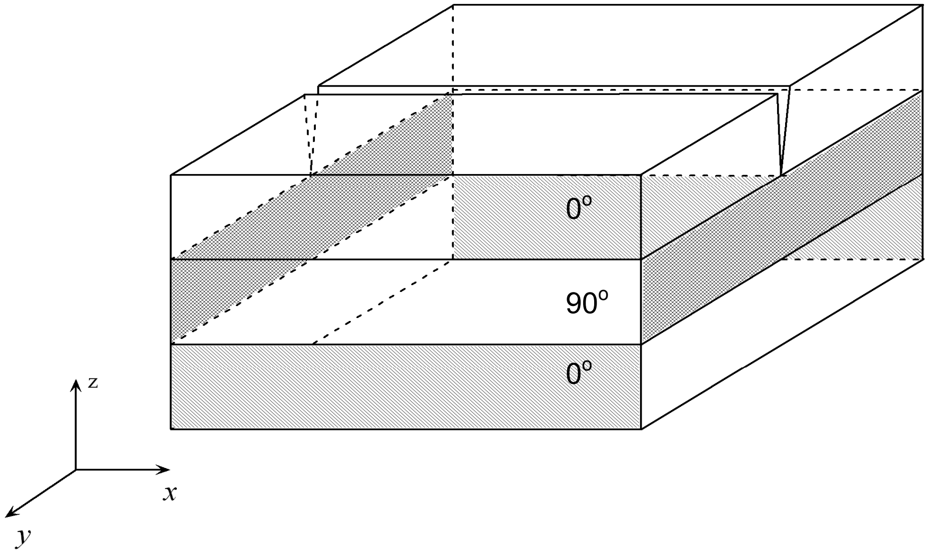

Figure 10: Three-dimensional unit cell with microcracks in both middle and surface plies.

As the wall of cryogenic tank, the composite laminate is under biaxial loading, and the hoop stress and the longitudinal stress are proportional to each other. Hence, it is reasonable to assume that the force resultants in the laminate in the form:

$$N_x = \alpha N_y \tag{14}$$

where α is proportional factor, whose value equals to 2 or 0.5 for the cylindrical body and 1 for the spherical cap of a pressure vessel. Substituting Eq. (14) into Eq. (12), the released strain energy can be rewritten as

$$G_m = \frac{1}{2}\frac{1}{\lambda_x}\frac{1}{\lambda_y}\left(\alpha^2 \Delta\overline{A}_{11} + 2\alpha\Delta\overline{A}_{12} + \Delta\overline{A}_{22}\right)N_y^2 \tag{15}$$

where $\Delta\overline{A}_{11}$, $\Delta\overline{A}_{12}$, and $\Delta\overline{A}_{22}$ are the entries of matrix $\Delta\overline{A}$.

According to the finite fracture mechanics, the strain energy released due to new crack formation should equal to the energy required to create new crack surfaces. There are three cases could happen for the microcrack formation:

- Case I: new microcracks form only in the surface plies. In this case, λ_x remains the same but λ_y is tripled.
- Case II: new microcrack form only in the middle ply. In this case, λ_x is doubled and λ_y remains the same.
- Case III: new microcracks form in both middle and surface plies. In this case, λ_x is doubled and λ_y is tripled.

The required surface energies for these three cases are given by

$$U_I = 4\frac{1}{\lambda_x}h_0 G_{mc}$$

$$U_{II} = \frac{1}{\lambda_y}h_{90} G_{mc} \tag{16}$$

$$U_{III} = \frac{1}{\lambda_y}h_{90} G_{mc} + 4\frac{1}{\lambda_x}h_0 G_{mc}$$

where h_0 and h_{90} are the thickness of 0°-ply and 90°-ply respectively.

Equating these surface energies to the released strain energy in Eq. (15), one can solve for the required force resultants for the three cases as follows

$$N_{y(I)} = \sqrt{\frac{8h_0\lambda_y G_{mc}}{\alpha^2\Delta\overline{A}_{11} + 2\alpha\Delta\overline{A}_{12} + \Delta\overline{A}_{22}}} \tag{17}$$

$$N_{y(II)} = \sqrt{\frac{2h_{90}\lambda_x G_{mc}}{\alpha^2\Delta\overline{A}_{11} + 2\alpha\Delta\overline{A}_{12} + \Delta\overline{A}_{22}}} \tag{18}$$

$$N_{y(III)} = \sqrt{\frac{G_{mc}\left(2h_{90}\lambda_x + 8h_0\lambda_y\right)}{\alpha^2\Delta\overline{A}_{11} + 2\alpha\Delta\overline{A}_{12} + \Delta\overline{A}_{22}}} \tag{19}$$

In reality only one case could happen, so the case that gives the smallest value of N_y will happen. In another word, for a given unit cell (λ_x and λ_y fixed), if $N_{y(II)}$ is the least values among three computed force resultant, then next microcrack will form in surface ply. Note that the values of $\Delta\overline{A}$ are different for these three cases.

This method can also be extended to the displacement control condition. For details, please refer to Bapanapalli, et al. (2006).

Predicted Analytical Results

Uniaxial Loading—First, the crack density in composite laminate is predicted under uniaxial loading condition. To compare with the available experimental data, laminates of type [0/90*n*/0] (*n*=1, 2, 4) are investigated. The material properties are the same as in Table 1.

In Eq. (17) - Eq. (19), for each combination of (λ_x, λ_y), the stiffness matrix [A] is different. Matrix [A] is computed using FE analysis, but if FE analysis is performed for every unit cell (given λ_x and λ_y), there will be too much computation since 3-D FE analysis is very time consuming. Hence, in the current work, the [A] matrices for certain (λ_x, λ_y) combinations are computed and then stiffness matrix is fitted as a complete cubic function of λ_x and λ_y based on the computed values using least the square approximation.

For a given unit cell, the [A] matrix is computed based on constitutive relation:

$$\begin{Bmatrix} N_x \\ N_y \end{Bmatrix} = \begin{bmatrix} A_{11} & A_{12} \\ A_{21} & A_{22} \end{bmatrix} \begin{Bmatrix} \varepsilon_x \\ \varepsilon_y \end{Bmatrix} \tag{20}$$

Displacement boundary conditions are applied to the unit cell to make the strain status be $\varepsilon_x = 1$ and $\varepsilon_y = 0$. The force resultants N_x and N_y are computed using volume average method. Then the first column in [A] matrix equals to the computed force resultants. Similarly, applying the boundary condition $\varepsilon_x = 0$ and $\varepsilon_y = 1$ will give the second column of [A] matrix. For each pair of (λ_x, λ_y), two FE analysis are needed to determine [A] matrix. In our case, seven λ_x (ranging from 0 to 9.5 cracks/cm) and eight λ_y (ranging from 0 to 12.6 cracks/cm) are taken. So totally 112 FE analysis are needed for each laminate to determine response surface of [A] matrix. It can be seen that this is a quite time consuming procedure. Figure 11 shows the response surfaces for the entries in [A] matrix of laminate [0/90/0]. The dot marks are data points. Other laminates also have similar response surfaces.

A MATLAB program is developed to predict the progressive crack densities λ_x and λ_y of laminate subjected to biaxial loading as a function of N_x or N_y. In this program, initial values of crack densities and the ratio between N_x and N_y. For uniaxial loading, the ratio α is taken as 0.

From experimental observation (Nairn, 2000) in [0/90$_n$/0] laminates, it has been found that initiation stress for microcracks in middle ply is lower for thicker middle ply and initial stress for microcracks in surface ply is higher for thicker middle ply. However, at high stress level, larger crack density was observed in the middle ply with thinner middle ply. The predicted crack densities of laminates [0/90$_n$/0] (n = 1, 2, 4) under uniaxial loading are shown in Fig. 12 and Fig. 13. The microcracking fracture toughness G_{mc} is taken as 240 J/m. In Fig. 12, the stress to initiate first microcrack increases as the middle ply thickness decreases. However, once the initiation stress is reached, the crack density increases faster in the laminate with thinner middle ply. For [0/90/0], even a negative slope is obtained, which means that the microcracks accumulate simultaneously in the laminate. As seen in Fig. 13, as middle ply thickness of laminate increases, the initiation stress increase as well. Hence, our prediction and experimental observation matches quite well qualitatively, which gives us confidence to use this approach to predict the crack densities of laminates under biaxial loading.

***Biaxial Loading*—**In reality, the laminate used in propellant tank is under bi-axial loading. The proportional constant α between force resultants N_x and N_y is taken as 0.5, 1.0, and 2.0 to represent different possible stress states in hydrogen tank. Figure 14 to Fig. 22 show the variations of crack densities in different laminates under different biaxial loading. For each laminate, crack densities λ_x and λ_y are plotted in same figure with respect to the average stress in y-direction (Ny divided by the laminate thickness). Figure 14 to Fig. 16 represent the cases when $\alpha = 0.5$, Fig. 17 to Fig. 19 represent $\alpha = 1.0$, and Fig. 20 to Fig. 22 represent $\alpha = 2.0$. From these figures, it can be seen that the initiation stresses for first microcrack in both x- and y-direction are lower than their corresponding values under uniaxial loading. With the same proportional constant α, the initiation stress for λ_x decrease dramatically as the middle ply thickness increase. On the contrary, the initiation stress for λ_y increases as the middle ply become thickness, but the increase step is not as large as that under the uniaxial loading. Loads in x-direction affect the crack densities in y-direction. For the same laminate, say [0/90/0], when α increases (σ_x increases), the initiation stress for λ_y decreases. No microcracks are generated in [0/90/0] for $\alpha = 0.5$ and 1.0 when λ_y already meet the preset limit. These predicted crack densities will be used to predict the progressive gas permeability later on.

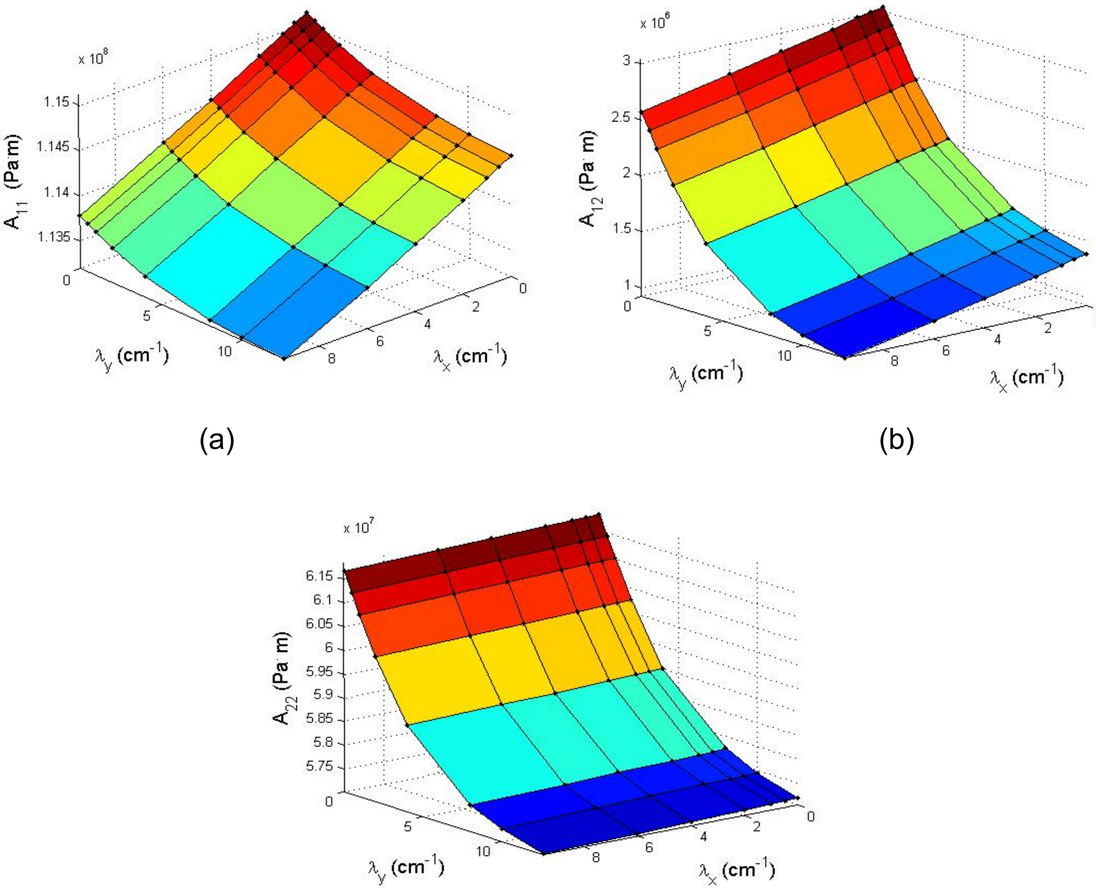

(a)

(b)

(c)

Figure 11: Response surface for [A] matrix of laminate [0/90/0]. (a). A11, (b). A12, (c). A22.

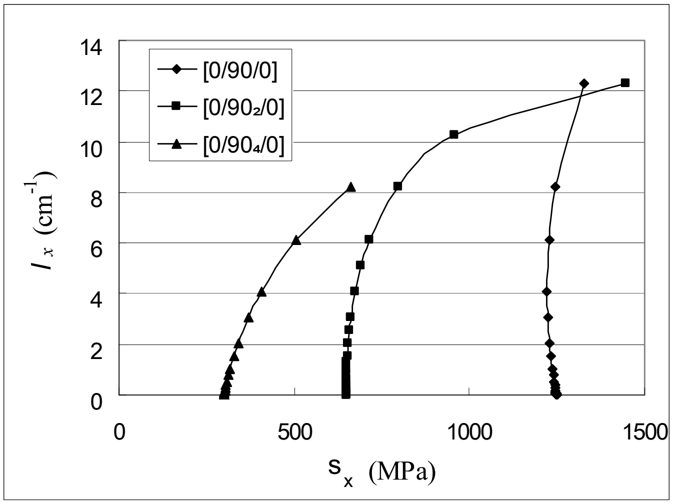

Figure 12: Crack density evolution in middle ply under loading in x-direction.

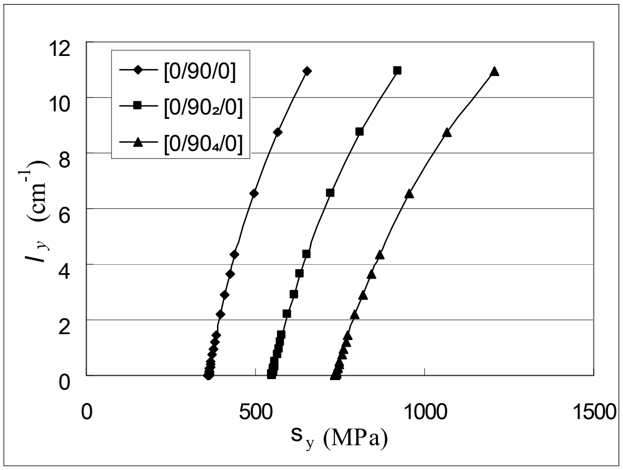

Figure 13: Crack density evolution in surface ply under loading in y-direction.

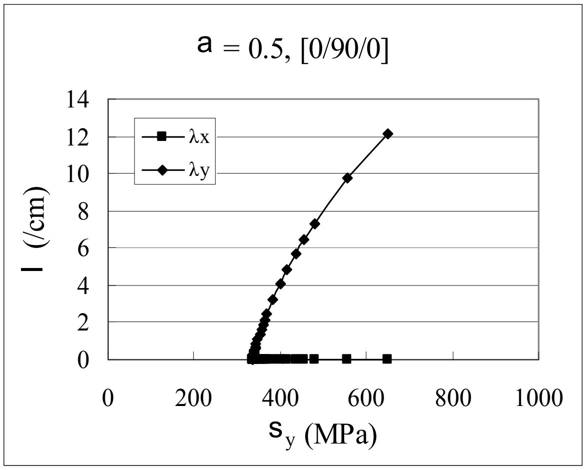

Figure 14: Crack density prediction for laminate [0/90/0]. Nx/Ny = 0.5.

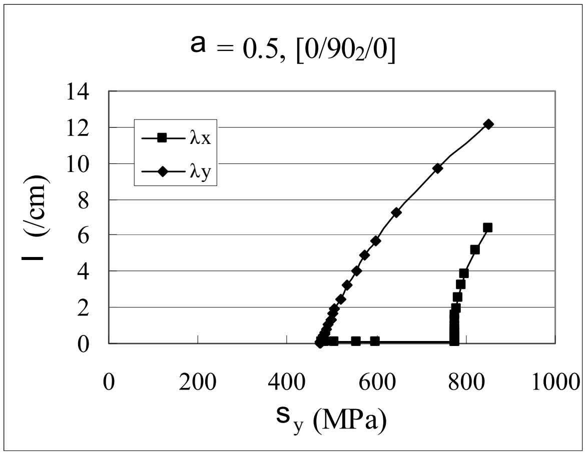

Figure 15: Crack density prediction for laminate [0/902/0]. Nx/Ny = 0.5.

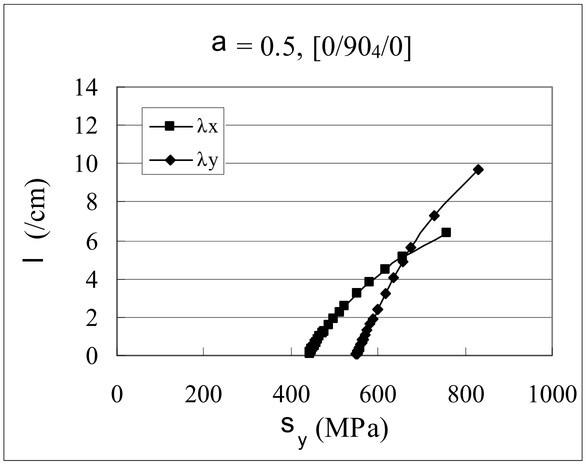

Figure 16: Crack density prediction for laminate [0/904/0]. Nx/Ny = 0.5.

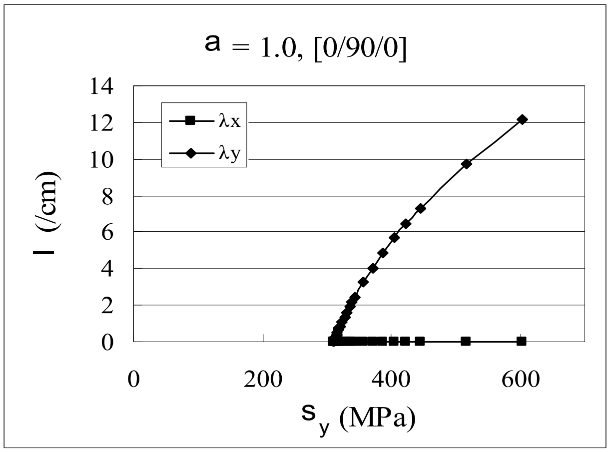

Figure 17: Crack density prediction for laminate [0/90/0]. Nx/Ny = 1.0.

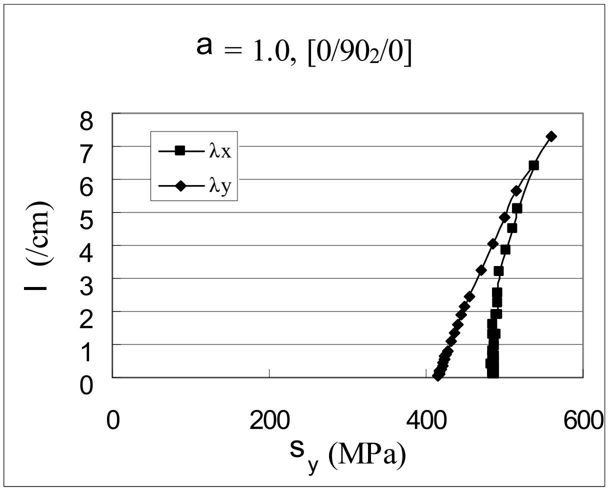

Figure 18: Crack density prediction for laminate [0/902/0]. Nx/Ny = 1.0.

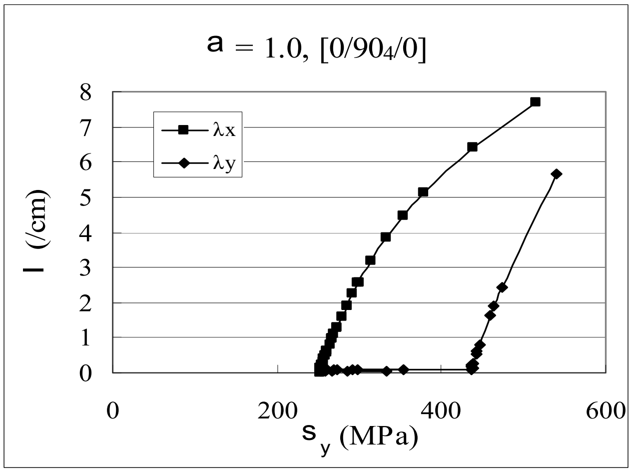

Figure 19: Crack density prediction for laminate [0/904/0]. Nx/Ny = 1.0.

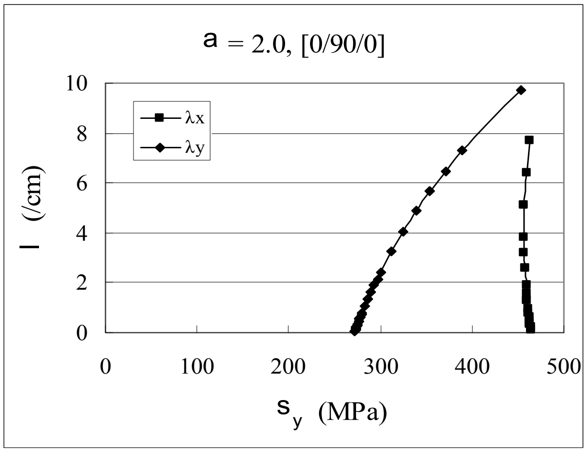

Figure 20: Crack density prediction for laminate [0/90/0]. Nx/Ny = 2.0.

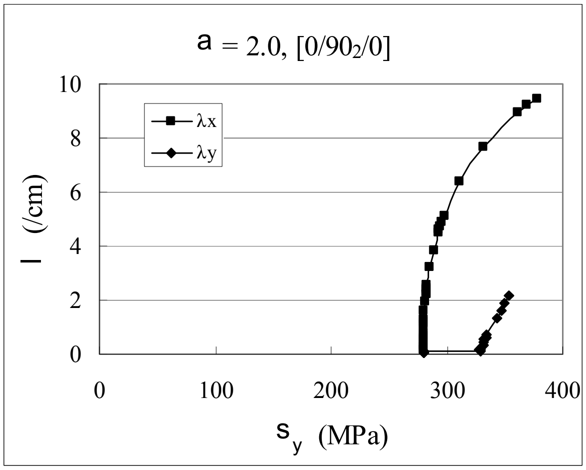

Figure 21: Crack density prediction for laminate [0/902/0]. Nx/Ny = 2.0.

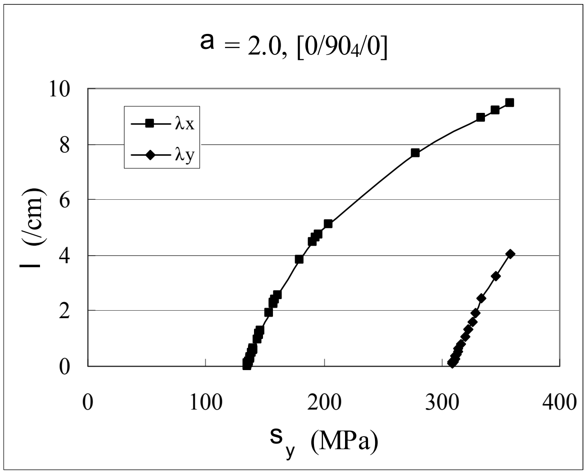

Figure 22: Crack density prediction for laminate [0/904/0]. Nx/Ny = 2.0.

Investigation of Intersection Area

After predicting the crack density, we will focus on crack intersection area and its variation due to different factors.

Model Description—Three-layer cross-ply composite laminate [0/90/0] is considered in the current model and following assumptions have been made for simplicity: the crack densities and the position of microcracks in two surface plies are identical; the microcracks in both surface plies and middle ply are evenly distributed. Once crack densities are given, the dimension of the unit cell is fixed as shown in Fig. 23. The upper figure in Fig. 23(a) represents the top view of the laminate with transverse matrix microcracks. The horizontal and vertical solid lines represent the microcracks in 0°- and 90°- plies respectively. Due to both in-plane symmetry and symmetry in thickness direction, only one-eighth of the unit cell is analyzed as shown in bottom figure in Fig. 23(a). Two free surfaces are the microcrack faces. Symmetric boundary conditions are applied to the surfaces opposite to the free surfaces and bottom surface and constant strains are applied as shown by the arrows. Delamination is introduced in this model since no contiguous gas-leak-pathway will be formed without delamination. The delaminations emanated from both surface ply and middle ply form a rectangle delamination front. In the current model, the crack densities in the 0°- and 90°-plies are taken as equal, $\lambda_x = \lambda_y = 1\ \text{cm}^{-1}$. The material properties are kept identical to those of the two-dimensional model as given in Table 1. Ply thickness is still taken as 0.33 mm. Twenty-node three-dimensional isoparametric solid elements and uniform mesh are used in the simulation. About 28,000 elements were used in the model. Figure 23(b) shows a typical deformation of the model under bi-axial loading. Note that the deformation is enlarged by a factor of 10.

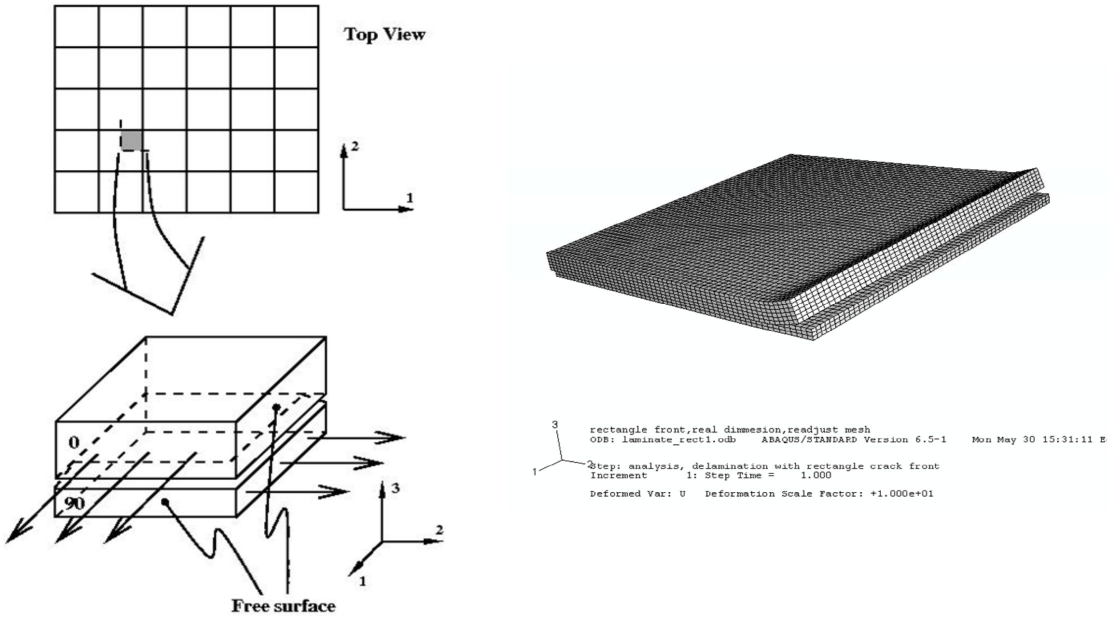

(a) (b)

Figure 23: Three-dimensional delamination model and typical deformation.

Kumazawa et al. (2003) and Roy and Benjamin (2004) proposed to superpose the two-dimensional CODs obtained from analytical methods to get the intersection area. In fact, if we monitor the COD along the path shown by the arrow in Fig. 24(a), the COD first remains as a constant at the straight edge, and then increases remarkably when close to the rectangular crack front. The constant value along the straight edge is identical to the result predicted by two-dimensional analytical model. The COD near the rectangular delamination front, however, is almost 50% larger than the two-dimensional result as shown in Fig. 24(b). Therefore, the local effects cannot be neglected and COD near the rectangular front computed from three-dimensional analysis should be used to compute the intersection area. Three-dimensional analytical model is too complicated, hence all the CODs in the current work are computed using FE analysis.

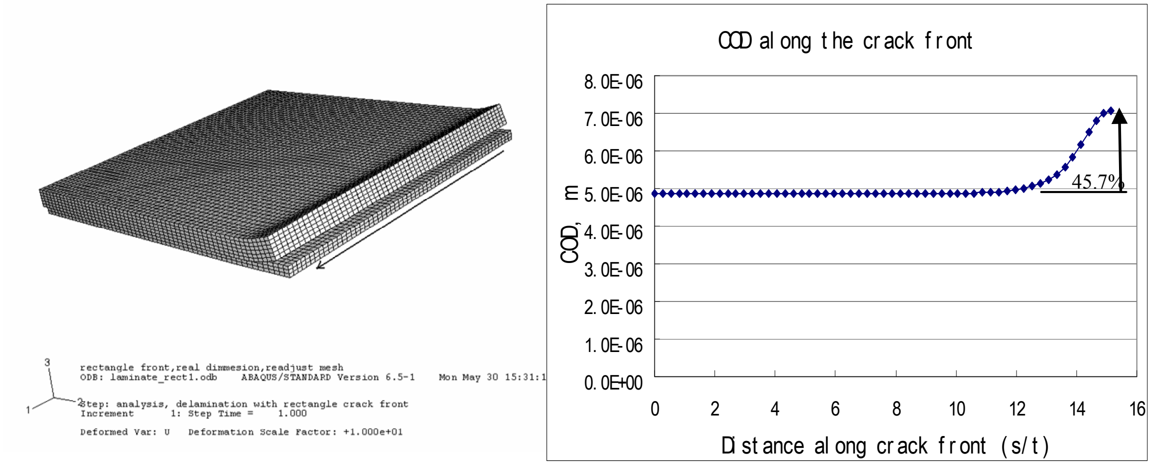

(a) (b)

Figure 24: COD along specific path shows the local effect.

***Intersection Area Computation*—**Due to the linear relation between COD and load, the intersection area under any loading case (N_x, N_y, ΔT) can be obtained once the COD for the following three basic cases are computed:

- $\varepsilon_x = 1\%, \quad \varepsilon_y = 0, \quad \Delta T = 0;$
- $\varepsilon_x = 0, \quad \varepsilon_y = 1\%, \quad \Delta T = 0;$
- $\varepsilon_x = 0, \quad \varepsilon_y = 0, \quad \Delta T = -223^{o}C$
  (From room temperature to cryogenic temperature).

For any combination of (N_x, N_y, ΔT), the corresponding (ε_x, ε_y, ΔT) can be obtained from the basic formula for composite laminate shown in Eq. (21), in which the matrices [A] and [α] can be determined from FE analysis of those three basic cases using the approach mentioned before.

$$\begin{Bmatrix} N_x \\ N_y \end{Bmatrix} = \begin{bmatrix} A_{11} & A_{12} \\ A_{21} & A_{22} \end{bmatrix} \left(\begin{Bmatrix} \varepsilon_x \\ \varepsilon_y \end{Bmatrix} - \Delta T \begin{Bmatrix} \alpha_x \\ \alpha_y \end{Bmatrix} \right) \tag{21}$$

The corresponding CODs for (Nx, Ny, ΔT) are then obtained by superposing the results of three typical cases with different weighting factors. The intersection area ΔA is computed by assuming that the cross-section formed by the CODs at corner is a rectangle. Figure 25 shows the variation of the intersection area with respect to the mechanical and thermal loads. In Fig. 25(a), different symbols represent different ratios between Ny and Nx, the solid lines represent the cases with thermal load and the dotted lines represent the cases without thermal load; in Fig. 25(b), each surface represents the intersection area variation with respect to Ny and Nx under certain thermal load.

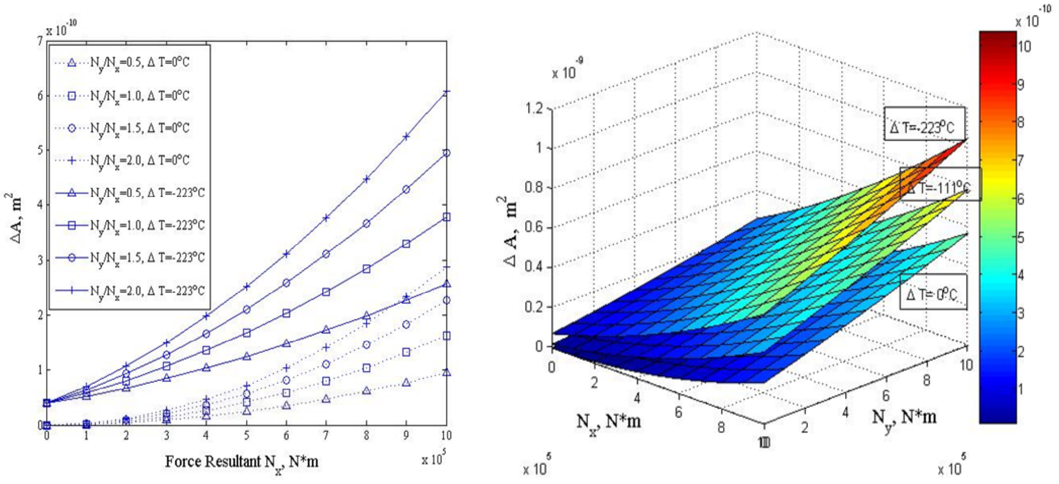

(a) (b)

Figure 25: Variation of cross-section area with respect to Nx, Ny, and ΔT.

Actually, from those three basic numerical tests, the CODs can be expressed explicitly in terms of Nx, Ny, and Δ*T*.

$$u = 0.592e^{-11}N_x + 0.446e^{-11}N_y - 1.082e^{-8}\Delta T \tag{22}$$

$$v = 0.204e^{-11}N_x + 1.156e^{-11}N_y - 1.036e^{-8}\Delta T \tag{23}$$

The corresponding interlaminar cross-sectional area ΔA is given by

$$\begin{aligned} A &= 4 \times u \times v \\ &= 0.121e^{-22}N_x^2 + 0.516e^{-22}N_y^2 + 0.112e^{-15}\Delta T^2 \\ &+ 0.775e^{-22}N_xN_y - 0.834e^{-19}N_x\Delta T - 0.171e^{-18}N_y\Delta T \end{aligned} \tag{24}$$

From Eq. (24), it is obvious that the intersection area shows parabolic variations with respect to Nx, Ny, and Δ*T*, which can be seen clearly in Fig. 25. Equations (22) to (24), however, are only valid for the current model. If any condition of the model, such as delamination length, material properties and ply thickness, is changed, we have to redo the computations of those three basic cases.

Effects of Delamination Shape and Delamination Length - The effects of delamination shape and the delamination length on the intersection area are investigated in this section. In previous section, the delamination fronts developed from the surface ply and the middle ply were connected by a pair of straight lines forming a rectangular delamination front. However, if three-dimensional J-integrals are computed along the crack front as shown in Fig. 26, it can be seen that the highest value occurs at the corner, i.e., the crack will first propagate at the corner. Hence, the delamination with a circular front might be a more appropriate scenario.

Figure 26(a) shows the top view of quarter of the RVE with delaminations and Fig. 26(b) shows the distribution of J-integrals with different connections. The model is subjected to thermal load only. As we can see J-integral values remains as constant at the straight crack front and increases near the connecting corner. For the case of rectangular front, the J-integral value computed at corner, which is extremely high due to the discontinuity of first order derivative, may not be meaningful and is eliminated from Fig. 26(b). As we expected, the circular delamination front reduces the highest value of J-integral at corner and the bigger is the radius, the lower is the value.

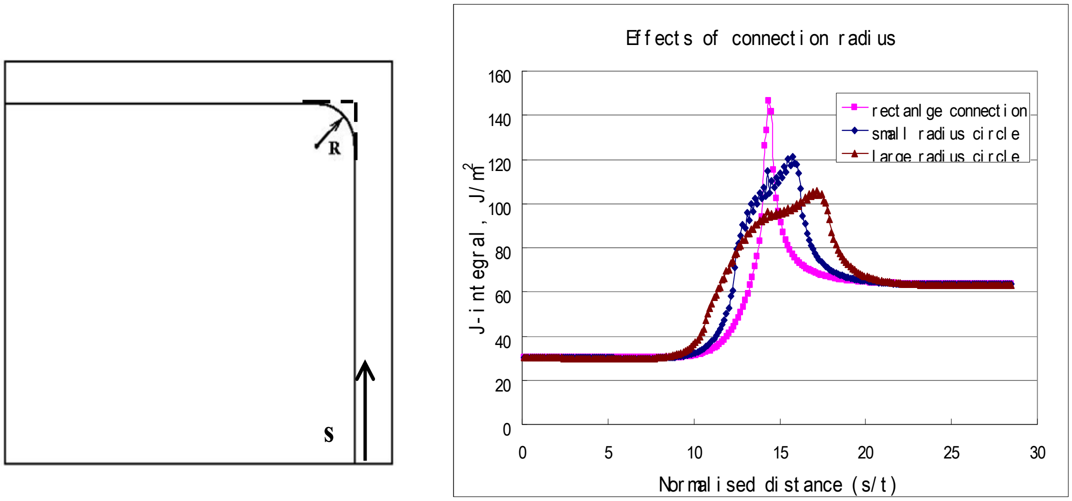

(a) (b)

Figure 26: J-integral distribution along crack front with different connect radius.

The intersection areas in models with different connecting radius are computed. Figure 27 shows the effects of the radius of the connecting circle. In all three basic cases, the cross-sectional area increases quadratically with respect to the radius.

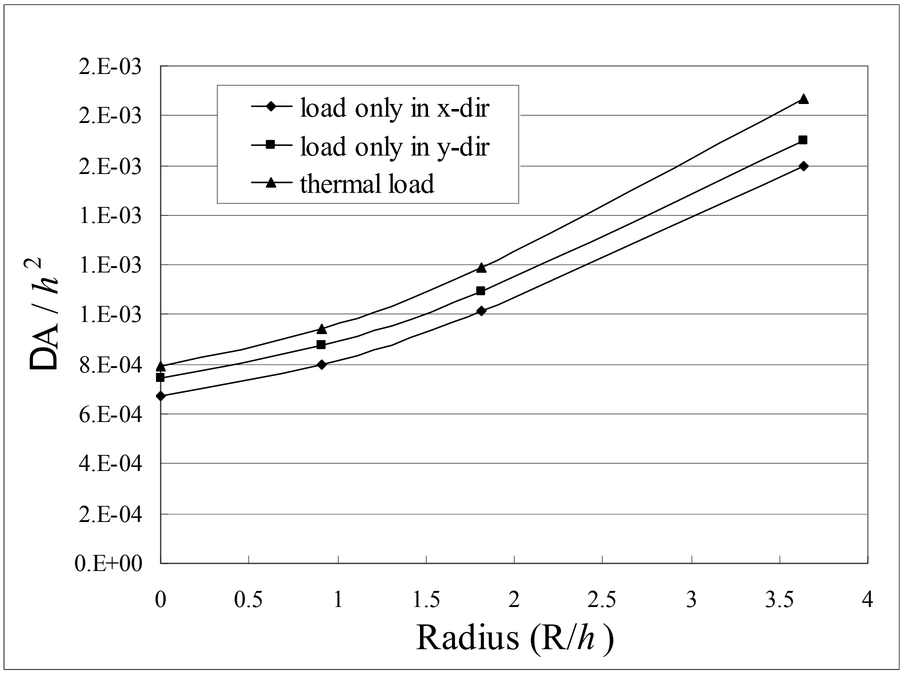

Figure 27: Effect of connecting radius of delamination on intersection area.

Moreover, the effect of delamination length is also investigated, as shown in Fig. 28. In this case, the rectangular front is still used and the delamination length changed from half of the ply thickness to twice the ply thickness. It can be seen that the intersection area is more sensitive to the delamination length than to the circle radius. It does not show the tendency to be a plateau as mentioned by Roy and Benjamin (2004).

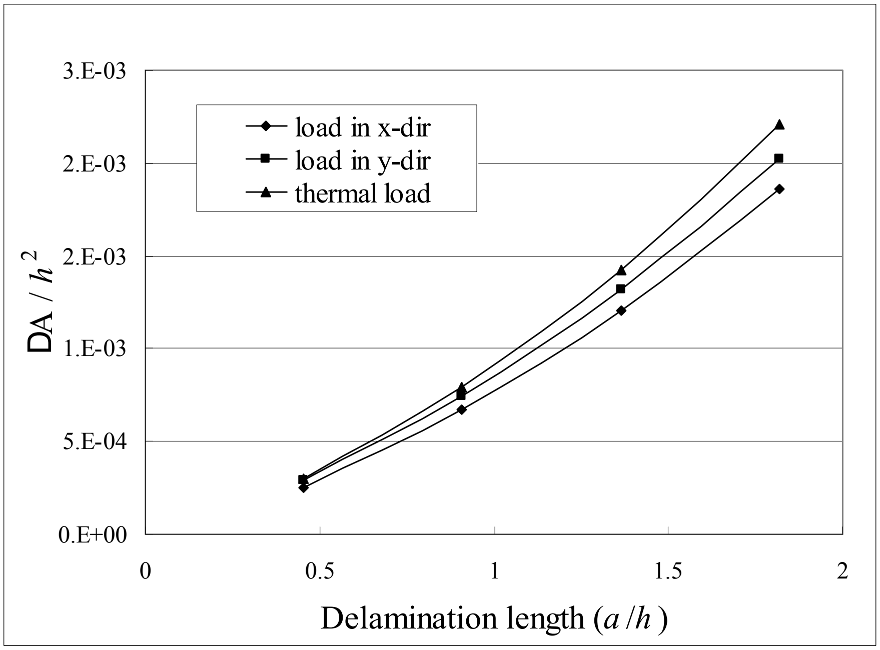

Figure 28: Effect of delamination length on intersection area.

***Single Delamination Model*—**Another phenomenon shown in Fig. 26(b) is that the steady state values on different sides are quite different even though both directions are under the same loading condition. Hence, delaminating from surface ply (high J-integral) is much easier to happen than delaminating from middle ply (low J-integral). From different view of the typical deformation of unit cell as shown in Fig. 29, it can be seen that delamination from middle ply (Fig. 29(a)) tries to close while the delamination from surface ply (Fig. 29(b)) tries to open up. Therefore, it is much possible that delamination only emanate from surface plies. Even if only one-side delamination appears, the path for gas leakage can still be formed as shown in Fig. 30. We call this model as “Single Delamination Model (SDM)”, and, correspondingly, the previous model is called “Double Delamination Model (DDM)”.

In this case, the intersection area is smaller than the one in the previous model. Figure 31 shows the comparison between the intersection areas computed using SDM and DDM under the same loading condition (N_y/N_x=0.5 and ΔT =-223 °C). The intersection area A computed using SDM also shows a parabolic variation, but the magnitude is only about half of that computed using DDM.

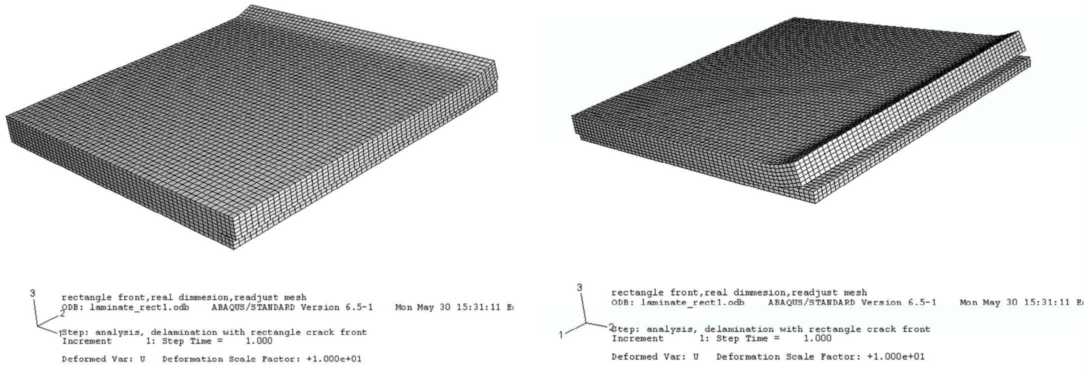

```
rectangle front,real dimmesion,readjust mesh
ODB: laminate_rect1.odb    ABAQUS/STANDARD Version 6.5-1    Mon May 30 15:31:11 E

Step: analysis, delamination with rectangle crack front
Increment      1: Step Time =    1.000

Deformed Var: U   Deformation Scale Factor: +1.000e+01
```

```
rectangle front,real dimmesion,readjust mesh
ODB: laminate_rect1.odb    ABAQUS/STANDARD Version 6.5-1    Mon May 30 15:31:11 E

Step: analysis, delamination with rectangle crack front
Increment      1: Step Time =    1.000

Deformed Var: U   Deformation Scale Factor: +1.000e+01
```

(a) (b)

Figure 29: Typical deformation of unit cell from different views.

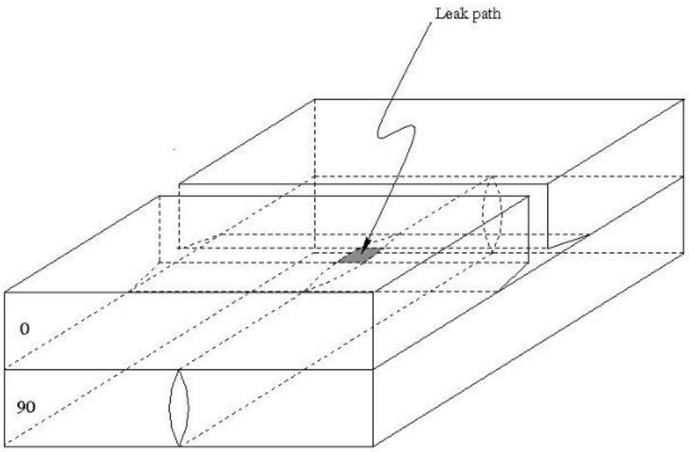

Figure 30: Gas leakage path formed by the delamination from surface ply only.

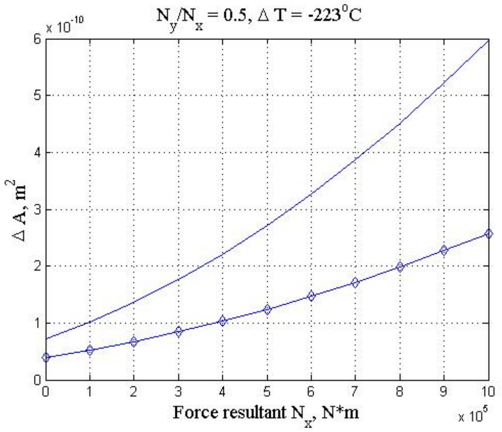

Figure 31: Comparison between two different scenarios.

***Effect of Lay-ups*—**Until now, only three-ply laminates are investigated. In reality, there are various lay-up possibilities. Choi (2005) did permeability tests for different laminates and found that for the same thickness the specimen with layers grouped together has higher permeability than the one with layers dispersed, i.e., laminate [$0/90/0_2/90/0$] performs better than laminate [$0_2/90_2/0_2$]. In this section, the current modeling technique will be used to demonstrate this phenomenon. In this investigation, exact same lay-up and material properties are used as in Choi's tests (Choi, 2005). For laminate [$0_2/90_2/0_2$], the unit cell is kept same as the one described in previous sections. For laminate [$0/90/0_2/90/0$], in order to describe the unit cell, the micro-cracks in the 0°-plies and in 90°-plies are assumed to appear in same position and the crack densities in all 0°-plies or in all 90°-plies are equal, as shown in Fig. 32. Due to the symmetry of the model, only one-eighth of the unit cell is considered. Figure 32(b) shows the typical deformation of the unit cell.

The crack densities in laminate [$0_2/90_2/0_2$] and in laminate [$0/90/0_2/90/0$] are kept as same. The permeabilities in both laminates are computed using Eq. (11). Since the material constant *C* is to be determined, the permeability is normalized by the constant *C*. In Table 2 the normalized permeability *k*/*C* for both specimens are tabulated and compared with the experimental results by Choi (2005). From this table, it can be seen clearly that the grouped specimen has a much higher permeability than the dispersed specimen. Note that the ratios between the permeability of the two specimens are quite different in the models and the experiments. This is due to the fact that the modeling procedure does not precisely reflect the testing procedure. In Choi's tests, the specimens are tested at room temperature after certain cryogenic cycles (cooling specimen down to cryogenic temperature and then warming it up to room temperature is defined as one cryogenic cycle) without mechanical loading. While in our modeling, crack density and delamination length is assumed and bi-axial loading is applied. Hence, the two sets of results can only be compared qualitatively for now.

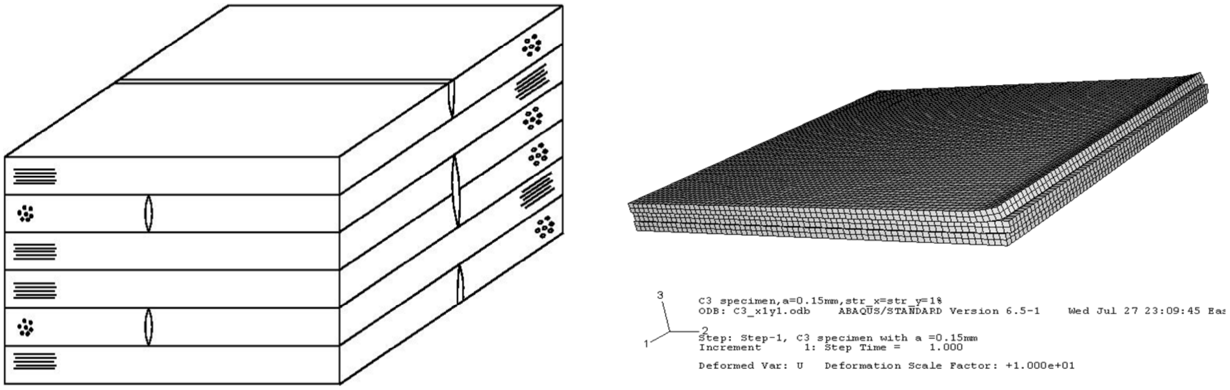

```
C3 specimen,a=0.15mm,str_x=str_y=1%
ODB: C3_x1y1.odb    ABAQUS/STANDARD Version 6.5-1    Wed Jul 27 23:09:45 Eas

Step: Step-1, C3 specimen with a =0.15mm
Increment      1: Step Time =    1.000

Deformed Var: U   Deformation Scale Factor: +1.000e+01
```

(a) (b)

Figure 32: Geometric model and typical deformation for multiple-layer laminates.

Table 2: Comparison between Computed and Tested Permeability

Laminates	Normalized Permeability *k*/*C*	Test results by Choi (2005) (mol/sec/m/Pa)
$[0_2/90_2/0_2]$	1.26×10^{-8}	2.23×10^{-18}
$[0/90/0_2/90/0]$	3.30×10^{-9}	1.16×10^{-20}

Temperature Dependent Properties**—**In this section, the effect of the temperature dependent properties is investigated. In previous sections all material properties are assumed to be temperature independent. For graphite/epoxy composite laminates, the matrix properties largely depend on the temperature while the fiber properties do not. Hence, the composite properties that depend mainly on matrix properties, such as transverse modulus E_2 and shear modulus G_{12}, vary remarkably with respect to temperature. Schulz (2005) and Speriatu (2005) have performed some experiments to measure the temperature dependent properties for graphite/epoxy composite IM7/977-2. Transverse modulus E_2, shear modulus G_{12}, and coefficient of thermal expansion α are measured at different temperature and fitted with polynomial functions. In the following simulation, these experimental results are used. Longitudinal modulus E_1 and Poisson's ratios are assumed to be temperature independent, and shear modulus G_{23} is assumed to follow the relation

$$G_{23} = \frac{E_2}{2(1+\upsilon_{23})} \tag{25}$$

In the simulation, constant strain boundary conditions are applied. Strains in both x-direction and y-direction are 1%. Thermal load is applied from room temperature to cryogenic temperature. Figure 33 shows the computed intersection area. The line with square symbols is the result with temperature independent material properties and the line with diamond symbols is the result with temperature dependent properties. From this figure, it can be seen that at cryogenic temperature the result with temperature dependent properties is almost 15% less than that with temperature independent properties. Hence, if temperature independent material properties were used, the simulation will give the upper bound of the permeability.

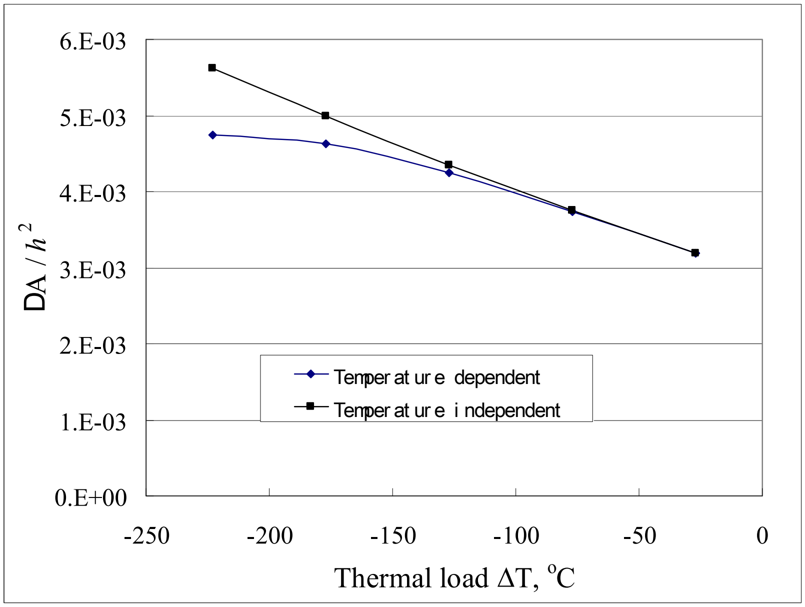

Figure 33: Effect of temperature dependent material properties on the intersection area.

Progressive Permeability Prediction

In this section, progressive gas permeability in laminates [0/90$_n$/0] (n = 1, 2, 4) is predicted in terms of applied load. Previously, the crack densities in laminates [0/90$_n$/0] are predicted under different biaxial loadings. A typical unit cell is taken to compute the intersection area. To keep same as the unit cell in crack density prediction, the surface cracks in the unit cell are not symmetric. The crack densities in this unit cell is taken as $\lambda_x = \lambda_y = 2$ cm^{-1}. Delaminations from both surface ply and middle ply are introduced in this model. Due to symmetry, only one-fourth of unit cell is taken for analysis, as shown in Fig. 34. In this section, only mechanical loads are considered, so only two basic cases are needed for each unit cell: (ε_x = 1%, ε_y = 0) and (ε_x = 0, ε_y = 1%). Figure 35 shows the deformation of the unit cell under loading case (εx = 1%, εy = 0). The deformation is enlarged by a factor of 10.

The two basic cases of intersection areas for laminates [0/90$_n$/0] are tabulated in Table 3. From this table, it can be seen that in both cases the intersection area increase as the thickness of the middle ply increase. A MATLAB program is then developed to predict progressive permeability and to plot the permeability versus the applied load. In this program, the predicted crack densities shown in Fig. 14 to Fig. 22 are fitted with cubic polynomials and then the intersection areas are computed from the two basic cases shown in Table 3. Finally, the progressive permeability is computed using Eq. (11).

Figures 36 through 38 show the predicted permeability as a function of average stress σ_y. Each figure represents one loading ratio. In Fig. 36, N_x/N_y = 0.5, in Fig. 37, N_x/N_y = 1.0, and in Fig. 38, N_x/N_y = 2.0. From these figures, it can be seen that the initiation stresses of gas permeability increase as the thickness of middle ply decrease. After initiation, however, the gas permeability in the laminate with thinner middle ply increases faster than in the one with thicker middle ply. This follows the same trend as the evolution of crack density. Even though the intersection area in [0/90$_4$/0] is the largest, the permeability in [0/90$_4$/0] increases slowest comparing to the other laminates. Hence, it can be conclude that the permeability is dependent more on the crack density than on the intersection area.

For laminate [0/90/0], no permeability is predicted for N_x/N_y = 0.5 and N_x/N_y = 1.0 under available stress level because the middle ply remains undamaged (see Fig. 14 and Fig. 17).

Table 3: Typical Intersection Areas (m^2) for Laminates [0/90$_n$/0]

Lay-ups	[0/90/0]	[0/90$_2$/0]	[0/90$_4$/0]
Case I: ε_x = 1%, ε_y = 0	8.32×10^{-11}	10.5×10^{-11}	12.5×10^{-11}
Case II: ε_x = 0, ε_y = 1%	7.72×10^{-11}	10.1×10^{-11}	11.8×10^{-11}

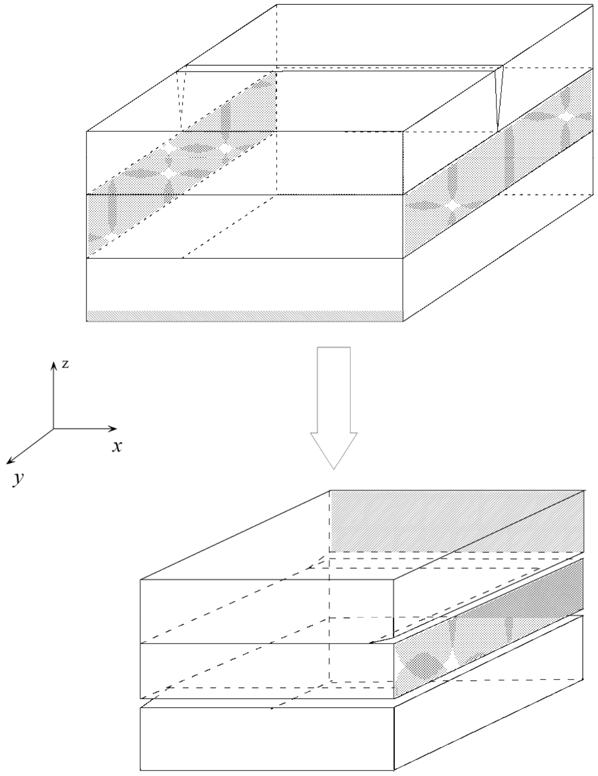

Figure 34: Unit cell used to compute typical intersection area. ($\lambda_x = \lambda_y$ = 2 cm^{-1})

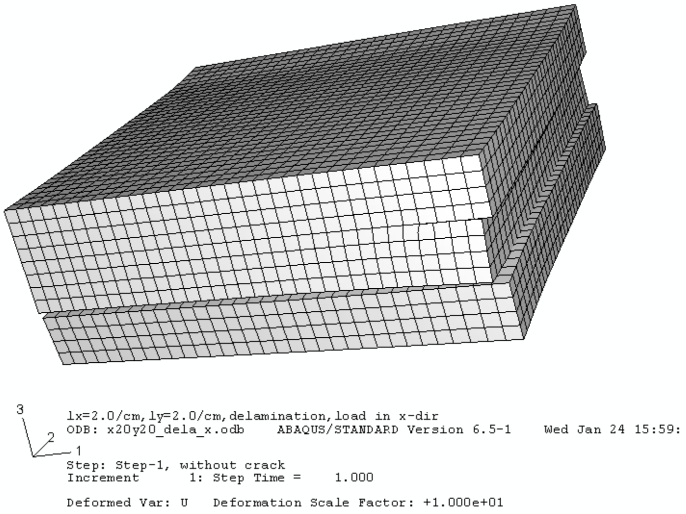

```
lx=2.0/cm,ly=2.0/cm,delamination,load in x-dir
ODB: x20y20_dela_x.odb    ABAQUS/STANDARD Version 6.5-1    Wed Jan 24 15:59:

Step: Step-1, without crack
Increment      1: Step Time =    1.000

Deformed Var: U   Deformation Scale Factor: +1.000e+01
```

Figure 35: Typical deformation of the unit cell of [0/90/0].

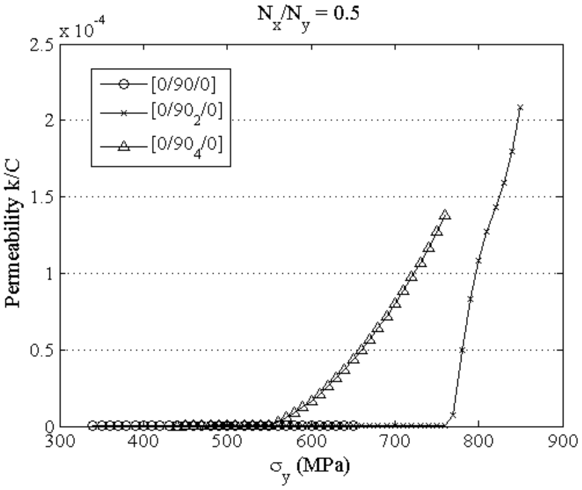

Figure 36: Progressive permeability in laminates with loading ratio $a = 0.5$.

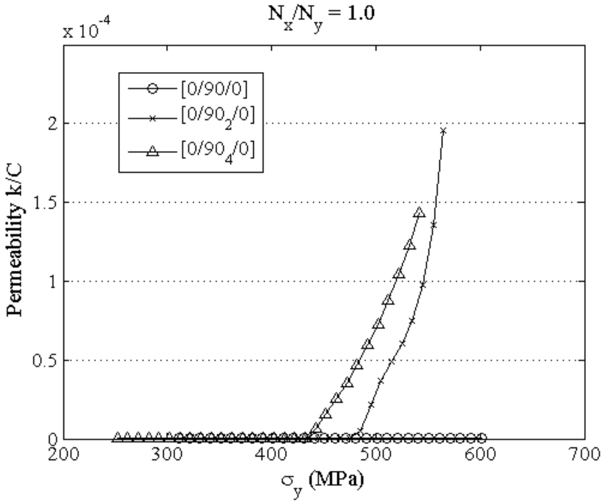

Figure 37: Progressive permeability in laminates with loading ratio *a* = 1.0.

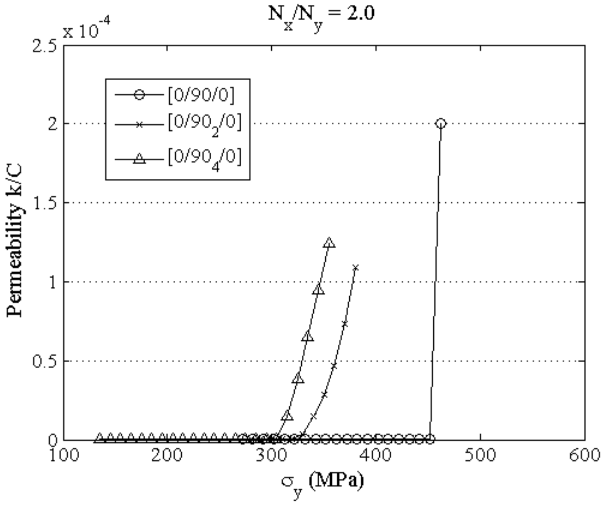

Figure 38: Progressive permeability in laminates with loading ratio *a* = 2.0.

Permeability Testing of Composite Laminates

The permeability is defined by the amount of gas that passes through a given material of unit area and unit thickness under a unit pressure gradient in unit time. The SI unit of the permeability is mol/sec/m/Pa. Experiments were performed to investigate the effect of cryogenic cycling on permeability of laminated composites and to provide useful comparison of permeabilities of various composite material systems.

Standard Test Method for Determining Gas Permeability

The standard test method for determining gas permeability is documented in ASTM D1434-82 (Re-approved in 1997) “Standard Test Method for Determining Gas Permeability Characteristic of Plastic Film and Sheeting [ASTM].” The permeability can be measured by two methods, manometric determination method and volumetric determination methods. The permeability experiment using the monometric determination method is shown in Figure 39. The lower pressure chamber is initially vacuumed and the transmission of the gas through the test specimen is indicated by an increase in pressure.

The permeability is measured using volumetric determination as shown in Figure 40. The lower pressure chamber is exposed to atmospheric pressure and the transmission of the gas through the test specimen is indicated by a change in volume. The gas volume-flow rate is measured by recording the rise of liquid indicator in a capillary tube per unit time. The gas transmission rate (GTR) is calculated using the ideal gas law. The permeance is determined as the gas transmission rate per pressure differential across a specimen. The permeability is determined by multiplying permeance by the specimen thickness.

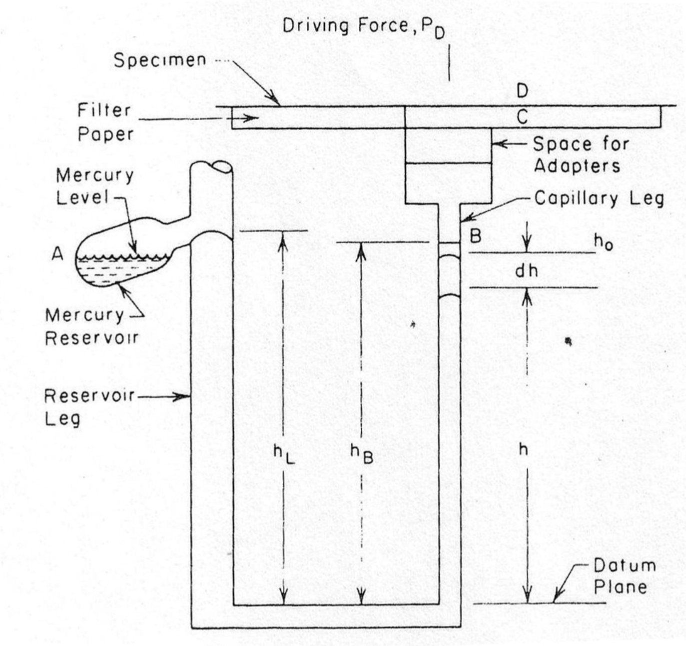

Figure 39. Permeability experimental setup for manometric determination method.

The monometric determination method was not considered for this study since it is dangerous to handle the mercury compound, which is considered as a health hazardous material. Therefore, the permeability facility was constructed based on the volumetric determination method as shown in Figure 40.

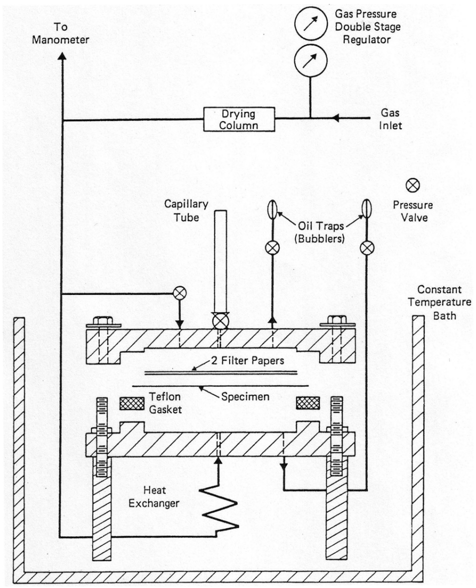

Figure 40. Permeability experimental setup for volumetric determination method

Permeability Apparatus

This apparatus basically consists of a specimen placed between two chambers as shown in Figure 41. The test gas is pressurized in the upstream chamber. The gas permeates through one side of the specimen and escapes out of the other side. The escaped gas is collected in the downstream chamber and flows into a glass capillary tube. The amount of gas escaping per unit time is measured. The permeance is determined by gas transmitted rate and the partial pressure differential across the specimen. The permeability $\overline{P}$ is defined by the product of permeance *P* and the specimen thickness *t*.

The gauge pressure of the gas in the upper upstream chamber is measured using a pressure transducer (P-303A from the Omega Engineering Inc.). The ambient pressure is measured by a barometric sensor (2113A from the Pasco Scientific). A precision pressure regulator provides constant gas pressure to the upstream chamber. The ambient temperature was measured using a glass capillary thermometer.

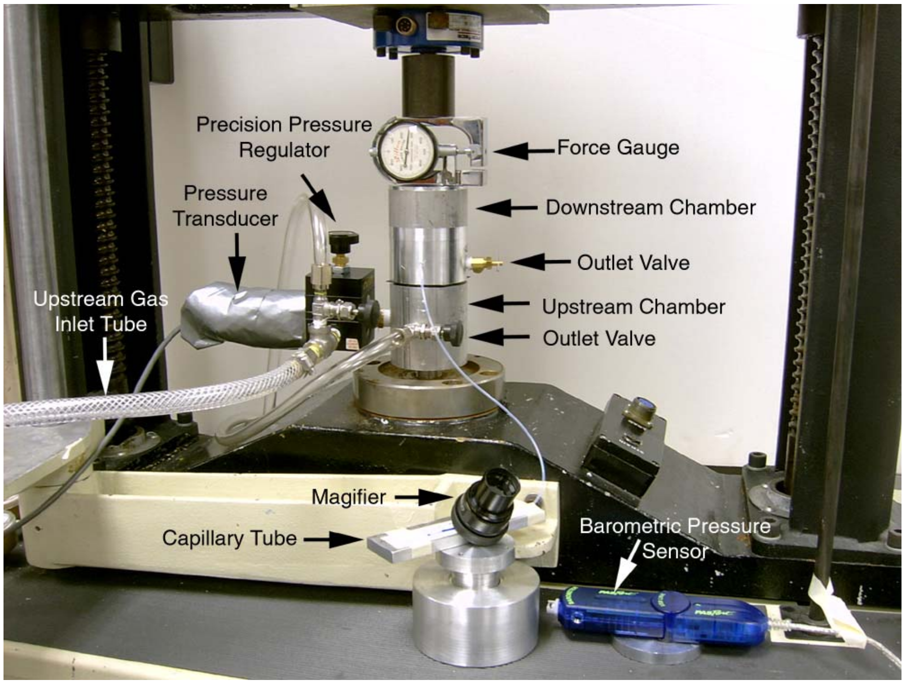

Figure 41. Permeability testing apparatus.

The specimens are mounted horizontally between the upstream and downstream chambers and clamped firmly by applying a compressive load as shown in Figure 42. The specimen is sealed with a rubber gasket and an O-Ring (38 mm inner diameter). A force gauge mounted at the top measures the compressive load to ensure that the same amount of compressive load is applied on the specimens for every test. The compressive load should be enough to prevent gas leakage, but should not damage the specimens. The upstream chamber has an inlet vent and an outlet vent. The inlet vent allows the gas flow into the upstream chamber and the outlet vents is used to purge the test gas to atmosphere (Figure 4-2). The downstream chamber has two outlet vents. One is used to purge the test gas to atmosphere and the other allows the gas flow to the glass capillary tube for measurements. The sensitivity of permeability measurement can be improved by increasing the gas transmitting area of a specimen.

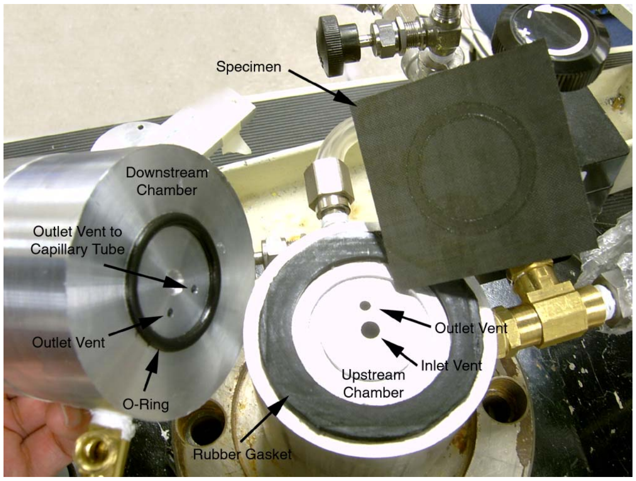

Figure 42. Specimen installation between upstream and downstream chambers.

The glass capillary tube is mounted on a rigid aluminum base horizontally to minimize the gravity effect on the capillary indicator and for easy reading of the scale marks on the capillary tube. Nettles (2001) found that there was no significant difference in the volumetric flow rate when capillary tube is placed vertically or slanted. The inner diameter of the glass capillary tube is 1.05 mm and the length is 100 mm. A magnifying glass is used to read the scale marks at the top of the meniscus of the liquid indicator.

The liquid indicator in the glass capillary tube is used to measure the rate of rise of the liquid indicator. The rate is used to calculate the volume flow rate of the escaped gas across the specimen. Nettles (2001) investigated the effects on the volume flow rates by using various types of liquid. The volume flow rates obtained using water, alcohol, and alcohol with PhotoFlo® were not significantly different. In the present study, methyl alcohol is chosen as the liquid indicator since alcohol has low viscosity and weight. The methyl alcohol is colored with a blue dye to obtain precise readings on the scale marks.

The primary investigation is the hydrogen permeability of a liquid hydrogen composite storage system. Since hydrogen gas is highly flammable and explosive when it mixed with air, it needed to be handled carefully during the test. Hence, other permeate gases were considered as a substitute for the hydrogen gas. The molecular diameter of various gases is listed in Table 4 below (Nettles, 1995). To choose a permeate gas, the molecular diameter determined from viscosity measurement is mainly considered since the permeability is related with the volumetric flow rate directly. Since helium has the smallest molecular diameter, the helium predicts the permeation results higher than other gases. Therefore, in the study, helium was chosen as the permeate gas instead of hydrogen.

Table 4: Molecular diameter of various gases

(CRC Handbook of Chemistry and Physics, 54th Edition)

Type of Gas	Molecular Diameter (cm)		
	From Viscosity	From van der Waal's Equation	From Heat Conductivity
Helium	1.9×10^{-8}	2.6×10^{-8}	2.3×10^{-8}
Hydrogen	2.4×10^{-8}	2.3×10^{-8}	2.3×10^{-8}
Nitrogen	3.1×10^{-8}	3.1×10^{-8}	3.5×10^{-8}

Specimen Description

The permeability tests were performed with various composite material systems. The details of specimens are described in Table 5. The specimens C1, C2, and C3 are various graphite/epoxy laminated composites. The specimen T1 is a textile composite. The specimen N1 is a laminated composite embedded with 36 μm aluminum oxide (Al_2O_3-alumina) nano-particles. The aluminum oxide was dissolved in alcohol and the compound was applied on a surface on a laminated prepreg using a paint blush. The nano-particles are capable of relieving the thermal stresses due to contraction of fiber and matrix phases. In addition, it can prevent the crack propagation in matrix phase by relieving the stress concentration at the crack-tip. The graphite/epoxy prepregs were fabricated with designed stacking orientations. The graphite/epoxy prepregs were cured in an autoclave and machined by a diamond saw to 3×3 inch specimens at low speed to avoid fiber shattering. The surface is cleaned with acetone and prepared carefully to avoid contamination or damages on the surface of the specimen during machining and subsequent handling.

Table 5: Description of composite specimens

Specimen	Prepreg Type	Stacking Sequence	Thickness (mm)
C1	Graphite/Epoxy laminates	$[0/90/0/90/0/90]_S$	1.52
C2	Graphite/Epoxy laminates	$[0_2/90_2/0_2]_T$	0.787
C3	Graphite/Epoxy laminates	$[0/90/0_2/90/0]_T$	0.914
C5	Graphite/Epoxy laminates	$[0/90_2/0]_T$	0.533
T1	Plain weave textile(SP Systems SE-84)	4 layers	0.686
N1	Graphite/Epoxy laminates with nano-particles	$[0/90/NP/90/0]_T$	0.483

The specimens were subjected to cryogenic cycling at specified number of times, representing multiple refueling process of a space vehicle. A single cryogenic cycle consisted of cooling down from room temperature to cryogenic temperature and then warming up to room temperature. Initially, specimens were placed at room temperature (T = 300K). And, then the specimens completely submerged in an insulated container filled with liquid nitrogen. The specimens stayed in the container for approximately 2 minutes. When the specimen reached the boiling temperature of liquid nitrogen (T = 77K), the liquid nitrogen boiling disappears. The specimens were taken out of the container and placed at room temperature. The specimen was held at room temperature for approximately 5 minutes. The cryogenic cycling procedure is repeated for desired number of times.

Testing Procedure

Before starting the permeability test, a thin coat of silicon grease was applied on the gasket and an O-ring was placed to improve sealing of contact surfaces on a specimen. The excessive silicon grease was wiped out to avoid obstructions of permeated gas on the transmitting surface of the specimen. All outlet valves were opened initially to avoid sudden pressurization of test gas. The specimen was placed horizontally on the gasket of the upstream chamber. And then, the downstream chamber was placed on the top surface of a specimen. The specimen was mounted between the chambers. Both chambers were aligned and mated as close as possible. The specimen was mounted between the chambers and clamped firmly with a compressive force. Then, even distributed forces were applied to the sealing materials of the chambers.

The test gas was admitted to the upstream chamber by opening the gas release valve of the gas tank. While all outlet valves remained opened, the test gas was filled in the upstream chamber and ventilated though the outlet vent to atmosphere. Any residual air in the upstream chamber was purged for 1 minute. The outlet valve on the upstream chamber was closed and the test gas was allowed to permeate across the specimen for a sufficient time to purge any residual air at downstream chamber. At this time, only test gas filled the chambers. When the outlet valve of the upstream chamber was closed, the upstream pressure increased slowly. The upstream pressure can be adjusted by controlling the pressure regulator. Sufficient time was allowed for attaining steady state of moving rate of the liquid indicator before beginning to take readings. The distance of rise of the liquid indicator was measured while the ambient pressures were recorded.

Calculations

The volumetric methodology is used to calculate the permeability by measuring gas volume transmitted through a specimen. The rate of rise of the liquid indicator is measured using the capillary tube. The volume flow rate is calculated as follows.

$$V_r = slope \times a_c \tag{26}$$

where a_c is the cross-sectional area of a capillary tube. The slope is the rate of rise of the liquid indicator in the capillary tube. The gas transmitted rate (GTR) is calculated using the ideal gas law as follows.

$$GTR = \frac{p_o \cdot V_r}{ART} \tag{27}$$

where p_o is ambient pressure, A is transmitting area of a specimen, R is the universal gas constant (8.3143×10^3 L·Pa/{mol·K}) and T is ambient temperature. The permeance P is defined by the ratio between the gas transmission rate and pressure differential across the thickness of a specimen. Therefore, the permeance P is calculated as follows.

$$P = \frac{GTR}{p - p_o} \tag{28}$$

where p is the upstream pressure. The S.I. units of permeance are [mol/(m^2·s·Pa)].

According to the standard test method, the permeability $\overline{P}$ is defined by the product of permeance P and the specimen thickness t and “the permeability is meaningful only for homogeneous materials [ASTM].” In this study, although the laminated composites are considered as orthotropic materials, its permeability $\overline{P}$ is calculated by following the corresponding definition for isotropic materials [Nettles, 2001].

Calibration

The position of capillary indicator is very sensitively to even small variations of testing conditions such as ambient pressure and temperatures caused by closing doors or air-conditioning system in the laboratory. For example, during one test, the variation of the ambient pressure was approximately 0.3% for a 13-hour period (Figure 43). For the permeability calculation, the ambient pressure is assumed to be constant. However, the variation is large enough to cause error in measuring the rate of rise of the capillary indicator. The moving distance is needed to be calibrated to compensate for error due to the variation of ambient pressure.

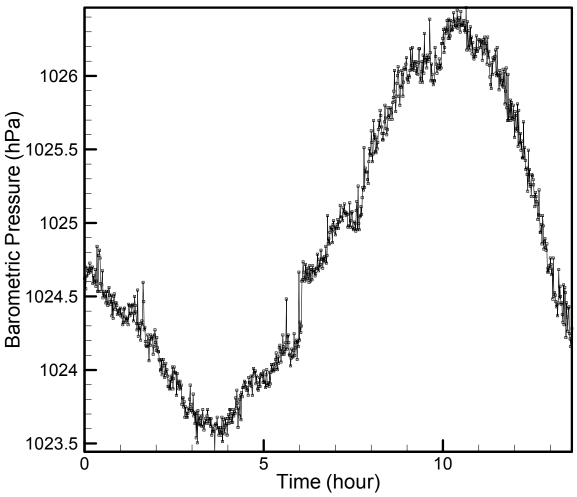

Figure 43. Variation of ambient pressure for 13 hours at test condition

The correction factor due to the variation of ambient pressure was calculated by performing the permeability test without applying the upstream pressure. An aluminum plate is used for the test to ensure that there is no gas permeation to the downstream chamber. Since there was not much variation in the ambient temperature, only ambient pressure causes changes in the position of the capillary indicator. After the outlet valve of the downstream chamber was closed, the displaced position of the capillary indicator and ambient pressure were measured simultaneously as shown in Figure 44.

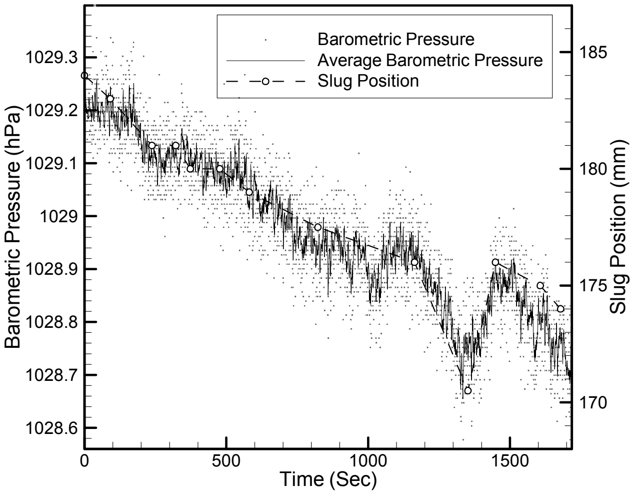

Figure 44. Variation of barometric pressure and indicator position as a function of time

The correction factor k is calculated by $k = \Delta h / \Delta p$ where h is the moving distance of the capillary indicator and p is the ambient pressure. The average correction factor is found to be 0.21 mm/Pa. Therefore, the corrected moving distance of the capillary indicator is calculated as follows:

$$h_{corrected} = h_{actual} + k \cdot \Delta p \tag{29}$$

where Δp is differential of ambient pressure between the beginning and end of the test.

Permeability Test Results

The permeability tests were performed with various composite material systems at room temperature. The permeability was measured at six different levels of upstream pressure. The average permeance P and average permeability $\overline{P}$ are tabulated in Table 6 for laminated composites, the results for textile composites are in Table 7 and the results for laminated composites with embedded with nano-particles in Table 8.

Table 6. Permeability of laminated composites for various number of cryogenic cycles

Specimen	Cryogenic cycles	Permeance, P (mol/sec/m^2/Pa)	Permeability, $\overline{P}$ (mol/sec/m/Pa)	Logarithm of $\overline{P}$
C1	0	5.60×10^{-18}	8.54×10^{-21}	-20.1
	1	1.52×10^{-17}	2.32×10^{-20}	-19.6
	5	2.39×10^{-17}	3.65×10^{-20}	-19.4
	10	2.39×10^{-17}	3.65×10^{-20}	-19.4
	20	2.11×10^{-17}	3.22×10^{-20}	-19.5
C2	0	7.02×10^{-18}	1.07×10^{-20}	-20.0
	1	1.06×10^{-17}	1.62×10^{-20}	-19.8
	5	1.47×10^{-15}	2.23×10^{-18}	-17.7
	10	1.42×10^{-15}	2.16×10^{-18}	-17.7
	20	1.49×10^{-15}	2.27×10^{-18}	-17.6
C3	0	6.22×10^{-18}	9.48×10^{-21}	-20.0
	1	7.56×10^{-18}	1.15×10^{-20}	-19.9
	5	7.60×10^{-18}	1.16×10^{-20}	-19.9
	10	8.37×10^{-18}	1.28×10^{-20}	-19.9
C5	0	5.85×10^{-18}	8.92×10^{-21}	-20.0
	1	9.52×10^{-16}	1.45×10^{-18}	-17.8
	5	8.67×10^{-16}	1.32×10^{-18}	-17.9
	20	8.81×10^{-16}	1.34×10^{-18}	-17.9

Table 7. Permeability of textile composites for various number of cryogenic cycles

Specimen	Cryogenic cycles	Permeance, P (mol/sec/m^2/Pa)	Permeability, $\overline{P}$ (mol/sec/m/Pa)	Logarithm of $\overline{P}$
T1	0	4.79×10^{-18}	7.30×10^{-21}	-20.1
	1	6.77×10^{-18}	1.03×10^{-20}	-20.0
	5	8.41×10^{-18}	1.28×10^{-20}	-19.9
	20	8.75×10^{-18}	1.33×10^{-20}	-19.9

Table 8. Permeability of laminated composites embedded with nano-particles for various number of cryogenic cycles

Specimen	Cryogenic cycles	Permeance, P (mol/sec/m^2/Pa)	Permeability, $\overline{P}$ (mol/sec/m/Pa)	Logarithm of $\overline{P}$
N1	0	6.82×10^{-18}	1.04×10^{-20}	-20.0
	1	2.72×10^{-15}	4.15×10^{-18}	-17.4
	5	1.30×10^{-14}	1.98×10^{-17}	-16.7
	20	9.83×10^{-15}	1.50×10^{-17}	-16.8

The test results show the permeability increases as the number of cryogenic cycles increases (see Figure 45). The permeability increased rapidly and becomes constant with further increase of cryogenic cycles. For specimens C2 and C3, which have approximately same thickness, the permeability of the specimen C3 was lower since the specimen C3 has the plies dispersed and not grouped together compared to the specimen C2.

The textile specimen T1 maintained constant permeability with the increase of cryogenic cycles. The textile composites resulted lower permeability than the laminated composites. The specimen N1 has same layer stacking orientations with the specimen C5 and nano-particles were dispersed between two 90-degree layers. Before cryogenic cycling, the permeabilities of the specimens N1 and C5 were approximately the same. However, as the number of cryogenic cycles increased, the permeability of the specimen N1 became higher. The use of nano-particles did not improve the permeability of laminated composites.

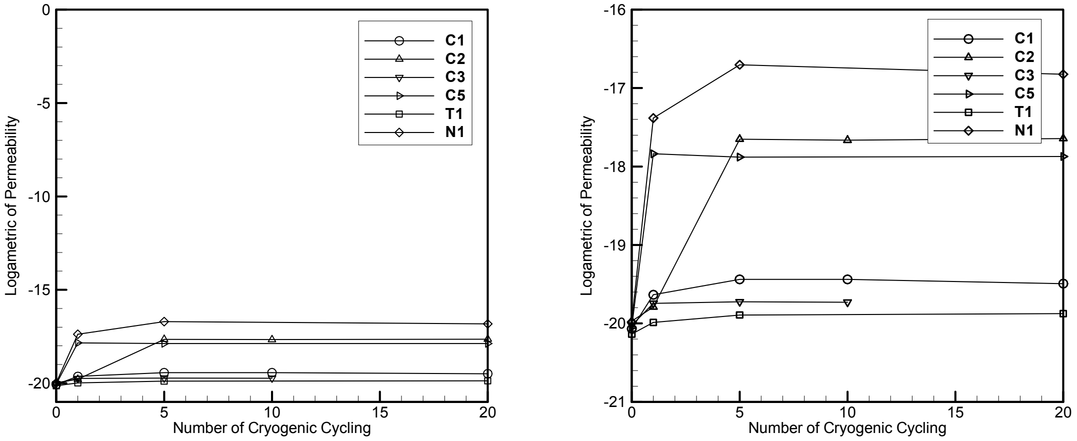

Figure 45. Logarithm of the permeability for composite specimens with increase of cryogenic cycles.

Optical Microscopic Analysis

The optical microscopic inspection was performed to evaluate the microcrack propagation and void content of various composite systems after cryogenic cycling. In the previous section, the experimental results showed that the permeability increases as the composite specimen underwent more cryogenic cycles. As the crack density increases, gas flow becomes easier though the specimen. Therefore, the microcrack propagation is correlated with cryogenic cycling.

The specimens were cut through the center using a diamond saw. A LECO grinder/polisher was used for the sample preparation process. The rough edge through the center was ground with 600-grit sand paper with water for 30 seconds. The fine grinding was performed with the 1000-grit and 1500-grit papers for 30 seconds. The surface of the edge was polished with the 58 μm aluminum oxide powder (Al_2O_3-alumina) dissolved in distilled water. The purpose of the lubricant is to both dissipate the heat from polishing and to act as a carrier for the abrasive materials. The ultrasonic cleaner was used to remove any abrasive particles and contaminants on the polished surface of a specimen. The optical analysis was conducted with a NIKON EPIPOT microscope.

The laminated composite specimen C2 and the textile composite specimen T1 were chosen for optical inspection. The specimen details are described in Table 5. The microscopic images for the specimens were compared before and after cryogenic cycling.

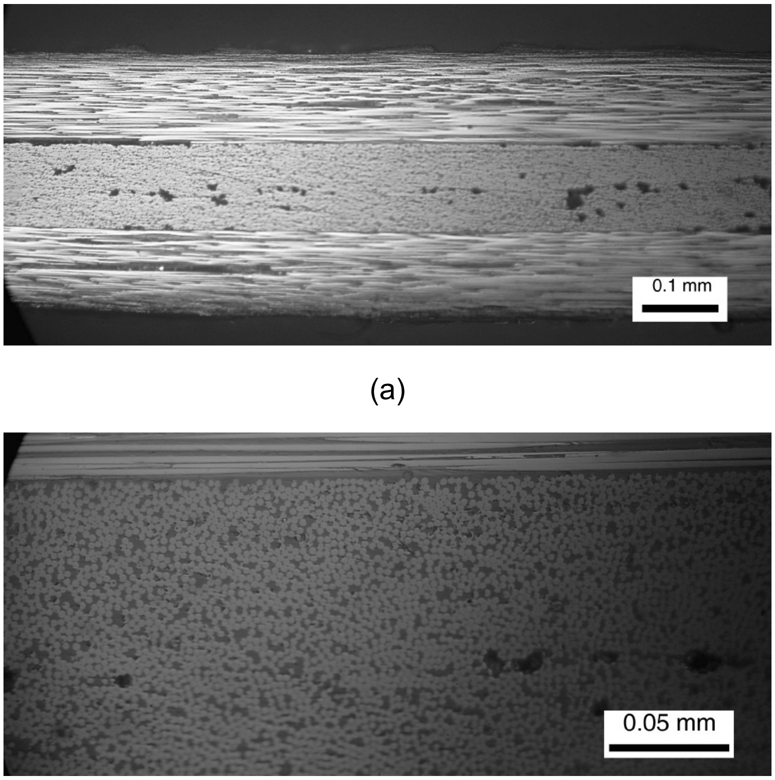

(a)

(b)

Figure 46. Cross sectional view of the graphite/epoxy composite specimen C2 before cryogenic cycling: (a) 10X magnification; (b) 40X magnification.

For the graphite/epoxy specimen C2 before cryogenic cycling, no microcrack propagation observed (see Figure 46). Some voids formed in the middle of the 90-degree layers and between the 0-degree layer and the 90-degree layers. The voids probably formed during composite fabrication in autoclave. When the graphite/epoxy prepreg was cured at high temperature, some air bubbles could have been trapped between layers. It is possible that external pressure applied on the vacuum bag was insufficient to remove the bubbles.

After cryogenic cycling on the specimen C2, microcracks were observed in the 90-degree layer as shown in Figure 47. The fiber breaks were not observed in the in 0-degree layer since the thermal stresses were not large enough. The delaminations propagated along the middle of the 90-degree layer where some voids were found. The transverse cracks branched with the delaminations. Since the gas can be transmitted through the transverse cracks across the specimen, the permeability increased after cryogenic cycling.

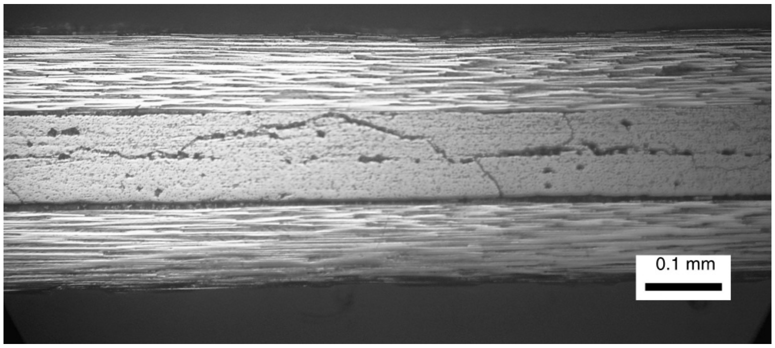

(a)

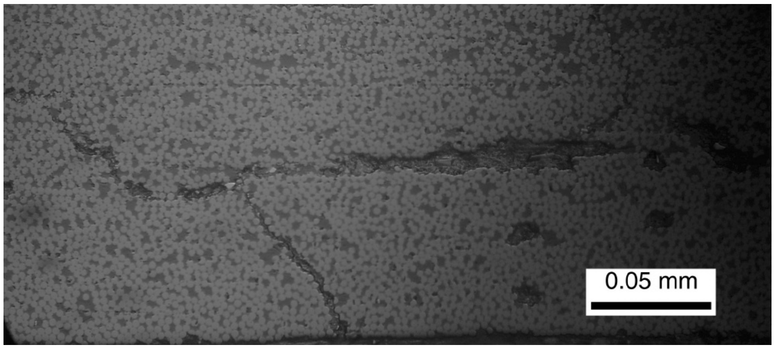

(b)

Figure 47. Microcrack propagation on the graphite/epoxy composite specimen C2 after cryogenic cycling: (a) 10X magnification; (b) 40X magnification.

For the textile composite specimen T1 before cryogenic cycling, no microcracks were observed as shown in Figure 48. Voids were observed at the location where two yarns are merging.

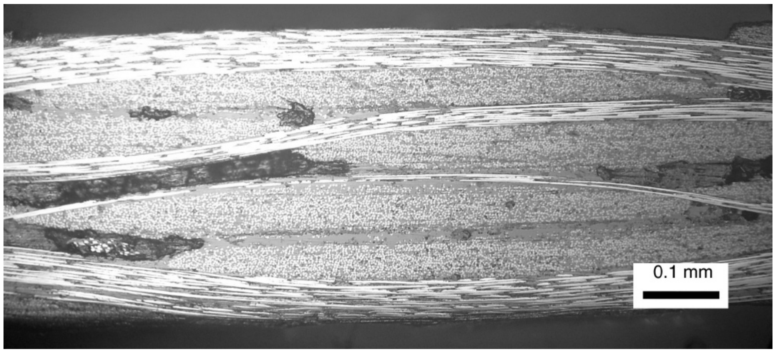

Figure 48. Cross sectional view of the textile specimen T1 before cryogenic cycling, 10X magnification.

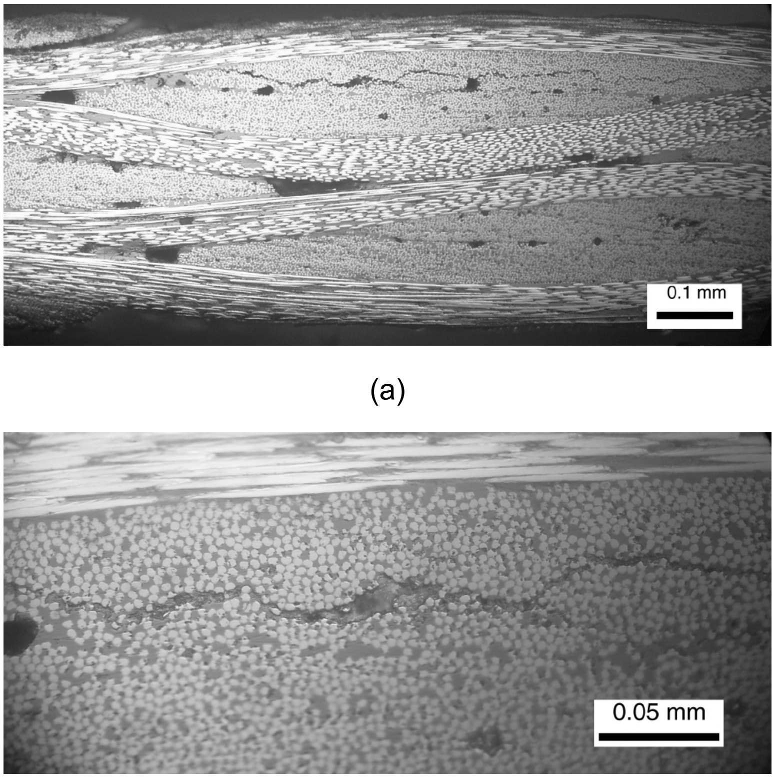

(a)

(b)

Figure 49. Microcrack propagation in the textile specimen T1 after cryogenic cycling: (a) 10X magnification; (b) 40X magnification.

After the textile specimen T1 underwent cryogenic cycles, microcrack were observed in 90-degree yarn as shown in Figure 49. The microcracks propagated in the in-plane direction of the specimen. Since transverse cracks were not propagated, the permeability of textile composites was almost the same before and after cryogenic cycling. The transverse cracks and delaminations provide the leakage path through composite laminates and thus directly related to the permeability. For the laminated composite specimen, the microscopic results showed that transverse crack propagation and delaminations of composite laminates. For the textile composite specimen, the transverse cracks propagation was not observed, which resulted low permeability of textile composites even after cryogenic cycling.

Conclusions

In this work, a permeation model for composite laminate is developed based on Darcy’s Law. The permeability constant is a function of crack density, intersection area and a material constant. From 2-D FE analysis, the problem is decoupled into two parts: crack density prediction and intersection area computation. The crack density in cross-ply laminate under biaxial loading is predicted as a function of applied load using an energy-release-rate-method based on 3-D FE analysis. Then the intersection area for a typical unit cell is computed using 3-D FEM because of the significant local effect. The effects of various factors on the intersection area are investigated, and it has been found that the intersection area is not only dependent on applied load but also dependent on delamination length, shape of the delamination front, temperature dependent material property and lay-ups. The progressive permeability in cross-ply laminate with different middle ply is predicted and it has been found that the initiation stress of leakage and the increase rate of leakage are dependent on the thickness of the middle ply. The laminate with thinner middle ply has higher initiation stress, but also has higher increase rate once it start to leak.

The experimental analysis was performed to measure the gas permeability of various composite material systems for the liquid hydrogen composite tank and the effect of cryogenic cycling of composite laminates on the permeability was investigated. The permeability test facility was constructed following the standard test method documented in ASTM D1434-82. The permeability test was conducted at room temperature. The sensitivity of permeability measurement can be improved by increasing the gas transmission area of a specimen. Since hydrogen is flammable and explosive when it mixed with air, the helium gas is substitute for hydrogen. The calibration is performed to compensate the ambient pressure differences during the test. The correction factor is found as 0.21 mm/Pa. The actual moving distance of the liquid indicator is calibrated by the correction factor.

The permeability of laminated composite was found to degrade after undergoing cryogenic cycling process. In thin laminate specimens the permeability increases significantly after cryogenic cycling. For thick laminated specimens the increase of permeability is less. The textile composite specimen has lower permeability than laminated specimens and the variation of permeability is very small with the increase of cryogenic cycles. The laminated composites were embedded with nano-particles, which are capable of reducing thermal stresses in the matrix phase. However, as results, the nano-particles did not show the improvement on permeability. Further studies are needed to investigate the effects of nano-particles. The optical analysis was performed to investigate the microcrack propagation and void contents of test specimens. The transverse cracks and delaminations provide the leakage path through composite laminates and thus directly related to the permeability. The optical micrographic analysis was performed to investigate the microcrack propagation and void contents of test specimens. For the laminated composite specimen, the microscopic results showed that transverse crack propagation and delaminations of composite laminates. For the textile composite specimen, the transverse cracks propagation was not observed, which resulted in low permeability of textile composites even after cryogenic cycling.

List of Students

Doctoral Students

Choi, Sukjoo. “Micromechanics, Fracture Mechanics and Gas Permeability of Composite Laminates for Cryogenic Storage Systems”, Doctoral Dissertation, University of Florida, May 2005

Xu, Jianlong. “Prediction of Gas Permeability in Composite Laminates Using Three-dimensional Finite Element Method”, Doctoral Dissertation, University of Florida, August 2007 (expected)

Master Theses

Noh, Won-Jong. “Mixed-Mode Interfacial Fracture Toughness of Sandwich Composites at Cryogenic Temperatures”, Master Thesis, University of Florida, August 2004

Kalarikkal, Sujit. “Fracture Toughness of Graphite/Epoxy Laminates at Cryogenic Conditions”, Master Thesis, University of Florida, August 2004

Van Pelt III, James. “Effect of Strain on the Gas Permeability of Laminated Composites”, Master Thesis, University of Florida, December 2006

List of Publications

Journal Papers

1. Choi, S., B.V. Sankar. “Gas Permeability of Various Graphite/Epoxy Composite Laminates for Cryogenic Storage Systems,” Composites Part B: Engineering (submitted for publication).
2. Xu, J., B.V. Sankar, S.K. Bapanapalli. “Finite Element Based Method to Predict Gas Permeability in Cross-ply Laminate,” Journal of Composite Materials. (submitted for publication).
3. Xu, J., B.V. Sankar. Parametric investigation of gas permeability in cross-ply composite laminates using three-dimensional finite elements. *AIAA Journal* 45(4) 2007 934-941.
4. Choi, S, B.V. Sankar. Fracture toughness of transverse cracks in graphite/epoxy laminates at cryogenic conditions. *Composites: Part B* 38 (2007) 193-200.
5. Choi, S., B.V. Sankar. Micromechanical Analysis of Composite Laminates at Cryogenic Temperatures. *J. Composite Materials*, 40(12) 2006 1077-1091.
6. Choi, S. and B.V. Sankar, 2005, “A Micromechanical method to predict the fracture toughness of cellular materials,” *International Journal of Solids & Structures*, 42/5-6, pp. 1797-1817.
7. Choi, S., B.V. Sankar. “Fracture toughness of carbon foam”, *Journal of Composite Materials*, 37(23):2101-2116, 2003.

6 Kalarikkal, S., B.V. Sankar, P.G. Ifju. Effect of Cryogenic Temperature on the Fracture Toughness of Graphite/Epoxy Composites. *ASME Journal of Engineering Materials and Technology* 128(2) 2006 151-157.

7 Choi, S., B.V. Sankar. “Gas Permeability of Graphite/Epoxy Composite Laminates for Cryogenic Storage Systems,” Composites Part B (under review).

Conference Papers

1. Van Pelt, J., B. V. Sankar, P. G. Ifju. “Gas Permeability of Composite Laminates for Cryogenic Storage Systems”, *21st Annual Technical Conference of the American Society for Composites*, CD ROM Proceedings, University of Michigan, Dearborn, MI, September 2006, Paper #212, 17 pages.
2. Xu, J., B.V. Sankar. “Prediction of Gas Permeability in Cross-ply Laminates using Finite Elements”, *21st Annual Technical Conference of the American Society for Composites*, CD ROM Proceedings, University of Michigan, Dearborn, MI, September 2006, Paper #207, 9 pages.
3. J. Xu and B.V. Sankar. “Parametric investigation of gas permeability in cross-ply composite laminates using three-dimensional finite elements”, AIAA Paper 2006-2093, 47th AIAA/ASME/ASCE/AHS/ASC Structures, Structural Dynamics, and Materials Conference, 1 - 4 May 2006, Newport, Rhode Island (12 pages).
4. Lee, S., S. Choi and B.V. Sankar. “A micromechanical model for predicting the fracture toughness of functionally graded foams”, Proceedings of the 22nd Southeastern Conference in Theoretical and Applied Mechanics (SECTAM), August 15-17, 2004, Center for Advanced Materials, Tuskegee University, Tuskegee, Alabama, pp. 613-622.
5. Choi, S., B.V. Sankar. “Thermal stresses in a composite pressure vessel at cryogenic temperatures”, *Developments in Theoretical and Applied Mechanics,* Proceedings of the 22nd Southeastern Conference in Theoretical and Applied Mechanics (SECTAM), August 15-17, 2004, Center for Advanced Materials, Tuskegee University, Tuskegee, Alabama, pp. 587-596.
6. Choi, S. and B.V. Sankar, “A micromechanics method to predict the fracture toughness of carbon foam”, *Fourteenth International Conference on Composite Materials*, CD ROM proceedings, San Diego, California, July 2003, Paper # 1355, 11 pages.

7. Choi, S. and B.V. Sankar, “A micromechanics method to predict the micro-cracking of the LH2 composite tank at cryogenic temperature,” Proceedings of the 5th International Congress on Thermal Stresses and Related Topics, TS 2003, Eds. L. Librescu and P. Marzocca, Virginia Polytechnic Institute & State University, Blacksburg, VA, 8-11 June 2003, pp. WM441-444.

References

- Aoki, T, Kumazawa, H, and Susuki, I (2002, Oct.). Propellant Leakage through Laminated Structures. Proceeding of American Society for Composites (ASC) 17th Annual Technical Conference, West Lafayette, IN.
- ASTM D1434-82 (1992). Standard Test Method for Determining Gas permeability Characteristics of Plastic Film and Sheeting. ASTM, 203-213.
- Bapanapalli, SK, Sankar, BV, and Primas, RJ (2006). Microcracking in Cross-ply Laminates due to Biaxial Mechanical and Thermal Loading. AIAA Journal, 44(12), 2949-2957.
- Bechel, VT, and Arnold, F (2006, May). Permeability of Polymer Composites for Cryogenic Applications. Proceeding of 47th AIAA/ASME/ASCE/AHS/ASC Structures, Structural Dynamics & Materials conference, Newport, RI, AIAA-2006-2015.
- Bechel, VT, Camping, JD, and Kim, RY (2005). Cryogenic/elevated Temperature Cycling Induced Leakage Paths in PMCs. Composites: Part B, 36(2), 171-182.
- Berthelot, JM (2003). Transverse Cracking and Delamination in Cross-ply Glass-fiber and Carbon-fiber Reinforced Plastic Laminates: Static and Fatigue Loading. Applied Mechanics Review, 56(1), 111-147.
- Choi, S (2005). Micromechanics, Fracture Mechanics and Gas Permeability of Composite Laminates for Cryogenic Storage Systems. Ph.D Dissertation. University of Florida, Gainesville, FL.
- Grenoble, RW and Gates, TS (2006, April). Hydrogen Permeability of Polymer Matrix Composites at Cryogenic Temperatures. Proceeding of 46th AIAA/ASME/ASCE/AHS/ASC Structures, Structural Dynamics & Materials conference, Austin, TX, AIAA-2005-2086.
- Hutchinson, JW and Suo, Z (1992). Mixed Mode Cracking in Layered Materials. Advances in Applied Mechanics, 29, 63-191.
- Jamison, RD, Schulte, K, Reifsnider, KL, and Stinchcomb, WW (1984). Characterization and Analysis of Damage Mechanism in Tension-Tension Fatigue of Graphite/Epoxy Laminates. In Wilkins DJ (Ed.), Effects of Defects in Composites Materials (pp. 21-55). West Conshohocken: ASTM International.
- Kessler, SS, Matuszeski, T, and McManus, H (2001, Sept.). Cryocycling and Mechanical Testing of CFRP for theX-33 Liquid H_2 Fuel Tank Structure. Proceedings of American Society for Composites (ASC) 16th Technical Conference, Blacksburg, VA, ASC-2001-093.
- Kumazawa, H, Aoki, T, and Susuki, I (2003). Analysis and Experiment of Gas Leakage Through Composite Laminates for Propellant Tanks. AIAA Journal, 41(10), 2037-2044.
- Kumazawa, H., Susuki, I, and Aoki, T (2006). Gas Leakage Evaluation of CFRP Cross-ply Laminates under Biaxial Loadings. Journal of Composite Materials, 40(10), 853-871.
- Lavoie, JA and Adolfsson, E (2001). Stitch Cracks in Constraint Plies Adjacent to a Cracked Ply. Journal of Composite Materials, 35(23), 2077-2097.
- McManus, HL, Faust, A, and Uebelhart, S (2001, Sept.). Gas Permeability of Thermally Cycled Graphite-epoxy Composites. Proceeding of American Society for Composites (ASC) 16th Technical Conference, Blacksburg, VA, ASC-2001-092.
- Nairn, JA (2000). Matrix Microcracking in Composites. In Talreja, R and Manson, JA (Eds.), Polymer Matrix Composites, Chapter 13 (pp. 403-432), Volume 2 of Kelly, A and Zweben (Eds.), Comprehensive Composite Materials. Elsevier Science.
- Nairn, JA, Hu, S, and Bark, JS (1993). A critical Evaluation of Theories for Predicting Microcracking in Composite Laminates. Journal of Materials Science, 28(18), 5099-5111.

- Nettles, A.T., “Permeability Testing of Composite Materials and Adhesive Bonds for the DC-XA Composite Feedline Program,” NASA Technical Memorandum 108483, March 1995
- Nettles, AT (2001). Permeability Testing of Impacted Composite Laminates for Use on Reusable Launch Vehicles. NASA/TM-2001-210799.
- Noh, J, Whitcomb, J, Peddiraju, P, and Lagoudas, D (2004, April). Prediction of Leakage Rate through Damage Network in Cryogenic Composite Laminates. Proceeding of 45th AIAA/ASME/ASCE/AHS/ASC Structures, Structural Dynamics & Materials Conference, Palm Springs, CA, AIAA-2004-1861.
- Peddiraju, P, Grenoble, R, Fried, K, Gates, T, and Lagoudas, D (2005, April). Analytical Predictions and Experimental Measurements of Hydrogen Permeability in a Microcrack Damaged Composite. Proceeding of 46th AIAA/ASME/ASCE/AHS/ASC Structures, Structural Dynamics & Materials Conference, Austin TX, AIAA-2005-2087.
- Peddiraju, P, Lagoudas, D, Noh, J, and Whitcomb, J (2004, April). Numerical Modeling of Cryogen Leakage through Composite Laminates. Proceeding of 45th AIAA/ASME/ASCE/AHS/ASC Structures, Structural Dynamics & Materials Conference, Palm Springs, CA, AIAA-2004-1862.
- Peddiraju, P, Noh, J, Whitcomb, J, and Lagoudas, DC (2007). Prediction of Cryogen Leak Rate through Damaged Composite Laminates. Journal of Composite Materials, 41(1), 41-71.
- Roy, S and Benjamin, M (2004). Modeling of Permeation and Damage in Graphite-epoxy Laminates for Cryogenic Fuel Storage. Composites Science and Technology, 64(13-14), 2051-2065.
- Roy, S and Nair A (2006). Modeling of Permeability in Composite Laminates with Delaminations and Stitch Cracks. Proceeding of 47th AIAA/ASME/ASCE/AHS/ASC Structures, Structural Dynamics & Materials Conference, Newport, RI, AIAA-2006-2094.
- Schulz, WA (2005). Determination of Residual Stress and Thermal Behavior for Composite Laminates, Master Thesis, University of Florida, Gainesville, FL.
- Speriatu, LM (2005). Temperature Dependent Mechanical Properties of Composite Materials and Uncertainties in Experimental Measurements. Ph.D Dissertation, University of Florida, Gainesville, FL.
- Stokes, E (2002, Sept.). Hydrogen Permeability of Polymer Based Composite Tank Material under Tetra-Axial Strain. Proceedings of the Fifth Conference on Aerospace Materials, Processes and Environment Technology (AMPET), Huntsville, Alabama.
- Sun, CT and Jih, CJ (1987). On Strain Energy Release Rate for Interfacial Cracks in Bimaterial media. Engineering Fracture Mechanics, 28(1), 13-20.
- Xu, JL and Sankar, BV (2007). Parametric Investigation of Gas Permeability in Cross-Ply Laminates Using Finite Elements. AIAA Journal, 45(4), 934-941.
- Yokozeki, T, Aoki, T, Ogasawara, T, and Ishikawa, T (2005). Effects of layup angle and ply thickness on matrix crack interaction in contiguous plies of composite laminates. Composites: Part A, 36(9), 1229-1235.
- Yokozeki, T and Ishikawa, T (2005). Through-Thickness Connection of Matrix Cracks in Laminate Composites for Propellant Tank. Journal of Spacecraft and Rockets, 42(4), 647-653.
- Yokozeki, T, Aoki, T, and Ishikawa, T (2005). Consecutive Matrix Cracking in Contiguous Plies of Composite Laminates. International Journal of Solids and Structures, 42(9-10), 2785-2802.

June 2007

3. Terrestrial Cryogenic Two-Phase Flow and Heat Transfer

Nucleate Flow Boiling Heat Transfer During Cryogenic Chilldown

Task PI: Dr. James F. Klausner, Mechanical & Aerospace Engineering, University of Florida
Co-Investigator: Dr. Renwei Mei, Mechanical & Aerospace Engineering, University of Florida
Graduate Student: Jelliffe Jackson, University of Florida

Research Period: August 3, 2004 to March 31, 2008

Abstract

This work focuses on measuring and predicting the heat transfer rates associated with the complex, unsteady, nucleate flow boiling heat transfer that occurs during cryogenic chilldown. An inverse numerical technique is used to extract the heat transfer coefficient from time dependent measurements of wall temperature. This technique utilizes knowledge of the local temperature of the pipeline coupled with numerical simulations of the unsteady heat transfer through the wall of the pipeline to determine the heat transfer coefficients. The spatially varying heat transfer coefficients are averaged and compared against four nucleate flow boiling heat transfer correlations. None of the correlations are satisfactory in accounting for the spatial variations in heat transfer rate.

Introduction

The recent interest in space exploration has placed a renewed focus on rocket propulsion technology. Cryogenic propellants are the preferred fuel for rocket propulsion since they are more energetic and environmentally friendly other current storable fuels. Voracious boiling occurs while transferring these fluids through a pipeline that is initially in thermal equilibrium with environment. This phenomenon is referred to as line chilldown. Large temperature differences, rapid transients, pressure fluctuations and the transition from the film boiling to the nucleate boiling regime characterize the chilldown process.

Although the existence of the chilldown phenomenon has been known for decades, the process is not well understood. Attempts have been made to model the chilldown process; however the results have been fair at best. A major shortcoming of these models is the use of heat transfer correlations that were developed for steady, non-cryogenic flows. The development of reliable heat transfer correlations for cryogenic chilldown has been hindered by the lack of experimental data.

An experimental facility was constructed that allows the flow structure, the temperature history and the pressure history to be recorded during the line chilldown process. Details of the experimental facility may be found in the work of Velat [1] and Jackson et al. [2]. The temperature history is then utilized in conjunction with an inverse heat conduction procedure that allows the unsteady heat transfer coefficient on the interior of the pipe wall to be extracted. It is observed that two predominant heat transfer regimes are encountered during chilldown. The first is the film boiling regime in which the liquid film is supported on a thin vapor layer adjacent to the wall, thus preventing the liquid from coming into contact with the interior pipe wall. This regime is immediately followed by the nucleate boiling regime in which the interior pipe wall temperature falls below the Leidenfrost point, hence the liquid contacts the inner wall of the pipe. This transition is marked by a sudden and significant decrease in wall temperature that is directly related to an increase in heat transfer associated with nucleate boiling. The prediction of heat transfer rates in the film boiling regime has been considered in another work [2]. This work explores cryogenic heat transfer in the nucleate flow boiling regime. The extracted heat transfer coefficients for the nucleate boiling regime are used to evaluate the predictive capability of various heat transfer correlations.

Experimental Facility

The experimental facility constructed to investigate the chilldown process is schematically illustrated in Fig. 1. The liquid nitrogen supply is stored in a 1580 kPa dewar. The driving potential for the nitrogen flow through the facility is supplied by the dewar pressure. Upon leaving the dewar the nitrogen is passed through a heat exchanger where it is cooled prior to entering the 12.5 mm I.D. vacuum jacketed Pyrex visual test section. The flow structure is captured using a high resolution CCD camera system.

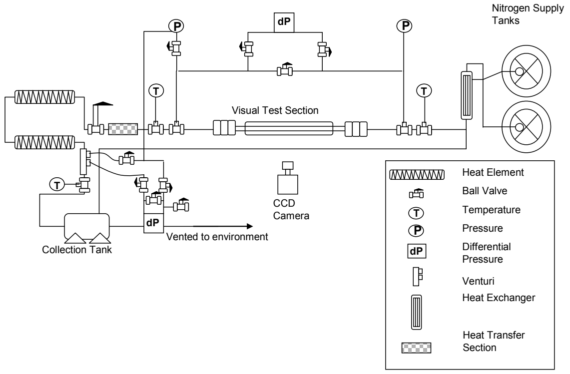

Figure 1. Cryogenic two-phase flow experimental facility.

The flow then enters the heat transfer measurement section of the facility, located 70 cm downstream of the visual test section. In this section two inline thermocouples measure the temperature of the fluid at the inlet and outlet, while a series of thermocouples are placed circumferentially on the surface of the pipe and on the outer surface of the melamine insulation, so that the temperature profile on the top, bottom and either side of the pipe is obtained, see Fig 2. A throttling valve is place after the heat transfer section to allow the mass flow to be varied. The two-phase flow is then passed through two heaters, which vaporize any remaining liquid, to ensure single–phase vapor enters the venturi flow meter. A thermocouple and pressure transducer located prior to the venturi allow for the correction of compressibility effects to be taken into account in the mass flow rate computations. The vapor is then collected in an expansion tank, and evacuated from the facility via a ventilation system.

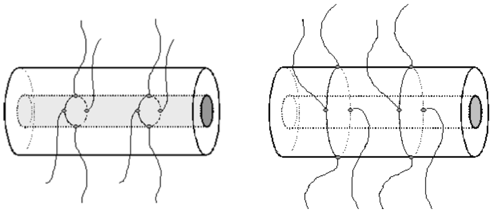

Figure 2. Thermocouple arrangements along the pipe wall and along the insulation of the heat transfer section.

A Validyne differential pressure transducer measures the pressure drop across the venturi. The analog signals from the instruments are transferred and recorded by a 16-bit Measurement Computing data acquisition board and multiplexer system. The instruments have been independently calibrated and tested to ensure they function properly. The reported accuracy of the Validyne pressure transducers is ±0.25% of full scale (0-1380 kPa for the static pressure transducers, 0-8.62 kPa for the differential pressure transducer across the test section, and 0-86.2 kPa for the differential pressure transducer across the venturi) that was confirmed via calibration. The static pressure transducers are accurate to ±3.5 kPa while the differential pressure transducer across the visual test section is accurate to within ±0.06 kPa and that measuring the pressure drop across the venturi is accurate to within ±0.35 kPa. Over the large temperature range experienced in these experiments the thermocouples used are accurate to within ±1.7 °C.

Sample Measurements

Experiments are carried out for mass fluxes that range from 66 to 500 kg/m^{2}s; and vapor qualities vary from 0.004 to 1. A typical plot of the temperature profile for the outer surface of the pipe in shown in Fig. 3; only one side wall temperature profile is shown since the difference between the to side thermocouples was within the error range of the thermocouples. The transition between the film boiling regime and the nucleate boiling regime is marked by the sudden and significant decrease in the wall temperature as highlighted in Fig. 3. The corresponding mass flux, vapor volume fraction and quality are also shown in Figs. 4, 5, and 6 respectively. The mass flux and vapor volume fraction profiles highlight the inherent unsteady nature of the chilldown process. The vapor volume fraction was computed from the digital images of the flow structure and smoothed by finding the best smooth curve fit to the measurements; these values from the curve fit are then used to compute the vapor quality using the Zuber and Findlay correlation [3]; the result is illustrated in Fig. 6.

This work focuses on the nucleate flow boiling regime and as such there are certain difficulties that are encountered while extracting the heat transfer coefficients from this region. The major difficulty results from the fact that the actual wetted perimeter of inner wall of the tube is not known and cannot be measured. In the film boiling regime the liquid film is supported on a thin layer of vapor adjacent to the pipe wall thus it is not in contact with the wall. Once the flow transitions to the nucleate boiling regime the liquid comes into contact with the wall, but this will not happen instantaneously over the entire region where liquid film is seen to reside. There will be a time lapse between the time the liquid at the bottom of the film touches the wall and the time the liquid at the top of the film touches the wall. Hence it is possible to overestimate the size of the wetted region when assuming that the wetted perimeter is equal to the liquid film height during the onset of nucleate flow boiling. The consequences of overestimating the size of the wetted region size are discussed when considering the inner surface boundary condition in the following section.

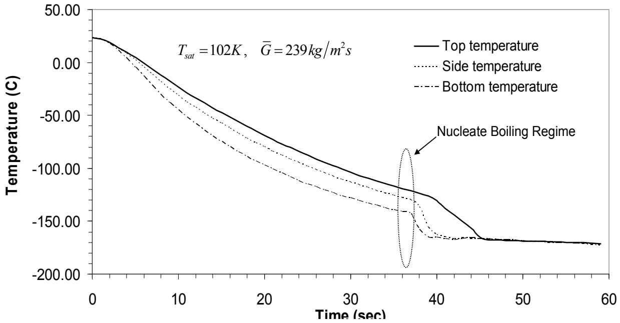

Figure 3. Outer wall temperature profile during chilldown process. Thermocouples are positioned at the top, bottom, left and right sides of the pipe.

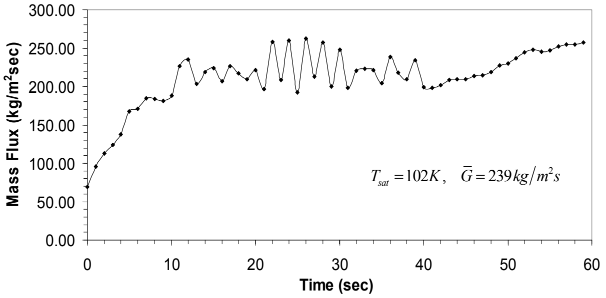

Figure 4. Mass flux variation with time for the chilldown process.

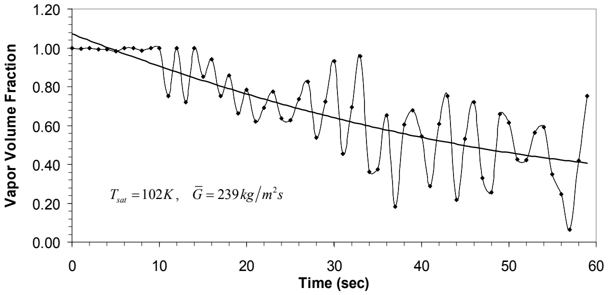

Figure 5. Vapor volume fraction variation with time for the chilldown process.

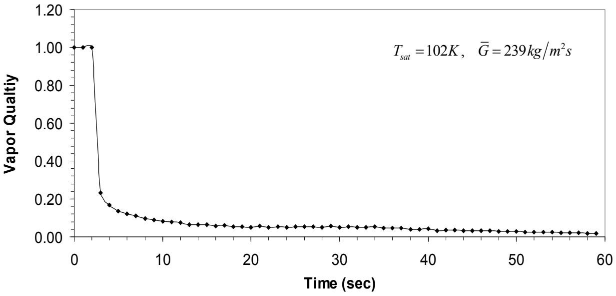

Figure 6. Vapor quality variation with time for the chilldown process.

Extracting the Heat Transfer Coefficient

In order to extract the heat transfer coefficient from the temporal profile of wall temperature; an inverse procedure is employed which varies from that of traditional inverse heat conduction methods. It does not require a system of least-square equations to be solved. Some of these traditional methods are reviewed by Ozisik [4].

The process used here for extracting the transient heat transfer coefficient on the inside of the pipe involves a number of iterative procedures, which are reported here as three major steps. These steps are illustrated in Fig. 7 and are carried out for each instance of time. These steps include (1) guess the heat transfer coefficient on the inside of the pipe, (2) knowing the heat transfer coefficient on the outside of the pipe via calibration, the temperature field is calculated, and (3) the temperatures calculated at the outer wall are then compared with those measured. If the temperatures match, the guessed heat transfer coefficient is taken as the actual heat transfer coefficient, otherwise a new guess is made and the process is repeated until the computed and measured temperatures match.

Computing the Temperature Field in the Pipe Wall

The unsteady 3-D form of the heat conduction equation in cylindrical coordinates, see Fig. 8, is written as follows:

$$c_p \rho \frac{\partial T}{\partial t} = \frac{\partial}{\partial z}\left(k \frac{\partial T}{\partial z} \right) + \frac{1}{r}\frac{\partial}{\partial r}\left(rk \frac{\partial T}{\partial r} \right) + \frac{1}{r}\frac{\partial}{\partial \phi}\left(\frac{k}{r}\frac{\partial T}{\partial \phi} \right), \tag{1}$$

where ρ is the density of the material, c_p is the specific heat capacity, t is the time variable, T is the temperature, r is the radial coordinate, z is the axial coordinate and ϕ is the azimuthal coordinate. This equation is non-dimensionalized using the following parameters:

$$\varphi = \frac{T - T_{sat}}{T_w - T_{sat}}\ ;\ z' = \frac{z}{d}\ ;\ r' = \frac{r}{d}\ ;\ c_p' = \frac{c_p}{c_{p0}}\ ;\ k' = \frac{k}{k_0}\ ;\ \rho' = \frac{\rho}{\rho_0},$$

where T_{sat} is the saturation temperature of the fluid within the pipe, T_w is the temperature on the outer wall of the pipe, d is the pipe wall thickness, and the subscript 0 denotes the property is to be evaluated at the initial temperature, T_0. Thus the original equation is transformed to

$$\frac{\rho_0 c_0 d^2}{k_0}\rho' c' \frac{\partial \varphi}{\partial t} = \frac{\partial}{\partial z'}\left(k' \frac{\partial \varphi}{\partial z'} \right) + \frac{1}{r'}\frac{\partial}{\partial r'}\left(r'k' \frac{\partial \varphi}{\partial r'} \right) + \frac{1}{r'}\frac{\partial}{\partial \phi}\left(\frac{k'}{r'}\frac{\partial \varphi}{\partial \phi} \right). \tag{2}$$

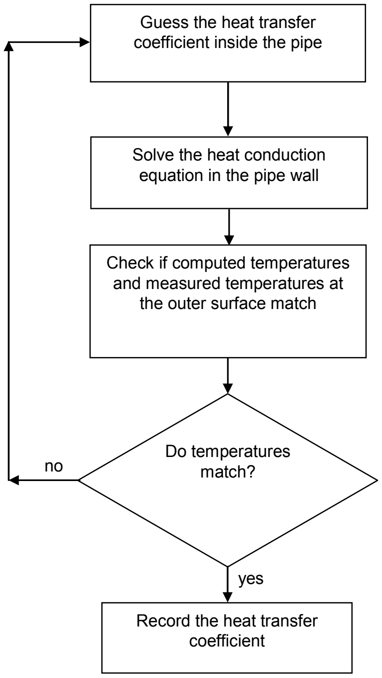

Figure 7. Flow chart for transient heat transfer coefficient extraction.

The temperature variations experienced by the pipe during the chilldown process are significant, and thus the thermal properties (k and c) of the pipe material vary significantly. These variations are taken into account by assigning the thermal properties as a function of the temperature at any given point.

A finite volume formulation is used to disceritize Eq. (2); a backward Euler scheme is employed for the temporal term and a central difference scheme is used for the spatial terms. The system of equations that result are solved using the Alternating Direction Implicit (ADI) method described in [5].

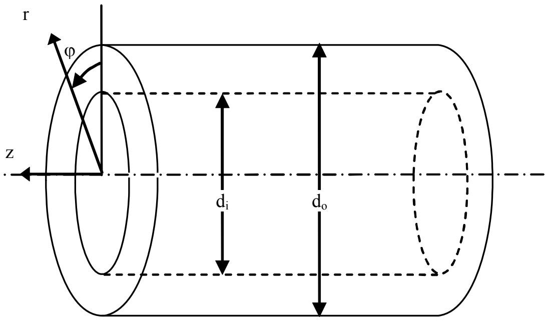

Figure 8. Coordinate system for heat conduction through the pipe wall.

In order to solve the system of equations, the energy entering the system from the ambient must be known; hence the heat transfer coefficient for the outside surface of the pipe insulation must be determined. This is accomplished through a steady-state calibration process in which cool nitrogen vapor is passed through the heat transfer section at various mass flow rates. A relationship between heat flux through the pipe insulation versus temperature difference (ambient temperature less the insulation surface temperature) is determined. A constant heat transfer coefficient is approximated as shown in Fig. 9. The slope of the line is the heat transfer coefficient for the outer pipe surface. The measurement of the heat flux into the pipe, q_w'', is quite difficult to measure due to the small temperature rise in the cryogenic vapor; thus there is some scatter in Fig. 9. However, the measured heat transfer coefficient, 4.38 W/m^2-K, is quite small, compared with convective heat transfer on the inner pipe wall. The errors in the calibration have a negligible impact on the computed thermal field in the pipe wall.

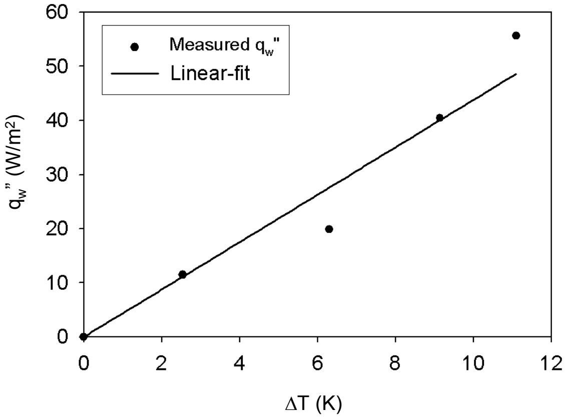

Figure 9. Calibration for determining the outer pipe surface heat transfer coefficient.

The boundary condition for the outer pipe surface is written,

$$-k\frac{\partial T}{\partial r} = h_{out}\left(T_{out} - T_{\infty}\right), \tag{3}$$

which is non-dimensionalized to give,

$$-k'\frac{\partial \varphi}{\partial r'} = \frac{h_{out}d}{k_0}\varphi + \frac{d}{k_0}\left(\frac{h_{out}T_{sat} - h_{out}T_{\infty}}{T_{wall} - T_{sat}}\right). \tag{4}$$

Here h is the heat transfer coefficient, and subscripts out and ∞ denote the outer surface of the pipe, and the outer insulation surface, respectively. The inner pipe boundary condition is written as,

$$-k\frac{\partial T}{\partial r} = h_{in}\left(T_{in} - T_{fl}\right), \tag{5}$$

which is then non-dimensionalized to give,

$$-k'\frac{\partial \varphi}{\partial r'} = \frac{h_i d}{k_0}\varphi + \frac{d}{k_0}\left(\frac{h_i T_{sat} - h_i T_{fl}}{T_{wall} - T_{sat}}\right) \tag{6}$$

Here the subscripts i and fl denote the inner surface of the pipe and the fluid flowing through the pipe, respectively. The fluid temperature is determined using an internal thermocouple that measures the temperature at the inlet of the heat transfer section.

The heat transfer coefficient on the inside of the pipe, h_i, is the quantity that is guessed during the calculation. The two-phase flow structure present for much of the experiment is stratified, and there is a significant difference between the temperature at the top of the pipe and the temperature at the bottom the pipe. This must be due to circumferential variations in the heat transfer coefficient. This problem is dealt with adequately by dividing the interior surface of the pipe into three distinct sections within which the heat transfer coefficient is assumed constant. Region 1 is such that $0 \le \alpha < \alpha_1$, and $h_i = h_{top}$, region 2 is such that $\alpha_1 \le \alpha < \alpha_2$, and $h_i = h_{side}$, and region 3 is such that $\alpha_2 \le \alpha \le \alpha_3$, and $h_i = h_{bottom}$ (see Fig. 10). In the film boiling regime it is adequate to allow all three regions to be equal in size, hence, $\alpha_1 = \alpha_2 - \alpha_1 = \pi - \alpha_2$. However in the nucleate boiling regime, where the temperature at the bottom changes suddenly by a significant amount very high heat transfer coefficients are present. Hence it is important not to overestimate the size of the region in which nucleate boiling occurs. If the region is overestimated then the amount of energy removed from the pipe would be too large in the adjacent region (in this case region 2) making it impossible to match the outer wall temperature. This is handled adequately by reducing the size of region 3 by increasing the value of α_2. When necessary, it is sufficient to reduce the size of region 3 by a factor of 2. For modeling purposes, a more systematic approach to describing different regions during nucleate boiling is desirable. However, the present approach is sufficient to match the measured and computed wall temperature variations.

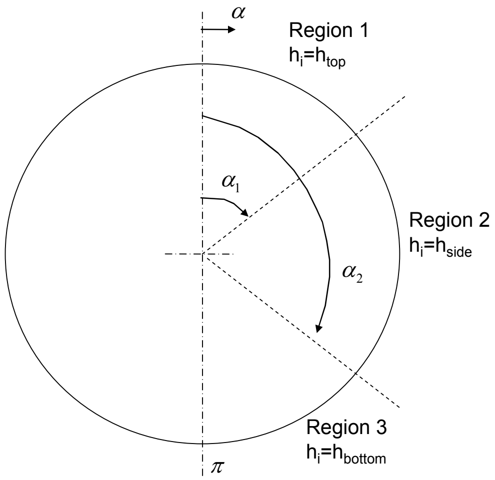

Figure 10. Assumed variation of heat transfer coefficient on the inside surface of the pipe.

Iteration Process for Guessing the Inner Heat Transfer Coefficient

Any number of methods may be used to obtain a new guess for the inner heat transfer coefficient; a systematic method for iterating is recommended. In this work after the initial guess is made subsequent guesses are determined using linear interpolation or linear extrapolation. Hence the new guess for inner heat transfer coefficient is given by,

$$h_{new} = \varepsilon \left(\frac{h_{pres} - h_{prev}}{T_{pres} - T_{prev}} \right) \left(T_{known} - T_{prev} \right) + h_{prev}, \tag{7}$$

where ε is a scaling factor that reduces oscillations and takes the value 0.3 in this work. The subscripts $pres$, $prev$, new, and $known$ denote the present, previous, new, and known quantities respectively.

Test for Convergence

The final step in the process is checking the computed temperature against the measured temperature. This is done using the temperatures at the top, side and bottom of the pipe. Once the computed temperature is within $\pm 1\text{x}10^{-8}$ K, the temperatures are considered a match. Care must be taken when determining the limit within which to consider the temperatures to be matched; if the value selected is too small the computation time increases significantly and the marginal improvement in accuracy does not justify the increased computational cost.

Testing the Inverse Procedure

In order to assess the performance and validity of this inverse method, it is first used to calculate the heat transfer coefficients for a single-phase flow simulation in which the heat transfer coefficient is known and varies in time. Second it is used to calculate the actual heat transfer coefficient for single-phase nitrogen gas flowing through the experimental facility, with the results being compared with the predictions of the Dittus-Boelter correlation for cooling. In the first test case, the heat transfer coefficient follows a parabolic path with time. A comparison of the specified heat transfer coefficient with that extracted using the inverse method is shown in Fig. 11. In Fig. 11 it is seen that a parabolic varying heat transfer coefficient is captured quite reliably with the inverse approach.

A comparison of the extracted single-phase heat transfer coefficient with the Dittus-Beoelter correlation for flowing nitrogen gas is shown in Fig. 12. The comparison is quite good. The heat transfer coefficient is not constant with time since the mass flux fluctuates around a mean of 196 kg/m^2-s.

The inverse technique is next applied to the experimental data for the chilldown process in the nucleate boiling regime. The unsteady heat transfer coefficients on the inner surface of the pipe are extracted over regions 1, 2, and 3. An average two-phase heat transfer coefficients is defined and compared with the correlations of Gungor and Winterton [7], Kandlikar [8], Müller-Steinhagen and Jamialahmadi [9] and Wojtan et al. [6,10].

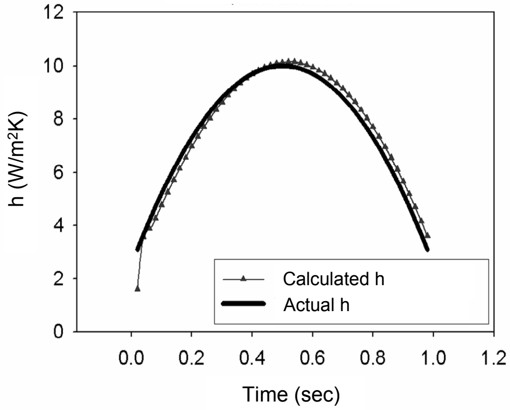

Figure 11. Computation of a parabolic varying heat transfer coefficient using the inverse method.

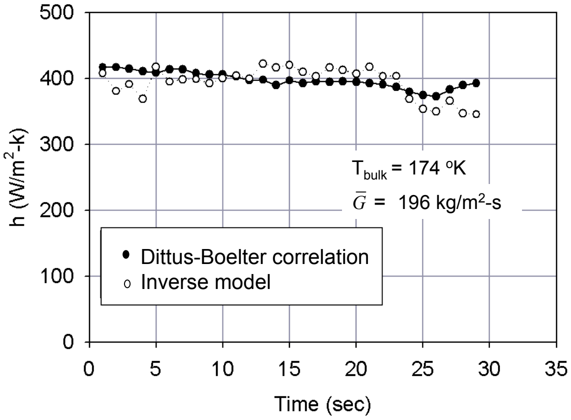

Figure 12. Comparison of heat transfer coefficient computed using the inverse procedure and the Dittus-Boelter correlation for single-phase nitrogen gas flow.

Computing the Two-Phase Heat Transfer Coefficient

Since the size of the regions may change from one data set to the other, it is convenient to define an average two-phase heart transfer coefficient. This is done by integrating the heat transfer coefficients assigned on the inner surface over the perimeter of the inner surface. This approach is also employed by Wojtan et al. [6]. Hence the average two-phase heat transfer coefficient, $\bar{h}_{tp}$, is computed as

$$\bar{h}_{tp} = \frac{2\alpha_1}{2\pi} h_{top} + \frac{2(\alpha_2 - \alpha_1)}{2\pi} h_{side} + \frac{2(\pi - \alpha_2)}{2\pi} h_{bottom}. \tag{8}$$

This allows the extracted heat transfer coefficients to be compared with the existing correlations.

Results and Discussion

Figure 13 illustrates the variation of the average two-phase heat transfer coefficient extracted from the experimental data with time for the chilldown process. It is clearly seen that the transition from the film boiling regime to the nucleate flow boiling regime is accompanied by an order of magnitude increase in the average two-phase heat transfer coefficient. The robust nature of the computational method is demonstrated in that it is able to handle the step change in heat transfer coefficient from the film to nucleate boiling regime.

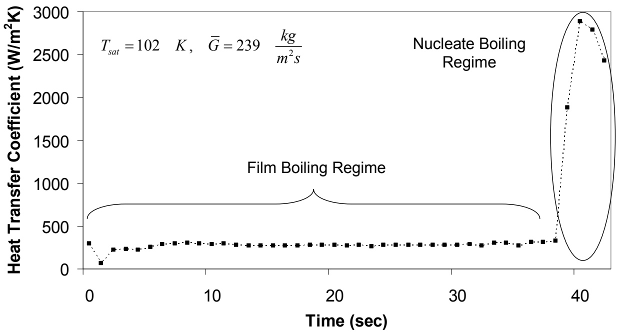

Figure 13. Average two-phase heat transfer coefficient variation with time.

The nucleate flow boiling heat transfer coefficients extracted from the experimental data are presented in Table 2. The mass flux, vapor quality, flow regime, and saturation temperature are shown. In addition, the fraction of the perimeter occupied by each region, the average wall temperature, and the contribution to the two-phase heat transfer in each region are tabulated. It is observed that the influence of region 1 on the average two-phase heat transfer coefficient in the nucleate flow boiling regime is small when compared to the influence of regions 2 and 3. This is as a result of the stratified nature for the flow structure, in which the liquid resides in the lower regions of the pipe while the vapor resides in the upper region. By examining the contributions from each region to the total heat transfer, it is observed that in some instances region 2 has a larger contribution than region 3. This occurs because of the unsteady nature of the flow which results in instances where region 2 is periodically wetted resulting in a thinner liquid film than in region 3. Hence the heat transfer rate in region 2 will be greater as a result of the lower thermal resistance of the liquid film.

In examining the fraction of the area assigned to each region it is evident that the flow structure influences the size of each region. For annular flow and stratified-wavy flow in which the liquid film height is greater than the radius of the pipe, the three regions may be constructed such that they are of equal size. While in the intermittent flow regime the size of each region is adjusted slightly. However, when the flow is in the stratified-wavy regime, a significant difference in the size of regions is observed. This results from the inability to determine the actual wetted area of the pipe. If the size of region 3 is overestimated the energy removed from the pipe wall would be too large in the adjacent region (in this case region 2) making it impossible to match the outer wall temperature. This problem is encountered mainly in the stratified-wavy regime, in which the height of the liquid film is less than the pipe radius. It is not encountered with the other flow structures since the wetted area is not overestimated. Provided the wetted region is not overestimated, the size of regions 1, 2, and 3 may have different values, and yet suitable agreement with measured data is found. Therefore, the solution presented is not unique. Nevertheless, it is found that the average heat transfer coefficient hardly changes with variations in the size of regions 1, 2, and 3. In order to maintain consistency, these regions were taken to be of equal size, unless the solution required differently. For this work the regions sizes were chosen to maintain as much symmetry as possible while ensuring that the size of the wetted region is not overestimated. The database of cryogenic nucleate flow boiling heat transfer coefficient for chilldown presented in Table 2 is the only one we are aware of.

Comparisons of the computed average flow boiling heat transfer coefficients with those determined experimentally are shown in Figs. 14, 15, 16, and 17. Figs. 14, 15, 16, and 17 show comparisons with the Gungor and Winterton, Kandlikar, Müller-Steinhagen and Jamialahmadi, and Wojtan et al. correlations, respectively. It is observed that the Müller-Steinhagen and Jamialahmadi correlation performs the best, predicting 47.6% of the data within the 25% error band. This is followed by the Gungor and Winterton correlation with 38.1%, then the Wojtan et al correlation with 21.4% and finally the Kandlikar carrleation with 9.5%.

The Kandlikar correlation and Gungor and Winterton correlation both over predict the data. Thus in applying these correlations care must be taken in order to account for the region that is actually wetted during the flow boiling process. The Wojtan et al. correlation under predicts the data. Although this correlation is the only one tested that takes into account the flow structure, it has not been extensively tested within the low quality range encountered in the chilldown experiments. The Müller-Steinhagen and Jamialahmadi perfoms the best for the present data, however this correlation does not account for the flow structure.

Further work is needed in developing a reliable correlation for nucleate flow boiling during cryogenic chilldown.

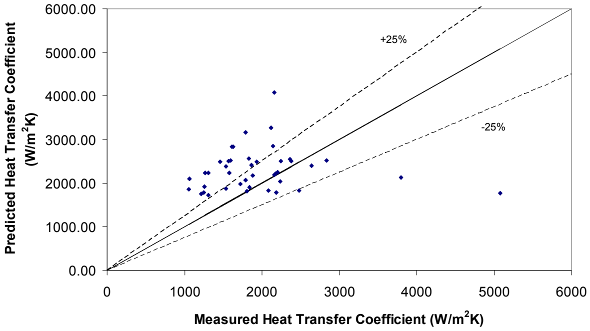

Figure 14. Comparison of predicted and measured average nucleate flow boiling heat transfer coefficients using Gungor and Winterton correlation.

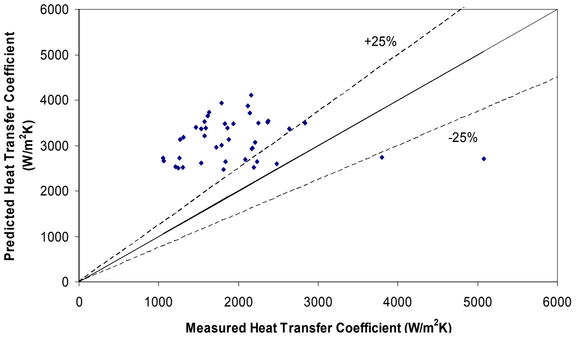

Figure 15. Comparison of predicted and measured average nucleate flow boiling heat transfer coefficients using Kandlikar correlation.

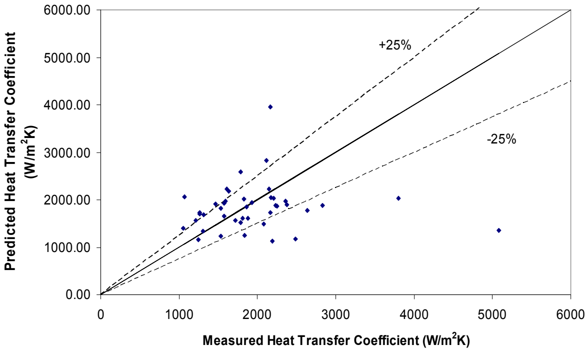

Figure 16. Comparison of predicted and measured average nucleate flow boiling heat transfer coefficients using Müller-Steinhagen correlation.

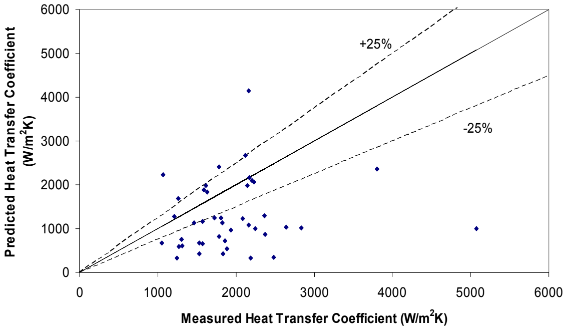

Figure 17. Comparison of predicted and measured average nucleate flow boiling heat transfer coefficients using Wojtan et al. correlation.

Table 2. Summary of measured nucleate flow boiling heat transfer coefficients using inverse method for regions 1, 2, and 3. SW (0.5+) denotes stratified wavy flow where the height of the liquid film greater than $d_i/2$; I denotes intermittent flow; SW (0.5-) denotes stratified wavy flow where the height of the liquid film less than $d_i/2$; A denotes annular flow.

Flow Regime	Mass Flux	Vapor Quality	T_{sat}	Fraction of area & Avg. Wall Temp for Region 1		Fraction of area & Avg. Wall Temp for Region 2		Fraction of area & Avg. Wall Temp for Region 3		Heat Transfer Coefficient Contribution of Region 1	Heat Transfer Coefficient Contribution of Region 2	Heat Transfer Coefficient Contribution of Region 3	h_{tp}
	kg/m^{2}s		°K	α_1/π	°K	$(\alpha_2-\alpha_1)/\pi$	°K	$(\pi-\alpha_2)/\pi$	°K	W/m^{2}K	W/m^{2}K	W/m^{2}K	W/m^{2}K
SW (0.5+)	144	0.063	98.7	0.333	151.5	0.333	131.0	0.333	105.3	40	336	1828	2203
SW (0.5+)	77	0.016	99.9	0.333	153.8	0.333	130.8	0.333	109.4	25	145	1390	1561
SW (0.5+)	78	0.016	99.9	0.333	151.2	0.333	125.2	0.333	110.1	17	382	1454	1852
SW (0.5+)	66	0.006	98.7	0.333	156.8	0.333	141.8	0.333	116.0	18	239	1008	1265
SW (0.5+)	66	0.005	99.2	0.333	155.2	0.333	136.6	0.333	106.9	22	458	1731	2211
SW (0.5+)	75	0.004	98.6	0.333	152.9	0.333	131.0	0.333	107.8	24	823	1660	2508
SW (0.5+)	234	0.040	101.8	0.333	151.0	0.333	127.3	0.333	112.1	53	654	1174	1881
SW (0.5+)	200	0.042	102.5	0.333	145.3	0.333	111.5	0.333	108.8	56	1543	1289	2888
SW (0.5+)	199	0.034	99.1	0.333	139.6	0.333	111.2	0.333	108.2	146	1503	1138	2787
SW (0.5+)	201	0.036	101.2	0.333	134.2	0.333	110.0	0.333	107.1	180	1224	1025	2429
SW (0.5+)	320	0.011	94.5	0.333	138.9	0.333	122.6	0.333	107.8	51	416	1047	1514
SW (0.5+)	310	0.019	94.4	0.333	135.3	0.333	107.7	0.333	102.2	10	1154	1209	2374
SW (0.5+)	302	0.014	94.2	0.333	132.6	0.333	105.3	0.333	103.2	16	1188	384	1588
SW (0.5+)	263	0.014	99.2	0.333	145.6	0.333	122.9	0.333	108.1	34	681	1252	1967
SW (0.5+)	262	0.009	99.7	0.333	142.0	0.333	111.4	0.333	107.5	5	1310	1066	2381
I	207	0.008	91.6	0.417	126.7	0.292	99.4	0.292	100.3	2	773	1015	1790
I	156	0.008	101.7	0.417	152.1	0.292	131.6	0.292	115.1	32	353	915	1300
I	203	0.009	102.2	0.417	148.6	0.292	118.1	0.292	111.3	19	986	875	1880
I	187	0.009	102.0	0.417	145.7	0.292	113.8	0.292	111.6	19	1199	336	1554
I	152	0.009	100.3	0.417	142.9	0.292	113.1	0.292	110.6	33	952	359	1345
I	182	0.007	98.7	0.417	140.1	0.292	112.3	0.292	108.4	54	820	757	1631
I	138	0.007	99.5	0.417	137.2	0.292	110.1	0.292	108.0	49	1322	560	1932
SW (0.5-)	94	0.066	83.8	0.417	121.0	0.417	107.2	0.167	93.1	33	311	903	1247
SW (0.5-)	128	0.023	85.9	0.417	119.5	0.417	93.0	0.167	90.2	18	1524	3555	5097
SW (0.5-)	90	0.095	86.7	0.417	117.9	0.417	101.0	0.167	89.2	39	645	1165	1848
SW (0.5-)	131	0.089	86.3	0.417	124.3	0.417	110.6	0.167	97.5	37	289	777	1103
SW (0.5-)	145	0.091	85.9	0.417	118.6	0.417	91.8	0.167	92.8	21	1215	1019	2255
SW (0.5-)	123	0.038	86.6	0.417	120.2	0.417	100.9	0.167	94.6	19	931	1153	2103
SW (0.5-)	135	0.052	84.7	0.417	118.1	0.417	105.4	0.167	97.2	70	523	738	1330
SW (0.5-)	141	0.095	84.7	0.417	115.4	0.417	90.4	0.167	94.4	6	2030	1770	3806
SW (0.5-)	181	0.020	85.4	0.417	115.5	0.417	99.4	0.167	96.3	181	993	729	1904
SW (0.5-)	173	0.068	87.1	0.417	119.7	0.417	96.4	0.167	96.0	57	1431	775	2264
SW (0.5-)	175	0.069	86.7	0.417	119.1	0.417	97.2	0.167	96.0	45	1310	864	2218
SW (0.5-)	89	0.035	91.8	0.417	140.1	0.417	120.5	0.167	101.3	37	402	903	1342
SW (0.5-)	116	0.020	93.8	0.417	138.9	0.417	114.7	0.167	103.7	27	376	677	1081
SW (0.5-)	254	0.049	91.8	0.417	124.0	0.417	107.1	0.167	105.5	113	1006	586	1706
A	345	0.044	94.5	0.333	130.8	0.333	114.7	0.333	108.4	41	676	936	1654
A	344	0.044	94.4	0.333	128.3	0.333	104.8	0.333	104.4	3	1304	841	2149
A	397	0.081	97.1	0.333	127.3	0.333	110.4	0.333	104.6	107	929	1189	2225
A	502	0.129	96.6	0.333	124.9	0.333	104.7	0.333	106.0	42	1664	497	2203
A	352	0.039	95.2	0.333	127.4	0.333	111.2	0.333	106.5	49	756	877	1682
A	415	0.053	95.0	0.333	124.9	0.333	104.0	0.333	105.7	21	1403	383	1808

Conclusion

1) The lower portion of the pipe (regions 2 and 3) contributes the majority of the heat transfer in the nucleate flow boiling regime.
2) The unsteady nature of the chilldown process may lead to region 2 being periodically wetted with a very thin liquid film and large heat transfer coefficient.
3) The inverse technique has proved to be computationally robust in determining nucleate flow boiling heat transfer coefficients for the chilldown process.
4) None of the nucleate flow boiling correlations tested is satisfactory, yet of those tested, the Müller-Steinhagen and Jamialahmadi correlation has the best agreement with the data.

Patents

There was no patent application.

Publications

Velat, C., Jackson, J., Klausner, J.F., and Mei, R., “Cryogenic Two-Phase Flow During Chilldown,” *Proceedings of the ASME HT-FED Conference*, HT-FED2004-56555 Charlotte, NC, 2004.

Jackson, J., Liao, J., Klausner, J.F., Mei, R., “Transient Heat Transfer During Cryogenic Chilldown,” *Proceedings of the ASME HT2005 Conference*, HT2005-72145, 2005.

Jackson, J., Klausner, J.F., and Mei, R., “Performance of Heat Transfer Correlations in Predicting the Heat Transfer During Cryogenic Chilldown,” *Proceedings of the Sixth International Conference on Boiling Heat Transfer*,” 2006.

Students from Research

1. Chris Velat graduated with an M.S. degree. He is currently an Air Force Pilot
2. Jelliffe Jackson graduated with a Ph.D. degree. He is currently a Professor at the University of Trinidad

Nomeclature

A	cross-sectional area, m^2
Bo	Boiling number
$C_1 - C_2$	constants in Kandlikar correlation
Co	Convection number
E	enhancement factor
F_{fl}	fluid-dependent parameter in Kandlikar correlation
F_p	pressure function in Müeller-Steinhagen correlation
Fr	Froude number
G	mass flux, kg/m^{2}s
M	molecular weight, a.m.u.
Pr	Prandtl number, $=\frac{c_p\mu}{k}$
Re	Reynolds number
R_p	surface roughness, m

S	suppression factor
T	temperature, °C
X_{tt}	Martenilli parameter
c_p	specific heat capacity, J/kgK
d	diameter, m
f	friction factor
g	acceleration due to gravity, m/s^2
h	heat transfer coefficient, W/m^{2}K
h_{fg}	latent heat of vaporization, J/kg
k	thermal conductivity, W/mK
n	exponent in nucleate boiling correlation of Gorenflo
p^*	reduced pressure
q	heat flux, W/m^2
r	radial coordinate, m
t	time, s
x	quality
z	axial coordinate, m

Greek Symbols

Φ	annular flow modification factor in Müller-Steinhagen correlation
δ	liquid film thickness, m
ε	scaling factor
ϕ	azimuthal coordinate
φ	non-dimensional temperature
μ	viscosity, Pa*s
θ_{dry}	dry angle of pipe perimeter, rad.
ρ	density, kg/m^3

Subscripts

0	reference parameter
∞	far field
dry	dry region of pipe perimeter
cb	convective boiling
fl	fluid
i	inner pipe surface
$known$	known
l	liquid phase
nb	nucleate boiling
out	outer pipe surface
$pres$	present time instant
$prev$	previous time instant
sat	saturation condition
tp	two-phase
v	vapor phase
w	pipe wall
wet	wetted region of pipe perimeter

Superscripts

‘ denotes non-dimensional variable

_ denotes average quantity

References

[1] C.J. Velat, Experiments in Cryogenic Two Phase Flow, M.S. Thesis, University of Florida, Gainesville, Florida, 2004.

[2] J.K. Jackson, J.F. Klausner and R. Mei, Cryogenic Chill-Down Model Inside Transportation Pipelines, *Proceedings of the ASME Summer Heat Transfer Conference*, San Francisco, CA, 2005.

[3] N. Zuber and J.A. Findlay, Average Volumetric Concentration in Two-Phase Flow Systems, *Journal of Heat Transfer*, vol. 87C, pp. 453-468, 1965.

[4] M.N. Özişik, Heat Conduction (2nd ed.), Wiley-Interscience, New York, pp. 571, 1993.

[5] C. Hirsch, Numerical Computation of Internal and External Flow, Volume 1, Fundamental of Numerical Discretization, Wiley, Indianapolis, Indiana, pp. 424, 1990.

[6] L. Wojtan, T. Ursenbacher and J.R. Thome, Investigation of Flow Boiling in Horizontal Tubes: Part II – Development of a New Heat Transfer Model for Stratified-Wavy, Dryout and Mist Flow Regimes, *International Journal of Heat and Mass Transfer*, vol. 48, pp. 2970-2985, 2005.

[7] K.E. Gungor and R.H.S. Winterton, A General Correlation for Flow Boiling in Tubes and Annuli, *International Journal of Heat and Mass Transfer*, vol. 29, pp. 351-358, 1986.

[8] S.G. Kandlikar, A General Correlation for Saturated Two-Phase Flow Boiling Heat-Transfer Inside Horizontal and Vertical Tubes, *Journal of Heat Transfer*, vol. 112, pp. 219-228, 1990.

[9] H. Müller-Steinhagen and M. Jamialahmadi, Subcooled Flow Boiling Heat Transfer to Mixtures and Solutions, *Convective Flow Boiling*, Editor J.C. Chen, Taylor & Francis, Washington D.C., pp. 277-283, 1996.

[10] L. Wojtan, T. Ursenbacher and J.R. Thome, Investigation of Flow Boiling in Horizontal Tubes: Part I – A New Diabatic Two-Phase Flow Pattern Map, *International Journal of Heat and Mass Transfer*, vol. 48, pp. 2955-2969, 2005.

[11] F.W. Dittus and L.M.K. Boelter, Heat Transfer in Automobile Radiators of the Tubular Type, *Publications in Engineering*, vol. 2, pp. 443, 1930.

[12] M.G. Cooper, Saturation Nucleate Pool Boiling. A Simple Correlation, *1st U.K. National Conference on Heat Transfer*, vol. 2, pp. 785-793, 1984.

[13] B.S. Petukhov, and V.N. Popov, Theoretical Calculation of Heat Exchanger in Turbulent Flow in Tubes of an Incompressible Fluid with Variable Physical Properties, *High Temperature*, vol. 1, pp. 69–83, 1963.

[14] G.K. Filonenko, Hydraulic Resistance in Pipes, *Teploenergetica*, vol. 1, pp. 69-83, 1954.

[15] D. Gorenflo, Behältersieden, *VDI-Wärmeatlas*, Sect. Ha (4th ed.) VDI-Verlag, 1984.

[16] D. Steiner and J. Taborek, Flow Boiling Heat Transfer in Vertical Tubes Correlated by an Asymptotic Model, *Heat Transfer Engineering*, vol. 13, pp. 43-69, 1992.

APPENDIX A: Flow Boiling Heat Transfer Correlations

Heat transfer coefficients from four well known nucleate flow boiling heat transfer correlations are used to compare against the experimentally determined average two-phase heat transfer coefficients defined in Eq. (8). Each correlation combines the contributions of the nucleate boiling and the convective mechanisms in different ways.

The correlation of Gungor and Winterton [7] employs a superposition technique and accounts for the interaction of the two mechanisms through the use of an enhancement factor and a suppression factor. The enhancement factor accounts for the increased convective heat transfer that results from increased vapor fraction in the flow as it evaporates. The suppression factor reduces the nucleate boiling influence as more nucleation sites are suppressed with increasing flow velocity. The Gungor and Winterton correlation is as follows,

$$h_{tp} = Eh_l + Sh_{nb}, \tag{9}$$

here h_{tp} is the two-phase heat transfer coefficient, h_l is the convective heat transfer coefficient for the liquid flow, h_{nb} is the nucleate boiling heat transfer coefficient, E is the enhancement factor and S is the suppression factor. The liquid convective heat transfer coefficient is calculated from the Dittus-Boelter correlation [11],

$$h_l = 0.023\,\mathrm{Re}_l^{0.8}\,\mathrm{Pr}_l^{0.4}\left(\frac{k_l}{d_i}\right). \tag{10}$$

Re_l is the liquid Reynolds number based on the liquid fraction flowing,

$$\mathrm{Re}_l = \frac{G(1-x)d_i}{\mu_l}. \tag{11}$$

Here G is the total mass flux, x is the vapor quality, μ is the viscosity, c_p is the specific heat, k is the thermal conductivity, d_i is the inner diameter of the pipe and the subscript l denotes the liquid phase. The nucleate boiling heat transfer coefficient is obtained from the Copper nucleate pool boiling correlation [12]:

$$h_{nb} = 55p_r^{0.12}\left(-0.4343\log p_r\right)^{-0.55} M^{-0.5} q^{0.67}, \tag{12}$$

where p_r is the reduce pressure and is computed as the ratio of the saturation pressure to the critical pressure of the fluid, M is the molecular weight of the fluid and q is the heat flux entering the system. The enhancement factor is a function of the Martinelli parameter, X_{tt} and the Boiling number, Bo,

$$E = 1 + 24000 Bo^{1.16} + 1.37\left(\frac{1}{X_{tt}}\right)^{0.86}, \tag{13}$$

where the Martinelli parameter and Boiling number are given as,

$$X_{tt} = \left(\frac{1-x}{x}\right)^{0.9}\left(\frac{\rho_v}{\rho_g}\right)^{0.5}\left(\frac{\mu_l}{\mu_v}\right)^{0.1}, \tag{14}$$

and

$$Bo = \frac{q}{Gh_{fg}}. \tag{15}$$

Here h_{fg} is the latent heat of vaporization, ρ is density and the subscript v denotes the vapor phase. The proposed boiling suppression factor is,

$$S = \left(1 + 1.15\times10^{-6} E^2 \,\mathrm{Re}_l^{1.17}\right)^{-1}. \tag{16}$$

In order to account for horizontal flows the enhancement factor is multiplied by a correction factor E_2 and the suppression factor is multiplied by a factor S_2 when the liquid Froude number, Fr_l is such that $Fr_l < 0.05$,

$$E_2 = Fr_l^{(0.1-2Fr_l)}, \tag{17}$$

and

$$S_2 = \left(Fr_l\right)^{\frac{1}{2}}, \tag{18}$$

where

$$Fr_l = \frac{G^2}{\rho_l^2 g d_i}. \tag{19}$$

The correlation of Kandlikar [8] accounts for the convective and nucleate boiling contributions to the heat transfer by introducing the Convection number, Co and the Boiling number, Bo. These quantities are used to enhance the single phase convective heat transfer coefficient; thus the correlation is often referred to as an enhancement model. The correlation takes the following form,

$$h_{tp} = \left(C_1 Co^{C_2}\left(25Fr_l\right)^{C_5} + C_3 Bo^{C_4} F_{fl}\right) h_l, \tag{20}$$

where Co is,

$$Co = \left(\frac{1-x}{x}\right)^{0.8}\left(\frac{\rho_v}{\rho_l}\right)^{0.5}. \tag{21}$$

The constants $C_1 - C_5$ are shown in Table 1 and are chosen based on the heat transfer regime for the given flow, and constant F_{fl} depends on the fluid that is being utilized; $F_{fl} = 4.70$ for nitrogen, other values may be found in [7].

Table 1. Constants used for the Kandlikar correlation

Constant	Convective region	Nucleate boiling region
C_1	1.1360	0.6683
C_2	-0.9	-0.2
C_3	667.2	1058.0
C_4	0.7	0.7
C_5	0.3	0.3

$C_5 = 0$ **for vertical tubes, and for horizontal tubes with** $Fr_l > 0.04$ **.**

The correlation of Müller-Steinhagen and Jamialahmadi [9] uses a superposition technique that accounts for the interaction of the convective and nucleate boiling mechanisms by employing an enhancement factor and a suppression factor. This formulation absorbs the enhancement factor into the computation of the convective heat transfer contribution, and the correlation takes the form,

$$h_{tp} = h_l + Sh_{nb}. \tag{22}$$

This correlation employs the correlation of Petukov and Popov [13], for the liquid phase convective heat transfer coefficient,

$$h_l = \frac{k_l\left(f/8\right)\mathrm{Re}_{tp}\,\mathrm{Pr}_l}{d_i\left(1+12.7\sqrt{f/8}\left(\mathrm{Pr}_l^{2/3}-1\right)\right)}, \tag{23}$$

where the friction factor is given by Filonenko [14],

$$f = (1.82\log\mathrm{Re}_{tp} - 1.64)^{-2}. \tag{24}$$

The two-phase Reynolds number is defined as

$$\mathrm{Re}_{tp} = \frac{G(1-x)d_i}{\mu_l}E^{1.25}, \tag{25}$$

and the enhancement factor, E is given by,

$$E = 2.35\left(\frac{1}{X_{tt}} + 0.213\right)^{0.736} \quad for \quad \frac{1}{X_{tt}} \geq 0.1$$
$$E = 1 \quad otherwise \tag{26}$$

For flow through annular tubes Eq. (23) is multiplied by a factor

$$\Phi = 0.86\left(\frac{d_i}{d_o}\right)^{-0.16}. \tag{27}$$

The suppression factor is computed as

$$S = \frac{1}{1 + 2.53 \times 10^{-6}\,\mathrm{Re}_{tp}^{1.17}}. \tag{28}$$

In order to compute the nucleate boiling contribution to heat transfer, the pool boiling correlation developed by Gorenflo [15] is used,

$$\frac{h_{nb}}{h_o} = F_p\left(\frac{q}{q_o}\right)^n\left(\frac{R_p}{R_{po}}\right)^{0.113}, \tag{29}$$

where R_p is the surface roughness of the pipe. The pressure function, F_p and the exponent n are calculated using the reduced pressure p^*,

$$F_p = 1.73p^{*0.27} + \left(6.1 + \frac{0.68}{1 - p^{*2}}\right)p^{*2}. \tag{30}$$

Equation (30) pertains to water and other low boiling point liquids and is used here; for the computation of F_p for organic liquids reference [8] should be consulted. The exponent is calculated from

$$n = 0.9 - 0.3p^{*a}, \tag{31}$$

with $a = 0.15$ for water and other low boiling point liquids including nitrogen. The reference heat transfer coefficient h_o, reference heat flux q_o, and reference surface roughness R_{po} for nitrogen are found in [16], and are $q_o = 10000\frac{W}{m^2}$, $h_o = 4380\frac{W}{m^2K}$, and $R_{po} = 1 \times 10^{-6}m$.

The correlation that accounts for flow structure for horizontal flow is that of Wojtan et al. [6,10]. It does so by first predicting the region of the pipe wall that is wetted and then computing the heat transfer for the wet and dry areas respectively. Only the heat transfer correlation is presented here. Determination of the flow structure is outlined in (10). The average two-phase heat transfer coefficient is predicted from

$$h_{tp} = \frac{\theta_{dry} h_v + \left(2\pi - \theta_{dry}\right) h_{wet}}{2\pi}, \tag{32}$$

where θ_{dry} is the portion of the pipe cross section that is in contact with only the vapor; the determination of θ_{dry} is described in [6]. The convective heat transfer contribution by the vapor phase, h_v, is computed using the Dittus-Boelter correlation, while the contribution of the liquid phase, h_{wet}, is computed as

$$h_{wet} = \left[\left(h_{cb}\right)^3 + \left(h_{nb}\right)^3\right]^{\frac{1}{3}}. \tag{33}$$

Here h_{cb} is the convective boiling heat transfer coefficient and is based on a liquid film thickness, δ, length scale

$$h_{cb} = 0.0133\,\mathrm{Re}_{\delta}^{0.69}\,\mathrm{Pr}_l^{0.4}\,\frac{k_v}{\delta} \tag{34}$$

With

$$\begin{aligned} \delta &= \frac{d_i}{2} - \sqrt{\left(\frac{d_i}{2}\right)^2 - \frac{2A_l}{\left(2\pi - \theta_{dry}\right)}} \qquad when \quad \delta \le \frac{d_i}{2} \\ \delta &= \frac{d_i}{2} \qquad\qquad otherwise. \end{aligned} \tag{35}$$

The nucleate boiling heat transfer coefficient is determined using the Copper nucleate pool boiling correlation [12], as is used in the work of Gungor and Winterton [7], and is modified by multiplying by a suppression factor of 0.8.

4. Numerical Investigation of Cryogenic Fluid Transport in Pipelines During Chilldown Process

Task PI: Dr. Renwei Mei, Mechanical and Aerospace Engineering, University of Florida
Co-Investigator: Dr. James F. Klausner, Mechanical and Aerospace Engineering,
University of Florida
Graduate Student: Hieu H. Tran, Mechanical and Aerospace Engineering, University of Florida

Research Period: August 3, 2004 to March 31, 2007

Sub-Task 1: Numerical Investigation of Cryogenic Fluid Transport in Horizontal Pipelines for Low Mass-flux Regime during Chilldown Process

Abstract

A pseudo-steady model has been developed to predict the chilldown history of pipe wall temperature in the horizontal transport pipeline for cryogenic fluids. A new film boiling heat transfer model is developed by incorporating the stratified flow structure for cryogenic chilldown. A modified nucleate boiling heat transfer correlation for cryogenic chilldown process inside a horizontal pipe is proposed. The efficacy of the correlations is assessed by comparing the model predictions with measured values of wall temperature in several azimuthal positions in a well controlled experiment by Chung et al. (2004). The computed pipe wall temperature histories match well with the measured results. The present model captures important features of thermal interaction between the pipe wall and the cryogenic fluid, provides a simple and robust platform for predicting pipe wall chilldown history in long horizontal pipe at relatively low computational cost, and builds a foundation to incorporate the two-phase hydrodynamic interaction in the chilldown process.

Nomenclature

Bo	Boiling number
c	solid heat capacity
c_p	heat capacity
D	pipe diameter
d	thickness of pipe wall
g	gravity
h	heat transfer coefficient
h_{pool}	pool boiling heat transfer coefficient
h_{conv}	convection boiling heat transfer coefficient
h_{fg}	latent heat
Ja	Jacob number
k	thermal conductivity
k_{eff}	effective thermal conductivity
Nu	Nusselt number
p	pressure
R	radius of pipe
R_1 and R_2	inner and outer radius of pipe
Ra	Rayleigh number
Re	Reynolds number
Pc	Peclet number
Pr	Prandtl number

S	suppression factor
T	temperature
T_1	Leidenfrost temperature
T_2	transition temperature between nucleate boiling to convection heat transfer
T_o	room temperature
t	time
U	velocity
u *and* v	vapor film velocity
x *and* y	vapor film coordinates
Z	transformed coordinate
z, r, *and* φ	cylindrical coordinates
α	liquid volume fraction
χtt	Martinelli number
δ	vapor film thickness
ε	emissivity
φ	azimuthal coordinate
μ	viscosity
θ	dimensionless temperature; azimuthal coordinate
σ	liquid surface tension; Stefan Boltzmann constant

Subscripts

0	characteristic value
i and o	inner and outer pipe
l	liquid
v	vapor
w	wall
sat	saturated

Superscripts

’	dimensionless variable

I. Introduction

The cryogenic chilldown is encountered in many applications but is of particular importance in cryogenic transportation pipelines. For example, in rockets or space shuttle launch facility, cryogenic liquids as fuel are filled from the storage tank to the internal fuel tanks of a space vehicle through a complex pipeline system. To avoid evaporated fuel entering the space vehicle, a cryogenic chilldown prior to the filling is required to reduce the pipe wall temperature to the saturation temperature of the cryogenic liquid.

Cryogenic chilldown involves complicated hydrodynamic and thermal interactions among liquid, vapor, and solid pipe wall. There exist few basic experimental studies and modeling efforts for chilldown of cryogenic fluids. Studies on cryogenic chilldown started in 1960’s accompanying the development of rocket launching system. Early experimental studies were conducted by Burke et al. (ref. 1), Graham (ref. 2), Bronson et al. (ref. 3), Chi and Vetere (ref. 4), Steward (ref. 5) among other researches. Bronson et al. (ref. 3) studied the flow regime in a horizontal pipe during the chilldown by liquid hydrogen. The results revealed that the stratified flow is prevalent in the cryogenic chilldown.

Flow regimes and heat transfer regimes in the horizontal pipe chilldown were also studied by Chi and Vetere (ref. 4). Information of flow regimes was deduced by studying the fluid temperature and volume fraction during the chilldown. Several flow regimes were identified: single phase vapor, mist flow, slug flow, annular flow, bubbly flow, and single-phase liquid flow. Heat transfer regimes were identified as: single-phase vapor convection, film boiling, nucleate boiling, and single-phase liquid convection.

Recently, Velat et al. (ref. 6) systematically studied cryogenic chilldown in a horizontal pipe. Their study included: visually recording the chilldown in a transparent Pyrex pipe, which is used to identify the flow regime and heat transfer regime; collecting temperature histories at different positions of wall in the chilldown; recording pressure drop along the pipe. Chung et al. (ref. 7) conducted a similar study on the nitrogen chilldown at relatively low mass flux and provided the data needed to assess various heat transfer coefficients in the present study.

Burke et al. (ref. 1) developed a crude chilldown model based on the 1–D heat transfer through the pipe wall and the assumption of infinite heat transfer rate from the cryogenic fluid to the pipe wall. The effects of flow regimes on the heat transfer rate were neglected. Graham et al. (ref. 2) correlated heat transfer coefficient and pressure drop with the Martinelli number (ref. 8) based on their experimental data. Chi (ref. 9) developed a 1–D model for energy equations of the liquid and the wall, based on film boiling heat transfer between the wall and fluid. An empirical equation for predicting chilldown time and temperature was proposed.

Steward (ref. 5) developed a homogeneous flow model for the chilldown. The model treated the cryogenic fluid as a homogeneous mixture. The continuity, momentum and energy equations of mixture were solved to obtain density, pressure and temperature of mixture. Various heat transfer regimes were considered: film boiling, nucleate boiling and single-phase convection heat transfer. Separate treatment of different heat transfer regimes resulted in a significant improvement in the prediction of the chilldown process. Homogeneous mixture model was also employed by Cross et al. (ref. 10) who obtained a correlation for the wall temperature in the chilldown with an oversimplified heat transfer model of the heat transfer between the wall and the fluid.

Stratified flow regime, which is the prevalent flow regime in horizontal chilldown, was first studied by Chen and Banerjee (refs. 11 to 13). They developed a separated flow model for the simulating cooldown by a stratified flow in a hot horizontal pipe. Both phases were modeled using 1–D mass and momentum conservation equations. The wall temperature was computed using a 2–D transient heat conduction equation. Their prediction for wall temperature agreed well with their experimental results. Although a significant progress was made on handling the momentum equations, the heat transfer correlations employed were not as advanced.

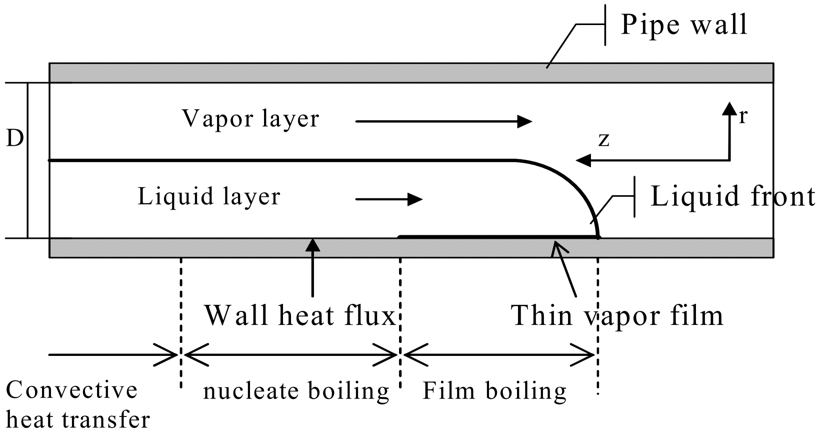

Figure 1. Schematic of chilldown heat transfer regimes in a horizontal pipe.

Typical chilldown involves several heat transfer regimes as shown in figure 1. Near the liquid front is the film boiling. The knowledge of the heat transfer in the film boiling regime is relatively limited, because i) film boiling has not been the central interest in industrial applications; and ii) high temperature difference causes the difficulties in experimental investigations. For the film boiling on vertical surfaces, early work was reported by Bromley (ref. 14), Dougall and Rohsenow (ref. 15) and Laverty and Rohsenow (ref. 16). Film boiling in a horizontal cylinder was first studied by Bromley (ref. 17); and the Bromley correlation was widely used. Breen and Westwater (ref. 18) modified Bromley's equation to account for very small tubes and large tubes. If the tube is larger than wavelength associated with the Taylor instability, the heat transfer correlation is reduced to Berenson's correlation (ref. 19) for a horizontal surface.

Empirical correlations for film boiling were proposed by Hendrick et al. (refs. 20 and 21), Ellerbrock et al. (ref. 22), von Glahn (ref. 23), Giarratano and Smith (ref. 24). These correlations relate a simple or modified Nusselt number ratio to the Martinelli parameter. Giarratano and Smith (ref. 24) gave detailed assessment on these correlations. All these correlations are for steady state cryogenic film boiling. They may not be suited for transient chilldown application.

When the pipe chills down further, film boiling ceases and transient boiling occurs, followed by nucleate boiling. The heat transfer in the transient boiling is even more complicated and it is usually assumed that the boiling switches from film boiling to nucleate boiling right away. The position of film boiling transitioning to the nucleate boiling is often called rewetting front, because from that position the cold liquid starts touching the pipe wall. Usually the Leidenfrost temperature indicates the transition from the film boiling to the nucleate boiling.

The study on the convection nucleate boiling is extensive. A general correlation for saturated boiling was introduced by Chen (ref. 25). Gungor and Winterton (ref. 26) modified Chen's correlation and extend it to subcooled boiling. Enhancement and suppression factors for macro-convective heat transfer were introduced. Gunger and Winterton's correlation can fit experimental data better than the modified Chen's correlation (ref. 27) and Stephan and Auracher correlation (ref. 28). Kutateladze (ref. 29) and Steiner (ref. 30) also provided correlations for cryogenic fluids in pool boiling and forced convection boiling. Although they are not widely used, they should be more applicable for cryogenic fluids as the correlation was directly based on cryogenic conditions.

As the wall temperature drops further, the nucleate boiling is replaced by pure convection. The convection heat transfer can be modeled using Dittus-Boelter equation (ref. 31) for the fully developed turbulent pipe flow or corresponding laminar heat transfer equation for laminar pipe flow (ref. 31). The condition in which nucleate boiling switches to single-phase convection heat transfer is that all nucleate sites are suppressed.

Although two-fluid model can describe the fluid dynamics aspect of the chilldown process, it suffers from computational instability for moderately values of slip velocity between two phases which limits its application. To gain fundamental insight into the thermal interaction between the wall and the cryogenic fluid and to be able to rapidly predict chilldown in a long pipe, an alternative pseudo-steady model is developed. In this model, liquid wave front speed is assumed to be constant and is the same as the bulk liquid speed (ref. 32). It is also assumed that steady state thermal fields for both the liquid and the solid exist in a reference frame that is moving with the wave front. The heat transfer between the fluid and the wall is modeled using different heat transfer correlations depending on the operating heat transfer regime at a given location. Various improvements on the correlations are introduced, including the development of a new film boiling heat transfer coefficient. The governing equation for the solid thermal field becomes a parabolic equation that can be efficiently solved. It must be emphasized that a great advantage of the pseudo-steady model is that one can assess the efficacy of the film boiling model independently from that of the nucleate boiling model since the down stream information in the nucleate boiling regime cannot affect the temperature in the film boiling regime. In another word, even if the nucleate boiling heat transfer coefficient is inadequate, the film boiling heat transfer coefficient can still be assessed in the film boiling regime by comparing with the measure temperature for the right period of time. After the satisfactory performance is achieved for the film boiling regime, the nucleate boiling heat transfer model can be subsequently assessed. In the Results section, those detailed assessments of the heat transfer coefficients are provided by comparing the computed temperature variations with the experimental measurements of Chung et al. (ref. 7). Satisfactory results are obtained.

II. Formulation

In pseudo-steady chilldown model, it is assumed that both the liquid and its wave front moves at a constant speed *U* which is taken from estimated experimental condition in the present model. Thus the main emphasis of the present study is on the modeling of the heat transfer coefficients in different heat transfer regimes and the computation of the thermal field within the solid pipe.

II.1. Solid Heat Transfer

The thermal field inside the solid wall is governed by the 3–D unsteady energy equation:

$$\rho c \frac{\partial T}{\partial t} = \frac{\partial}{\partial z}\left(k \frac{\partial T}{\partial z}\right) + \frac{1}{r}\frac{\partial}{\partial r}\left(rk \frac{\partial T}{\partial r}\right) + \frac{1}{r}\frac{\partial}{\partial \varphi}\left(\frac{k}{r}\frac{\partial T}{\partial \varphi}\right) \tag{1}$$

Since the wave front speed *U* is assumed to be a constant, it can be expected that when the front is reasonably far from the entrance region of the pipe, the thermal field in the solid is in a steady state when it is viewed in the reference frame that moves with the wave front. Thus, the following coordinate transformation is introduced,

$$Z = z + Ut \tag{2}$$

Equation (1) is then transformed to:

$$\rho c U \frac{\partial T}{\partial Z} = \frac{\partial}{\partial Z}\left(k \frac{\partial T}{\partial Z}\right) + \frac{1}{r}\frac{\partial}{\partial r}\left(rk \frac{\partial T}{\partial r}\right) + \frac{1}{r}\frac{\partial}{\partial \varphi}\left(\frac{k}{r}\frac{\partial T}{\partial \varphi}\right). \tag{3}$$

For further simplification, the following dimensionless parameters are introduced,

$$\theta = \frac{T - T_w}{T_w - T_{sat}},\ Z' = \frac{Z}{d}, r' = \frac{r}{d}\quad c' = \frac{c}{c_0} \text{ and } k' = \frac{k}{k_0} \tag{4}$$

where k_0 is the characteristic thermal conductivity, and c_0 is the characteristic heat capacity.

Equation (3) can be normalized as

$$Pc * c' \frac{\partial \theta}{\partial Z'} = \frac{\partial}{\partial Z'}\left(k' \frac{\partial \theta}{\partial Z'}\right) + \frac{1}{r'}\frac{\partial}{\partial r'}\left(r'k' \frac{\partial \theta}{\partial r'}\right) + \frac{1}{r'}\frac{\partial}{\partial \varphi}\left(\frac{k'}{r'}\frac{\partial \theta}{\varphi}\right) \tag{5}$$

where $Pc = \dfrac{\rho c_0 U d}{k_0}$ is the Peclet number.

Under typical operating condition for the cryogenic chill-down process, Pc ~ O(10^2) - O(10^3). The first term on the RHS of Eq. (5) is quite small compared with the rest of terms and can be neglected. Eq. (5) becomes

$$Pc * c' \frac{\partial \theta}{\partial Z'} = \frac{1}{r'}\frac{\partial}{\partial r'}\left(r'k' \frac{\partial \theta}{\partial r'}\right) + \frac{1}{r'}\frac{\partial}{\partial \varphi}\left(\frac{k'}{r'}\frac{\partial \theta}{\varphi}\right), \tag{6}$$

which is parabolic. Hence in the *Z'*-direction, only one condition is needed. In theφ-direction, periodic boundary conditions are used. On inner and outer surfaces of the pipe wall, where $r = R_1$ and R_2, proper boundary conditions for the temperature are required.

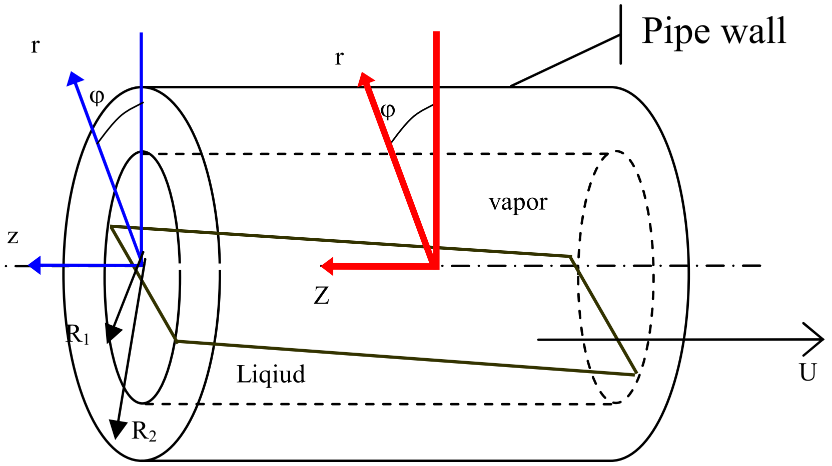

Figure 2. Coordinate systems: laboratory frame is denoted by z; moving frame is denoted by Z.

For convenience, $Z' = 0$ at the liquid wave front. In the region of $Z' < 0$, the inner wall is exposed to the pure vapor. Even though there may be some liquid droplets in the vapor that can cause evaporative cooling when the droplets deposit on the wall and the cold flowing vapor can absorb some heat from the wall, the heat flux due to these two mechanisms is quit small compared with the heat transfer between liquid and solid wall in the region of $Z' > 0$. Hence, heat transfer for $Z' > 0$ is neglected and it is assumed that $\theta = 1$ at $Z' = 0$. The computation start from the $Z' = 0$ to $Z' \to \infty$, until a steady state solution in the Z'-direction is reached. An implicit scheme in the Z'-direction is employed to solve eq. (6).

II.2. Liquid and Vapor Flow

The two-phase flow is assumed to be stratified as was observed in (ref. 7). Both liquid and vapor phases are assumed to be at the saturated state. Liquid volume fraction determining which part of wall is in contact with the liquid or the vapor, is specified at every cross-section along the Z′-direction based on experimental information. The visual studies (refs. 6 and 7) show that the liquid volume fraction increases gradually, rather than abruptly, near the liquid wave front and becomes almost constant during most of the chilldown. Hence, the following liquid volume fraction α as a function of time is used in the computation of the solid-fluid heat transfer coefficient,

$$\begin{aligned} \alpha &= \alpha_0 \sin\left(\frac{t}{t_0} \cdot \frac{\pi}{2}\right) & t &< t_0 \\ \alpha &= \alpha_0 & t &\geq t_0 \end{aligned} \tag{7}$$

where t_0 is characteristic chilldown time, and α_0 is characteristic liquid volume fraction. Here the time when the nucleate boiling is almost suppressed and slope of the wall temperature profile becomes flat is set as characteristic chilldown time.

The vapor phase velocity is assumed to be a constant. However, it was not directly measured. It is computationally determined by trial-and-error by fitting the computed and measured wall temperature variations for numerous positions.

II.2.1. Heat Transfer Between Cryogenic Fluid and Solid Pipe Wall

During the chilldown, the fluid in contact with the pipe wall is either liquid or vapor. The mechanisms of heat transfer between the liquid and the wall and between the vapor and the wall are different. Based on experimental measurements and theoretical analysis, liquid-solid heat transfer accounts for a majority of the total heat transfer. However, the prediction for heat transfer is much more complicated than the heat transfer between the vapor and the wall. The heat transfer between the liquid and the wall is discussed first.

II.2.1.1. Heat Transfer Between Liquid and Solid wall

Heat transfer between liquid and solid wall includes film boiling, nucleate boiling, and single-phase convection heat transfer. The transition from one type of boiling to another depends on many parameters, such as wall temperature, wall heat flux, and various properties of fluid. For simplicity, a fixed temperature approach is adopted to determine the transition points. That is, if the wall temperature is higher than the Leidenfrost temperature, film boiling dominates. If the wall temperature is between Leidenfrost temperature and a transition temperature, T_2, nucleate boiling takes place. Here, the transient boiling regime between film boiling and nucleate boiling is neglected. The reason is mainly the difficulty associated with the determination of the conditions for the transient boiling to occur and the lack of a reliable transient heat transfer correlation. If the wall temperature is below the transition temperature T_2, pure convection heat transfer dominates. The values of Leidenfrost temperature and transition temperature are determined by matching model prediction with the experimental results.

II.2.1.1.1. Film boiling heat transfer.

Because of the nature of high wall superheat in chilldown, the film boiling plays a major role in chilldown in terms of the time span and in terms of the total amount of heat removed from the wall. Currently there exists no specific film boiling correlation for chilldown applications with such high superheat. If one uses conventional film boiling correlations, necessary modifications for cryogenic application must be made for chilldown.

One of cryogenic film boiling heat transfer correlations was provided by Giarratano and Smith (ref. 24)

$$\left(\frac{Nu}{Nu_{calc}}\right) * Bo^{-0.4} = f(\chi_{tt}) \tag{8}$$

where Nu_{calc} is the Nusselt number for the forced convection heat transfer. In this correlation, the heat transfer coefficient is the averaged value for the whole cross section. Similar correlations for cryogenic film boiling also exist in literature. The correlations were obtained from measurements conducted under steady states. The problem with the use of this steady state film boiling correlation is that it does not take into account the change of flow regime as encountered in the chilldown. For example, for the same quality, the heat transfer rate in annular flow is much different from that in stratified flow, while those empirical correlations cannot take such difference into account.

Furthermore, in this study, local heat transfer coefficient is needed in order to incorporate the thermal interaction with the pipe wall. Since the two-phase flow regime information is available through visualization in the present study, the modeling effort needs to take into account the knowledge of the flow regimes.

There are several correlations for the film boiling based on the analysis of vapor film boundary layer and stability of the thin vapor film, such as Bromley's correlation (ref. 17) and Breen and Westerwater's correlation (ref. 18) for film boiling on the outer surface of a hot tube, Frederking and Clark's (ref. 33) and Carey's (ref. 34) correlations for film boiling on the surface of a sphere. However, none of these was obtained for cryogenic fluids or for film boiling on the inner surface of a pipe.

A new correlation for the film boiling in cryogenic chilldown inside a tube is presented here. The schematic of film boiling inside a pipe is shown in figure 3 with a cross-sectional view. Bulk liquid is near the bottom of the pipe. Beneath the liquid is a thin vapor film. Due to buoyancy force, the vapor in the film flows upward along the azimuthal direction. Heat is transferred through the thin vapor film from the solid to the liquid. Reliable heat transfer correlation for film boiling in pipes or tubes requires the knowledge of the thin vapor film thickness which can be obtained by solving the film layer continuity, momentum, and energy equations.

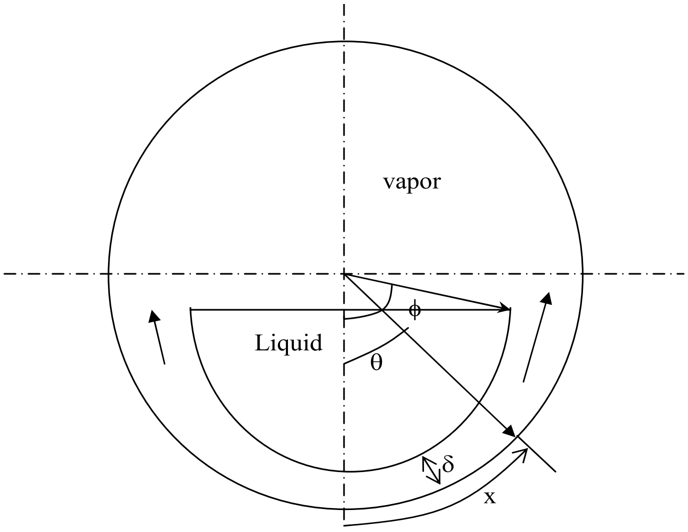

Figure 3. Schematic diagram of film boiling at stratified flow

To simplify the analysis for the vapor film heat transfer, it is assumed the liquid velocity in the azimuthal direction is zero and the vapor flow in the direction perpendicular to the cross-section is negligible. It is further assumed that the vapor film thickness is small compared with the pipe radius and vapor flow is in steady state, incompressible and laminar. The laminar flow assumption can be confirmed post priori as the Reynolds number, Re, based on the film velocity and film thickness is typically of $O\left(10^0 \sim 10^2\right)$. In terms of the *x*- and *y*-coordinates and *(u, v)* velocity components shown in figure 3, the governing equations for the vapor flow are similar to boundary-layer equations:

$$\frac{\partial u}{\partial x}+\frac{\partial v}{\partial y}=0, \tag{9}$$

$$u\frac{\partial u}{\partial x}+v\frac{\partial u}{\partial y}=-\frac{1}{\rho_v}\frac{\partial p}{\partial x}+\nu_v\frac{\partial^2 u}{\partial y^2}-g\sin\theta, \tag{10}$$

$$u\frac{\partial T}{\partial x}+v\frac{\partial T}{\partial y}=\alpha_v\frac{\partial^2 T}{\partial y^2}, \tag{11}$$

where subscribe *v* represents properties of vapor.

Because the length scale at *x* direction is much larger than the length scale at y direction, the *v* velocity can be neglected. Furthermore, convection term is assumed small and is neglected, and the momentum equation is simplified to

$$\frac{1}{\rho_v}\frac{\partial p}{\partial x}=\nu_v\frac{\partial^2 u}{\partial y^2}-g\sin\theta. \tag{12}$$

The vapor pressure can be evaluated by considering the hydrostatic pressure from liquid core as:

$$p = p_0 + \rho_l gR\left(\cos\left(\frac{x}{R}\right) - \cos\phi\right) \tag{13}$$

where ϕ is angular position where the film merges with the vapor core. The momentum equation becomes

$$\frac{(\rho_l - \rho_v)}{\rho_v} g\sin\left(\frac{x}{R}\right) + \nu_v \frac{\partial^2 u}{\partial y^2} = 0 \tag{14}$$

The vapor velocity boundary condition is $u = 0$ at $y = 0$ and $u = u_l = 0$ at $y = \delta$. The vapor velocity profile is:

$$u = \frac{(\rho_l - \rho_v)}{2\nu_v \rho_v} g\sin\left(\frac{x}{R}\right) * \left(\delta y - y^2\right) \tag{15}$$

The mean $\bar{u}$ velocity is defined as

$$\bar{u} = \frac{1}{\delta}\int_0^\delta u dy = \frac{(\rho_l - \rho_v)\delta^2 g}{12\nu_v \rho_v}\sin\left(\frac{x}{R}\right) \tag{16}$$

The energy and mass balance on the vapor film requires that

$$\frac{k_v}{h_{fg}} dx * \left[-\left(\frac{\partial T}{\partial y}\right)_{y=\delta}\right] = d\dot{m} = \rho_v d(\bar{u}\delta) \tag{17}$$

Neglecting the convection, the vapor energy equation is:

$$\frac{\partial^2 T}{\partial y^2} = 0 \tag{18}$$

The following linear temperature profile is thus obtained,

$$\frac{T - T_{sat}}{T_w - T_{sat}} = 1 - \frac{y}{\delta} \tag{19}$$

Substituting the temperature and velocity profiles into eq. (17) yields

$$\frac{\delta}{R}\frac{d}{d\theta}\left(\left(\frac{\delta}{R}\right)\sin\theta\right) = \frac{12k_v \nu_v}{h_{fg}(\rho_l - \rho_v)gR^3}\left(T_w - T_{sat}\right) \tag{20}$$

Equation (20) has analytical solution:

$$\frac{\delta}{R} = 2\left(\frac{6Ja}{Ra}\right)^{\frac{1}{4}} F(\theta), \tag{21}$$

where Ja is Jacob number and Ra is Raleigh number:

$$Ja = \frac{C_{p,v}\left(T_w - T_{sat}\right)}{h_{fg}}, \tag{22}$$

$$Ra = \frac{gD^3\left(\rho_l - \rho_v\right)}{\nu_v \alpha_v \rho_v}, \tag{23}$$

and $F(\theta)$

$$F(\theta) = \left(\frac{\frac{4}{3}\int_0^{\theta} \sin^{1/3}\theta' d\theta'}{\sin^{4/3}\theta}\right)^{\frac{1}{4}} \tag{24}$$

describes the geometric dependence of vapor film thickness.
The mean velocity $\bar{u}$ as a function of θ is thus

$$\bar{u} = \left(\frac{\left(T_w - T_{sat}\right)\left(\rho_l - \rho_v\right)gR}{12\nu_v \rho_v^2 h_{fg}}\right)^{\frac{1}{2}} F^2(\theta)\sin(\theta) \tag{25}$$

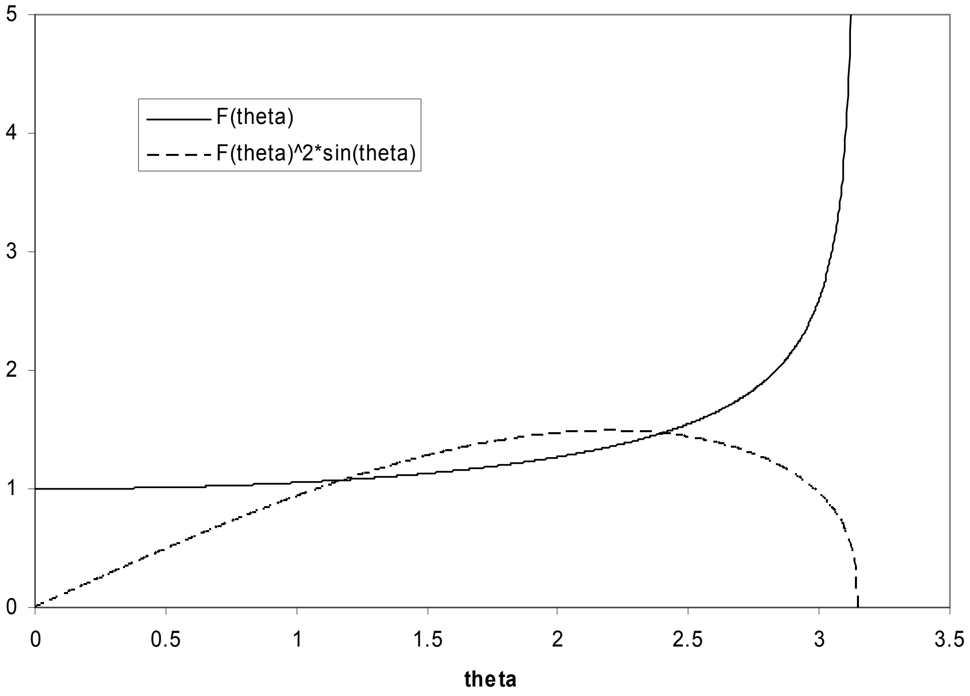

Figure 4. Numerical solution of the vapor thickness and velocity influence functions.

Curves for $F(\theta)$ and $F(\theta)^2 \sin\theta$ based on numerical integration are shown in figure 4. The vapor film thickness has a minimum at $\theta = 0$ and is nearly constant for $\theta < \frac{\pi}{2}$. It rapidly grows after $\theta > \frac{\pi}{2}$. The singularity at the top of tube when $\theta \to \pi$ is of no practical significance since the film will merge with the vapor core at the vapor-liquid interface. The vapor velocity is controlled by $F(\theta)^2 \sin\theta$ which is zero at the bottom of the pipe and increases almost linearly in the lower part of the tube where the vapor film thickness does not change substantially. In the upper part of the tube, due to the increase in the vapor film thickness, the vapor velocity gradually drops back to zero at the top of the tube. Thus a maximum velocity may exist in the upper part of the tube.

The local film boiling heat transfer coefficient is easily obtained from the linear temperature profile. It is

$$h = \frac{k_v}{\delta} = 0.6389 \frac{k_v}{DF(\theta)} \left(\frac{Ra}{Ja} \right)^{\frac{1}{4}} \tag{26}$$

II.2.1.1.2. Nucleate Boiling and Convection Heat Transfer

For the nucleate flow boiling heat transfer, Gungor and Winterton's correlation (ref. 26) is widely used due to its relatively better accuracy in predicting heat transfer coefficients. However, a closer examination on this correlation shows that it is based mainly on the following parameters: Pr, Re, and quality *x*. Similar to the development of conventional film boiling correlations, these parameters all reflect overall properties of the flow in the pipe and are not directly related to flow regimes. Thus it cannot be used to predict the local heat transfer coefficients in chilldown. Chen's (ref. 25) flow boiling correlation is based on separating the heat transfer to micro- and macroconvection heat transfer. Micro-convection heat transfer represents the contribution from boiling heat transfer, and macro-convection represents the contribution from the forced convection heat transfer. However his correlation fits best for annular flow because of the derivation of suppression factor. In stratified flow regime, which is common in cryogenic chilldown, Chen's correlation may not be applicable.

Several correlations have been tried in this study, including Gungor and Winterton's correlations (ref. 26), Chen's correlation (ref. 25), and Kutateladze's correlations (ref. 29). None gives a satisfactory heat transfer rate that is need to match the experimentally measured temperature histories in (ref. 7) in the nucleate boiling regime. Among them, Kutateladze's correlation gives more reasonable result. In this correlation, the total heat transfer coefficient *h* is

$$h = h_{conv} + h_{pool} \tag{27}$$

where h_{conv} is given by Dittus-Boelter equation for fully developed pipe flow,

$$h_{conv} = 0.023 * \mathrm{Re}_l^{0.8}\, \mathrm{Pr}_l^{0.4} * k_l / D \tag{28}$$

And h_{pool} is pool nucleate boiling heat transfer coefficient,

$$h_{pool} = 0.487 * 10^{-10} * \left[\frac{k_l \rho_l^{1.282} p^{1.750} \left(C_p\right)_l^{1.5}}{\left(h_{fg}\rho_v\right)^{1.5} \sigma^{0.906} \mu_l^{0.626}} \right] \Delta T^{1.5} \tag{29}$$

In which ΔT is wall superheat.

Kutateladze's correlation (ref. 29) was proposed without considering the effect of nucleate site suppression. This obviously leads to an overestimation of the nucleate boiling heat transfer rate. Hence a modified version of Kutateladze's correlations (28) is used,

$$h = h_{conv} + S * h_{pool} \tag{30}$$

where *S* is suppression factor.

When ΔT drops to a certain range all the nucleate sites are suppressed. The heat transfer is dominated by single phase forced convection. The heat transfer coefficient can then be predicated using Dittus-Boelter equation, eq. (27), if flow is turbulent, or eq. (30), if flow is laminar.

$$h_{conv} = 4.36 * k_l / D \tag{31}$$

II.2.1.2. Heat Transfer between Vapor and Solid Wall

The heat transfer between the vapor and the wall can be estimated by treating the flow as a fully developed convection flow, neglecting the liquid droplets that are entrapped in the vapor. The heat transfer coefficient of vapor forced convection flow is

$$h_v = 0.023 * \mathrm{Re}_v^{0.8}\,\mathrm{Pr}_v^{0.4} * k_v / D, \text{ (turbulent flow)} \tag{32}$$

or

$$h_v = 4.36 * k_v / D, \text{ (laminar flow)} \tag{33}$$

II.2.2. Heat Transfer between Solid Wall and Environment

For a cryogenic flow facility, although serious insulation is applied, the heat leakage to environment is still considerable due to the large temperature difference between the cryogenic fluid and the environment. It is necessary to evaluate the heat leakage from the inner pipe to environment in order to make realistic assessment of the model prediction with the experimental results (ref. 7).

Vacuum insulation chamber between the inner and outer pipes is used in cryogenic transport pipe (ref. 7), as shown in figure 5. Radiation heat transfer exists between the inner and outer pipe. Furthermore, the space between the inner and outer pipe is not an absolute vacuum. There is residual air that causes free convection between the inner and outer pipes driven by the temperature difference of the inner and outer pipe.

The radiation between the inner pipe and outer pipe becomes significant when the inner pipe is chilled down. The heat transfer coefficient is proportional to the difference of the fourth power of wall temperatures. Exact evaluation of the radiation heat transfer between the inner and outer pipe is a difficult task. Hence a simplified model based on the overall radiation heat transfer between long concentric cylinders with constant temperature at inner pipe and outer pipe (ref. 31) is used to evaluate the heat transfer rate at every axial location of the pipe. It is not quantitatively correct, but can provide reasonable estimate for the magnitude of the radiation heat transfer between pipes through the vacuum. The local radiation heat transfer rate per unit area on the surface of inner pipe rad q'_{rad}. is

$$q'_{rad} = \frac{\sigma (T_{wall}^4 - T_o^4)}{\dfrac{1}{\varepsilon_i} + \dfrac{1-\varepsilon_o}{\varepsilon_o}\left(\dfrac{r_i}{r_o}\right)} \tag{34}$$

where the σ is Stefan Boltzmann constant, (r_i, ε_i) and (r_o, ε_o) are the radius and emissivity of inner pipe and outer pipe, respectively, and T_{wall} is the local inner wall temperature, T_o is the room temperature that is assumed constant in the entire outer pipe. Here the emissivity is also assumed to be constant during the entire chilldown process.

For the free convection heat transfer due to the residual air in the vacuum chamber between the inner pipe and outer pipe, Raithby and Hollands' correlation (ref. 35) is used for the heat transfer rate. The average heat transfer rate per unit length of the cylinder is

$$q'_{frc} = \frac{2\pi k_{eff}}{\ln\left(D_o / D_i \right)} \left(T_i - T_o \right) \qquad (35)$$

where *T* is assumed constant on the inner and outer wall along the azimuthal directions, and *eff k* is the effective thermal conductivity.

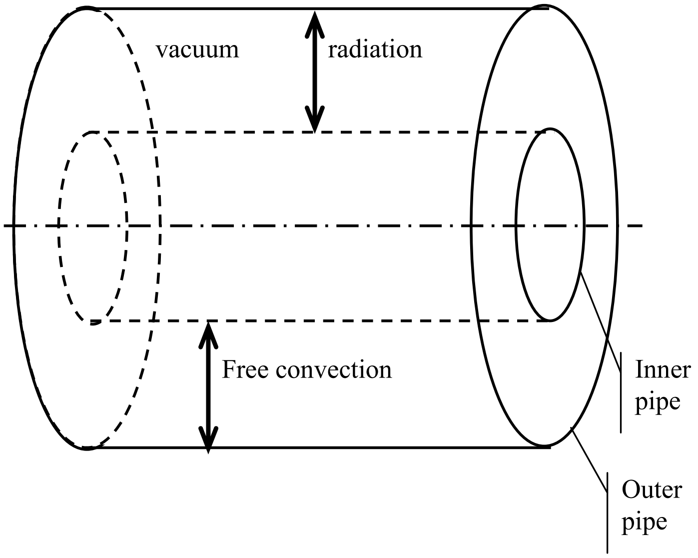

Figure 5. Schematic of vacuum insulation chamber.

III. Results and Discussions

In experiment by Chung et al. (ref. 7), liquid nitrogen was used. The flow regime is revealed to be stratified flow by visual observation, as shown in figure 7, and wall temperature history in several azimuthal positions is measured by thermal couples and recorded on a computer.

III.1. Experiment of Chung et al.

In experiment of Chung et al. (ref. 7), a concentric pipe test section (fig. 6) was used. The chamber between the inner and outer pipe is vacuumed, but about 20 percent air remained. The inner diameter (i.d.) and outer diameter (o.d.) of inner pipe are 11.1 and 15.9 mm, and i.d. and o.d. of outer pipe are 95.3 and 101.6 mm, respectively. Numerous thermal couples were placed at different locations of the inner pipe. Some were embedded very closely to the inner surface of the inner pipe while others measure the outside wall temperature of inner pipe. Experiments were carried out at room temperature and atmosphere pressure. Liquid nitrogen flows from a reservoir to the test section driven by gravity. As liquid nitrogen flows through the pipe, it evaporates and chills the pipe. Some of the typical visual results are shown in figure 7. The measured average liquid nitrogen velocity is *U* ~ 5 cm/s. Vapor velocity is not measured in this experiment. In this study, it is determined through trial-and-error by fitting the computed and measured temperature histories. The characteristic liquid volume fraction is 0.3 from the recorded video images. The characteristic time used in this computation is $t_0 = 100s$. The Leidenfrost temperature for the nitrogen is around 180 K; hence the temperature when the film boiling ends and nucleates boiling starts is set at 180 K. The transition temperature at which the nucleate flow boiling switches to purely convection heat transfer is 140 K based on experimental results. The material of the inner pipe and outer pipe used in the experiment of (ref. 7) are Pyrex glass with emissivity of 0.82 at room temperature.

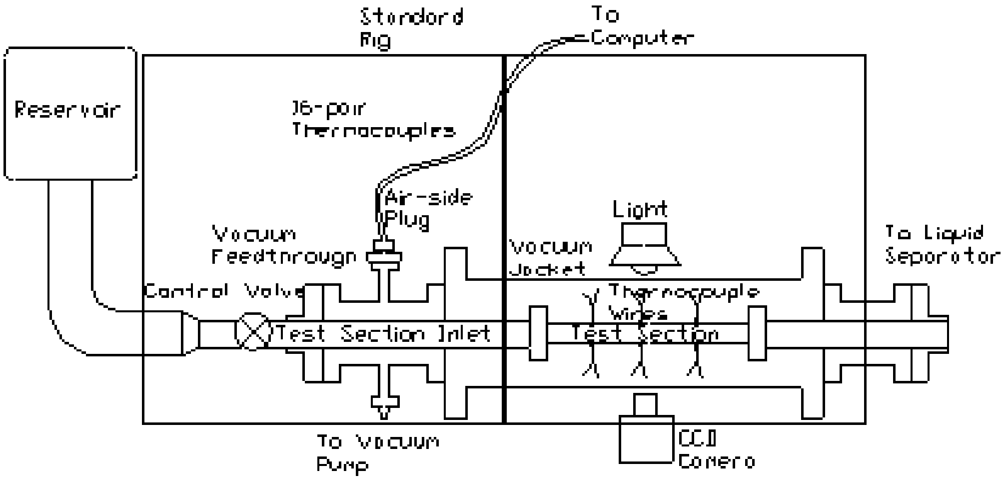

Figure 6. Schematic of Chung et al.'s cryogenic twophase flow test apparatus (ref. 7).

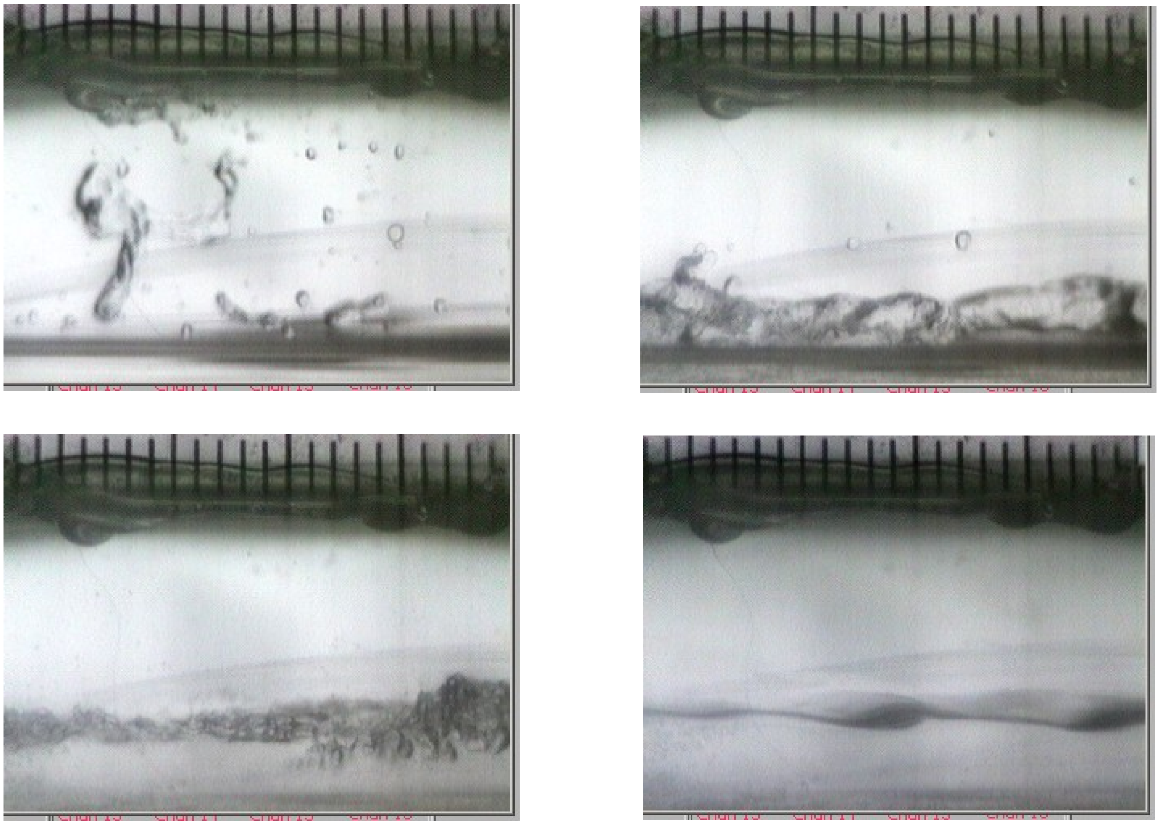

Figure 7. Experimental visual observation of Chung et al.'s cryogenic two-phase flow test (ref. 7).

III.2. Comparison of pipe wall temperature

In the computation, there are 40 grids along the radial direction and 40 grids along azimuthal direction for the inner pipe (fig. 8). The results of temperature profile at 40·40 grids and higher grids resolution show that 40·40 grids are sufficient. Figures 9 and10 compare the measured and computed wall temperature as a function of time at positions 11, 12, 14, and 15 shown in figure 8. For the modified Kutateladze's correlation a suppression factor 0.01 is used. Vapor velocity is 0.5 m/s based on the best fit.

The overall temperature histories agree well in the film boiling stage. Thus, the film boiling heat transfer coefficient based on the first principle and incorporated the flow structure gives very reliable prediction. It must also be noted that the value of the Leidenfrost temperature does not affect the computed temperature history prior to that transition point since the governing equation is parabolic. The good agreement before the Leidenfrost temperature is reached is entirely due to the superior performance of the new film boiling heat transfer coefficient.

During the stage of the rapidly decreasing wall temperature after the Leidenfrost temperature, the computed wall temperature drops slightly faster than the measured value. The rapid decrease in the wall temperature is due to initiation of nucleate boiling which is more efficient for heat transfer than the film boiling. Reasonable agreement between the computed and measured histories in this nucleate boiling regime is due to: i) the good agreement already achieved in the film boiling stage; ii) valid choice for the Leidenfrost temperature that switches the heat transfer regime correctly; and iii) appropriate modification of Kutateladze's correlations.

In the final stage of chilldown, the wall temperature decreases slowly, and the computed wall temperature shows the same trend as the measured one but tends to be a little lower. Figure 11 shows the temperature distribution of a given cross-section at different times of chilldown. Because the upper part of pipe wall is exposed to nitrogen vapor, cooling effect is much reduced.

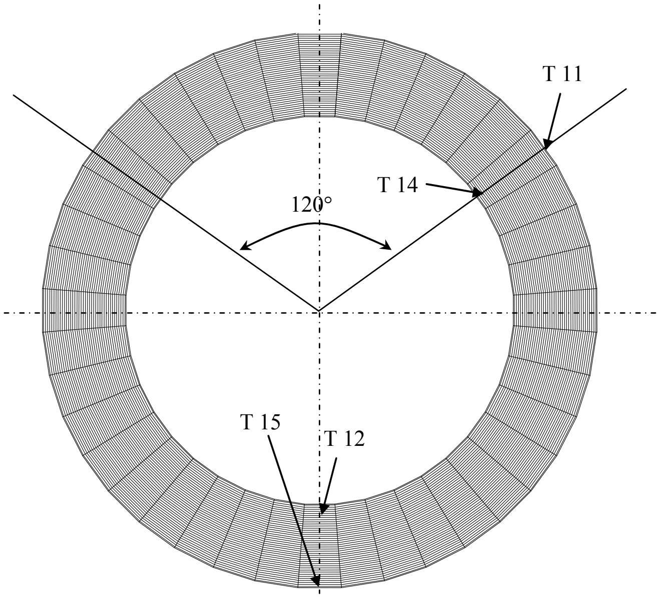

Figure 8. The computational grids arrangement and positions of thermal couples.

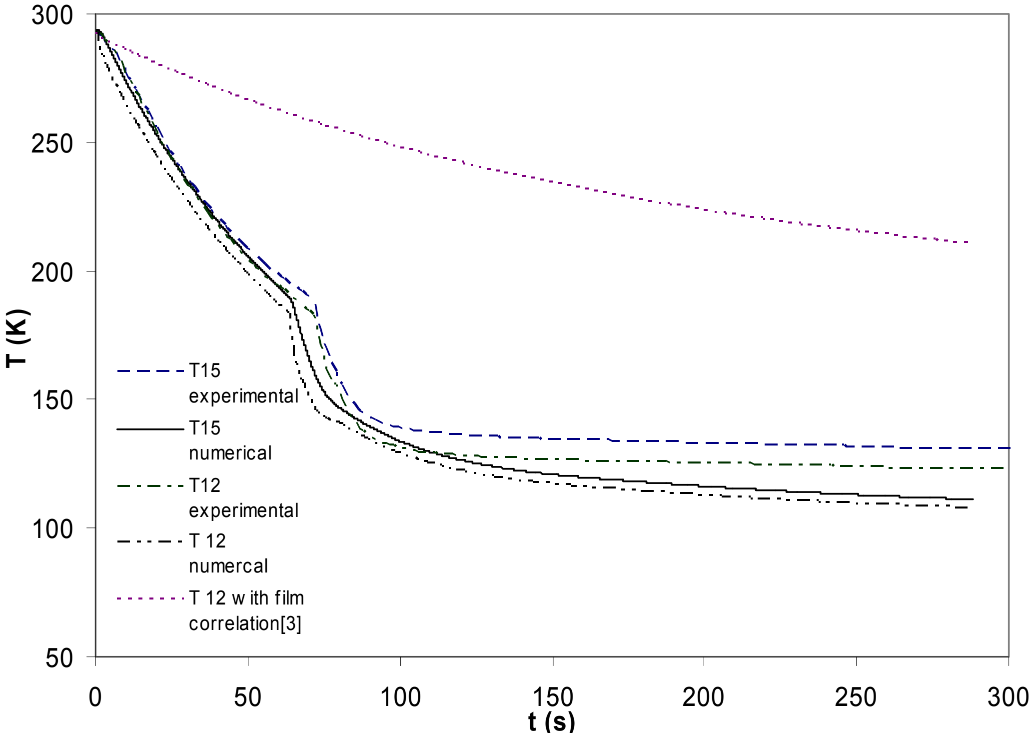

Figure 9. Comparison of wall temperature of transducer 12 and 15, which is at the bottom of pipe, between the experiment and computation. For comparison purpose, the solution in the *Z*- direction is converted to time *t*.

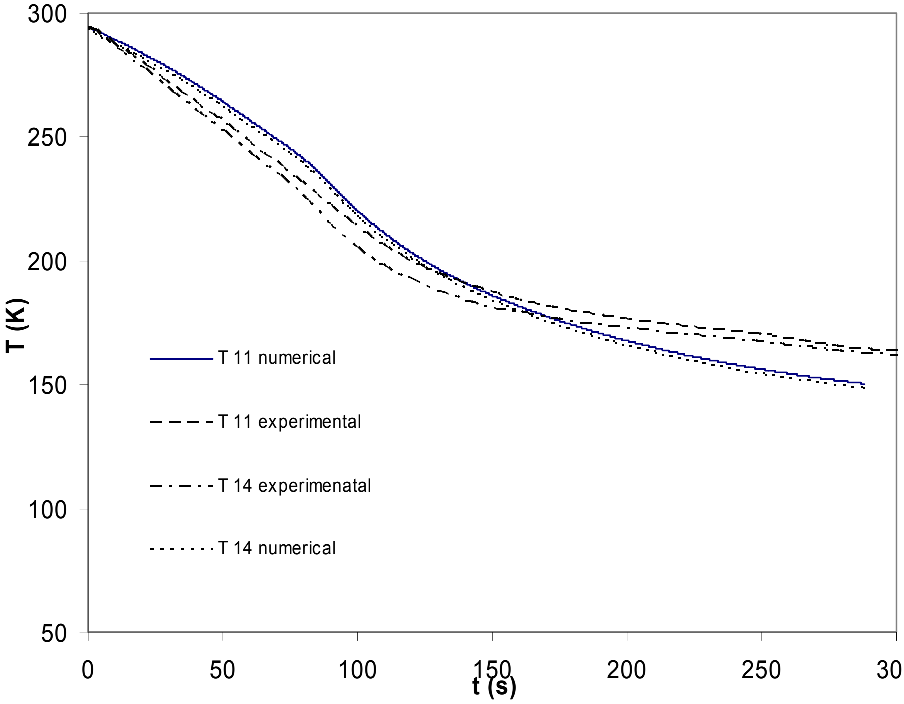

Figure 10. Comparison of wall temperature of transducer 11 and 14, which are at the upper part of the pipe, between the experiment and computation. For comparison purpose, the solution in the *Z*-direction is converted to time *t*.

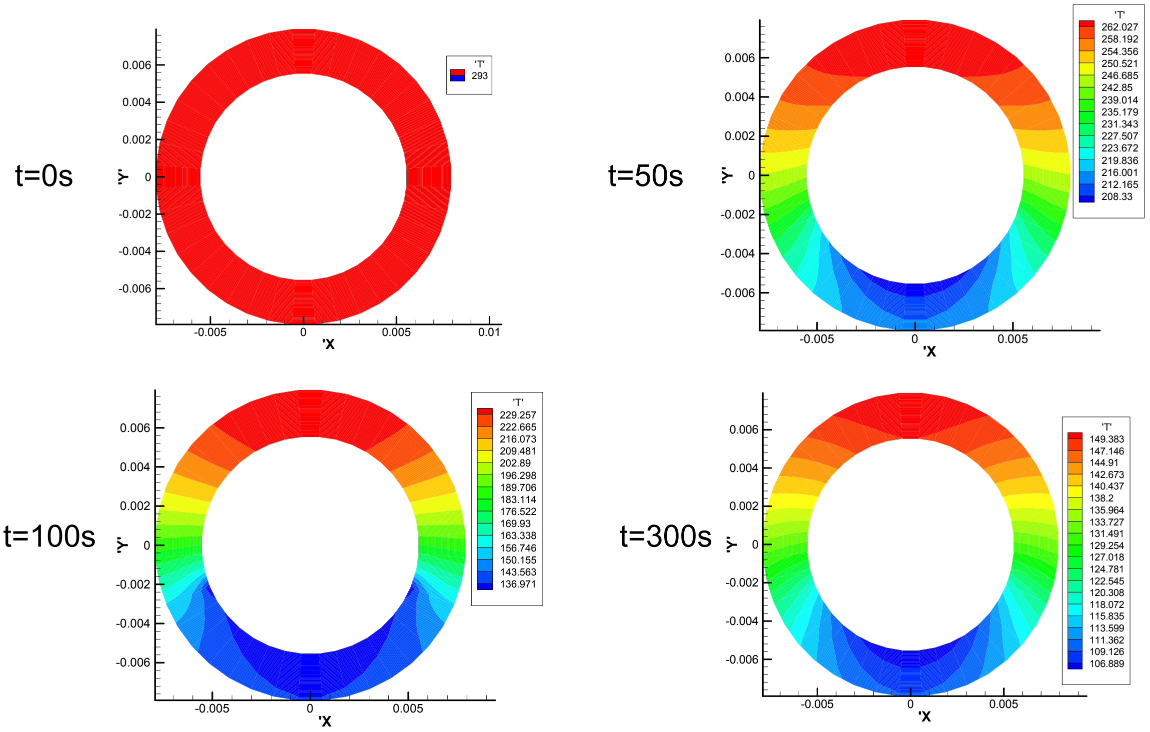

Figure 11. Wall temperature distribution across the section at *t* = 0, 50, 100, and 300 sec.

III.3. Remarks

In figure 9, the wall temperature based on the film boiling correlation of Giarratano and Smith (ref. 24) is also shown. Apparently, the correlation of Giarratano and Smith (ref. 24) gives a very low heat transfer rate so that the wall temperature remains high. This comparison confirms our earlier argument that correlations based on the overall flow parameter, such as quality and averaged Reynolds number, are not applicable for the simulation of unsteady chilldown.

The nucleate flow boiling correlations of Gungor and Winterton (ref. 26), Chen (ref. 25), Kutateladze's correlations (ref. 29) are also compared in this study. Gungor and Winterton's correlation fails to give a converged heat transfer rate during the transition from the film boiling to the nucleate boiling. Chen's correlation overestimates the heat transfer rate, and cause unrealistically large temperature drop on the wall, which results in the halt of the computation. Only Kutateladze's correlation gives a reasonable heat transfer rate. However, the temperature drop near the bottom of the pipe is still faster than the measured one as shown in figure 9. This may be due to the fact that most of nucleate boiling correlations were obtained from experiments of low wall superheat. However, in this cryogenic chilldown, wall superheat is much higher than that in the normal nucleate boiling experiments. Another reason is that the original Kutateladze's correlation does not include suppression factor. This leads to overestimating heat transfer coefficient. The modified Kutateladze's correlation with suppression factor gives reasonable chilldown result in figure 9.

Further examination of figures 9 and 10 indicates that although we have considered the heat leak from the outer wall to the inner wall through radiation and free convection, the computed temperature is still lower than the measured temperature during the final stage of chilldown, where the heat transfer rate between fluid and wall is low due to lower wall superheat and possibly heat leak. The temperature difference between the computed and measured values at position 12 and position 15 suggests that there may be additional heat leak, which affects the measurements but is not taken in account in the present modeling.

In this study, the pseudo-steady chilldown model is developed to predict the chilldown process in a horizontal pipe in stratified flow regime. This model can also be extended to describe annular flow chilldown in the horizontal or the vertical pipe with minor changes on the boundary condition for solid temperature. It can also be extended to study the chilldown in the slug flow as long as we specify the contact period between the solid and the liquid or the vapor. The disadvantage of the current pseudosteady chilldown model is that the fluid interaction inside the pipe is largely neglected and both vapor and liquid velocities are assumed to be constant. Compared with a more complete model that incorporates the two-fluid model, the present pseudo-steady chilldown model requires more experimental measurements as inputs. However, the pseudo-steady chilldown model is computationally more robust and efficient for predicting chilldown process. It provides overall reasonable results for the solid wall temperature. While a more complete model for chilldown process that incorporates the mass, momentum, and energy equations of vapor and liquid is being developed to reduce the dependence of the experimental inputs for the liquid velocity and trial-and-error for the vapor velocity, the present study has revealed useful insights into the key elements of two-phase heat transfer encountered in the chilldown process which have been largely ignored. It also laid the necessary modeling foundation for the incorporation of the two-fluid model.

IV. Conclusions

A pseudo-steady chilldown computational model has been developed to understand the heat transfer mechanisms of cryogenic chilldown and predict the chilldown wall temperature history in a horizontal pipeline. The model assumes the constant speed of the moving liquid wave front, and steady state of the thermal field in the solid in a reference frame that moves with the liquid wave front, and saturated temperature of both liquid and vapor so that the 3–D unsteady problem can be transformed to a 2–D, parabolic problem. A new film boiling heat transfer coefficient in the cryogenic chilldown condition is developed using the first principle and incorporating the stratified flow structure. The existing nucleate boiling heat transfer correlations may not work well under cryogenic condition. A modified Kutateladze's correlations with suppression factor adequately describes heat transfer coefficient. With the new and modified heat transfer correlations, the pipe wall temperature history based on the pseudo-steady chilldown model matches well with the experimental results by Chung et al. (ref. 7) for almost the entire chilldown process. The pseudo-steady chilldown model has captured the important features of thermal interaction between the pipe wall and the cryogenic fluid.

V. Patents, Publications, Presentations and Students From Research

Publications

1. Liao, J., Yuan, K., Mei, R., Klausner, J.F., Chung, J., 2005, "Cryogenic Chill-Down Model Inside Transportation Pipelines," Proceedings of the ASME Summer Heat Transfer Conference, San Francisco, CA.

Students from Research

Jun Liao: Recived PhD. Employed with Westinghouse Electric Company, Monroeville, PA.

VI. Acknowledgements

This Work was supported by NASA Glenn Research Center under contract (NAG3-2930) and NASA Kennedy Space Center.

VII. References

1. Burke, J.C., Byrnes, W.R., Post, A.H., and Ruccia, F.E., 1960, "Pressure Cooldown of Cryogenic Transfer Lines," Advances in Cryogenic Engineering, 4, pp. 378–394.
2. Graham, R.W., Hendricks, R.C., Hsu, Y.Y., and Friedman, R., 1961, "Experimental Heat Transfer and Pressure Drop of Film Boiling Liquid Hydrogen Flowing through A Heated Tube," Advances in Cryogenic Engineering, 6, pp. 517–524.
3. Bronson, J.C., Edeskuty, F.J., Fretwell, J.H., Hammel, E.F., Keller, W.E., Meier, K.L., Schuch, and A.F, Willis, W.L., 1962, "Problems in Cool-Down of Cryogenic Systems," Advances in Cryogenic Engineering, 7, pp. 198–205.
4. Chi, J.W.H., and Vetere, A.M., 1963, "Two-Phase Flow During Transient Boiling of Hydrogen and Determination of Nonequilibrium Vapor Fractions," Advances in Cryogenic Engineering, 9, pp. 243-253.
5. Steward, W.G., Smith and R.V., Brennan, J.A., 1970, "Cooldown Transients in Cryogenic Transfer Lines," Advances in Cryogenic Engineering, 15, pp. 354–363.
6. Velat, C., Jackson, J., Klausner, J.F., and Mei, R., 2004, "Cryogenic Two-Phase Flow During Chilldown," in Proceedings of the ASME HT-FED Conference, Charlotte, NC.
7. Chung, J.N., Yuan, K., and Xiong, R., 2004, "Two-Phase Flow and Heat Transfer of a Cryogenic Fluid during Pipe Chilldown," Proceedings of 5th International Conference on Multiphase Flow, Yokohama, Japan, pp. 468.
8. Martinelli, R.C., and Nelson, D.B., 1948, "Prediction of Pressure Drop During Forced – Circulation Boiling of Water," Transaction of ASME, 70, pp. 695–701.
9. Chi, J.W.H., 1965, "Cooldown Temperatures and Cooldown Time During Mist Flow," Advances in Cryogenic Engineering, 10, pp. 330–340.
10. Cross, M.F., Majumdar, A.K., Bennett Jr., and J.C., Malla, R.B., 2002, "Model of Chilldown in Cryogenic Transfer Linear," Journal of Spacecraft and Rockets, 39, pp. 284–289.
11. Chan, A.M.C., and Banerjee, S., 1981, "Refilling and Rewetting of a Hot Horizontal Tube part I: Experiment," Journal of Heat Transfer, 103, pp. 281–286.
12. Chan, A.M.C., and Banerjee, S., 1981, "Refilling and Rewetting of a Hot Horizontal Tube part II: Structure of a Two-Fluid Model," Journal of Heat Transfer, 103, pp. 287–292.
13. Chan, A.M.C., and Banerjee, S., 1981, "Refilling and Rewetting of a Hot Horizontal Tube part III: Application of a Two-Fluid Model to Analyze Rewetting," Journal of Heat Transfer, 103, pp. 653–659.
14. Bromley, J.A., 1950, "Heat Transfer in Stable Film Boiling," Chemical Engineering Progress, 46, no. 5, pp. 221–227.
15. Dougall, R.S., Rohsenow, W.M., 1963, "Film boiling on the inside of vertical tubes with upward flow of the fluid at low qualities," MIT report no 9079–26, MIT.
16. Laverty, W.F., and Rohsenow, W.M., 1967, "Film Boiling of Saturated Nitrogen Flowing in a Vertical Tube," Journal of Heat Transfer, 89, pp. 90–98.
17. Bromley, J.A., 1950, "Heat Transfer in Stable Film Boiling," Chemical Engineering Progress, 46, no. 5, pp. 221–227.
18. Breen, B.P., and Westwater, J.W., 1962, "Effect if Diameter of Horizontal Tubes on Film Heat Transfer," Chemical Engineering Progress, 58, no. 7, pp. 67.
19. Berenson, P.J., 1961, "Film-Boiling Heat Transfer from a Horizontal Surface," Journal of Heat Transfer, 83, pp. 351–358.

20. Hendricks, R.C., Graham, R.W., Hsu, Y.Y., and Friedman, R., 1961, “Experimental Heat Transfer and Pressure Drop of Liquid Hydrogen Flowing Through a Heated Tube,” NAS TN D–765.
21. Hendricks, R.C., Graham, R.W., Hsu, Y.Y., and Friedman, R., 1966, “Experimental Heat Transfer Results for Cryogenic Hydrogen Flowing in Tubes at Subcritical and Supercritical Pressure to 800 pounds per Square Inch Absolute,” NASA TN D–3095.
22. Ellerbrock, H.H., Livingood, J.N.B., and Straight, D.M., 1962, “Fluid-Flow and Heat-Transfer Problems in Nuclear Rockets,” NASA SP–20.
23. von Glahn, U.H., 1964, “A Correlation of Film-Boiling Heat Transfer Coefficients Obtained with Hydrogen,” Nitrogen and Freon 113 in Forced Flow, NASA TN D–2294.
24. Giarratano, P.J., Smith, R.V., 1965, “Comparative study of Forced Convection Boiling Heat Transfer Correlations for Cryogenic Fluids,” Advances in Cryogenic Engineering, 11, pp. 492–505.
25. Chen, J.C., 1966, “Correlation for Boiling Heat Transfer to Saturated Fluids in Convective Flow,” Industry Engineering Chemistry Process Design and Development, 5, pp. 322–329.
26. Gungor, K.E., Winterton, R.H.S., 1996, “A General Correlation for Flow Boiling in Tubes and Annuli,” International Journal of Heat Mass Transfer, 29, no. 3, pp. 351–358.
27. Bennett, D.L., and Chen, J.C., 1980, “Forced Convection for the in Vertical Tubes for Saturated Pure Components and Binary Mixture,” A.I.Ch.E. Journal, 26, pp. 454–461.
28. Stephan, K., and Auracher, H., 1981, “Correlation for Nucleate Boling Heat Transfer in Forced convection,” International Journal of Heat Mass Transfer, 24, pp. 99–107.
29. Kutateladze, S.S., 1952, “Heat Transfer in Condensation and Boiling,” Atomic Energy Commission Translation 3770, Tech. Info. Service, Oak Ridge, Tennessee.
30. Steiner, D., May 1986, “Heat Transfer During Flow Boiling of Cryogenic Fluids in Vertical and Horizontal Tubes,” Cryogenics, 26, pp. 309–318.
31. Incropera, F.P., Dewitt, D.P., 2002, Fundamentals of Heat and Mass Transfer, 5th edition, John Willey& Sons.
32. Thompson, T.S., 1972, “An Analysis of the Wet-Side Heat-Transfer Coefficient during Rewetting of a Hot Dry Patch,” Nuclear Engineering and Design, 22, pp. 212–224.
33. Ferderking, T.H.K., and Clark, J.A., 1963, “Nature Convection Film Boling on A Sphere,” Advanced Cryogenic Engineering, 8, pp. 501–506.
34. Carey, V.P., 1992, Liquid-Vapor Phase-Change Phenomena, Taylor & Francis Press.
35. Raithby, G.D., and Hollands, K.G.T., 1975, “A General Method of Obtaining Approximate Solutions to Laminar and Turbulent Free Convection Problems,” Advances in Heat Transfer, 11, pp. 265–315 Academic Press, New York.

Sub-Task 2: A Study on Numerical Instability of Inviscid Two-Fluid Model near Ill-posedness Condition

Abstract

Two-fluid model is widely used in studying gas-liquid flow inside pipeline, because it can qualitatively predict the flow field at low computational cost. However, the two-fluid model is quite unstable when it reaches or is near ill-posedness. In this study a pressure correction algorithm for inviscid two-fluid model is carefully designed to improve stability near ill-posedness. Through von Neumann stability analysis, the wave growth rates by pressure correction scheme with first order upwind, second order upwind, and central difference dicretization scheme are studied. The von Neumann analysis shows that central difference scheme is more accurate and stable than other two schemes. Compared with first order upwind scheme, second order upwind scheme, which is supposed to be more accurate and widely used by CFD community, is much unstable for low frequent harmonics and inaccurate for high frequency harmonics in two-fluid model. Von Neumann stability analysis also shows the instability by ill-posedness of two-fluid model is significantly different from the instability of the discretized two-fluid model. Furthermore, comparisons between actual wave growth and predicted wave growth by von Neumann stability analysis are taken. The comparison shows the accuracy of the new pressure correction scheme and success of von Neumann stability analysis in two-fluid model. Accordingly, the relation between the ill-posedness of two-fluid model and numerical stability of algorithm for inviscid two-fluid model is elucidated.

Nomenclature

c	wave speed
E	common amplitude factor
G	amplification factor
g	gravity
k	wavenumber
H	hydraulic depth
p	pressure
N	grids number
t	time
u	velocity
x	space coordinate
α	volume fraction
β	angle of inclination from the horizontal
ε	amplitude factor
φ	phase angle
λ	characteristic root
ρ	denisty

Subscripts

e	east face of control volume
g	gas
l	liquid
i	interface, grid index
P	center of main control volume
w	west face of control volume

I. Introduction

Gas-liquid flow inside a pipeline is prevalent in the handling and transportation of fluid. A reliable flow model is essential to the prediction of flow field inside the pipeline. To fully simulate the system, Navier–Stokes equations in three-dimensions are required. However, it is not feasible for simulating flow in a long pipe by today's computer. To reduce the computational cost in simulating the flow in a long pipe and obtain basic and essential flow properties, such as gas volume fraction, liquid and gas velocity, pressure, one-dimensional model is necessary. Two-fluid model as one of one-dimensional model is recognized as a realistic tool to simulate the gas-liquid flow inside the pipeline. Two-fluid model is also called separated flow model, which consists of two sets of conservation equation for mass, momentum and energy of gas phase and liquid phase. It was proposed by Willis (1969), and further refined in Ishii (1975).

Although two-fluid model shows its success in simulating the two-phase flow in pipeline, the two-fluid model suffers ill-posedness problem that is, when relative velocity between liquid and gas exceeds a critical value, the governing equations do not possess real characteristic (Gidaspow, 1974; Jones and Prosperettii, 1985; Song and Ishii, 2000). This ill-posedness condition suggests that the results of two-fluid model at that condition do not reflect real flow situation inside the pipe. The two-fluid model only gives meaningful results when the relative velocity between gas and liquid phase is less than a criterion, which is determined by gravity, liquid level, surface tension, and other conditions. However, the criterion is coincident with the stability criterion of inviscid Kelvin-Helmholtz instability (IKH) analysis (Issa and Kempf, 2002). Because the instability of IKH analysis results in the flow regime transition from stratified flow to slug flow or annular flow (Barnea and Taitel, 1994a), ill-posedness of two-fluid model also implies the flow regime transition (Brauner and Maron, 1992).

The computational methods to solve governing equations of two-fluid model were researched by many investigators. In this study, a further assumption on two-fluid model is both liquid and gas phases are incompressible, which is reasonable because most of stratified flows are at relative low speed compared with sound speed. However, if the fluids are assumed incompressible, the governing equations of two-fluid model are not pure hyperbolic. Therefore hyperbolic type solver cannot be used on incompressible two-fluid model. To solve the incompressible two-fluid model, one approach is to simplify the governing equations to two governing equations about liquid phase volume fraction and liquid velocity, but transient terms in gas mass and momentum equations are neglected (Chan and Banerjee, 1981; Barnea and Taitel, 1994b). The governing equations of simplified incompressible two-fluid model are hyperbolic, and can be solved by characteristic method or finite difference method. Another more effective method of solving incompressible two-fluid model is to use pressure correction scheme (Patanka 1980). Issa and Kempf (2000) successfully applied the pressure correction scheme in two-fluid model and successfully simulated stratified flow and slug flow inside a pipe.

When two-fluid model becomes ill-posed, the solution of the model becomes unstable. The discretized model should demonstrate the instability of two-fluid model, but numerical instability may not be identical to the instability caused by the ill-posedness. Inappropriate numerical schemes may trigger the numerical instability earlier than the actual one. Lyczkowski et al. (1978) used von Neumann stability analysis to study a compressible two-fluid model with their numerical scheme. Their study shows numerical instability and ill-posedness may not be identical. However, their study is incomplete, lacking gravity term and analysis on different discretization schemes. Stewart (1979), Ohkawa and Tomiyama (1995) tried to illustrate the numerical stability of incompressible two-fluid model with a simplified model equation as a replacement. Their study shows that higher order upwind schemes yield more unstable numerical solution than the first order upwind scheme.

A complete study on the numerical stability of two-fluid model and the relation between numerical instability and ill-posedness are desired.

In this study, a pressure correction scheme designed to increase the stability of numerical scheme when flow is near ill-posedness will be present. Von Neumann stability analysis is employed to study the stability of discretized two-fluid model with different interpolation schemes. The performances of different schemes at various flow configurations will be compared. The results of von Neumann stability analysis can be used to validate the computer code. Comparisons will be taken at various flow configurations. Furthermore, test of wave propagation inside pipe shows the scheme has the ability to handle the real flow in the pipe.

Ill-posedness of two-fluid model is the major concern in this study. Since ill-posedness and IKH stability are not related to the viscosity of two-fluid model. To simplify the analysis on the two-fluid model and concentrate our major concern, only inviscid two-fluid model are considered. Furthermore all of results of study on the inviscid two-fluid model are also applicable to the viscous two-fluid model.

II. Numerical Method

II.1. Governing Equations

The basis of the two-fluid model is a set of one-dimensional conservation equations for the balance of mass, momentum and energy for each phase. The one-dimensional conservation equations are obtained by integrating the flow properties over the cross-sectional area of the flow.

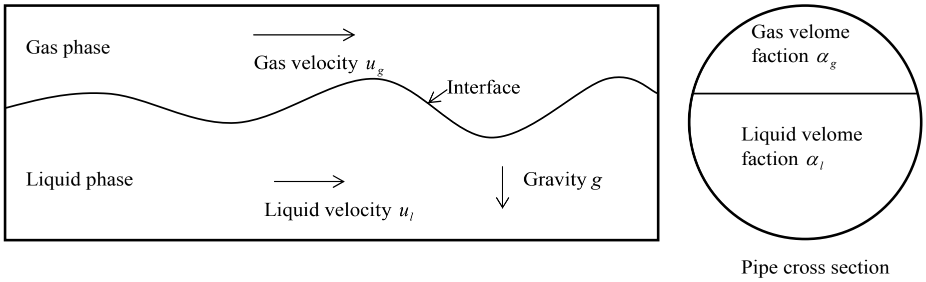

Fig.1 Schematic of two-fluid model for pipe flow.

Because the ill-posedness originates from the hydrodynamic instability of the two-fluid model, only continuity and momentum equations are considered in the inviscid two-fluid model. Surface tension is also neglected since it only acts on small scales, while the waves determining the flow structure in pipe flows are usually of long wavelength. The gas phase is assumed incompressible, as the Mach number of the gas phase is usually very low for stratified flow. Hence, the governing equations are as follows:

$$\frac{\partial}{\partial t}(\alpha_l)+\frac{\partial}{\partial x}(u_l\alpha_l)=0 \tag{1}$$

$$\frac{\partial}{\partial t}\left(\alpha_g\right)+\frac{\partial}{\partial x}\left(u_g\alpha_g\right)=0 \tag{2}$$

$$\frac{\partial}{\partial t}\left(u_l\alpha_l\right)+\frac{\partial}{\partial x}\left(u_l^2\alpha_l\right)=-\frac{\alpha_l}{\rho_l}\frac{\partial p_i}{\partial x}-g\cos\theta H_l\frac{\partial\alpha_l}{\partial x}-\alpha_l g\sin\theta \tag{3}$$

$$\frac{\partial}{\partial t}\left(u_g\alpha_g\right)+\frac{\partial}{\partial x}\left(u_g^2\alpha_g\right)=-\frac{\alpha_g}{\rho_g}\frac{\partial p_i}{\partial x}-g\cos\theta H_g\frac{\partial\alpha_l}{\partial x}-\alpha_g g\sin\theta \tag{4}$$

where t and x are the respective time and axial coordinates, α is the volume fraction, u is the velocity, p is the pressure, ρ is the density, H is the hydraulic depth, g is the gravitational acceleration, β is the angle of inclination of the pipe; the subscripts l and g denote the liquid and gas, respectively, and the subscript i denotes the interface.

II.2. Computational Procedure

The governing Eqs. (1-4) are solved iteratively. The basic procedure is to solve the continuity equation of liquid, Eq. (1) for liquid volume fraction, and liquid and gas phase momentum equations are used to obtain liquid and gas phase velocity. However without an appropriate pressure fluid, the new calculated liquid volume fraction and liquid and gas velocity may not satisfy the gas continuity equation. The key lies in the handling of pressure term, which cannot be explicitly calculated from these four governing equations. However, a governing equation for pressure can be easily constructed by combining Eq. (1) and Eq. (2) to a total mass constraining equation

$$\frac{\partial}{\partial x}\left(u_g\alpha_g\right)+\frac{\partial}{\partial x}\left(u_l\alpha_l\right)=0 \tag{5}$$

Substituting the liquid and gas momentum equations into (5) yields a constraint on pressure. SIMPLE type of pressure correction scheme [10] is then used.

A finite volume method is employed to discretize the governing equations. A staggered grid (Fig. 2) is adopted to obtain a compact stencil for pressure [15]. On the staggered grids, the flow properties such as volume fraction, density and pressure are located at the center of the main control volume, and the liquid and gas velocities are located at the cell face of the main control volume.

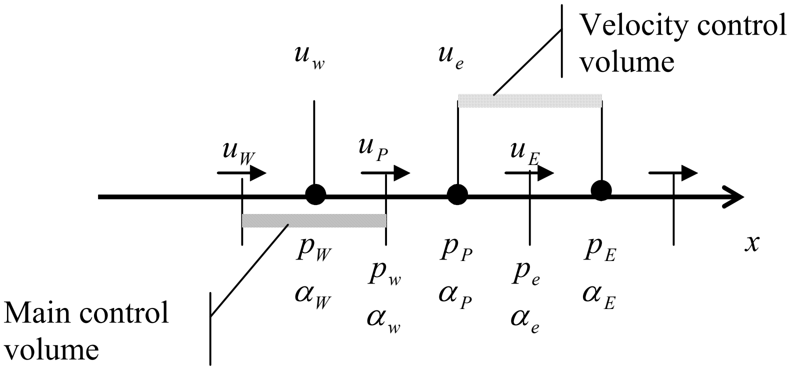

Fig. 2. Staggered grid arrangement in two-fluid model.

The Euler backward scheme is employed for the transient term. The discretized liquid continuity equation becomes

$$\frac{\Delta x}{\Delta t}\left((\alpha_l)_P-(\alpha_l)_P^0\right)+(\alpha_l u_l)_e-(\alpha_l u_l)_w=0 \tag{6}$$

where the superscript 0 represents the values of last time step. The symbol *P* refer to the center of main control volume, symbols *e* and *w* refer to the east face and west face of main control volume respectively. The liquid velocity at the cell face is known, and the volume fraction at the cell face can be evaluated using various interpolation schemes. Among them, central difference (CDS), 1st order upwind (FOU), 2nd order upwind (SOU) and QUICK schemes are commonly used. Eq. (2) for the gas phase is similarly discretized.

The liquid momentum equation is integrated on the velocity control volume. Using similar notations, one obtains

$$\begin{aligned}\frac{\Delta x}{\Delta t}\left((\alpha_l u_l)_P-(\alpha_l u_l)_P^0\right)+(u_l)_e(\alpha_l u_l)_e-(u_l)_w(\alpha_l u_l)_w &= \\ \frac{(\alpha_l)_P}{\rho_l}(p_w-p_e)+\left((\alpha_l)_w-(\alpha_l)_e\right)&H_l g\cos\theta-\Delta x(\alpha_l)_P g\sin\theta\end{aligned} \tag{7}$$

It is important to note that the interpolation schemes used in Eq. (7) must be exactly the same as those in Eq. (6) in order to reduce the dissipation and dispersion errors.

The gas phase momentum equation is similarly treated,

$$\begin{aligned}\frac{\Delta x}{\Delta t}\left((\alpha_g u_g)_P-(\alpha_g u_g)_P^0\right)+(u_g)_e(\alpha_g u_g)_e-(u_g)_w(\alpha_g u_g)_w &= \\ \frac{(\alpha_g)_P}{\rho_g}(p_w-p_e)+\left((\alpha_l)_w-(\alpha_l)_e\right)&H_g g\cos\theta-\Delta x(\alpha_g)_P g\sin\theta\end{aligned} \tag{8}$$

For the pressure correction scheme, Eq. (5) is integrated across the main control volume. The discretized equation is

$$(\alpha_g u_g)_e-(\alpha_g u_g)_w+(\alpha_l u_l)_e-(\alpha_l u_l)_w=0 \tag{9}$$

Because Eq. (5) is obtained by combining Eq. (1) and Eq. (2), the discretization of Eq. (9) should be exactly the same as that of Eqs. (2, 6). The final pressure equation is obtained by substituting two momentum equations, Eqs. (7, 8) to Eq. (9).

II.3. Characteristics and Ill-Posedness

Eqs. (1-4) form a system of 1st order PDEs and characteristic roots, λ, of the system can be found. If λ's are real, the system is hyperbolic. Complex roots imply an elliptic system which causes the two-fluid model system to become illposed because only initial conditions can be specified in the temporal direction. Any infinitesimal disturbance will cause the waves to grow exponentially without bound.

The characteristic roots of Eqs. (1-4) are

$$\lambda = \frac{\left(\frac{\rho_l u_l}{\alpha_l} + \frac{\rho_g u_g}{\alpha_g}\right) \pm \sqrt{\rho \frac{\rho_l - \rho_g}{\alpha_l'} g \sin\theta - \frac{\rho_l \rho_g}{\alpha_l \alpha_g}\left(u_g - u_l\right)^2}}{\frac{\rho_l}{\alpha_l} + \frac{\rho_g}{\alpha_g}} \tag{10}$$

When $g = 0$, Eq. (10) can have real roots only if $\lambda = u_v = u_l$. Otherwise, the two-fluid model is ill-posed (Gidaspow, 1974). If $g \neq 0$, the real roots (or well-posedness) requirement gives

$$\left(u_g - u_l\right)^2 < \left(\frac{\alpha_l}{\rho_l} + \frac{\alpha_g}{\rho_g}\right) \frac{\rho_l - \rho_g}{\alpha_l'} g \sin\theta \tag{11}$$

Eq. (11) gives the critical value for the two phase slip velocity beyond which the system becomes ill-posed. The two-fluid model well-posedness condition is exactly the same as from the IKH analysis on the two-fluid model [7].

II.4. Von Neumann Stability Analysis for Various Discretization Schemes

Von Neumann stability analysis is commonly used for analyzing the stability of a finite difference scheme.

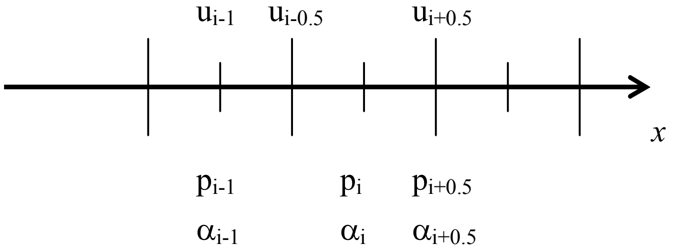

Fig. 3. Grids index number in staggered grid for von Neumann stability analysis.

In this derivation, the 1st order upwind (FOU) scheme is used as an example, and both liquid and gas velocities are assumed positive. Discretization of Eq. (6) using FOU leads to

$$\frac{\left(\alpha_l\right)_i^n - \left(\alpha_l\right)_i^{n-1}}{\Delta t}\Delta x + \left(\left(u_l\right)_{i+\frac{1}{2}}^n \left(\alpha_l\right)_i^n - \left(u_l\right)_{i-\frac{1}{2}}^n \left(\alpha_l\right)_{i-1}^n\right) = 0 \tag{12}$$

Splitting the variables into base value and disturbances, the linearized equation for the disturbance α_l is

$$\frac{\left(\hat{\alpha}_l\right)_i^n - \left(\hat{\alpha}_l\right)_i^{n-1}}{\Delta t}\Delta x + \left(\alpha_l\left(\left(\hat{u}_l\right)_{i+\frac{1}{2}}^n - \left(\hat{u}_l\right)_{i-\frac{1}{2}}^n\right) - u_l\left(\left(\hat{\alpha}_l\right)_i^n - \left(\hat{\alpha}_l\right)_{i-1}^n\right)\right) = 0 \tag{13}$$

where “^” denotes disturbance values. Expressing disturbances as

$$\left(\hat{\alpha}_l\right)_i^n = \varepsilon E^n e^{Ikx} \tag{14}$$

$$\left(\hat{u}_l\right)_i^n = \varepsilon_l E^n e^{Ikx} \tag{15}$$

$$\left(\hat{u}_v\right)_i^n = \varepsilon_v E^n e^{Ikx} \tag{16}$$

where *E* is a common amplitude factor, *k* is the wavenumber, and *I* represents imaginary unit. Eq. (13) is simplified to

$$\varepsilon\left(\frac{\Delta x}{\Delta t}\left(1-G^{-1}\right)+u_l\left(1-e^{-I\phi}\right)\right)+\varepsilon_l\alpha_l\left(e^{\frac{1}{2}I\phi}-e^{-\frac{1}{2}I\phi}\right)=0 \tag{17}$$

where *G* is the amplification factor:

$$G=\frac{E^n}{E^{n-1}} \tag{18}$$

and ϕ is phase angle:

$$\phi = k\cdot\Delta x \tag{19}$$

defined over $[0,\pi]$ which represents all the resolvable wave components in the computational domain for the given grid. Short waves correspond to the region near $\phi=\pi$

The wave growth equation for the gas phase mass conservation equation is similarly obtained:

$$\varepsilon\left(\frac{\Delta z}{\Delta t}\left(1-G^{-1}\right)+u_g\left(1-e^{-I\phi}\right)\right)-\varepsilon_g\alpha_g\left(e^{\frac{1}{2}I\phi}-e^{-\frac{1}{2}I\phi}\right)=0 \tag{20}$$

For the liquid momentum equation, Eq. (10) is discretized with the FOU scheme to

$$\begin{aligned}&\frac{\left(u_l\right)_{i+\frac{1}{2}}^n\left(\alpha_l\right)_{i+\frac{1}{2}}^n-\left(u_l\right)_{i+\frac{1}{2}}^{n-1}\left(\alpha_l\right)_{i+\frac{1}{2}}^{n-1}}{\Delta t}\Delta x+\left(\left(u_l\right)_{i+1}^n\left(\alpha_l u_l\right)_{i+\frac{1}{2}}^n-\left(u_l\right)_i^n\left(\alpha_l u_l\right)_{i-\frac{1}{2}}^n\right)\\&=\frac{\left(\alpha_l\right)_{i+\frac{1}{2}}^n}{\rho_l}\left(\left(p\right)_i^n-\left(p\right)_{i+1}^n\right)+g\cos\theta H_l\left(\left(\alpha_l\right)_i^n-\left(\alpha_l\right)_{i+1}^n\right)-\Delta x\rho_l\left(\alpha_l\right)_{i+\frac{1}{2}}^n g\sin\theta\end{aligned} \tag{21}$$

which is subsequently linearized and simplified with the aid of the liquid mass conservation equation,

$$\begin{aligned}&\frac{\Delta x}{\Delta t}\left(\rho_l\left(\left(\hat{u}_l\right)_{i+\frac{1}{2}}^n-\left(\hat{u}_l\right)_{i+\frac{1}{2}}^{n-1}\right)\right)+\rho_l u_l\left(\left(\hat{u}_l\right)_{i+\frac{1}{2}}^n-\left(\hat{u}_l\right)_{i-\frac{1}{2}}^n\right)\\&=\left(\hat{p}_i^n-\hat{p}_{i+1}^n\right)+\rho_l g\cos\theta\frac{H_l}{\alpha_l}\left(\left(\hat{\alpha}_l\right)_i^n-\left(\hat{\alpha}_l\right)_{i+1}^n\right)\end{aligned} \tag{22}$$

For the gas phase, the velocity disturbance is governed by

$$
\begin{aligned}
&\frac{\Delta x}{\Delta t}\left(\rho_g\left(\left(\hat{u}_g\right)^n_{i+\frac{1}{2}}-\left(\hat{u}_g\right)^{n-1}_{i+\frac{1}{2}}\right)\right)+\rho_g u_g\left(\left(\hat{u}_g\right)^n_{i+\frac{1}{2}}-\left(\hat{u}_g\right)^n_{i-\frac{1}{2}}\right)\\
&\qquad=\left(\hat{p}^n_i-\hat{p}^n_{i+1}\right)+\rho_g g\cos\theta\frac{H_g}{\alpha_g}\left(\left(\hat{\alpha}_l\right)^n_i-\left(\hat{\alpha}_l\right)^n_{i+1}\right)
\end{aligned}
\tag{23}
$$

The pressure term can be canceled by combining Eqs. (22-23),

$$
\begin{aligned}
&\varepsilon\left(\rho_l-\rho_g\right)g\cos\beta\frac{H_l}{\alpha_l}\left(e^{\frac{1}{2}I\phi}-e^{-\frac{1}{2}I\phi}\right)\\
&+\varepsilon_l\left(\frac{\Delta z}{\Delta t}\rho_l\left(1-G^{-1}\right)+\rho_l u_l\left(1-e^{-I\phi}\right)\right)-\varepsilon_g\left(\frac{\Delta z}{\Delta t}\rho_g\left(1-G^{-1}\right)+\rho_g u_g\left(1-e^{-I\phi}\right)\right)=0.
\end{aligned}
\tag{24}
$$

Eqs. (17, 20, 24) can be written in the form of an amplification matrix. Non-trivial solutions for $\left(\varepsilon,\varepsilon_g,\varepsilon_l\right)^T$ exist only when the determinant of the matrix is zero. Hence,

$$
a\left(G^{-1}\right)^2+b\left(G^{-1}\right)+c=0 \tag{25}
$$

where

$$
a=\rho\,, \tag{26a}
$$

$$
b=-2\left(\frac{\rho_g}{\alpha_g}\left(1+CFL_g\Delta(\phi)\right)+\frac{\rho_l}{\alpha_l}\left(1+CFL_l\Delta(\phi)\right)\right), \tag{26b}
$$

$$
\begin{aligned}
c=&\frac{\rho_g}{\alpha_g}\left(1+CFL_g\Delta(\phi)\right)^2+\frac{\rho_l}{\alpha_l}\left(1+CFL_l\Delta(\phi)\right)^2\\
&+\left(\frac{\Delta t}{\Delta x}\right)^2\left(\rho_l-\rho_g\right)g\cos\theta\frac{H_l}{\alpha_l}\left(4\sin^2\left(\frac{\phi}{2}\right)\right),
\end{aligned}
\tag{26c}
$$

where CFL are Courant number

$$
CFL_l=\frac{\Delta t}{\Delta x}u_l \text{ and } CFL_g=\frac{\Delta t}{\Delta x}u_g \tag{27}
$$

The values of $\Delta(\phi)$ are given in Table 1. From Eq. (25), the amplification factor can be easily found,

$$
G=\frac{2a}{-b\pm\sqrt{b^2-4ac}} \tag{28}
$$

Stability requires $|G|\le 1$ for all ϕ.

Table. 1. $\Delta(\phi)$ for different numerical schemes.

Scheme	$\Delta(\phi)$
1st order upwind	$1-e^{-I\phi}$
Central difference	$\dfrac{e^{I\phi}-e^{-I\phi}}{2}$
2nd order upwind	$\dfrac{3-4e^{-I\phi}+e^{-2I\phi}}{2}$
QUICK	$\dfrac{3e^{I\phi}+3-7e^{-I\phi}+e^{-2I\phi}}{8}$

II.5. Inviscid Kelvin-Helmholtz (IKH) Analysis

IKH analysis provides a stability condition for the two-fluid model as well as useful information on the growth rate of disturbance in the two-fluid model. Eqs. (1-4) are linearized and substituted for the perturbed liquid volume fraction, liquid and gas phase velocities, and pressure in the form of $\varepsilon \exp(I(\omega t - kx))$ in which ε is the amplitude, ω is the angular frequency, and *k* is the wavenumber. The following system is obtained for the disturbance amplitude:

$$\begin{vmatrix} \omega - u_l k & -\alpha_l k & 0 & 0 \\ \omega - u_g k & 0 & \alpha_g k & 0 \\ -k\dfrac{H_l}{\alpha_l} g\cos\theta & \omega - u_l k & 0 & \dfrac{k}{\rho_l} \\ -k\dfrac{H_l}{\alpha_l} g\cos\theta & 0 & \omega - u_g k & \dfrac{k}{\rho_g} \end{vmatrix} \begin{vmatrix} \varepsilon \\ \varepsilon_l \\ \varepsilon_g \\ \varepsilon_p \end{vmatrix} = 0 \tag{29}$$

The dispersion relation is obtained as:

$$c = \frac{\omega}{k} = \frac{\left(\dfrac{\rho_l u_l}{\alpha_l} + \dfrac{\rho_g u_g}{\alpha_g}\right) \pm \sqrt{\rho \dfrac{\rho_l - \rho_g}{\alpha_l'} g\sin\theta - \dfrac{\rho_l \rho_g}{\alpha_l \alpha_g}\left(u_g - u_l\right)^2}}{\dfrac{\rho_l}{\alpha_l} + \dfrac{\rho_g}{\alpha_g}} \tag{30}$$

where *c* is the wave speed. It is note that the negative imaginary part of ω determines growth rate of perturbation wave in two-fluid model. Eq. (30) is identical to Eq. (10), only with □being replaced by *c*. Details of IKH analysis can be found in [7].

III. Results and Discussions

III.1. Computational Stability Assessment based on von Neumann Stability Analysis

Comparison of stability of the 1st order upwind, 2nd order upwind, central difference, and QUICK schemes are conducted first for flow conditions before near, and after the instability.

It is well known that for ordinary convection-diffusion equations the 1st order upwind scheme is less accurate with high numerical diffusion, and high order schemes, such as SOU, CDS, and QUICK, have lower numerical diffusion. In this study, for illustration purposes, water and air are considered and the pipe diameter is taken to be 0.078m. The computational domain is 1m long, the grid number is N = 200. The pipe incline angle is θ is 0. The unperturbed values are: $a_l = 0.5$, $u_l = 1 m/s$, $u_g = 17 m/s$ and $CFL_l = 0.1$. Stability condition based on Eq. (10) or (30) for the above parameters is $\Delta U = u_g - u_l < 16.0768$. Thus, the two-fluid model for this condition is well-posed. It serves as an ideal testing case to assess the performances of various schemes since the system is quite close to being ill-posed. There are two values of G given by Eq. (28) and the larger one determines the instability; so that only the larger growth rate is used here.

Fig. 4 compares the amplification factors *G* of four discretization schemes. The solid line is the amplification factor by IKH analysis (*G* = 1). The dotted line is for the CDS scheme. It is slightly lower than one but quite close to one with a slight diffusion error at high wavenumber range. This implies the CDS is an ideal scheme to compute the two-fluid model. The dashed line is for the FOU scheme which possesses excessive numerical diffusion at high *k*. Furthermore, $G > 1$ at low *k*. Thus the computation using FOU is unstable under this flow condition. The dashed and dotted line is for the SOU scheme. Although SOU is regarded as a better scheme than FOU with less numerical diffusion, its performance in the two-fluid model is very poor. For large *k*, the numerical diffusion of SOU is much larger than that of FOU. For small *k*, the amplification factor of SOU is much larger than that of FOU. Dashed double dotted line is the amplification factor of the QUICK scheme. Its numerical diffusion at high *k* is lower than that of FOU and SOU, but it is still much larger than that of CDS. At small *k*, *G* is slightly larger than 1 indicating that QUICK is unstable as well. The reason that the amplification factor of CDS is close to the analytical amplification factor is probably due to a lack of 2nd order diffusion error and low dispersion error. Compared with SOU, numerical diffusion of FOU scheme is much higher and dispersion is slightly lower. Overall performance of FOU is better than that of SOU which suggests that the dispersion error in the two-fluid model is much more important than it is in the simple convection-diffusion equation. The interpolation of QUICK is essentially linear interpolation with the upwind correction. Therefore its numerical diffusion and stability is worse than that of CDS, but better than that of FOU and SOU.

Next, the effect of the slip velocity $\Delta U = u_g - u_l$. on the numerical stability is discussed. Fig. 5 shows the amplification factors of the CDS scheme for a range of values of ΔU .

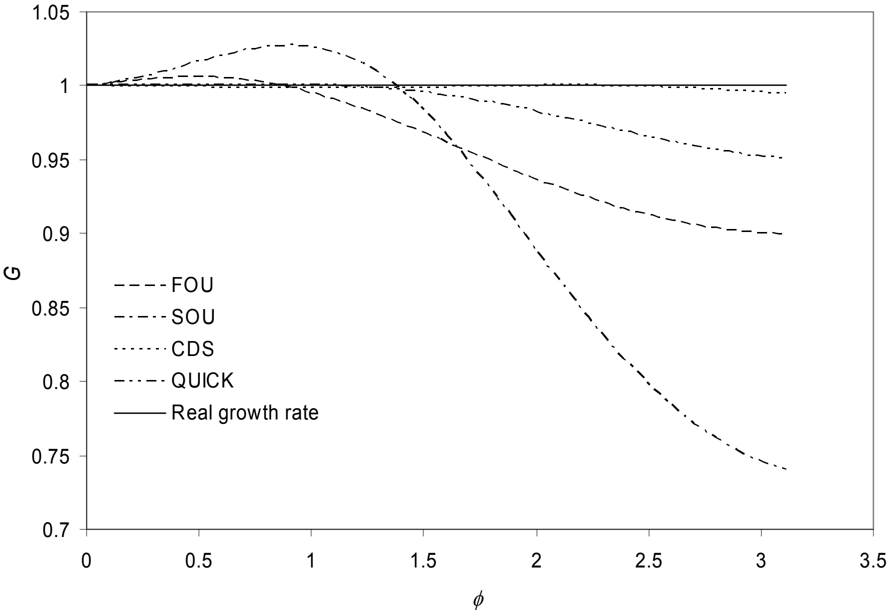

Fig. 4. Comparisons of amplification factors of numerical schemes. $N = 200$, $\theta = 0$, $a_l = 0.5$, $u_l = 1 m/s$, $u_g = 17 m/s$ and $CFL_l = 0.1$.

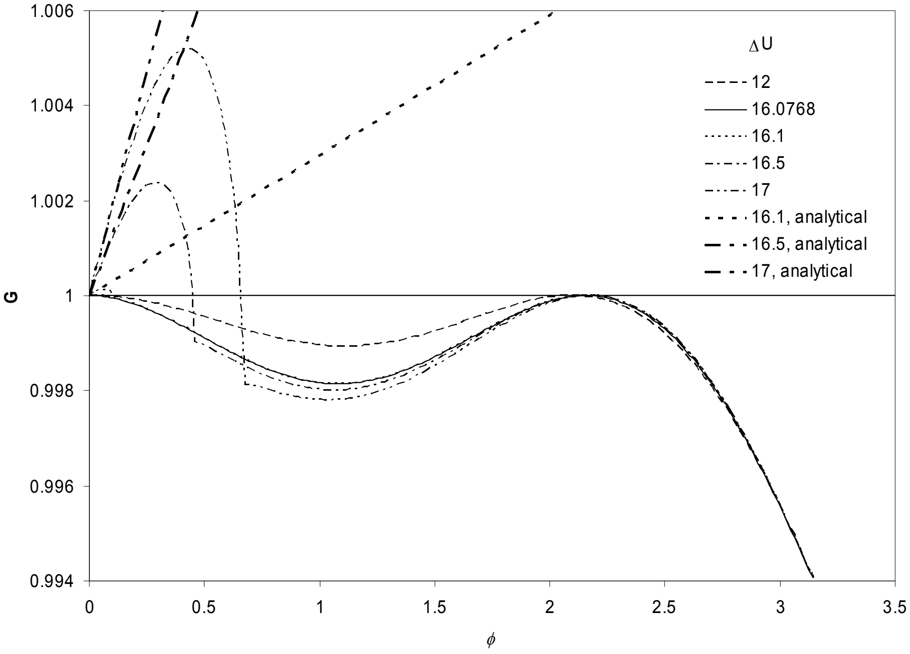

Fig. 5. Amplification factor of CDS scheme at different $\Delta U = u_g - u_l$. $N = 200$, $\theta = 0$, $a_l = 0.5$, $u_l = 1 m/s$, and $CFL_l = 0.1$.

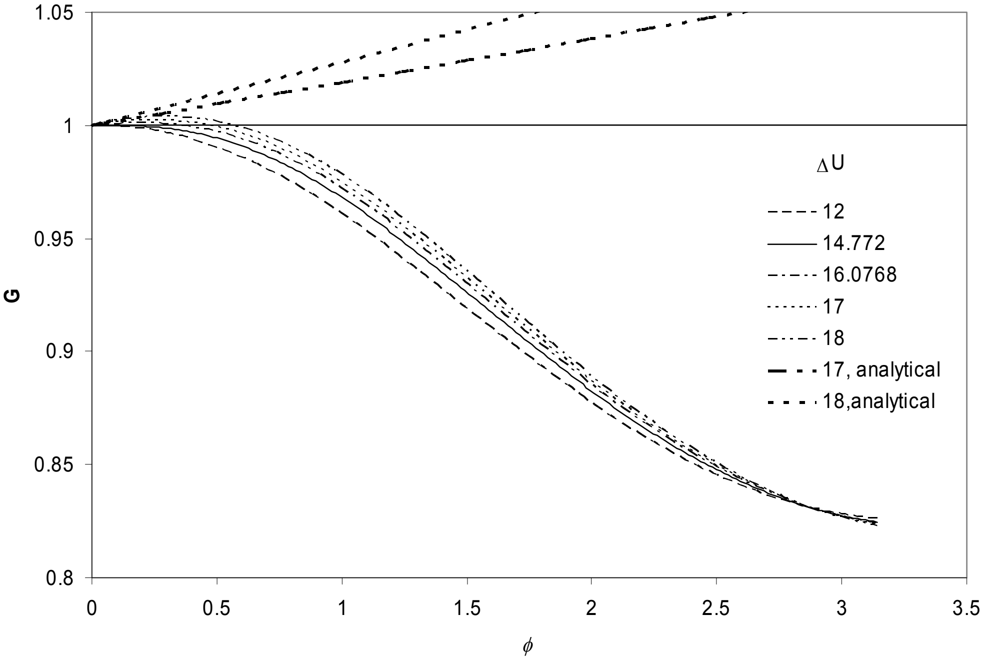

Fig. 6. Amplification factor of FOU scheme at different $\Delta U = u_g - u_l$. $N = 200$, $\theta = 0$, $a_l = 0.5$, $u_l = 1 m/s$, and $CFL_l = 0.1$.

When ΔU is smaller than that given by the IKH stability, the amplification factors of all the harmonics in the computational domain are less than one. However, if ΔU is higher than the IKH stability criteria, the two-fluid model is analytically ill-posed, and *G* for small *k* exceeds one, as shown by the curve for $\Delta U = 16.1 m/s$ in Fig. 5. From numerical results, a neutral stability condition of CDS is found to be near $\Delta U = 16.0773 m/s$ for the condition used in Fig. 5, which is quite close to IKH stability condition of 16.0768 m/s. As ΔU further increases, *G* increases too. The range of unstable harmonic wavenumber becomes wide. The amplification factor of CDS scheme matches that of IKH only at very low wavenumber. In the high *k* range, numerical damping causes *G* to be much lower than one.

Fig. 6 shows the amplification factors of the FOU scheme at different values of ΔU. Unlike the CDS scheme, there is no significant change of *G* when ΔU varies. Numerical results indicate that the neutral stability for the condition shown in Fig. 6 is $\Delta U = 14.772 m/s$, which is much lower than the analytical value of $16.0768/m/s$. The behavior of SOU and QUICK scheme is similar to the FOU. The stability condition for SOU is $\Delta U = 13.73 m/s$ and for QUICK it is $\Delta U = 16.03 m/s$.

Fig. 7 shows the effect of the liquid velocity on the amplification factors of CDS with $\Delta U = 16 m/s$ and $\Delta t/\Delta x = 0.1$. For $u_l = 0.01 m/s$ and $u_l = 0.1 m/s$, *G* decreases monotonically with the phase angle. Damping appears at high *k*. When u_l increases, *G* at high k range rises significantly, leaving a high damping saddle at the intermediate *k* range. On the other hand, if ΔU is constant, CFL_g / CFL_l is much larger than one when u_l is small so that it is hard to keep both CFL_l and CFL_g in the moderate range, which is essential to the computational stability.

Fig. 8 shows the effect of u_l on G for the FOU scheme with $\Delta U = 16 m/s$ and $\Delta t / \Delta x = 0.1$. The behavior of FOU is much different with that of CDS. When l u is small, most harmonics are unstable. For a larger u_l , excessive numerical diffusion makes the computations stable.

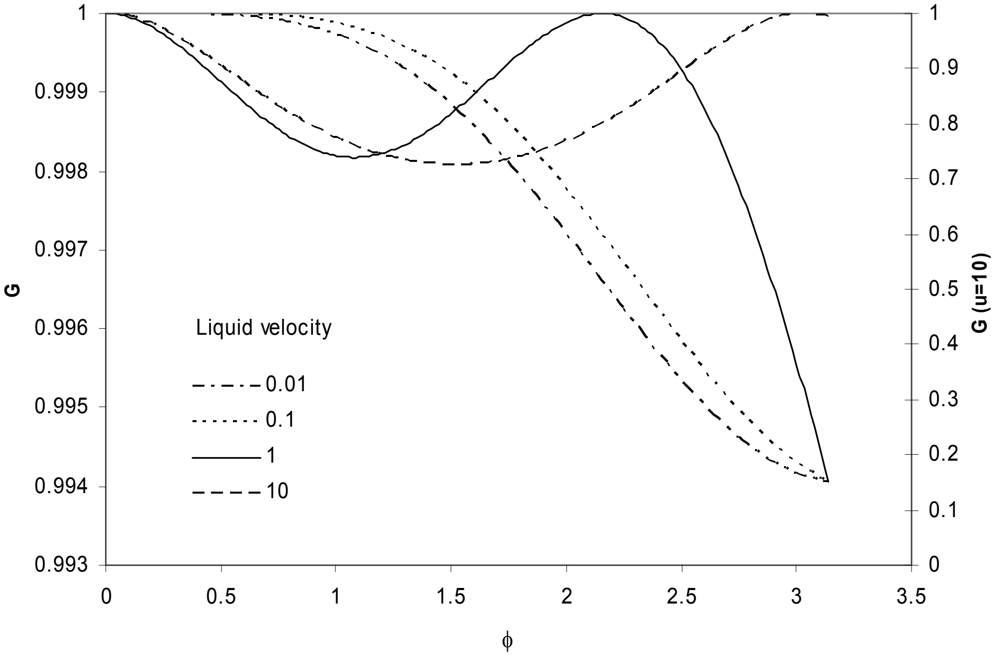

Fig. 7. Amplification factor of CDS scheme at different u_l. $N = 200$, $\Delta U = 16 m/s$, $\theta = 0$, $a_l = 0.5$, and $\Delta t / \Delta x = 0.1$.

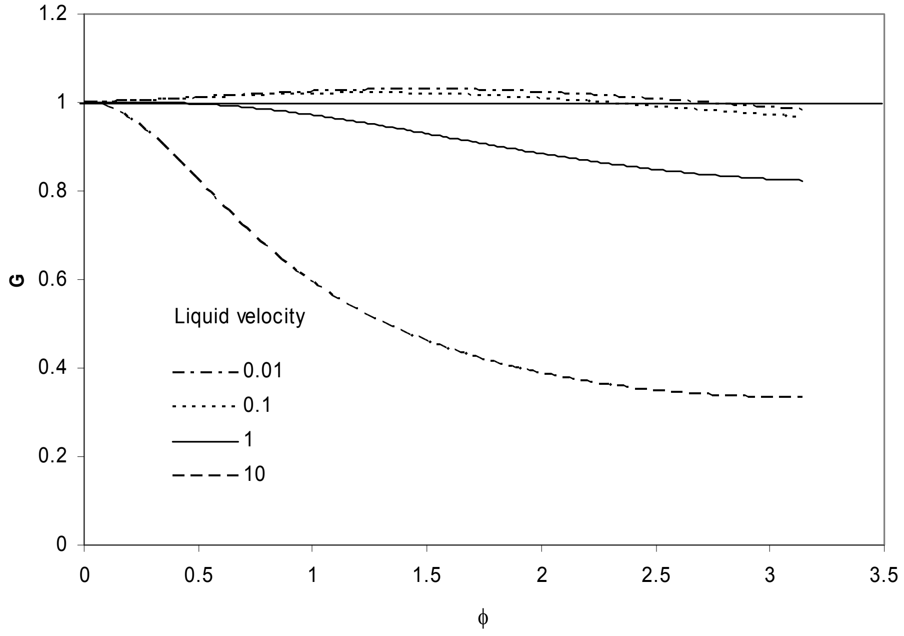

Fig. 8. Amplification factor of FOU scheme at different u_l. $N = 200$, $\Delta U = 16 m/s$, $\theta = 0$, $a_l = 0.5$, and $\Delta t/\Delta x = 0.1$.

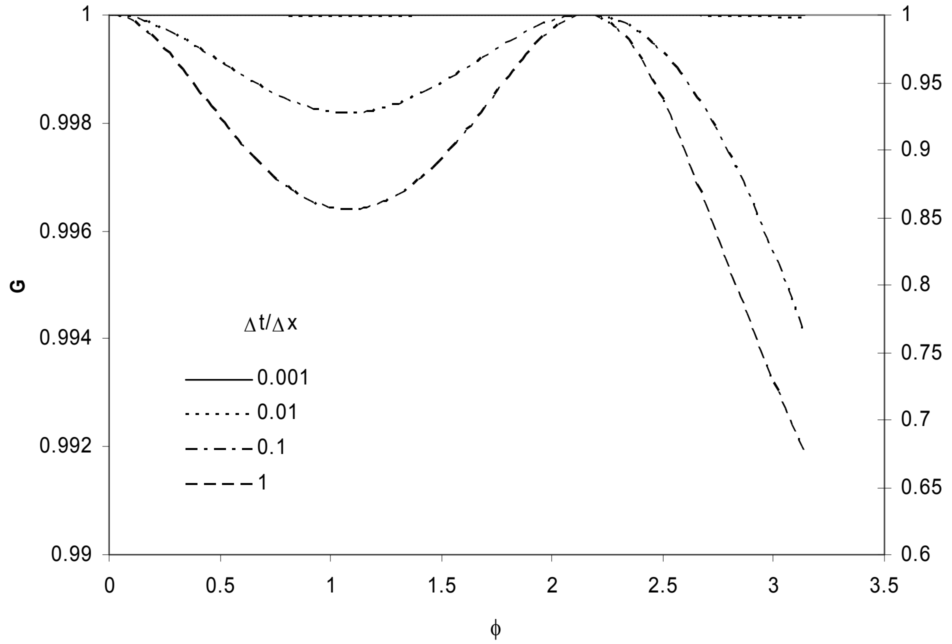

Fig. 9. Amplification factor of CDS scheme at different $\Delta t/\Delta x$. $N = 200$, $u_l = 1 m/s$, $\Delta U = 16 m/s$, $\theta = 0$, and $a_l = 0.5$.

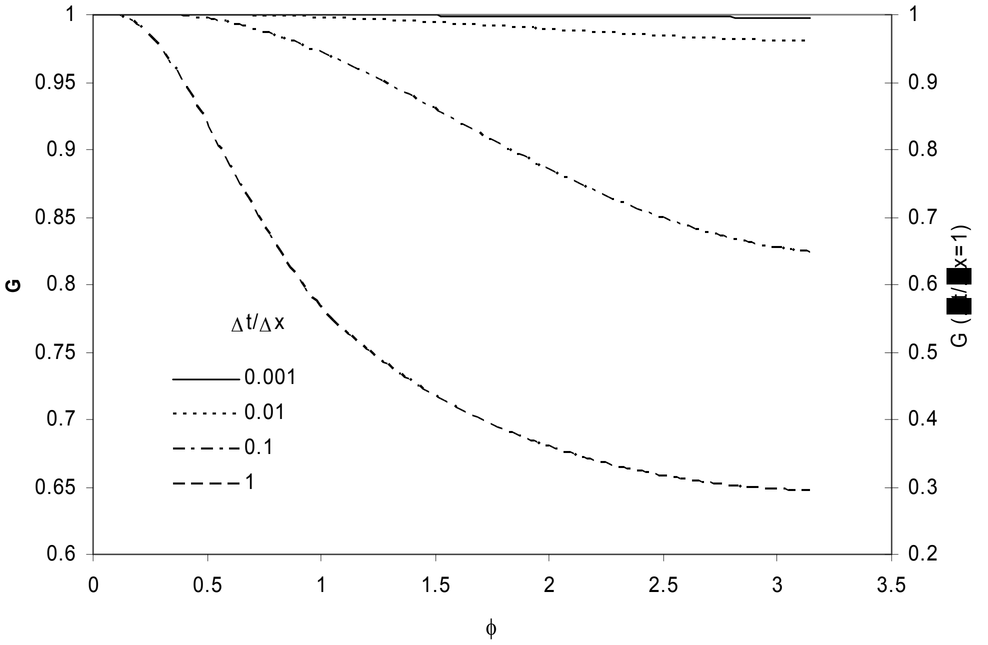

Fig. 10. Amplification factor of FOU scheme at different $\Delta t/\Delta x$. $N = 200$, $u_l = 1 m/s$, $\Delta U = 16 m/s$, $\theta = 0$, and $a_l = 0.5$.

Figs. 9-10 show the effect of $\Delta t/\Delta x$ on *G* for the CDS and FOU schemes. Both show increasing numerical diffusion with increasing $\Delta t/\Delta x$ resulting in a decrease in *G*. This can be explained by examining Eq. (26c), where the last term is related to the gravitational effect. It is well known that gravity stabilizes the flow. Thus increasing $\Delta t/\Delta x$ computationally helps the stability.

IV. Conclusions

Numerical instability for the incompressible two-fluid model near the ill-posed condition is investigated for various discretization schemes, while the pressure correction method is used to obtain the pressure. The von Neumann stability analysis is carried out to obtain the amplification factor of a small disturbance in the discretized system. The central difference scheme has the best stability characteristics in handling the two-fluid model, followed by the QUICK scheme. It is quite interesting to note that the excessive numerical diffusion in the 1st order upwind scheme seems to promote the numerical instability in comparison with the central difference scheme. Despite its nominal 2nd order accuracy and popularity, the 2nd order upwind scheme is much more unstable than the 1st order upwind scheme for solving two-fluid model equations. Different discretization schemes for the convection term with varying degrees of the numerical diffusion and dispersion cannot cause a delay in the stability; they often promote instability in the two-fluid model.

The analytically predicted wave amplitude growth is also compared with that obtained from carefully implemented computations using various discretization schemes for the convection term. Excellent agreement between the numerical results and the predicted results is obtained for the growth of the wave amplitude and the dominant wavenumber when the computation becomes unstable. The relation between the computational instability and the ill-posedness is discussed. In the presence of the smallamplitude long-wave disturbance, whose amplitude is much larger than the machine round-off error, the growth of the disturbance exactly matches the prediction of the von Neumann stability analysis when the computational stability condition is violated. In the meantime, a shorter wave emerges from the machine round-off error, and eventually dominates the entire disturbance, which causes the computation to blow up. This computational instability is widely interpreted as the result of ill-posedness of the two-fluid model. The results of the present study suggest that the computational instability is largely the property of the discretized two-fluid model and is strongly affected by the inherent ill-posedness of the two-fluid model differential equations. Introduction of numerical diffusion and/or dispersion can significantly change the instability of the discretized system; however, such steps often yield unfavorable computational results. For solving two-fluid models, central difference is recommended since it is much more accurate and dependable than other schemes investigated.

V. Patents, Publications, Presentations and Students from Research

Publications

1. Liao, J., Mei, R., Klausner, J.F. 2005, “A Study on Numerical Instability of Inviscid Two-Fluid Model Near Ill-Posedness Condition”, Proceedings of the ASME Summer Heat Transfer Conference, San Francisco, CA.

Students from Research

Jun Liao: Recived PhD. Employed with Westinghouse Electric Company, Monroeville, PA.

VI. Acknowledgements

This Work was supported by NASA Glenn Research Center under contract (NAG3-2750) and NASA Kennedy Space Center.

VII. References

1. Wallis, G.B., 1969, One-Dimensional Two-Phase Flow, McGraw-Hill, New York.
2. Ishii, M., 1975, Thermo-Fluid Dynamic Theory of Two Phase Flow, Eyrolles, Paris.
3. Gidaspow, D., 1974, “Modeling of Two Phase Flow”, Proceedings of the Fifth International Heat Transfer Conference, VII, pp. 163.
4. Jones, A.V., and Prosperettii, A., 1985, “On the Stability of First-Order Differential Models for Two-Phase Flow Prediction”, International Journal of Multiphase Flow, 11, pp. 133-148.
5. Song, J.H., and Ishii, M., 2000, “The Well-Posedness of Incompressible One-dimensional Two-Fluid Model”, International Journal of Heat and Mass Transfer, 43, pp. 2221-2231.
6. Issa, R.I., and Kempf, M.H.W., 2003, “Simulation of Slug Flow in Horizontal and Nearly Horizontal Pipes with the Two-Fluid Model”, International Journal of Multiphase Flow, 29, pp. 69-95.
7. Barnea, D., and Taitel, Y., 1994, “Interfacial and Structural Stability of Separated Flow”, International Journal of Multiphase Flow, 20, Suppl., pp. 387-414.
8. Brauner, N., and Maron, D.M., 1992, “Stability Analysis of Stratified Liquid-Liquid Flow”, International Journal of Multiphase Flow, 18, pp. 103-121.
9. Chan, A.M.C., and Banerjee, S., 1981, “Refilling and Rewetting of a Hot Horizontal Tube part II: Structure of a Two-Fluid Model”, Journal of Heat Transfer, 103, pp. 287- 292.
10. Patankar, S.V., 1980, “Numerical Heat Transfer and Fluid Flow,” McGraw-Hill, New York.

11. Issa, R.I., and Woodburn, P.J., 1998, “Numerical Prediction of Instabilities and Slug Formation in Horizontal Two-Phase Flows”, 3rd International Conference on Multiphase Flow, ICMF98, Lyon, France.
12. Lyczkowski, R.W., Gidaspow, D., Solbrig, C.W., and Hughes, E.D., 1978, “Characteristics and Stability Analyses of Transient One-Dimensional Two-Phase Flow Equations and Their Finite Difference Approximations”, Nuclear Science and Engineering, 66, pp. 378-396.
13. Stewart, B.H., 1979, Stability of Two-Phase Flow Calculation Using Two-Fluid Models, Journal of Computational Physics, 33, pp. 259-270.
14. Ohkawa, T., and Tomiyama, A., 1995, “Applicability of High-Order Upwind Difference Methods to the Two-Fluid Model”, Advances in Multiphase Flow, Elsevier Science, pp. 227-240.
15. Ferziger, J.H., and Peric, M., 1996, Computational Methods for Fluid Dynamics, Springer, Berlin.
16. Hirsch, C., 1988, “Numerical Computation of Internal and External Flows, volume I: Fundamentals of Numerical Discretization”, John Wiley & Sons, New York.
17. Liao, J., 2005, “Modeling Two-Phase Transport During Cryogenic Chilldown in a Pipeline”, Ph.D Dissertation, University of Florida.

Sub-Task 3: Numerical Investigation of Cryogenic Fluid Transport in Horizontal Pipelines During Turbulent Chilldown Process

Abstract

A numerical model has been proposed to predict the chilldown history of pipe wall temperature during the transport of cryogenic fluid in horizontal pipeline under unsteady high mass flow rate regime. The model then is compared with existing experimental data for verification. There is very good agreement between simulation results and experiment data of Jackson et al. (2005) measured at the four locations on the pipelines. The proposed model has captured important heat transfer features between phases and between liquid and pipe wall, and also provides a very inexpensive tool for predicting thermal history during chilldown process.

Nomenclature

c_p	heat capacity
D	inner pipe diameter
d	thickness of pipe wall
g	gravity
h	heat transfer coefficient
h_{pool}	pool boiling heat transfer coefficient
h_{conv}	convection boiling heat transfer coefficient
h_{fg}	latent heat
k	thermal conductivity
p	pressure
Nu	Nusselt number
Re	Reynolds number
S	suppression factor
T	temperature
T_{Lei}	Leidenfrost temperature
T_{crit}	transition temperature from nucleate boiling to convection heat transfer
T_o	ambient temperature
t	time
U	velocity

Greek Symbols

z, r, and φ	cylindrical coordinates
α	liquid volume fraction
δ	vapor film thickness
μ	viscosity
θ	dimensionless temperature
σ	liquid surface tension

Subscripts

i and o	inner and outer pipe
l	liquid
v	vapor
w	wall
sat	saturated
fb	film boiling
nb	nucleate boiling

I. Introduction

I.1. Literature review of experimental and numerical studies on cryogenic Chilldown

Cryogenic chilldown process is encountered in many engineering applications. One of the most important things is the transport of cryogenic propellants in internal fuel tanks of space shuttle in space shuttle launch facilities through a complex pipeline system. To maintain liquid fuel entering the fuel tanks, a cryogenic chilldown prior to the filling is required to cool the pipe wall so that its temperature goes down to the saturated temperature of the core cryogenic liquid fuel.

Cryogenic chilldown process has intrinsic complication due to the interactions among two phases of the cryogenic fluid and the solid. It is a complicated problem due to the coupling between fluid dynamics and heat transfer. The studies of cryogenic chilldown process emerged during 60's decade parallel to the development of space technology. The so-called "space race" between developed countries during these times has promoted researches involving cryogenic engineering, both experimentally and computationally.

Several experimental studies of cryogenic fluids were conducted in the early of 1960s. Burke et al. [1] studied chill down in various stainless-steel lines by flowing liquid nitrogen. A model to predict chill down time was developed by treating the entire line as a single control volume. They have assumed an infinite heat transfer rate from the cryogenic fluid to the pipe wall. The effects of flow regimes on the heat transfer rate were neglected. This system has provided a simple estimate of chill down time but lacked accuracy due to the averaging of fluid properties and flow rates over the chill down time. The experimental results reported by Bronson et al. [2] shown that stratified flow is prevalent during cryogenic chilldown system.

Flow regimes and heat transfer regimes in horizontal pipe during cryogenic chilldown were also studied by Chi and Vetere [3]. Several flow regimes were identified: single vapor phase, mist flow, slug flow, annular flow, bubbly flow, single liquid phase. Heat transfer regimes were also identified as single phase vapor convection, film boiling, nucleate boiling, and single phase liquid convection. Graham et al. [4] correlated heat transfer coefficient and pressure drop with Martinelli number based on their experimental data.

Chi [5] developed a one-dimensional model for energy equations of the liquid and the wall, based on the film boiling heat transfer between the wall and fluid. This model of the chilldown was developed under the assumptions of constant flow rate, constant heat transfer coefficient, constant fluid properties, homogeneous fluid flow, and film-boiling-dominated heat transfer. An empirical equation for predicting chilldown time and temperature was proposed. The assumption of constant flow rate is not very realistic because usually the transfer line inlet and exit pressures are set while the flow rate may vary greatly according to the flow condition. The assumptions of constant heat transfer coefficient and constant fluid properties are highly restrictive, but can provide useful estimates of temperature and chill down time.

Steward [6] numerically developed a homogeneous flow model for cryogenic chilldown using finite difference formulation. The model treated the cryogenic fluid as a homogeneous mixture. The continuity, momentum and energy equations were solved simultaneously to obtained density, pressure and temperature of the mixture. Various heat transfer regimes were considered: film boiling, nucleate boiling and single-phase convection. Heat transfer coefficients were determined using superposition of single-phase forced convection correlations and pool boiling correlations for both nucleate and film boiling. Correct modeling of flow film boiling is especially crucial with cryogenic hydrogen because film boiling occurs to as low as a tube wall to fluid saturation temperature difference of approximately 11K resulting in a large portion of the chill down occurring under film boiling.

The stratified flow regime, which is the prevalent flow regime in horizontal chilldown, was first studied by Chan and Banerjee [7-9]. They developed a separated flow model for the simulation of the quenching by a stratified flow in a hot horizontal pipe. Both phases were modeled using one-dimensional mass and momentum conservation equations. The wall temperature was computed using a two-dimensional transient heat conduction equation. Their prediction for the wall temperature agreed well with their experimental results. Although significant progress was made in handling the momentum equation, the heat transfer correlations employed were not as advanced.

Recently, Velat et al. [10] systematically conducted experiments involving cryogenic chilldown with liquid nitrogen in horizontal pipe. Their studies included a visual recording the chilldown process in a transparent Pyrex pipe (used to identify flow regimes and heat transfer regimes), collecting temperature histories at different positions of the wall in chilldown, and recording pressure drop along the pipe. Chung et al. [11] conducted similar study with nitrogen chilldown at relatively low mass flux and provided data needed to assess various heat transfer coefficients.

Liao et al. [12] developed an analytical model for film boiling heat transfer for stratified laminar flow of cryogenic fluid. By analytically solving the mass, momentum and energy equations in the vapor film layer, an analytic solution of the vapor film thickness is obtained. Then, the film boiling heat transfer in the vapor film layer is obtained simply by the ratio of the thermal conductivity and the thickness of the vapor film. This model is then tested with experimental data of Chung et al. [11] and some agreement is achieved.

Jackson et al. [13] conducted experiment with liquid nitrogen to measure the heat transfer coefficients in nucleate boiling regime during chilldown process. The recorded temperature history of the pipe wall and numerical study of the unsteady heat transfer through pipe wall are used to determine heat transfer coefficients which then are compared with well-known nucleate flow boiling heat transfer correlations of Gungor and Winterton, Kandlikar, Muller-Steinhagen, etc. However, due to the complication of the unsteady, high mass flux cryogenic flow, the predicted heat transfer coefficients obtained by this inverse technique do not agree well with current correlations.

I.2. Heat transfer regimes of cryogenic chilldown

A typical chilldown process involving several heat transfer regimes is shown in Fig. 1. Due to the large difference between temperature of the pipe wall (typically at laboratory temperature) and the cryogenic temperature of the entering liquid, film boiling occurs in which the liquid phase is supported on a thin vapor layer adjacent to the wall. As shown in Fig. 1, near the liquid front is the thin vapor film boiling. The knowledge of the heat transfer in the film boiling is limited because it is not the major interest of industrial applications and more importantly the experiment carrying out to capture the behavior at this stage is extremely difficult due to the high difference in temperature as mentioned above.

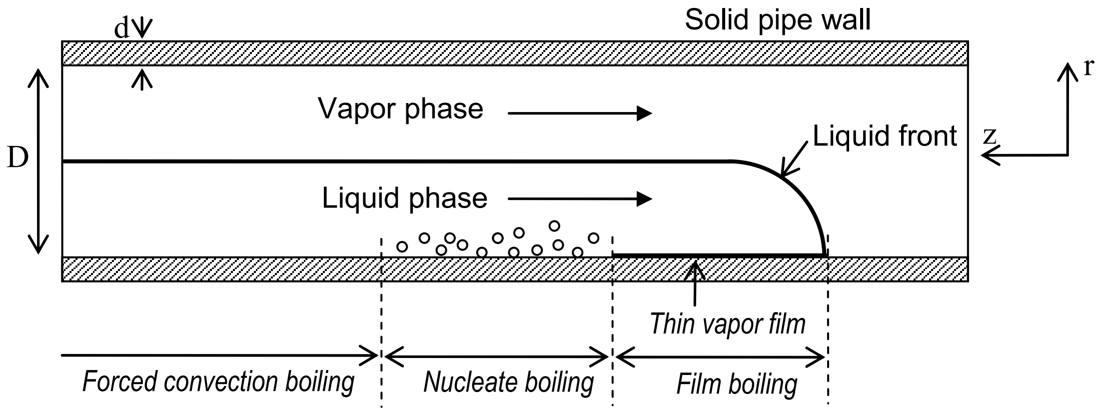

Fig. 1. Heat transfer regimes of cryogenic chilldown process inside a horizontal pipe.

There are several works from Bromley [14], Dougall and Rohsenow [15] and Laverty and Rohsenow [16] that showed experimental results on the vapor film boiling on vertical surfaces. Film boiling on horizontal surfaces was first studied also by Bromley [14] and the Bromley's correlation was widely used. Then, Breen and Westwater [17] modified Bromley's correlation to take into account the various changes in diameter of the horizontal tubes. Empirical correlations for cryogenic film boiling were also proposed by Hendrick et al. [18-19], Ellerbrock et al. [20], von Glahn [21]. Giarratano and Smith [22] gave a more detailed assessment of these correlations. All the correlations proposed above were constructed based on experiment for steady state cryogenic film boiling. Therefore, their validity for transient chilldown applications is still suspicious.

When the pipe wall chills down further, film boiling ceases and nucleate boiling occurs in which the temperature of the interior pipe wall falls below the Leidenfrost temperature. In this stage, the liquid phase comes into contact with the pipe wall. For simplification, it is often assumed that the switch from film boiling to the nucleate boiling is immediate, not passing through a transition boiling regime. The position from film boiling transitioning to the nucleate boiling is often called the rewetting front as the liquid phase stars to contact with the pipe wall. Normally, we utilize the Leidenfrost temperature as an indicator of the transition from the film boiling to the nucleate boiling.

There are numerous studies on the forced convection boiling heat transfer. A general correlation for saturated boiling was first introduced by Chen [23]. In this work, he developed a two-phase flow boiling correlation where the heat transfer coefficient was divided into a nucleate pool boiling coefficient and a bulk convective coefficient. Bennett and Chen [24] modified the Chen's correlation using a larger data set. They implemented a new correlation for the nucleate pool boiling suppression factor. The two-phase enhancement factor was still a function of the Lockhart-Martinelli two-phase multiplier. Gungor and Winterton [25] modified Chen's correlation and made the extension to subcooled boiling. They also introduced the enhancement and suppression factors for macro-convective heat transfer. Their expression for the pool boiling convective heat transfer coefficient included reduced pressure, molecular weight, and heat flux. Kutateladze [26] and Steiner [27] also provided correlations for cryogenic fluids in pool boiling and forced convection boiling. These correlations are applicable for cryogenic fluids since they are developed directly based on cryogenic conditions.

As the wall temperature decreases further over time or the wall superheat drops to a certain range, nucleate boiling is suppressed and heat transfer regime is governed by single phase forced convection [28], [32].

II. Formulation

To gain the fundamental insight into the thermal interaction between the cryogenic fluid and solid pipe wall and to predict chilldown process varies in time, various heat transfer coefficients must be evaluated. For heat transfer in solid pipe wall, we need to solve the diffusion equation to obtain temperature field and then obtain heat flux from inner pipe wall into the cryogenic liquid. The heat transfer between the cryogenic fluid and the wall is modeled using different heat transfer correlations depending on the operating heat transfer regime at a given location. These issues will be addressed in details in the following sections.

II.1. Heat transfer in solid pipe wall

The unsteady three-dimensional heat conduction equation in cylindrical coordinates in the solid pipe wall is as follows [29].

$$\rho_s c_{p,s} \frac{\partial T}{\partial t} = \frac{\partial}{\partial z}\left(k_s \frac{\partial T}{\partial z}\right) + \frac{1}{r}\frac{\partial}{\partial r}\left(r k_s \frac{\partial T}{\partial r}\right) + \frac{1}{r}\frac{\partial}{\partial \varphi}\left(\frac{k_s}{r}\frac{\partial T}{\partial \varphi}\right), \tag{1}$$

where ρ_s is the material density of the solid pipe wall, $c_{p,s}$ is the specific heat capacity and k_s is the thermal conductivity of the solid pipe wall, respectively. *T* is the temperature, *t* is the time variable and (r, φ, z) denote the cylindrical coordinates. Since the first term on the RHS of Eq. (1) is small compared with the other terms [29], it is therefore neglected. Eq. (1) becomes:

$$\rho_s c_{p,s} \frac{\partial T}{\partial t} = \frac{1}{r}\frac{\partial}{\partial r}\left(r k_s \frac{\partial T}{\partial r}\right) + \frac{1}{r}\frac{\partial}{\partial \varphi}\left(\frac{k_s}{r}\frac{\partial T}{\partial \varphi}\right) \tag{2}$$

Equation (2) can be further non-dimensionalized by using the following non-dimensional parameters:

$$\theta = \frac{T - T_{sat}}{T_w - T_{sat}},\ r^* = \frac{r}{d},\ c^*_{p,s} = \frac{c_{p,s}}{c_{p0}},\ k^* = \frac{k_s}{k_0},\ \rho^* = \frac{\rho_s}{\rho_0}$$

where T_{sat} is the saturated temperature of the cryogenic fluid, T_w is the temperature on the outer wall of the pipe, d is the thickness of the pipe wall. The subscript "0" denotes the properties at the reference temperature T_0. Then, Eq. (2) is transferred to:

$$\left(\frac{\rho_0 c_0 d^2}{k_0}\right)\rho^* c^* \frac{\partial \theta}{\partial t} = \frac{1}{r^*}\frac{\partial}{\partial r^*}\left(r^* k^* \frac{\partial \theta}{\partial r^*}\right) + \frac{1}{r^*}\frac{\partial}{\partial \varphi}\left(\frac{k^*}{r^*}\frac{\partial \theta}{\varphi}\right) \tag{3}$$

The boundary condition for the outer pipe wall is written as follows.

$$-k_s \frac{\partial T}{\partial r} = h_{out}\left(T_{out} - T_{amb}\right) \tag{4a}$$

where h_{out} is the heat transfer coefficient between the outer pipe wall with the surroundings. It is usual that h_{out} is very small as one wants to reach the insulated boundary condition. h_{out} is obtained by experimental measurement. T_{amb} is the ambient temperature and T_{out} is the temperature at the outer surface of the pipe.

The boundary condition for the inner pipe wall is as follows.

$$k_s \frac{\partial T}{\partial r} = h_{fb}\left(T_{in} - T_{sat}\right) \tag{4b}$$

where h_{fb} is the heat transfer coefficient between the inner pipe wall with the vapor film due to high wall superheat during the cryogenic chilldown process. The subscript *"fb"* stands for "film boiling". T_{in} is the temperature at the inner surface of the pipe. h_{fb} is a very important quantity since film boiling plays a major role in heat transfer between cryogenic liquid and solid pipe wall. Detailed computational approach for estimating h_{fb}, which is the major task of this work, is given in details in section II.2.2.1.

II.2. Heat transfer between cryogenic fluid and solid pipe wall

The cryogenic fluid entering the pipe firstly is in liquid phase. However, due to the high superheat from pipe wall, in which the pipe temperature usually is in room temperature, part of the cryogenic liquid vaporizes into vapor phase. Hence, the cryogenic fluid inside the pipe after initial setup comprises both liquid and vapor phases. Therefore, we need to calculate both heat transfer regimes between vapor phase and solid pipe wall and between liquid phase and solid pipe wall.

The heat transfer coefficient between vapor phase and solid pipe wall is computed via available correlation. However for the heat transfer between cryogenic liquid and solid pipe wall, as we already addressed above, comprises three stages: film boiling, nucleate boiling and forced convection boiling. Numerical investigation of heat transfer coefficient for nucleate boiling and forced convection boiling is not the main interest in this work; hence, we use available correlations with some modifications to compute these heat transfer regimes. The main issue here is to analytically and numerically investigate the heat transfer coefficient during film boiling regime since currently there exists no suitable correlation for the present problem.

II.2.1 Heat transfer between cryogenic vapor and solid pipe wall

Heat transfer between cryogenic vapor and solid pipe wall can be predicted by assuming that the vapor flow is fully developed convection vapor flow, i.e., we neglect the cryogenic liquid droplets entrained in the vapor flow which is due to the fact that the vapor flow is moving faster than the liquid flow. The heat transfer coefficient for single phase turbulent forced convection vapor flow is adopted from Dittus-Boelter's correlation [30] and is a given as follows.

$$h_v = 0.023 \operatorname{Re}_v^{0.8} \operatorname{Pr}_v^{0.4} \left(\frac{k_v}{D_v} \right) \tag{5}$$

Re_v and Pr_v is the vapor Reynolds number and Prandtl number respectively.

$$\operatorname{Re}_v = \frac{u_v D_v}{\mu_v} \tag{6}$$

$$\operatorname{Pr}_v = \frac{c_{p,v} \mu_v}{k_v} \tag{7}$$

Here u_v is the vapor velocity which is measured from the experiment, μ_v is the vapor viscosity, k_v is the vapor thermal conductivity, $c_{p,v}$ is the heat capacity of vapor phase and D_v is the hydraulic diameter of the vapor phase.

II.2.2. Heat transfer between cryogenic liquid and solid pipe wall

As we mentioned above, heat transfer regimes between cryogenic liquid and solid wall consists of film boiling, nucleate boiling and forced convective boiling. The transition from one to another depends on many parameters and flow conditions. For simplicity, we exploit the Leidenfrost temperature as the transition point to determine the boiling heat transfer regime. If wall temperature is higher than the Leidenfrost temperature, film boiling dominates. If the wall temperature is between Leidenfrost temperature and a critical temperature T_{crit}, nucleate boiling occurs. If the wall temperature is below T_{crit}, single phase forced convective heat transfer is assumed. It is hard to tell exactly what Leidenfrost temperature and critical temperature T_{crit} for different types of cryogenic fluid because they highly depend on various flow conditions. In this work, they are extracted from experimental results where we observe the sudden changes in measured solid wall temperature over time.

II.2.2.1. Film boiling heat transfer

a. Introduction

Due to the high wall superheat in cryogenic chilldown process as the cryogenic liquid enters the pipes in room temperature, film boiling heat transfer regime play a very important role in terms of both time span and fraction amount of heat removed from the solid pipe wall. It is to be noted again that there is no specific correlation available for this film boiling regime that has an intrinsic high wall superheat. If one wants to use existing conventional correlations, one needs to make significant modifications because those correlations were established on non-cryogenic conditions. It must also be noticed that correlations that were obtained for steady flow film boiling are not appropriate for the chilldown process due to the inherent unsteadiness of the present problem.

There are several correlations for film boiling heat transfer in the literature that were based on the analyses of the thin vapor film boundary layer and the stability of the thin vapor film. Bromley

[14] and Breen and Westwater [17] introduced correlations for film boiling on the outer surface of a hot tube. Ferderking and Clark [31] and Carey [32] introduced correlations for film boiling on the surface of a sphere.

Recently, Liao et al. [12] developed an analytical model for film boiling heat transfer of stratified flow during cryogenic chilldown process. This model was obtained by analytically solving the mass, momentum and energy equations in the vapor film layer. Since this model is only applied for stratified laminar cryogenic flow and with further assumptions, all the conservative equations can be solved analytically and an analytic solution of the vapor film thickness is obtained. Then, the film boiling heat transfer in the vapor film layer is obtain simply by the ratio of the thermal conductivity and the thickness of the vapor film due to the linear temperature profile. This model is the first attempt for solving cryogenic film boiling. However, it is only applicable for low mass flux flow regime. For flow with high mass flux, this model is no longer valid and we need a suitable model to take into account the effect of high flow rate which is more prevalent in industrial processes.

With high mass flow rate, the liquid and vapor film flows are supposed to be in turbulent regime. Then, the problem turns out to be convective heat transfer in turbulent boundary layer problem and solving for this type of problem is the main issue of this work.

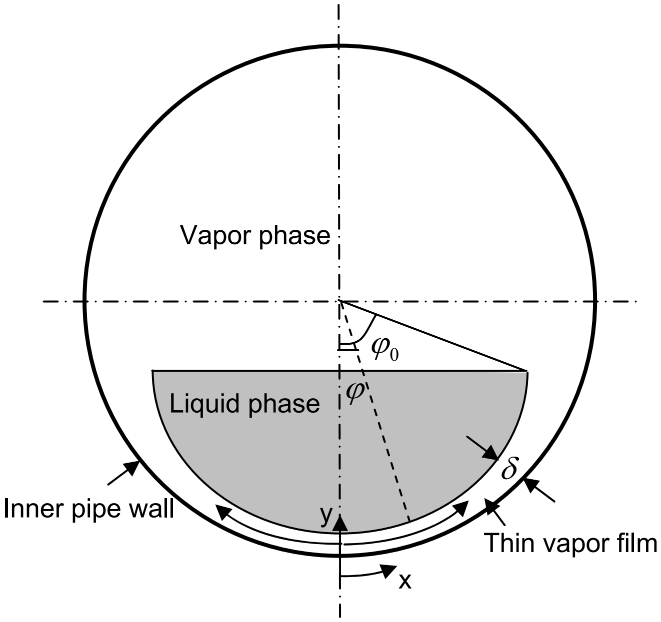

Fig. 2. Schematic of film boiling model.

The schematic plot of the model for film boiling inside a horizontal pipe is shown in Fig. 2. The bulk liquid is near the bottom of the pipe. Between the liquid and the solid pipe wall is a thin vapor film as a result of the occurrence of film boiling. Due to buoyancy effect, the vapor in the film flows upward along the azimuthal direction. However, due to the high wall superheat, the vapor film is produced to separate the cryogenic liquid from touching the solid pipe wall. The balance between these two physical phenomena leads to presence of the thin vapor film and heat is transfer from the solid wall to the liquid through this thin vapor film.

There are certain assumptions that can be made to simplify the analysis; however, the physical insight of the problem is still remained. These assumptions are as follows.

- The liquid flow is incompressible and turbulent.
- The vapor film thickness δ is small compared to the solid pipe radius R and is a function of position only: $\delta = \delta(\varphi)$.
- Phase change occurs at the liquid-vapor interface.

b. Formulation

The continuity, momentum and energy equations for that thin vapor film boundary layer are as follows.

$$\frac{\partial u}{\partial x} + \frac{\partial v}{\partial y} = 0 \tag{8}$$

$$u\frac{\partial u}{\partial x} + v\frac{\partial u}{\partial y} = -\frac{1}{\rho_v}\frac{\partial p}{\partial x} + \nu_v \frac{\partial^2 u}{\partial y^2} - g\sin\varphi \tag{9}$$

$$u\frac{\partial T}{\partial x} + v\frac{\partial T}{\partial y} = \alpha_v \frac{\partial^2 T}{\partial y^2} \tag{10}$$

The momentum in *y*-direction yields $\frac{\partial p}{\partial y} = 0$, then $p = p(x) = const$ along *y*-direction. The hydrostatic pressure can be evaluated by:

$$P = P_o + \rho_l gR(\cos\varphi - \cos\varphi_o) \tag{11}$$

Then:

$$\frac{dP}{dx} = -\rho_l g\sin\varphi \tag{12}$$

Using the following well-known Reynolds decompositions

$$\begin{aligned} u &= U + u' \\ v &= V + v' \\ p &= P + p' \end{aligned} \tag{13}$$

Then the governing equations become as follows:

$$\frac{\partial U}{\partial x} + \frac{\partial V}{\partial y} = 0 \tag{14}$$

$$U\frac{\partial U}{\partial x}+V\frac{\partial U}{\partial y}=\frac{1}{\rho_v}(\rho_l-\rho_v)g\sin\varphi+\frac{1}{\rho_v}\frac{\partial}{\partial y}\left((\mu_v+\varepsilon_M)\frac{\partial U}{\partial y}\right) \tag{15}$$

$$U\frac{\partial T}{\partial x}+V\frac{\partial T}{\partial y}=\frac{\partial}{\partial y}\left((\alpha_v+\varepsilon_H)\frac{\partial T}{\partial y}\right) \tag{16}$$

In Eq. (15) $\mu_v\frac{\partial U}{\partial y}$ is the molecular shear stress acting in x-direction, $-\rho\overline{u'v'}=\rho\varepsilon_M\frac{\partial U}{\partial y}$ is the turbulent stress, and ε_M is the eddy viscosity.

In Eq. (16) $\alpha_v\frac{\partial T}{\partial y}$ is the heat flux due to molecular motion, $-\rho c_p\overline{v'T'}=\rho c_p\varepsilon_H\frac{\partial T}{\partial y}$ is the turbulent heat flux, and ε_H is eddy thermal diffusivity.

Because the turbulent diffusion across the thin vapor film is typically much greater than convection in azimuthal direction, the convective terms in momentum and energy equations are neglected. Thus the further simplified momentum and energy equations and the corresponding boundary conditions are given as follows.

Simplified momentum equation:

$$\frac{d}{dy}\left((\mu_v+\varepsilon_M)\frac{dU}{dy}\right)=(\rho_v-\rho_l)g\sin\varphi \tag{17}$$

Boundary conditions:

1. At wall: no-slip condition: $y=0,\ U=0$ (18a)
2. At the liquid /vapor interface: no frictional force: $y=\delta,\ \frac{dU}{dy}=0$ (18b)

Simplified energy equation:

$$\frac{d}{dy}\left((\alpha_v+\varepsilon_H)\frac{dT}{dy}\right)=0 \tag{19}$$

Boundary conditions:

1. At wall: $y=0, T=T_w$ (20a)
2. At the liquid /vapor interface: $y=\delta, T=T_{sat}$ (20b)

At this stage, in order to solve the simplified momentum and energy equations, we need a model to approximate the eddy viscosity and eddy thermal diffusivity. The well-known Kays's model [33] is employed.

$$\varepsilon_M = \begin{cases} 0.001\nu_v {y^+}^3 & y^+ < 5 \\ \left[\kappa y\left(1-\exp\left(-\frac{y^+}{25}\right)\right)\right]^2 \left|\frac{dU}{dy}\right| & y^+ \geq 5 \end{cases} \tag{21}$$

$$y^+ = \frac{yu^*}{\nu_v},\ u^* = \sqrt{\frac{\tau_w}{\rho_v}},\ \tau_w = \mu_v \left.\frac{dU}{dy}\right|_{y=0},\ \kappa = 0.41 \tag{22}$$

$$\frac{\varepsilon_M}{\varepsilon_H} = \Pr_t \tag{23}$$

$$\Pr_t = \begin{cases} 1.07 & y^+ < 5 \\ 1 + 0.855 - \tanh\left[0.2(y^+ - 7.5)\right] & y^+ \geq 5 \end{cases} \tag{24}$$

c. Analytical solution

Velocity field

From Eq. (17), let:

$$A(x) = (\rho_l - \rho_v)g\sin\varphi = (\rho_l - \rho_v)g\sin\left(\frac{x}{R}\right) \tag{25}$$

Then, integrate Eq. (17):

$$\frac{dU}{dy} = \frac{-A(x)}{\mu_v + \varepsilon_M(y)}y + \frac{C_1}{\mu_v + \varepsilon_M(y)} \tag{26}$$

At $y = 0$: $y^+ = 0$ then from Eq. (21): $\varepsilon_M(y = 0) = 0$, hence from Eq. (26):

$$\left.\frac{dU}{dy}\right|_{y=0} = \frac{C_1}{\mu_v} \tag{27}$$

Then from Eq. (22):

$$\tau_w = \mu_v \left.\frac{dU}{dy}\right|_{y=0} = C_1 \tag{28}$$

At $y = \delta$: exploiting Eq. (18b), Eq. (26) yields:

$$\left.\frac{dU}{dy}\right|_{y=\delta} = 0 = \frac{-A(x)}{\mu_v + \varepsilon_M(\delta)}\delta + \frac{C_1}{\mu_v + \varepsilon_M(\delta)} \tag{29}$$

And then:

$$C_1 = A(x)\delta \tag{30}$$

With this expression for integration constant C_1, we can obtain the following expression for u^* in Eq. (22) and $\frac{dU}{dy}$ in Eq. (26) as follows.

$$u^* = \sqrt{\frac{A(x)\delta}{\rho_v}} \tag{31}$$

$$\frac{dU}{dy} = \frac{A(x)\delta}{\mu_v + \varepsilon_M(y)}\left[1 - \left(\frac{y}{\delta}\right)\right] = f(y) \tag{32}$$

At this stage, we can integrate Eq. (32) with information from Eq. (21), (22), (25), and (31) to obtain the velocity field.

Temperature field

Integrate Eq. (19) we obtain:

$$\frac{dT}{dy} = \frac{C_2}{\alpha_v + \varepsilon_H(y)} \tag{33}$$

We then integrate Eq. (33) from 0 to δ and using the two boundary conditions given by Eq. (20a) and (20b), we obtain the expression for C_2 as follows.

$$C_2 = \frac{T_{sat} - T_w}{\int_0^\delta \frac{dy}{\alpha_v + \varepsilon_H(y)}} \tag{34}$$

Then, plug Eq. (34) into (33) yields:

$$\frac{dT}{dy} = \frac{C_2}{\alpha_v + \varepsilon_H(y)} = g(y) \tag{35}$$

At this stage, we can integrate Eq. (35) with information from Eq. (21), (22), (23), (24), (25), (31), and (34) to obtain the temperature field.

Constraint on vapor film thickness

The energy and mass balance on the vapor film requires the following condition:

$$\left[-k_v \left.\frac{dT}{dy}\right|_{y=\delta}\right]dx = h_{fg}\,dm = h_{fg}\rho_v d\left(\overline{U}\delta\right) \tag{36}$$

or:

$$-\frac{k_v}{h_{fg}\rho_v}\frac{dT}{dy}\bigg|_{y=\delta}=\frac{d\left(\overline{U}\delta\right)}{dx} \tag{37}$$

Where $\overline{U}$ is the mean velocity and given as follows by definition:

$$\overline{U}=\frac{1}{\delta}\int_0^{\delta}Udy \tag{37}$$

And from Eq. (35):

$$\frac{dT}{dy}\bigg|_{y=\delta}=\frac{C_2}{\alpha_v+\varepsilon_H(\delta)} \tag{38}$$

Eq. (37) is the key for this analysis since it is the constraint for the vapor film thickness. Once δ is obtained, the film boiling heat transfer coefficient is computed as follows.

$$h_{fb}=\frac{q''}{\Delta T_{sat}}=\frac{-k_v\left.\dfrac{dT}{dy}\right|_{y=\delta}}{\Delta T_{sat}} \tag{39}$$

Where $\Delta T_{sat}=T_w-T_{sat}$ is the wall superheat.

Interestingly, we may recover the analytical result of Liao et al. [12] for the film boiling heat transfer coefficient. By plugging Eq. (38) into Eq. (39) and using Eq. (34), the resulting equation is given as follows.

$$h_{fb}=\frac{k_v}{\left[\int_0^{\delta}\dfrac{dy}{\alpha_v+\varepsilon_H(y)}\right]\left(\alpha_v+\varepsilon_H(\delta)\right)} \tag{40}$$

For Liao et al. model, there is no eddy viscosity as well as eddy thermal diffusivity since they consider the laminar flow regime (or low mass flux flow regime), hence by letting $\varepsilon_H(y)=\varepsilon_H(y)=0$ in Eq. (40) yields:

$$h_{fb}=\frac{k_v}{\alpha_v\left[\int_0^{\delta}\dfrac{dy}{\alpha_v}\right]} \tag{41}$$

Since α_v is constant and $\int_0^{\delta}dy=\delta$, we recover Liao et al. result [12].

$$h_{fb} = \frac{k_v}{\delta} \tag{42}$$

By recovering the analytical result from previous work of Liao et al. [12], we have just shown that our analysis is not only consistent but it also is the general case of the low mass flux flow regime.

II.2.2.2. Nucleate boiling heat transfer

In the nucleate boiling stage, there are several correlations are available in the literature and are commonly used, such as Chen's [23], Gungor and Winterton's [25], Kutateladze's [26]. Liao et al. [12] suggested that a modified Kutateladze's correlation is suitable for the nucleate boiling heat transfer of cryogenic liquid.

In this work, a modified Kutateladze's correlation [26] with a suppression factor is used.

$$h_{nb} = h_{conv} + S \times h_{pool} \tag{43}$$

Here h_{conv} is given by the Dittus-Boelter's correlation [30] for turbulent fully developed pipe flow and h_{pool} is the pool nucleate boiling heat transfer coefficient. They are given as follows.

$$h_{conv} = 0.023\,\mathrm{Re}_l^{0.8}\,\mathrm{Pr}_l^{0.4}\left(\frac{k_l}{D_l}\right) \tag{44}$$

$$h_{pool} = 0.487 \times 10^{-10} \times \left[\frac{k_l \rho_l^{1.282} p^{1.750} c_{p,l}^{1.5}}{h_{fg}^{1.5} \rho_v^{1.5} \sigma^{0.906} \mu_l^{0.626}}\right] \Delta T_{sat}^{\ \ 1.5} \tag{45}$$

Re_l and Pr_l is the vapor Reynolds number and Prandtl number respectively.

$$\mathrm{Re}_l = \frac{u_l D_l}{\mu_l} \tag{46}$$

$$\mathrm{Pr}_l = \frac{c_{p,l}\mu_l}{k_l} \tag{47}$$

Here u_l is the liquid velocity which is measured from the experiment, μ_l is the liquid viscosity, k_l is the liquid thermal conductivity, $c_{p,l}$ is the heat capacity of liquid phase, D_l is the hydraulic diameter of the vapor phase, p is the pressure, σ is the surface tension and ΔT_{sat} is the wall superheat.

II.2.2.3. Forced convective heat transfer

When the wall superheat drops to a certain range, all the nucleate sites are suppressed [32], then single phase forced convection heat transfer dominates. The heat transfer coefficient in this case can be predicted by using Dittus-Boelter's correlation [30] for turbulent flow regime and given in Eq. (44).

III. Results and Discussions

III.1. Experiment of Jackson et al.

In experiment by Jackson et al. [13], liquid nitrogen was stored in a 1580 kPa dewar and used as cryogen. The dewar pressure was the driving force for the liquid nitrogen flow. Upon leaving the dewar, nitrogen was cooled by passing through a heat exchanger prior to entering the vacuum jacketed concentric Pyrex visual test section. The test section has inner diameter of 12.57 mm and the thickness is 1.65 mm. The flow structure was captured by a high resolution CCD camera system.

The flow then entered the heat transfer measurement section located at 70 cm downstream of the visual test section. In this section there were two thermocouples measure the temperature of the fluid at the inlet and outlet. The inner and outer pipe wall temperature in several circumferential positions were measured by thermocouples and recorded on a computer. The thermocouple arrangements and dimensions of the test section are shown in Fig. 3.

Experiments were carried out at room temperature and atmosphere pressure. The mass fluxes ranged from 66 to 500 kg/m^{2}s, vapor qualities varied from 0.004 to 1 and ambient heat fluxes ranged from 716 W/m^2 to 995 W/m^2.

The Leidenfrost temperature for the nitrogen in this experiment was observed around 130K; hence the temperature when the film boiling ends and nucleate boiling starts is set at 130K. The transition temperature at which the nucleate boiling switches to single phase convection heat transfer was observed around 105K based on experimental results.

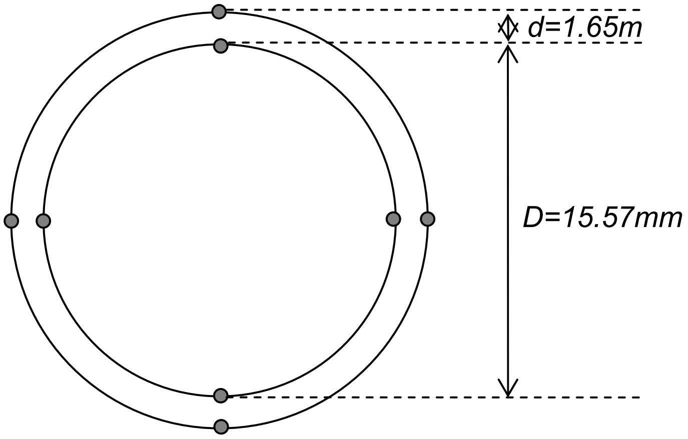

Fig. 3. Thermocouple positions in the circumference of the Pyrex pipe.

III.2. Computational Procedure

Finite Volume Method is employed in computing the thermal field in the solid pipe wall. The computational domain consists of 40 grids in the radial direction and 40 grids in the azimuthal direction. The grid resolution is sufficient in capturing the thermal behavior. The computational procedure is as follows.

First, we need to read in the experimental data including the following information:

- Dimension of test section
- Solid and fluid properties at initial stage
- Raw vapor velocity data
- Raw liquid velocity data
- Raw liquid height data
- Raw liquid pressure data

Then, for each time step, we need to implement the computational procedure as shown in Fig. 4. It can be interpreted as follows.

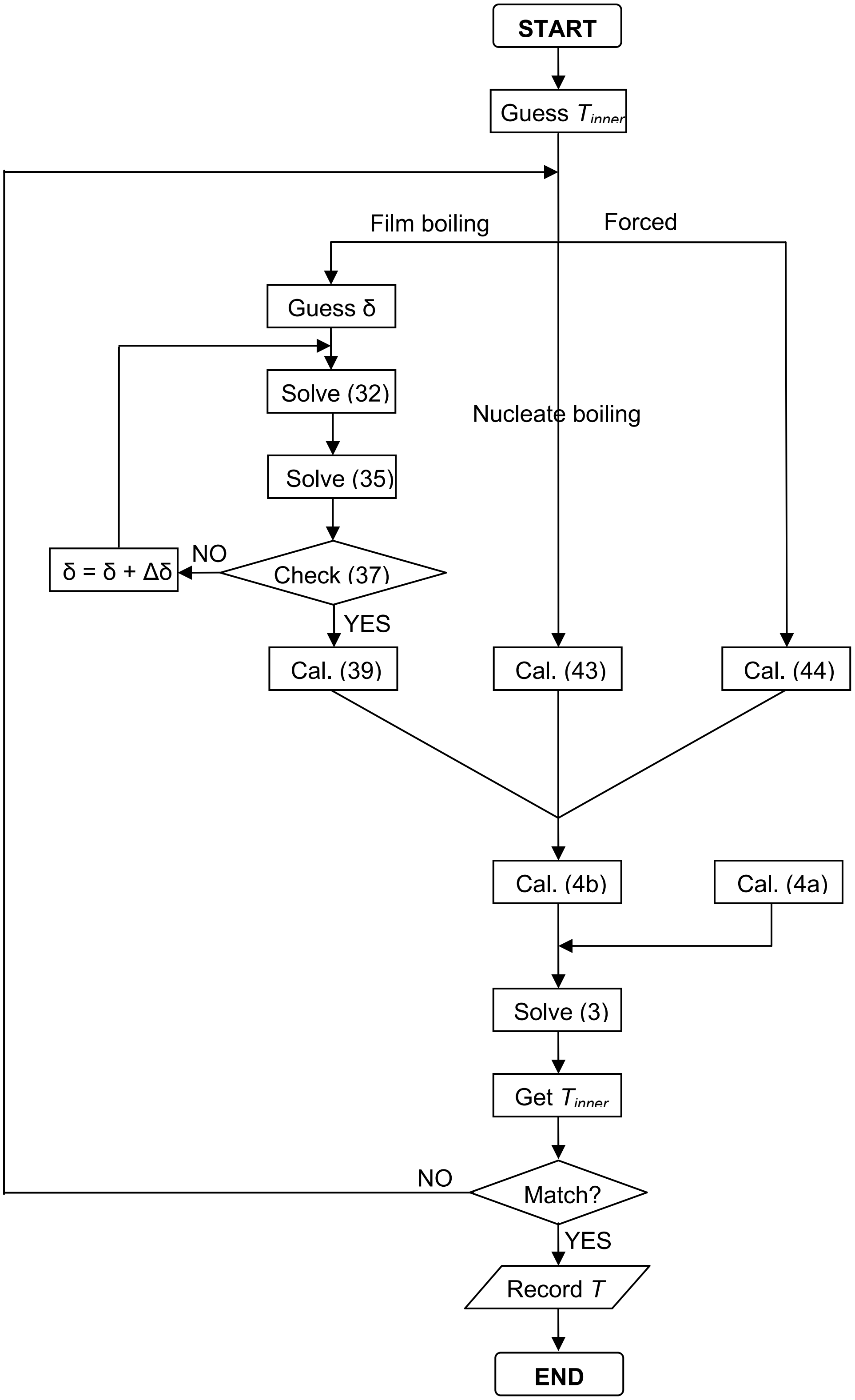

Fig. 4. Flow chart of computational procedure for each time step.

- First we guess a temperature profile at the inner solid pipe wall.
- Then, by comparing the inner temperature at every location in the azimuthal direction with the Leidenfrost and critical temperature, we obtain the corresponding heat transfer coefficient for each type of boiling regimes.
- For film boiling heat transfer, we need to iterate to obtain the correct vapor film thickness in order to get film boiling heat transfer coefficient. First we guess a value of vapor film thickness, then following the procedure addressed in section 2.2.1, we obtain the velocity and temperature field throughout the vapor film layer. The iteration for vapor film thickness stops when the mass and energy balance satisfies.
- After getting all the heat transfer coefficients at the inner pipe wall, it is obviously that we have all the information needed for boundary condition at the inner pipe. We also have the information of ambient temperature as well as the experimental heat transfer coefficient of the surroundings; we can compute the boundary condition at the outer pipe wall.
- We then solve for the temperature field in the solid pipe wall by finite volume method with the above two boundary conditions. The system of equation is solved efficiently by Thomas algorithm.
- The iteration for inner wall temperature stops when the difference between the new obtained inner wall temperature with the guessed one less than a chosen criterion.
- Record the temperature information and then we move to the next time step.

III.3. Comparison of pipe wall temperature

Since the major effort is in the modeling of film boiling stage, only numerical results in this boiling regime are shown. Following is some comparison between the numerical results obtained by exploiting the above developed model with the experimental results.

The mass flow rate for the first experiment ranges from 80 to 100 kg/m^{2}s. The numerical simulation started at 20s since as the experiment needs that amount of time for starting-up.

For the top pipe wall, the computed temperature is less than that measured from experiment about 10 to 20% as shown in Fig. 5.

For the side pipe wall, the discrepancy between computed temperature and experiment result is still large but less than that for the top pipe wall as shown in Fig. 6.

For the bottom pipe wall, we can observe a very good agreement between the numerical result and experimental result for the temperature history as shown in Fig. 7.

The mass flow rate for the second experiment ranges from 130 to 200 kg/m^{2}s. The numerical simulation started at 20s since as the experiment needs that amount of time for starting-up. The same observation for top, side and bottom walls can be concluded from Figs. 8, 9, and 10.

From above observations, we see that for the top and the side pipe wall, the predicted temperature is not so good. It can be explained by some of the following reasons. First reason may be due to the error in recording experiment results. Remember that the input for our computation is the raw data from experiment, hence, the numerical results depends a lot on those data. The second reason may be the correlations we are using are not quite suitable or we need to modify them in order to take into account the effect of high mass flow rate conditions.

However, the predicted temperature at the bottom pipe wall agrees quite well with the experimental results. It shows that our model for the film boiling heat transfer is a very good one and is also reliable. Since this is the high mass flux regime, we expect the cryogenic flows to be in turbulent regime and that we build the model to take into account the turbulent effects which manifest via eddy viscosity and eddy thermal diffusivity.

Besides, we are also able to compute the thin vapor film thickness that varies for each location in the azimuthal direction for each time step. That information is very useful since it is impossible for us to measure and record the vapor film thickness by conducting experiment, especially under such unsteady and high mass flow rate regime.

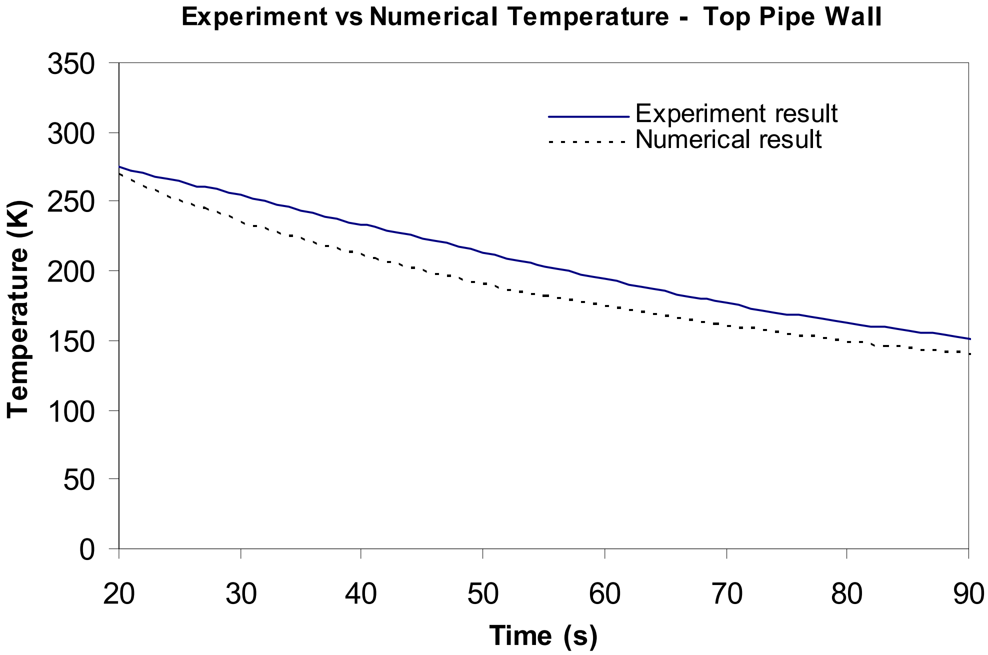

Fig. 5. Comparison between experimental and numerical results for temperature at top wall. Mass-flux ranging from 80-100 kg/m^{2}s.

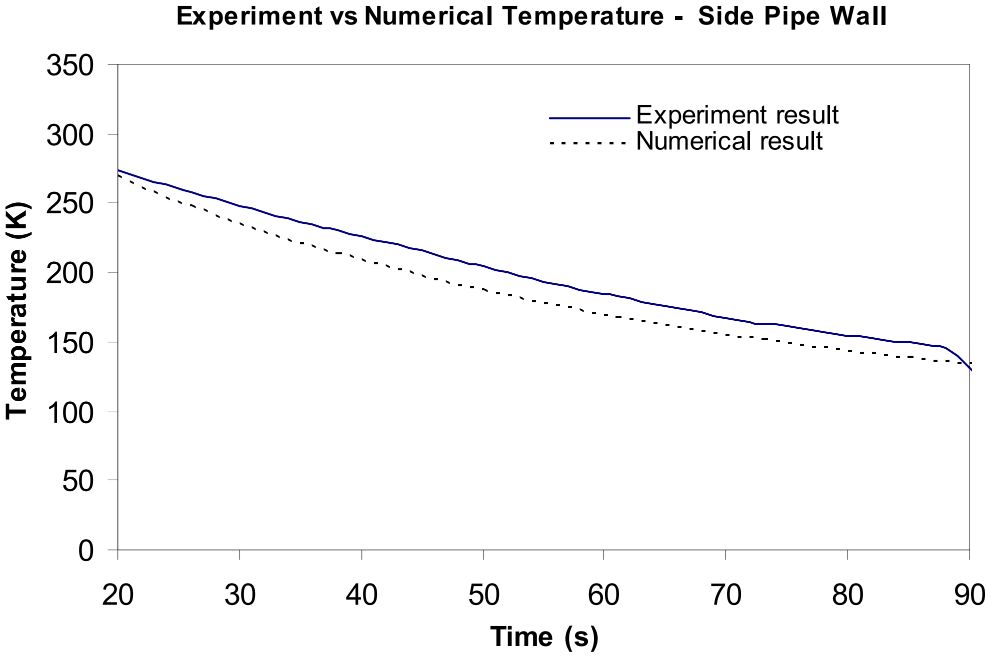

Fig. 6. Comparison between experimental and numerical results for temperature at side wall. Mass-flux ranging from 80-100 kg/m^{2}s.

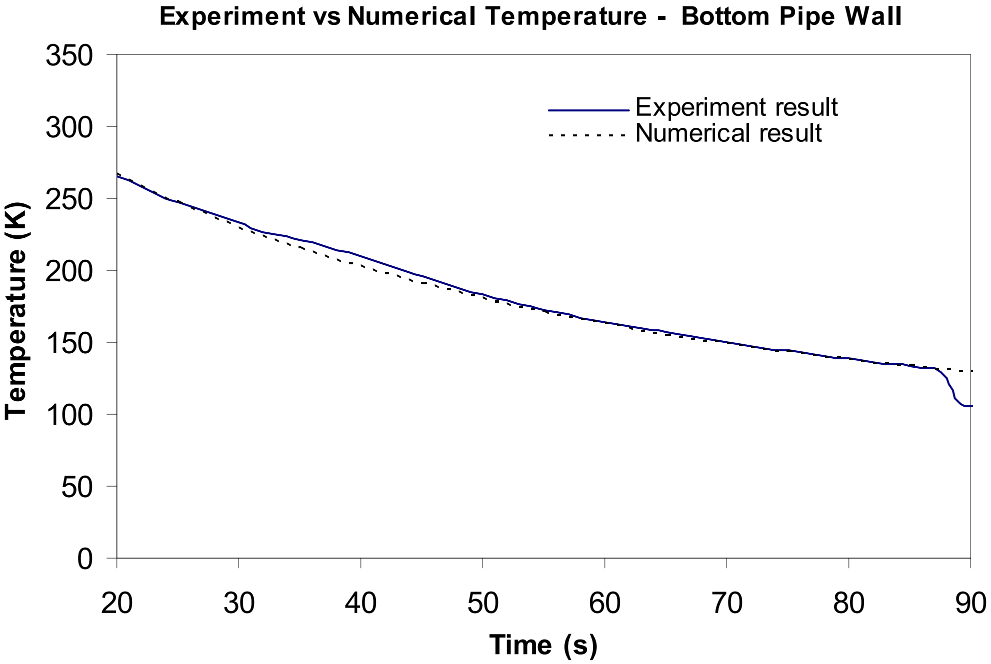

Fig. 7. Comparison between experimental and numerical results for temperature at bottom wall. Mass-flux ranging from 80-100 kg/m^{2}s.

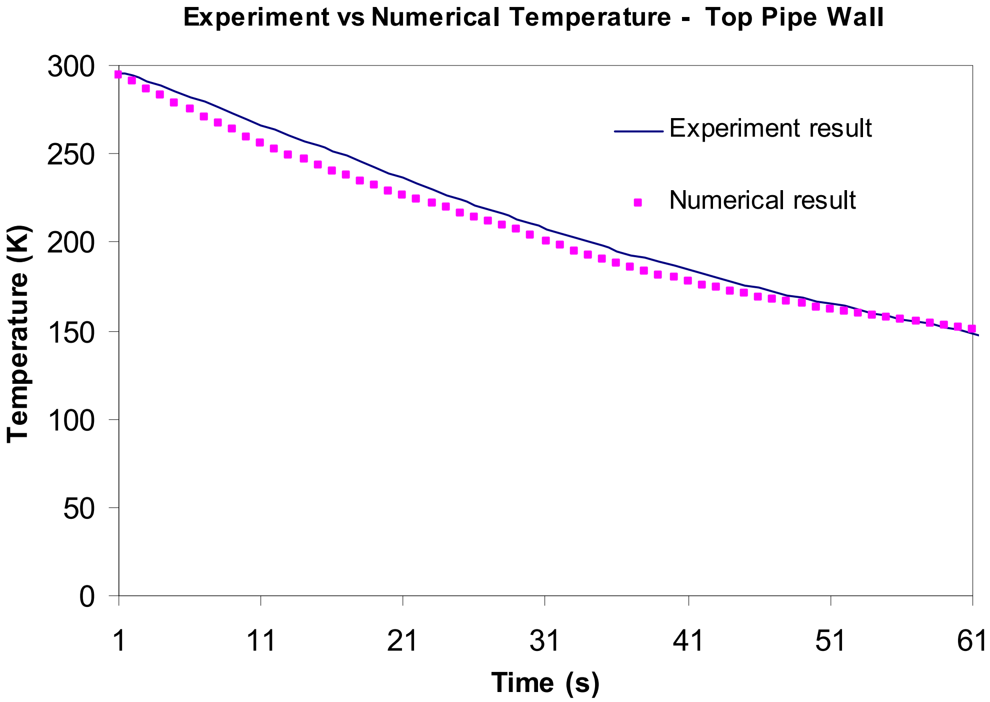

Fig. 8. Comparison between experimental and numerical results for temperature at top wall. Mass-flux ranging from 130-200 kg/m^{2}s.

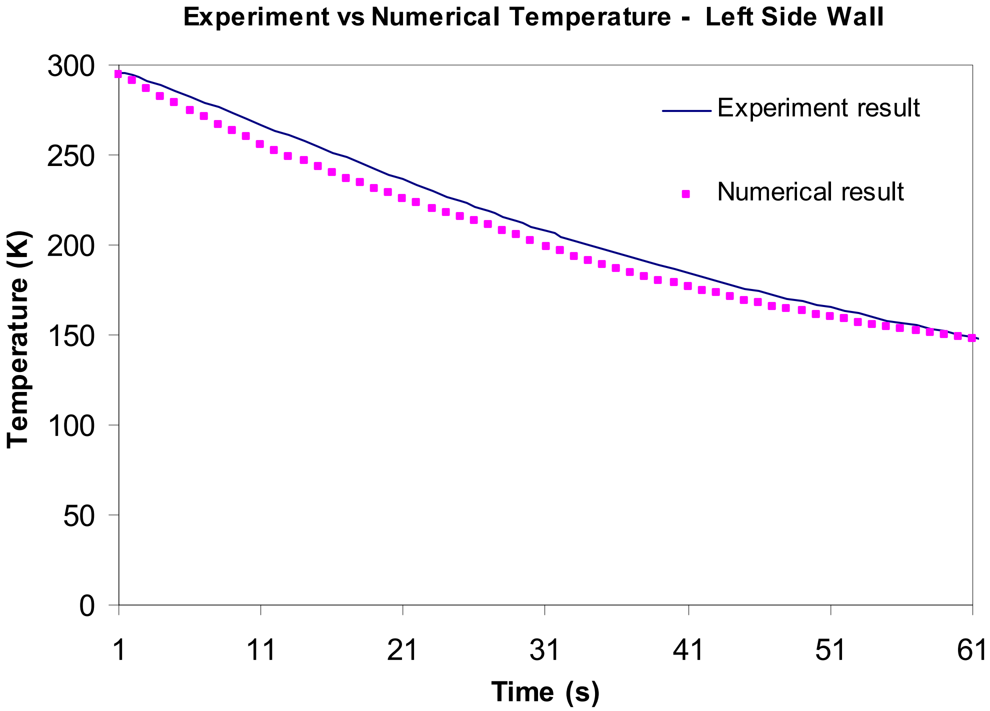

Fig. 9. Comparison between experimental and numerical results for temperature at side wall. Mass-flux ranging from 130-200 kg/m^{2}s.

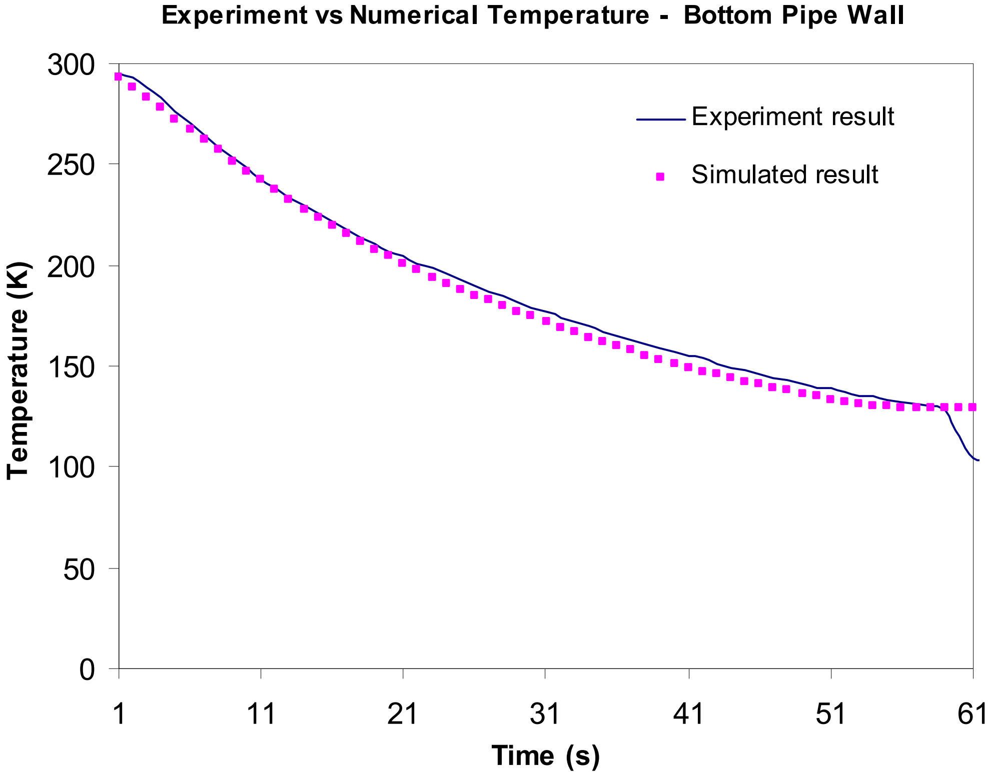

Fig.10. Comparison between experimental and numerical results for temperature at bottom wall. Mass-flux ranging from 130-200 kg/m^{2}s.

IV. Conclusions

A computational model has been developed for understanding the heat transfer mechanisms during cryogenic chilldown process. With this model, one can predict the thermal interactions among cryogenic liquid phases and between phases and solid pipe wall. Especially, a model for simulation of film boiling heat transfer is developed based on transport equations in the vapor film layer and the effect of high mass flow rate. This model is tested with experimental results and the agreement between the two is quite acceptable.

V. Patents, Publications, Presentations and Students from Research

Publications

No publications.

Students from Research

Hieu H. Tran: Received MSc.

VI. Acknowledgements

This Work was supported by NASA Glenn Research Center under contract (NAG3-2930) and NASA Kennedy Space Center.

VII. References

1. Burke, J.C., Byrnes, W.R., Post, A.H., and Ruccia, F.E., 1960, “Pressure Cooldown of Cryogenic Transfer Lines”, Advances in Cryogenic Engineering, 4, pp. 378-394.
2. Bronson, J.C., Edeskuty, F.J., Fretwell, J.H., Hammel, E.F., Keller, W.E., Meier, K.L., Schuch, and A.F, Willis, W.L., 1962, “Problems in Cool-Down of Cryogenic Systems”, Advances in Cryogenic Engineering, 7, pp. 198-205.
3. Chi, J.W.H., and Vetere, A.M., 1963, “Two-Phase Flow During Transient Boiling of Hydrogen and Determination of Nonequilibrium Vapor Fractions”, Advances in Cryogenic Engineering, 9, pp. 243-253.
4. Graham, R.W., Hendricks, R.C., Hsu, Y.Y., and Friedman, R., 1961, “Experimental Heat Transfer and Pressure Drop of Film Boiling Liquid Hydrogen Flowing through A Heated Tube”, Advances in Cryogenic Engineering, 6, pp. 517-524.
5. Chi, J.W.H., 1965, “Cooldown Temperatures and Cooldown Time During Mist Flow”, Advances in Cryogenic Engineering, 10, pp. 330-340.
6. Steward, W.G., Smith and R.V., Brennan, J.A., 1970, “Cooldown Transients in Cryogenic Transfer Lines”, Advances in Cryogenic Engineering, 15, pp. 354-363.
7. Chan, A.M.C., and Banerjee, S., 1981, “Refilling and Rewetting of a Hot Horizontal Tube part I: Experiment”, Journal of Heat Transfer, 103, pp. 281-286.
8. Chan, A. M. C., and Banerjee, S., 1981, “Refilling and Rewetting of a Hot Horizontal Tube part II: Structure of a Two-Fluid Model”, Journal of Heat Transfer, 103, pp. 287-292.
9. Chan, A.M.C., and Banerjee, S., 1981, “Refilling and Rewetting of a Hot Horizontal Tube part III: Application of a Two-Fluid Model to Analyze Rewetting”, Journal of Heat Transfer, 103, pp. 653-659.
10. Velat, C., Jackson, J., Klausner, J.F., and Mei, R., 2004, “Cryogenic Two-Phase Flow During Chilldown”, Proceedings of the ASME HT-FED Conference, Charlotte, NC.
11. Chung, J.N., Yuan, K., and Xiong, R., 2004, “Two-Phase Flow and Heat Transfer of a Cryogenic Fluid During Pipe Chilldown”, Proceedings of 5th International Conference on Multiphase Flow, Yokohama, Japan, pp. 468.
12. Liao, J., Yuan K., Mei, R., Klausner, J.K., Chung, R., 2005, “Cryogenic Chilldown Model for Stratified Flow inside a Pipe”, Proceedings of ASME Summer Heat Transfer Conference, San Francisco, California, USA.
13. Jackson, J., Klausner, J.K., Mei, R., 2006, “Performance of Current Heat Transfer Correlations in Predicting the Heat Transfer During Cryogenic Chilldown”, ECI International Conference on Boiling Heat Transfer, Spoleto, Italia.
14. Bromley, J.A., 1950, “Heat Transfer in Stable Film Boiling”, Chemical Engineering Progress, 46, No. 5, pp. 221-227.
15. Dougall, R.S., Rohsenow, W.M., 1963, “Film Boiling on the Inside of Vertical Tubes with Upward Flow of the Fluid at Low Qualities”, Report #9079-26, MIT.
16. Laverty, W.F., and Rohsenow, W.M., 1967, “Film Boiling of Saturated Nitrogen Flowing in a Vertical Tube”, Journal of Heat Transfer, 89, pp. 90-98.
17. Breen, B.P., and Westwater, J.W., 1962, “Effect if Diameter of Horizontal Tubes on Film Heat Transfer”, Chemical Engineering Progress, 58, no. 7, pp. 67.
18. Hendricks, R.C., Graham, R.W., Hsu, Y.Y., and Friedman, R., 1961, “Experimental Heat Transfer and Pressure Drop of Liquid Hydrogen Flowing Through a Heated Tube”, NAS TN D-765.
19. Hendricks, R.C., Graham, R.W., Hsu, Y.Y., and Friedman, R., 1966, “Experimental Heat Transfer Results for Cryogenic Hydrogen Flowing in Tubes at Subcritical and Supercritical Pressure to 800 pounds per Square Inch Absolute”, NASA TN D-3095.
20. Ellerbrock, H.H., Livingood, J.N.B., and Straight, D.M., 1962, “Fluid-Flow and Heat-Transfer Problems in Nuclear Rockets”, NASA SP-20.

21. von Glahn, U.H., 1964, "A Correlation of Film-Boiling Heat Transfer Coefficients Obtained with Hydrogen", Nitrogen and Freon 113 in Forced Flow, NASA TN D-2294.
22. Giarratano, P.J., Smith, R.V., 1965, "Comparative Study of Forced Convection Boiling Heat Transfer Correlations for Cryogenic Fluids", Advances in Cryogenic Engineering, 11, pp. 492-505.
23. Chen, J.C., 1966, "Correlation for Boiling Heat Transfer to Saturated Fluids in Convective Flow", Industry Engineering Chemistry Process Design and Development, 5, pp. 322-329.
24. Bennett, D.L., and Chen, J.C., 1980, "Forced Convection for the in Vertical Tubes for Saturated Pure Components and Binary Mixture", A.I.Ch.E. Journal, 26, pp. 454-461.
25. Gungor, K.E., Winterton, R.H.S., 1986, "A General Correlation for Flow Boiling in Tubes and Annuli", International Journal of Heat Mass Transfer, 29, No. 3, pp. 351-358.
26. Kutateladze, S.S., 1952, "Heat Transfer in Condensation and Boiling", Atomic Energy Commission Translation 3770, Tech. Info. Service, Oak Ridge, Tennessee.
27. Steiner, D., May 1986, "Heat Transfer During Flow Boiling of Cryogenic Fluids in Vertical and Horizontal Tubes", Cryogenics, 26, pp. 309-318.
28. Incropera, F.P., Dewitt, D.P., 2002, Fundamentals of Heat and Mass Transfer, 5th edition, John Willey&Sons.
29. Ozisik, M.N., 1993, Heat Conduction, 2nd edition, Wiley-Interscience, New York.
30. Dittus, F.W., Boelter, L.M.K., 1930, "Heat Transfer in Automobile Radiators of the Tubular Type", Publications in Engineering, Vol. 2, pp. 443.
31. Ferderking, T.H.K., and Clark, J.A., 1963, "Nature Convection Film Boling on A Sphere", Advanced Cryogenic Engineering, 8, pp. 501-506.
32. Carey, V.P., 1992, Liquid-Vapor Phase-Change Phenomena, Taylor & Francis Press.
33. Kays, W.M., Journal of Heat Transfer, 1994, 116/285, pp. 284-295.

5. Two Phase Flow Characteristics and Boiling Heat Transfer Rates During Cryogenic Chilldown and Transport in Reduced Gravity

Task PI: Dr. Jacob N. Chung, Mechanical and Aerospace Engineering, University of Florida

Graduate Student: Kun Yuan, Mechanical and Aerospace Engineering

Research Period: August 3, 2004 to March 31, 2008

Abstract

For many industrial, medical and space technologies, cryogenic fluids play indispensable roles. An integral part of the cryogenic transport processes is the chilldown of the system components during initial applications. In this paper, we report experimental results for a chilldown process that is involved with the unsteady two-phase vapor-liquid flow and boiling heat transfer of the cryogen coupled with the transient heat conduction inside pipe walls. We have provided fundamental understanding on the physics of the two-phase flow and boiling heat transfer during cryogenic quenching through experimental observation, measurement and analysis. Based on the temperature measurement of the tube wall, the terrestrial cryogenic chilldown process is divided into three stages of film boiling, nucleate boiling and single-phase convection that bears a close similarity to the conventional pool boiling process. In earth gravity, cooling rate is non-uniform circumferentially due to a stratified flow pattern that gives rise to more cooling on the bottom wall by liquid filaments. In microgravity, there is no stratified flow and the absence of the gravitational force sends liquid filaments to the central core and replaces them by low thermal conductivity vapor that significantly reduces the heat transfer from the wall. Thus, the chilldown process is axisymmetric, but longer in microgravity.

Keywords: *Cryogenics; Boiling heat transfer; Two-phase flow; Chilldown; Microgravity*

1. Introduction

Cryogenic fluids are widely used in industrial, aerospace, cryosurgery systems and so on. For example, liquid hydrogen is used in industrial applications such as metal processing, plate glass production, fat and oil hardening, semiconductor manufacturing, and pharmaceutical and chemical manufacturing. In these systems, proper transport, handling and storage of cryogenic fluids are of great importance. However, the chilldown or quenching process which initiates cryogenic fluids transport is complicated, involving unsteady two-phase heat and mass transfer, and has not been fully understood.

1.1 Role of Cryogenics in Space Exploration

The extension of human space exploration from a low earth orbit to a high earth orbit, then to Moon, Mars, and possibly asteroids and moons of other planets is one of NASA's biggest challenges for this new millennium. Integral to this is the effective, affordable, and reliable supply of cryogenic fluids. The efficient and safe utilization of cryogenic fluids in thermal management, power and propulsion, and life support systems of a spacecraft during space missions involves the transport, handling, and storage of these fluids in terrestrial and reduced gravities.

Chilldown process is the inevitable initial stage during cryogenic fluid transport. Due to their low boiling points, boiling and two-phase flows are encountered in most of the cryogenic operations.

The complexity of the problem results from the intricate interaction of the fluid dynamics and heat transfer, especially when phase-change (boiling and condensation) is involved. Because of the large stratification in densities between the liquid and vapor phases, the reduced gravity condition in space would strongly change the terrestrial flow patterns and accordingly affect the momentum and energy transport characteristics. Therefore, boiling and two-phase flow behave quite differently when the gravity levels are varied. The uncertainties about the flow pattern, pressure drop and heat transfer characteristics pose a severe design concern. For example, there is considerable disagreement over the chilldown heat fluxes and whether a unique rewetting temperature exists [1-2]. Different definitions of rewetting temperatures are reported in chilldown researches: Leidenfrost temperature, minimum film boiling temperature, quenching temperature from thermocouple observations and the temperature at which critical heat flux occurs [1]. For similar experimental observations, quiet different explanations were also suggested by different researchers. For example, it was reported that the rewetting velocity increased with increasing inlet flow rate, given the same initial wall temperature [3-5]. Duffey and Porthouse [4] suggested that the flow rate effect resulted from increasing the wet side heat transfer coefficient with higher inlet flow. This improves the rate of axial heat conduction and hence leads to a faster rewetting rate. Thompson [5], however, argued that the inlet flow rate affects precooling on the dry side rather than the heat transfer in the wet side. Additionally, because of the experimental difficulties, in general, there is very little heat transfer data for cryogenic flow boiling in reduced gravity. A representative work is reported by Adham-Khodaparast et al. [6].

The proposed research will focus on addressing specific fundamental and engineering issues related to the microgravity two-phase flow and boiling heat transfer of cryogenic fluids that require well-designed and meaningful experimentation. In this paper, liquid nitrogen chilldown process is investigated and divided into several stages based on the flow image and temperature data. The outcome of the research will provide fundamental understanding on the transport physics of cryogenic boiling and two-phase flows in a reduced gravity.

2. Background and Literature Review

2.1 Boiling Curve

A boiling curve shows the relationship between the heat flux that the heater supplies to the boiling fluid and the heater surface temperature. According to the typical boiling curve as shown in Fig. 1, a cryogenic chilldown (quenching) process usually starts from point E and then goes towards point D in the film boiling regime as the wall temperature decreases. Point D is called the Leidenfrost point which signifies the minimum heater temperature required for the film boiling. For the film boiling process, the wall is so hot that liquid will vaporize before reaching the heater surface which causes the heater to be always in contact with vapor. When cooling beyond the Leidenfrost point, if a constant heat flux heater were used, then the boiling would shift from film to nucleate boiling (somewhere between points A and B) directly with a substantial decrease in the wall temperature because the transition boiling is an unstable process. If the heater wall temperature can be controlled independently, then the boiling process will proceed from D to C in the transition boiling mode.

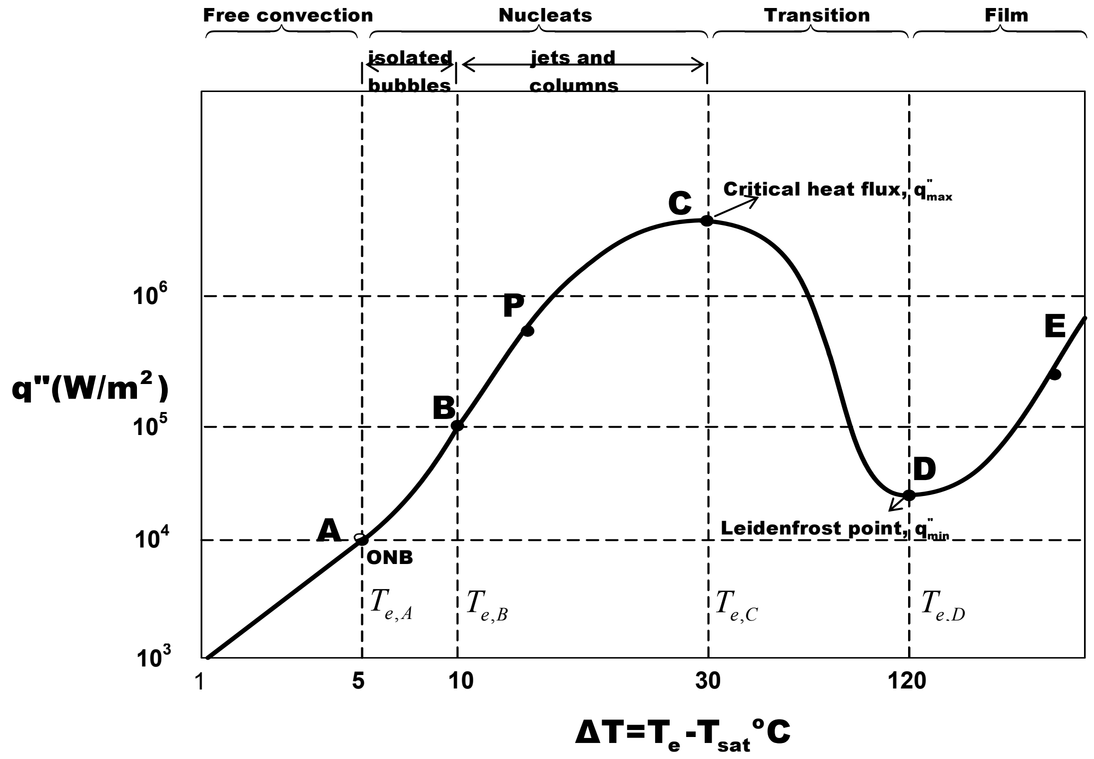

Fig. 1. Typical boiling curve.

2.2 The Effects of Gravity

Because of the differences in density and inertia, the two phases in the flow are usually non-uniformly distributed across the pipe under the terrestrial condition. The absence of gravity has important effects on flow patterns, pressure drop and heat transfer. Surface-tension-induced forces and surface phenomena are likely to be much more important in outer space than they are on earth. Actually, all flow-pattern-specific phenomena will be influenced by the gravity level [7]. As an example, in one of our own experiments, for the same mass flow rates, Fig. 2 compares the flow patterns under both terrestrial and microgravity conditions and the difference is significant as the liquid filament is on the bottom and suspended in the middle of the tube for terrestrial and microgravity conditions, respectively.

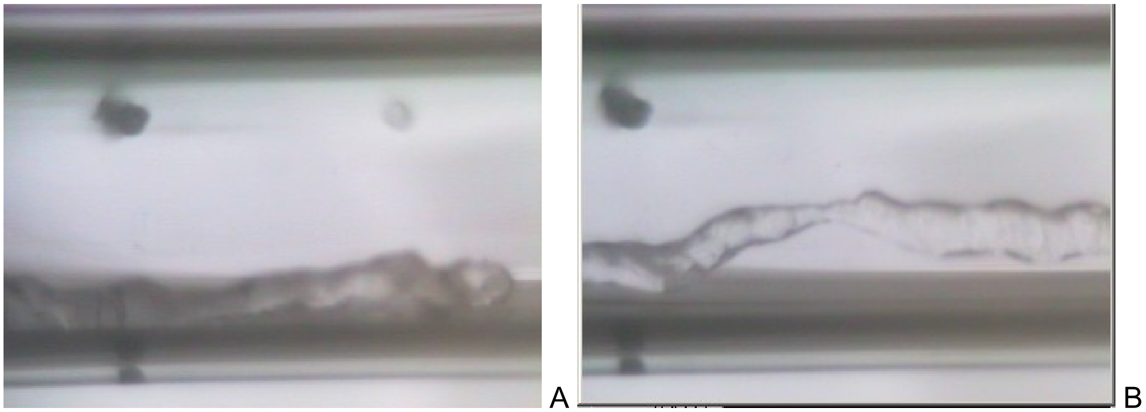

Fig. 2. Gravity effect on flow patterns. A) Flow pattern in 1-g test. B) Flow pattern in microgravity test.

Momentum and energy transport in two-phase flow and boiling under microgravity is a relatively new field. This is a complex problem for the scientific community to solve. The rewards are rich, however, as new ways to propel future space missions and more intensive space activities have been planned. Currently, there exists a limited quantity of literature, data, and test facilities to even begin to answer these questions. Microgravity cryogenic boiling research was initiated more than fifty years ago, but the progress has been limited. The following summarizes the accomplishments.

2.3 Terrestrial Cryogenic Boiling and Two-Phase Flow

Numerous studies of cryogenic boiling in the one-g environment were conducted in the 1950's and 60's. Brentari et al.'s work [8] is a comprehensive review of the experimental studies and heat transfer correlations. For oxygen, nitrogen, hydrogen and helium, it was found that for pool boiling, the Kutateladze [9] correlation had the greatest reliability for nucleate boiling while the Breen and Westwater [10] correlation was best for film boiling. Maximum nucleate flux data were reasonably well predicted by the Kutateladze correlation. Although these correlations were selected as the best available, neither has particularly good agreement with experimental data. For the case of forced convection boiling, Brentari et al [8] reported that no correlation was found to be distinctly better. Some simple predictive methods were found to work as well as more complex schemes. In all boiling cases, it was questioned as to whether or not the predictive correlations include all of the significant variables that influence the boiling process. In particular, it was suggested that more detailed and better controlled experiments are needed and that more attention to surface and geometry effects is required.

Another comprehensive review of cryogenic boiling heat transfer addressing hydrogen, nitrogen and oxygen is given by Seader et al. [11]. It was reported that nucleate pool boiling results cannot be correlated by a single line but cover a range of temperature difference for a given heat flux. The spread is attributed to surface condition and geometry, and orientation. Maximum heat flux can be reduced by about 50% when going from normal-g to near zero-g. Seader et al [11] reported a fair amount of data for film pool boiling. Film boiling heat flux is reduced considerably at near zero-g conditions. Only a very limited amount of data is available for subcooled or saturated forced convection boiling and few conclusions were drawn. Relatively recent correlations have been published for normal-g saturated flow boiling of cryogens using the Convection, Boiling and Froude numbers as correlating parameters [12-15]. For example, Van Dresar et al. [15] experimentally studied the near-horizontal two-phase flow of nitrogen and hydrogen. Unlike most of the other works which based on turbulent liquid flow, their work focused on laminar liquid flow conditions and the results for low mass and heat flux flow were correlated with Froude number.

2.4 Reduced Gravity Cryogenic Boiling and Two-Phase Flow

In general, there is little heat transfer data for cryogenic flow boiling in reduced gravity. We were able to find just two reports. Adham-Khodaparast et al. [6] have investigated the flow film boiling during quenching of R-113 on a hot flat surface. They reported lower heat transfer rates during microgravity as compared to normal gravity and contributed that to thickening of the vapor layer. The wall superheat and the surface heat flux at the onset of rewetting and maximum heat flux were found to increase with the inlet liquid subcooling, mass flux and gravity level. The effect of gravity was determined to be more important for low flow rates and less relevant for high flow rates. Antar and Collins [16] reported flow visualization and measurements for flow film boiling of liquid nitrogen in tubes on board KC-135 aircraft. They were particularly interested in the vapor/liquid flow pattern and the thermal characteristics. They identified a new vapor/liquid flow pattern that is unique in low gravity. They also observed that a sputtering leading core followed by a liquid filament annular flow pattern. This new flow pattern is composed of a long and connected liquid column that is flowing in the center of the tube and is surround by a thick vapor layer. The vapor annulus that separates the liquid filament from the wall is much thicker than that observed in the terrestrial experiment. They attributed the filamentary flow to the lack of difference in the speed of vapor and liquid phases. On the heat transfer side, they reported that the quench process is delayed in low gravity and the tube wall cooling rate was diminished under microgravity conditions.

3. Experimental System

To investigate the cryogenic chilldown process, a liquid nitrogen two-phase flow experimental facility has been designed, fabricated and tested under both terrestrial and microgravity conditions. A drop tower is used to provide the microgravity condition.

The experimental system is designed as a once-through flow pass using either gravity or motor-driven bellows as flow generator. Fig. 3 shows the schematic of the experimental system, which locates in two side-by-side aluminum cubicles and is fabricated for both terrestrial and microgravity experiments. The experimental system mainly consists of a nitrogen tank, a motor-driven bellows, test section inlet portion, test section, test section outlet portion, vacuum jacket, vacuum pump, data acquisition system, lighting and video system. A photographic view of the apparatus is shown in Fig. 4. Each component in the system is described separately below.

3.1 Flow Delivery Mechanisms

We have used two different flow delivery systems, one is a gravity-driven flow and the other is a constant flow rate bellows-driven flow. In the gravity-driven system, an insulated reservoir is used to generate the flow. By reviewing the recorded flow images, the mass flux in the gravity flow is estimated to be between 18-23 kg/m^{2}s which provides a liquid entering flow velocity around 3-4 cm/s.

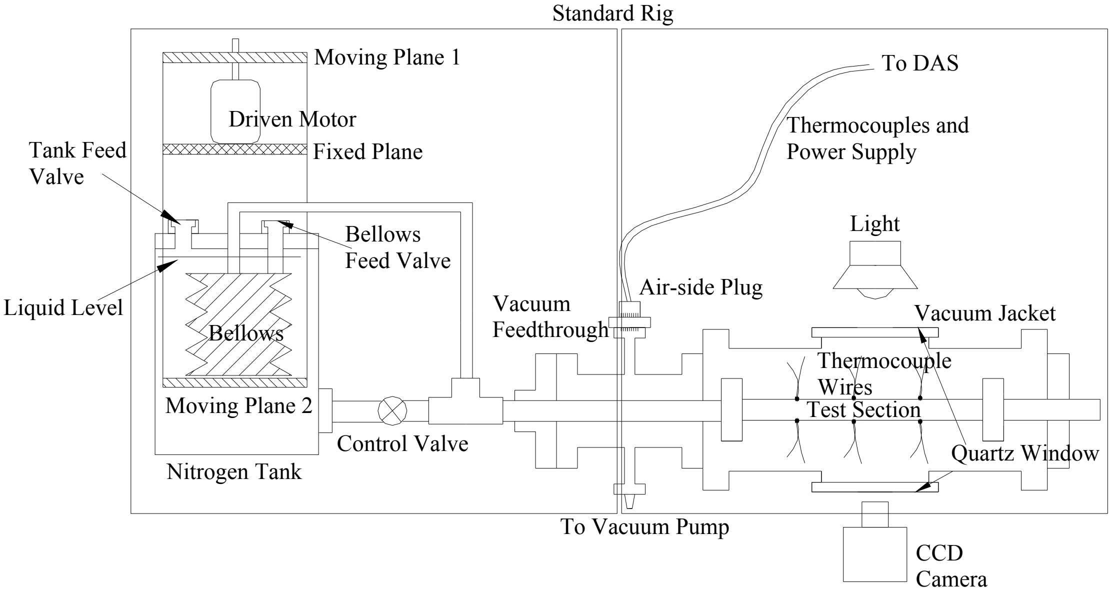

Fig. 3. Schematic of cryogenicnd two-phase flow test apparatus.

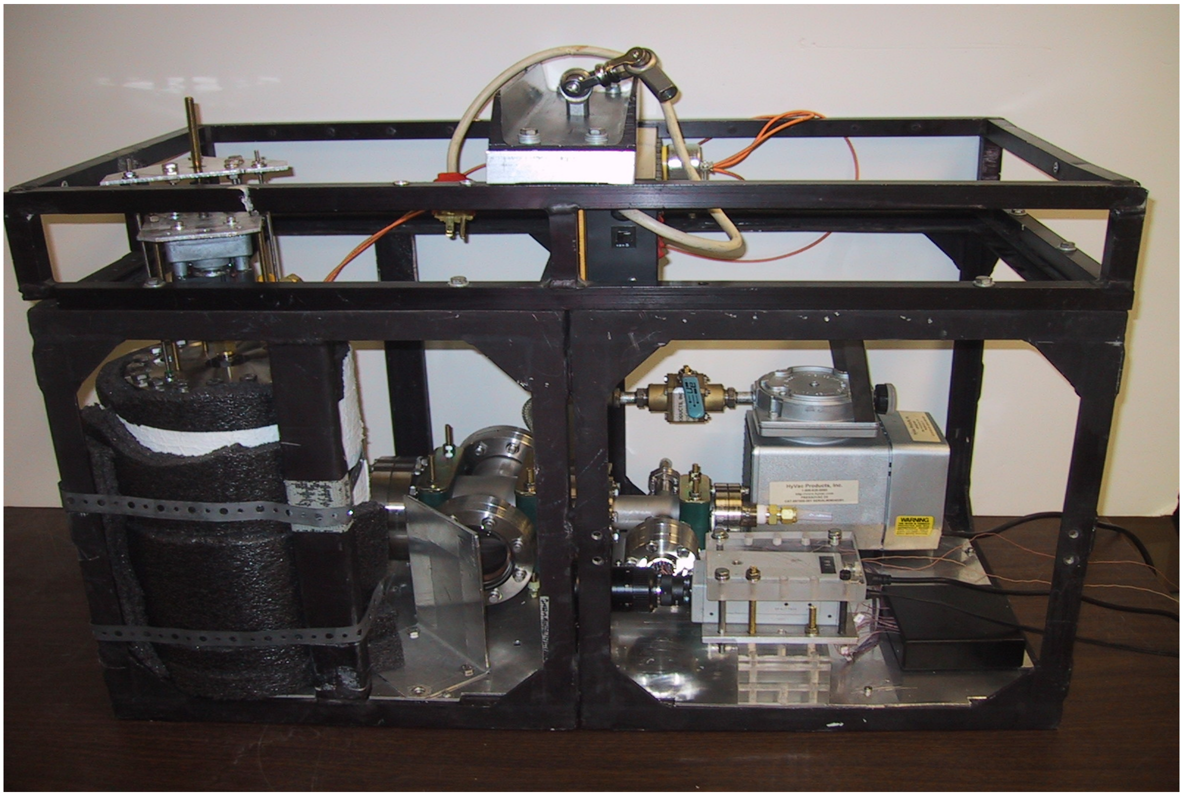

Fig. 4. Experimental apparatus located in cubicles.

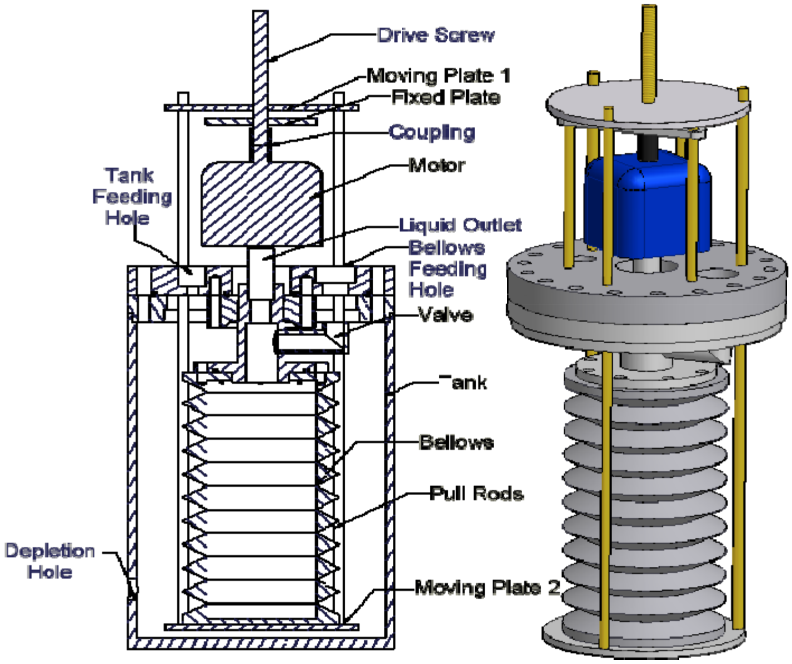

Fig. 5. Cryogenic flow driven system.

Table 1. Bellows-driven flow delivery system parameters

Motor speed (rpm)	Liquid velocity entering the test section (cm/s)	Mass flux kg/m^2s	Approximated test duration limit (minute)
5	0.446	3.606	15
10	0.891	7.205	7.5
15	1.337	10.811	5

In the bellow-driven system, we followed the traditional method to control cryogenic flow, where the nitrogen flow is generated by a motor-driven stainless steel bellows (Fig. 5). The basic idea is using a constant speed motor to pull a moving plate which is attached to the bottom of a bellows filled with liquid nitrogen. The bellows is submerged in liquid nitrogen inside a nitrogen tank. During the experiment, the state of the flow at the exit of the bellows is saturated liquid. As the bellows being compressed at a constant speed, a constant volumetric flow rate can be achieved, and the corresponding mass flow rate can be calculated. Details of the flow delivery component are given in Yuan et al. [17]. Table 1 shows the three motor speeds used in the experiment and the corresponding mass flux, flow velocity and maximum time of operation. It is noted that the bellows-driven flows are considered lower flow rates while the gravity driven flows are higher flow rates.

3. 2 Test Section

The test section is a Pyrex glass tube of 25.4 cm long. The ID and OD of the test section are 11.1 mm and 15.8 mm, respectively. The test section inlet and outlet are stainless steel tubes. At both ends of the test section, stainless steel adaptors and Teflon ferrules are used to connect the test section to the test section inlet and outlet portion.

There are nine drilled holes of approximately 2mm depth in the test section. The diameter of each hole is 1 mm. A total of 16 type-T thermocouples are placed on the test section, nine are embedded very close to the inner surface through drilled holes at three downstream cross-sections. At each cross-section, three thermocouples are located circumferentially at equal separation distance. The other seven thermocouples are used to measure the outside wall temperatures at two cross-sections, also located circumferentially at equal separation distance. The test section can be rotated along its axis before being fastened at two ends. Fig. 6 sketches the test section and the thermocouple locations in one of the tests. Fig. 7 is a photograph of the test tube with attached thermocouples.

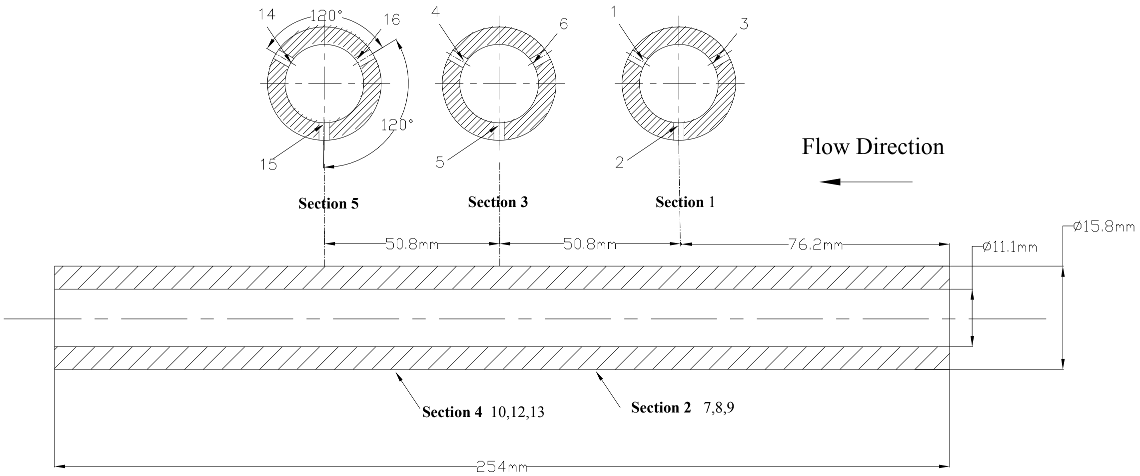

Fig. 6. Test section and thermocouple locations.

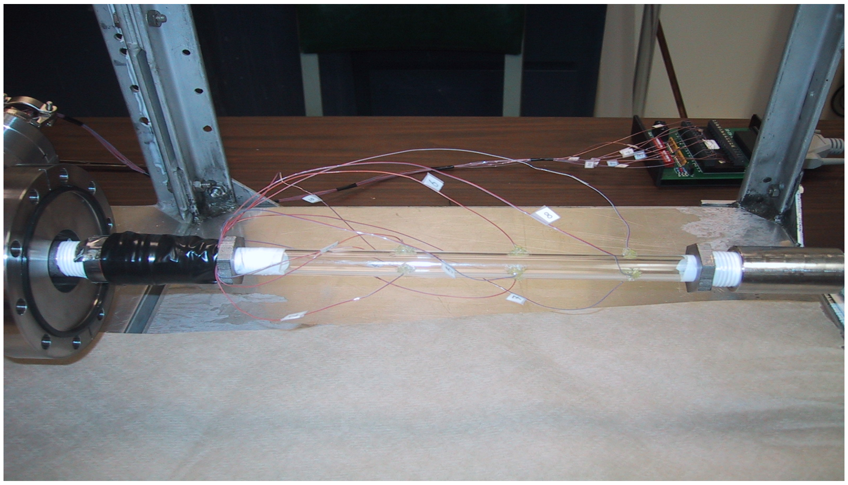

Fig. 7. Photograph of cryogenic two-phase flow test apparatus.

The test section inlet, test section and test section outlet are enclosed in a vacuum jacket built from stainless steel vacuum components. Two transparent quartz windows in the vacuum jacket enable the observation and record of the two-phase flow regimes inside the test section. The diameter of each window is 7.62 cm. A ceramic sealed vacuum feed-through flange is used to connect the thermocouple wires from the vacuum side to the air side. The vacuum is maintained by a potable vacuum pump during the experiments. A CCD camera (CV-730 from Motion

Analysis Inc.) faces one of the quartz windows to record flow images, while lighting is provided by a fluorescent light at the other widow.

3.3 Drop Tower Apparatus

The microgravity environment was provided by the University of Florida drop tower. The drop tower is 5-story high and is equipped with an airbag for deceleration. Fig.8 shows the overall drop tower schematic. At the current drop height of 15.25 m, UF's drop tower produces 1.7 sec of free fall. The experiment is actually located in a drag shield which prevents the experiment from the aerodynamic drag. As a result, the microgravity level is measured between 10^{-5} to 10^{-4} g. Details of the drop tower system and its operation are given in Yuan et al. [17].

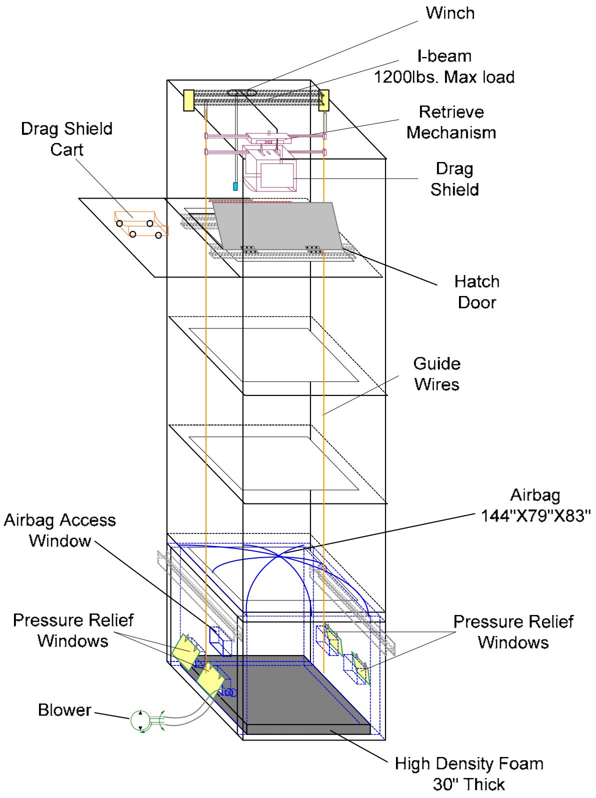

Fig. 8. A schematic of the drop tower system.

3.4 Data Acquisition Component and Experimental Uncertainties

A data acquisition system is built for recording temperatures and flow images during experiments. Type-T thermocouples (Omega) are used for temperature measurement. The thermocouples are wired to a screw terminal board and then connected to a 16-channel thermocouple board (PCI-DAS-TC from Measurement Computing) plugged into the PCI slot of a computer. All the thermocouples are tested and calibrated with boiling nitrogen prior to the chilldown experiments. A Labview program is developed to read the temperature measurements to the computer. Video images are monitored and recorded by connecting the CCD camera to a frame grabber board. A commercial software records the flow images and also shows the real-time images on the computer screen.

For the bellows-driven system, the uncertainty of mass flux mainly comes from accuracy of the driven-motor speed, and it is calculated that the relative error for mass flux measurement is 6.88%. The type-T thermocouples used for temperature measurement have the uncertainty of ±0.5 °C declared by the manufacturer. For highly transient process like chilldown the response time of the thermocouples is also important. To get quick response, the tip style of the thermocouples is chosen as exposed and the wire diameter of the thermocouples is used as smaller as possible. With the wire diameter of 0.25 mm the responding time is less than 0.2 second according to the chart given by the manufacturer.

Another uncertainty source of temperature measurement comes from the data acquisition (DAQ) system. The DAQ board for temperature measurement has programmable gain ranges and A/D pacing, and accepts all the thermocouple types. The accuracy of the measurement depends on the gain, the sample rate and the thermocouple type. The uncertainty of type-T thermocouple is ±0.9 °C for worst case from the product specification. For current experiment, the gain is set at 400 and the sample rate is about 60 Hz. It is found that the uncertainty for current settings is about ±0.3 °C. The relative error for mass flux measurement is ±6.88%.

4. Experimental Results and Discussion

During the "pipe chilldown" experiment, cryogenic transport pipes experience a fast cooling on the walls due to an initially large temperature difference (liquid nitrogen at 77K and wall at 300K). The purpose of the chilldown experiment is to provide an overall characterization of the system that includes both flow visualization and heat transfer measurements, and also to offer flow patters and heat transfer characteristics during the pipe chilldown process that takes place in many cryogenic applications in a room temperature environment. The following discussions are classified into two categories: low flow rates (bellows-driven) and high flow rates (gravity driven). In the beginning of the chilldown experiment, liquid nitrogen enters the Pyrex glass tube that is at the room temperature (25 °C). The bulk velocities of the entering liquid flows are estimated in the range of 0.5 to 4 cm/s with both gravity-driven and bellow-driven techniques. With this flow range, the role of gravity is measured by the dimensionless Froude number, Fr. which defined as the ratio of flow inertia to gravitational force, U^2/gD, where U is the entering bulk velocity, g is the gravitational acceleration constant and D is the tube diameter. If the Fr number is much larger than unity, then the flow inertia is dominant that renders the gravity insensitive. On the other hand, if the Fr number is much less than unity, then gravity is dominant. The range of the Fr number corresponding to the flow velocities between 0.5 and 4 cm/s is from 1.83×10^{-4} to 1.47×10^{-2}. Since the Fr number is less than unity by two orders of magnitude, it is safe to conclude that gravity plays an important role for both gravity-driven and bellow-driven flows, but the gravity is totally dominant for the bellows-driven case. Because the glass tube is unheated, the tube wall is going through a transient cooling process. In the following, the measured wall temperature history is presented first and then flow visualization pictures are given to provide the correlations between the wall temperature and flow pattern.

4.1 Gravity-Driven Flows – High Flow Rate Case

4.1.1 Boiling Phenomenon during Quenching

A. Terrestrial Gravity Case

For the chilldown process, the temperature histories of the tube walls were measured by the thermocouples at three downstream locations (near inlet, middle and near outlet). The results are given in Fig. 9. Based on the characteristics of the temperature history curves, the chilldown process is generally divided into three stages: (i) Film boiling, (ii) Nucleate boiling and (iii) Single-phase convection.

(i) ***Film boiling***. At the beginning of the process, the wall temperature of the test section is near the room temperature, which is much higher than the temperature of the liquid nitrogen and above the Leidenfrost pint, therefore film boiling is taking place on the tube wall surface. Based on the flow visualization presented in the next section, the initial quenching stage is associated with a hot wall which causes the two-phase flow to take the form of a vapor core with scattered small liquid chunks (Dispersed Flow Film Boiling, DFFB). In general, the temperatures measured by thermocouples that are located in the bottom of the tube (Channels 12, 15, 9, 6, and 3) are lower than those from thermocouples embedded in the upper portion. This is mainly due to the gravity effects that bring liquid fragments cooling to the bottom walls.

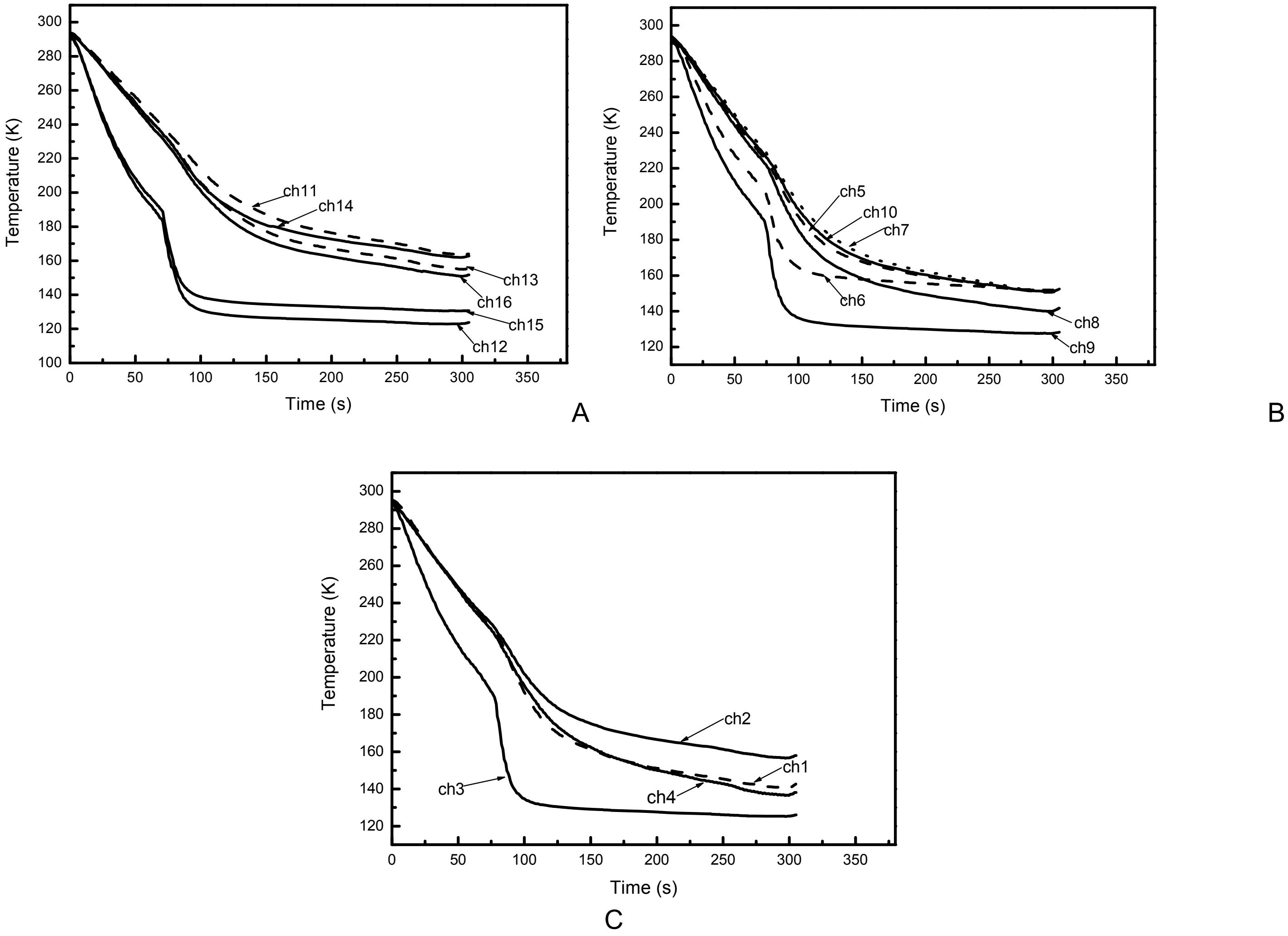

Fig. 9. Temperature profiles at three downstream locations during the chilldown process. A) Temperature profile of section 1 (near inlet), B) Temperature profile of section 2 (middle point), C) Temperature profile of section 3 (near outlet).

(ii) ***Nucleate boiling***. A distinctive character of the bottom wall temperature history is the sharp increase in the slope at the wall temperature of about 190 K. This phenomenon is seen at all three downstream locations. The physical explanation is based on the transition of boiling regimes from film boiling to transition boiling and then to nucleate boiling as mentioned earlier and shown in Fig. 1. Even though, the transition boiling regime is very short.

(iii) **Single-phase convection**. Finally when the wall is chilled down enough such that the wall temperature (<140 K, point A in Fig. 1) is too low to support nucleate boiling, the heat transfer switches to single-phase forced convective boiling

(iv) ***Chilldown boiling curve.*** A 2-D transient conduction model is used to calculate heat transfer data from the transient temperature profiles [17]. In this model, energy balance is performed locally on a control volume of the tube wall at inside wall thermocouple location. The change in stored heat in the control volume is equated to the heat transported to the fluid and heat transferred by conduction, minus losses to the environment. The error of this model is evaluated to be in the range of 5-11%.

Based on the temperature data, the heat transfer coefficient history for the bottom wall at section 1 is estimated using the temperature data and plotted in Fig. 10. Left side of Fig. 10 shows the calculated bottom wall heat flux as a function of bottom wall temperature at the outlet cross-section, while the right side represents the corresponding temperature profiles re-plotted from Fig. 9C.

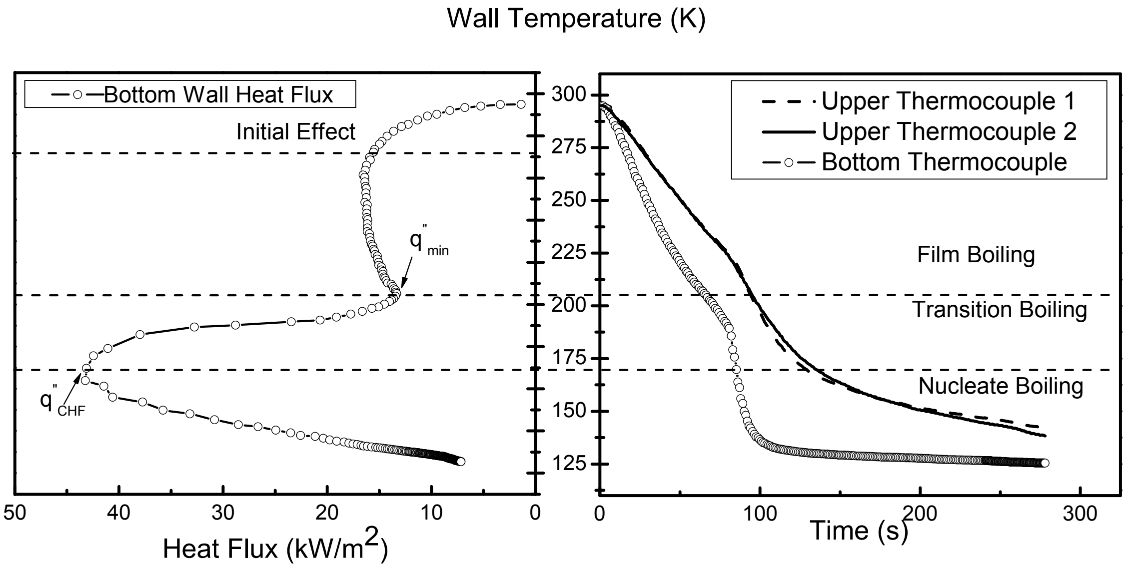

Fig. 10. Estimated heat transfer coeficient.

The shape of the heat flux on the bottom of the tube is similar to the boiling curve from steady-state pool boiling experiments. This suggests that the chilldown process may share many common features with the pool boiling process. Following the method to characterize different heat transfer mechanisms in pool boiling experiments, a local maximum or critical heat flux (CHF) q''_{CHF} and a local minimum heat flux $q''_{\min}$ are used to divide the chilldown heat transfer into three stages, which are film boiling, transition boiling and nucleate boiling, as shown in Fig. 10 similar to that defined in Fig. 1 for pool boiling.

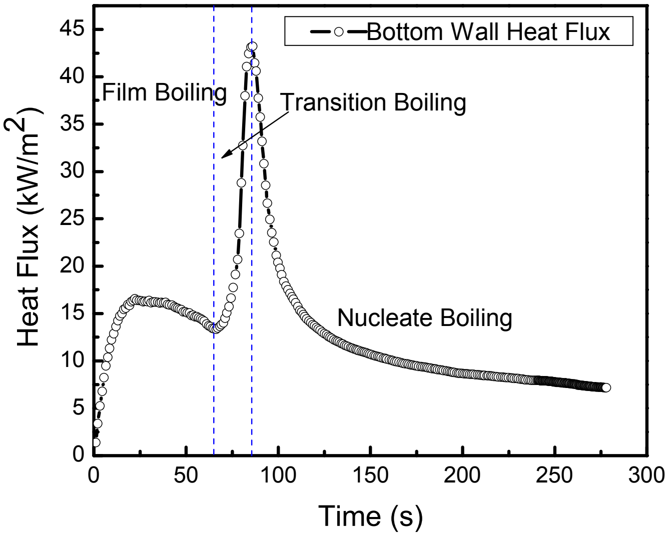

Fig. 11. Bottom wall heat flux at the outlet cross section as a function of time.

Initially, the wall temperature is very high and above the Leidenfrost point, so the liquid phase can not contact the tube wall (non-wettable). As a result, liquid nitrogen evaporates intensively when entering the test section; a vapor film blanket will cover the wall surface and separate the liquid from contacting the wall, the two-phase flow is therefore in the film boiling state. As the wall temperature decreases during quenching and drops below the Leidenfrost temperature, the liquid begins to contact the wall; the heat transfer is in the transition boiling regime, which is characterized by an increasing wall heat flux with a decreasing wall superheat that is contrary to the trends in the film boiling region and nucleate boiling region. After passing through the CHF point the heat transfer mechanism then enters the nucleate boiling regime. The calculated bottom wall heat flux as a function of time is shown in Fig. 11. It is obvious that the time of transition boiling is very short as compared with the other two boiling stages.

The similarity between the chilldown boiling curve and the pool boiling curve naturally leads one to compare the chilldown data with pool boiling correlations. The comparison between the two turning points, namely the minimum heat flux and the CHF, is given below. For a steady state film boiling, the correlation developed by Zuber [18] is widely used to predict the minimum heat flux:

$$q''_{\min} = C h_{lv} \rho_v \left[\frac{\sigma g \left(\rho_l - \rho_v \right)}{\left(\rho_l - \rho_v \right)^2} \right]^{1/4} \tag{1}$$

Here, σ is surface tension; g is gravitational acceleration; h_{lv} is the latent heat of vaporization, while *C* , a constant, was suggested by various researchers as 0.177 [18], 0.13 [19], or 0.09 [20]. The resulting $q''_{\min}$ is then 13.0 kW/m^2, 9.6 kW/m^2, or 6.6 kW/m^2, respectively. In Fig. 11, the $q''_{\min}$ for chilldown is calculated as 13.3 kW/m^2, which is slightly larger than the steady state prediction with *C* = 0.177. Based on the similarity between the CHF condition and the column flooding, Kutateladze [21] derived the following relation for the pool boiling CHF:

$$q''_{\mathrm{CHF}} = 0.131 h_{lv} \rho_v \left[\frac{\sigma g \left(\rho_l - \rho_v \right)}{\rho_v^2} \right]^{1/4} \tag{2}$$

Zuber [18] developed the identical correlation based on the analysis of Taylor and Helmholtz instability. For liquid nitrogen under the atmospheric pressure, Equation (2) gives a CHF value of 160.7 kW/m^2. The chilldown measurement in Fig. 11 is only about 27% of this value. This big discrepancy is believed to come from the following possible sources: (i) Equation (2) was developed for pool boiling over a large horizontal cylinder or a sphere, while the current case is boiling inside a small tube, and (ii) different experimental conditions between the chilldown and the pool boiling processes. In the pool boiling experiment, the heat supplied to the fluid is maintained by a heater, while in chilldown tests it comes from the stored heat in the tube wall. In the film boiling region, the heat flux is generally small, therefore the tube wall can maintain a near constant heat flux condition and function like the heater used in the pool boiling tests. However, in the transition boiling region, the stored energy in the tube wall is depleted so quickly that the experimental condition is very different form that of the pool boiling tests. The limited energy stored in the tube wall put a restriction on the value of CHF, which, therefore, is much less than the pool boiling data. Previous work by Bergles and Thompson [22] also quantitatively concluded that the differences between chilldown and steady-state boiling curves can be very large.

For Eqs. (1) and (2), the minimum heat flux and the CHF, thermal properties of the wall are not factored in the equations. However, as seen from the above, the available heat flux to the flow is closely related to the energy stored in the wall. Therefore, the thermal properties, e.g., thermal conductivity, heat capacity, of the wall are expected to play a role in the chilldown correlations. For example, for a wall with higher thermal conductivity, the energy transferred to the fluid can be more quickly supplied by the walls, and therefore it will result in a higher value of CHF.

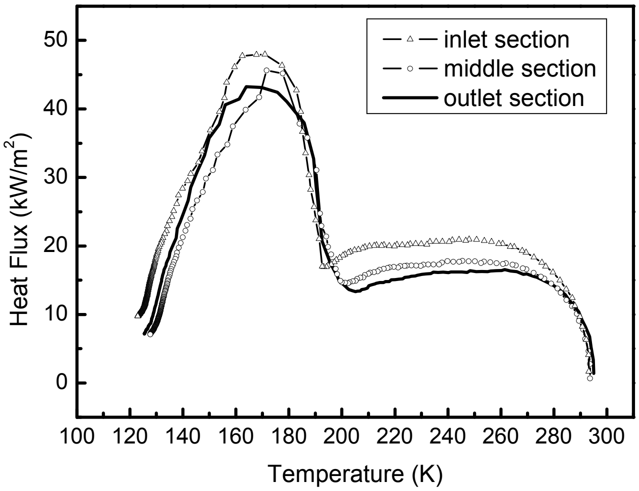

Fig. 12. Bottom wall heat fluxes at different axial locations.

Fig. 12 shows the estimated heat fluxes in different axial locations of the tube. It is found that both the CHF and the minimum heat flux decrease with increasing axial distance from the inlet. This is also associated with an increase in the rewetting temperature.

In most of the previous quenching experiments, the film boiling heat flux was reported as either a relatively constant value along the axial direction [23;24] or that it decreases downstreams as the test section is chilled down [22;25]. In our experiments, however, the local heat flux first increases in a short period then decreases gradually. This is consistent with the transient nature of the experiments. Generally the increasing period is expected to be shorter at higher mass fluxes if the other conditions are kept the same. The mass fluxes in previous investigations were much larger than that in current experiments, and therefore associated with very a short time period of increasing heat fluxes in the film boiling regime. This might be the reason that the increases of the heat flux were not recorded before.

B. Microgravity Case

Because that the gravity-driven flow delivery system could not fit into the limited two-cubicle frame as shown in Fig. 4, therefore we do not have high-flow rate microgravity results. However, the microgravity drop tower results are provided in the low flow rate section. It is also noted that the gravity effects are dominant for the low flow rate case as mentioned before. But for higher flow rates, we can speculate that the wall temperature history curve in microgravity would be very similar to those of the two upper portion locations (Ch. 11 and 14 or 13 and 16) where the walls are in contact with vapor phase only. In microgravity, there would be no stratification and a perfect inverted annular flow would prevail, which causes the vapor to cover all the tube wall and leave liquid in the central core area.

4.1.2 Two-Phase Flow Dynamics During Quenching

A. Terrestrial Condition

This phase of the experimentation was intended to provide not only some physical understanding of the two-phase flow characteristics during the chilldown process, but also the performance evaluation for the apparatus which includes both image and data acquisition.

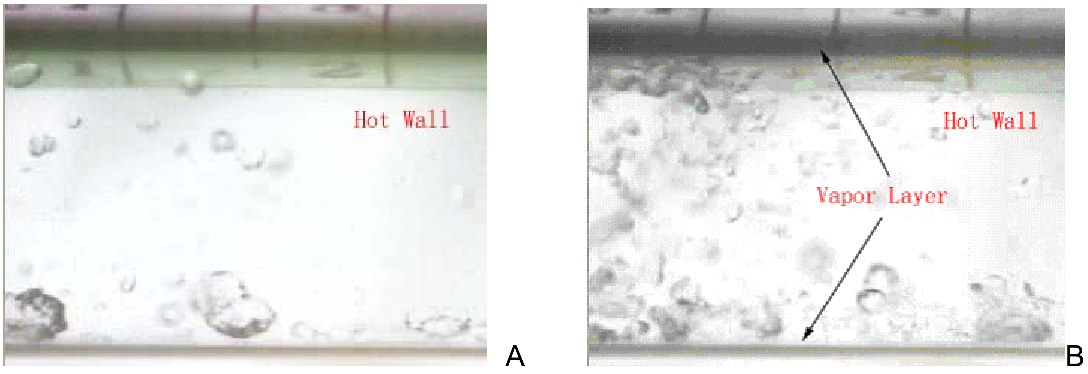

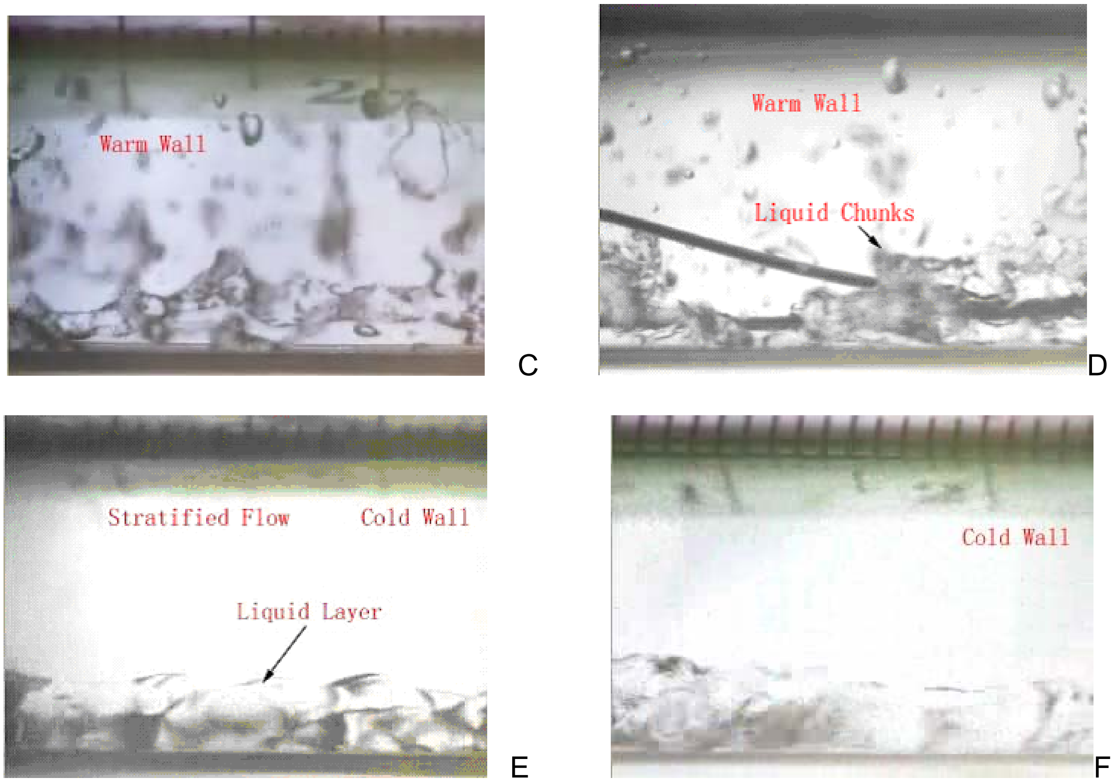

Fig.13. Two-phase flow images under 1-g condition for chilldown process. A) Initial stage of chilldown-vapor core with scattered liquid chunks, B) Initial stage – inverted annular flow, C) Transition stage, D) Transition stage, E) Cold wall – stratified flow, F) Cold wall - stratified flow.

The chilldown process is divided into three stages based on the temperature of the tube wall as discussed above. The initial stage as shown in Fig. 13A is associated with a hot wall which causes the two-phase flow to take the form of a vapor core with scattered small liquid chunks. When the wall becomes slightly cooler, the inverted annular flow is seen as given in Fig. 13B where the liquid is occupying most of the tube with a vapor layer adjacent to the tube wall. For both cases as shown in Fig. 13A and Fig. 13B, it is believed that film boiling is the main mechanism (portion between D and E in Fig. 1). When the wall temperature decreases further, the two-phase flows are experiencing a transition from the film boiling (inverted annular flow) to the stratified flow. Fig. 13C and Fig. 13D show the transition flows for warmer tube walls where liquid chunks are starting to accumulate near the bottom side of the tube wall due to the gravity effects. Finally when the wall is chilled down enough, a stable stratified two phase flow was observed. As shown in Fig. 13E and Fig. 13F, a stable and continuous liquid layer is located on the bottom of the tube and a pure vapor core is flowing on top of the liquid layer. As discussed in the previous section that for the stratified flow here, nucleate boiling (portion between A and B in Fig. 1) is taking place between the liquid layer and the cold bottom wall while the film boiling is the mode between the vapor core and the tube wall. Therefore under the stratified flow, there is a circumferential temperature variation on the tube wall.

As mentioned before, the liquid entering velocity is around 3-4 cm/s but the gravity force is still two orders of magnitude larger than the inertia force as mentioned previously. Therefore, the gravity effect overpowers the flow inertia. This is the reason why we observed the stratified flow when the wall temperature drops below the Leidenfrost point that allows the wall to be wetted by the liquid phase.

B. Microgravity Case

Fig. 14 provides a series of two pictures for the chilldown experiment in a microgravity condition. We followed a large chunk of liquid as it traveled downstream. It is seen that basically it is an inverted annular flow where the vapor is filling the tube with liquid chunks in the center. The size of the liquid chunk is decreasing due to vaporization as it flows downstream.

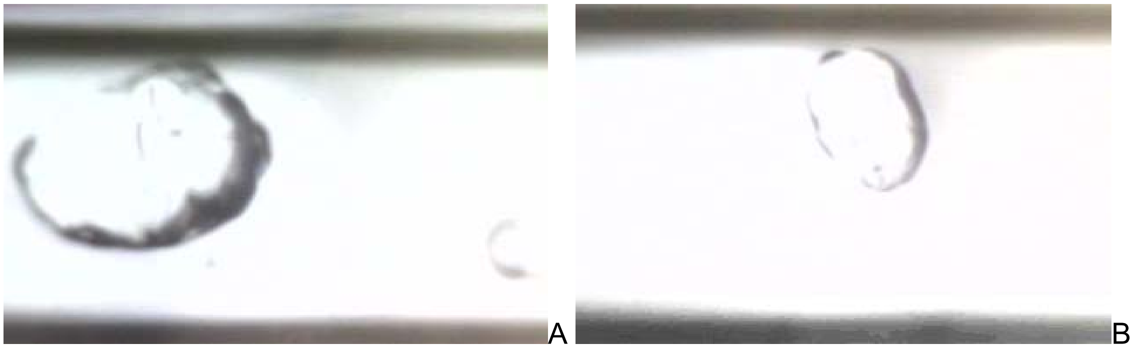

Fig. 14. Photographs of flow pattern in microgravity.

4.2 Bellows-Driven Flows – Low Flow Rate Case

4.2.1 Boiling Phenomenon During Quenching

First, for lower flow rates, the gravity dominates more than the flow inertia that makes the cryogenic transport in microgravity to behave differently from that on earth. Also as the flow rate lowers, the heat transfer generally slows down that extends the film boiling period and causes the vapor film to thicken. Especially in microgravity, there is no possibility of a stratified flow and, the heat transfer is generally lower under the microgravity condition due to the replacement of liquid filaments by the vapor film near the bottom walls that makes the chilldown even longer. In this section, the heat transfer and two-phase flow in the film boiling region during chilldown is investigated for both terrestrial and microgravity conditions.

A. Wall Temperature Profiles

To measure more data points during the microgravity period, the wall temperatures are measured only at one cross-section near the inlet. Fig. 15 gives the typical temperature profiles with three different mass fluxes.

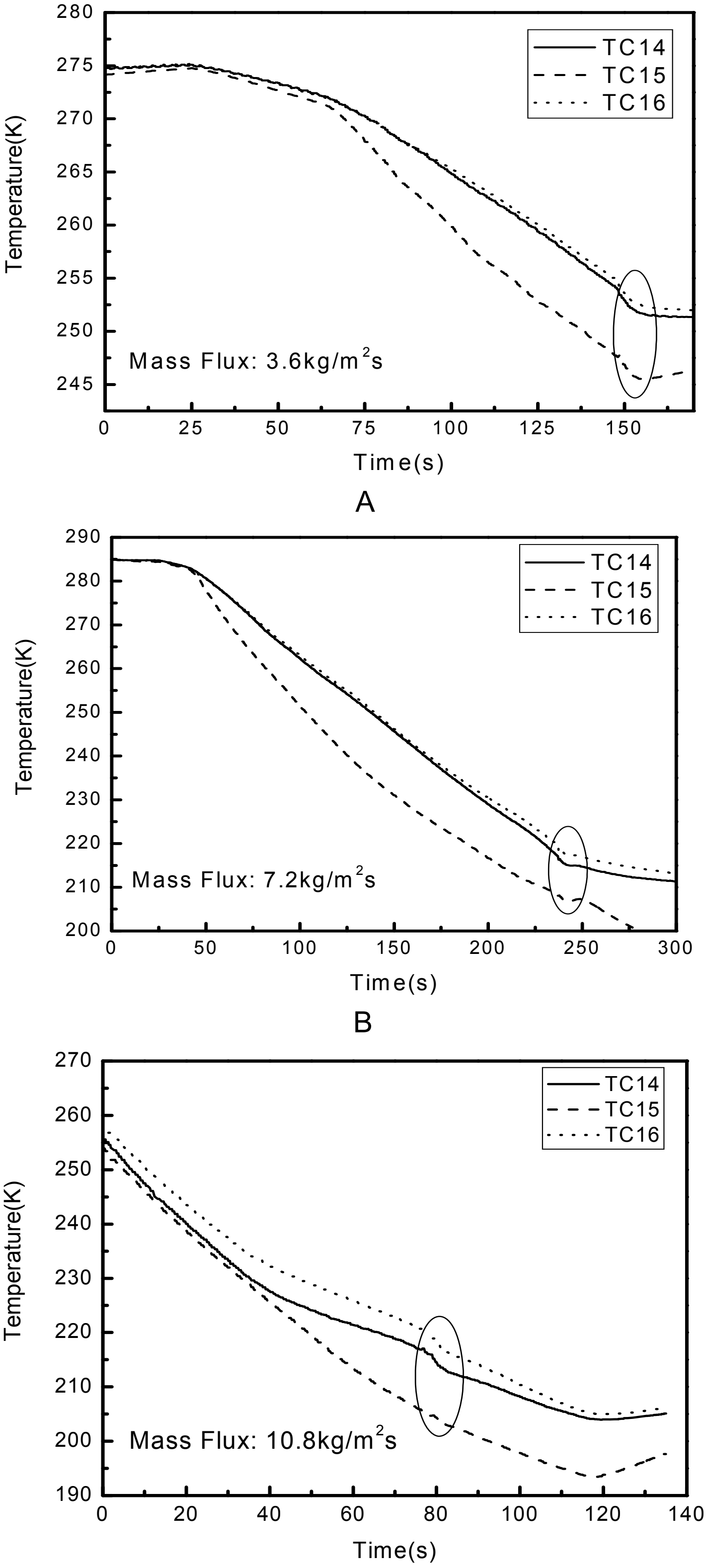

C

Fig. 15. Temperature profiles with different mass fluxes in microgravity test. A) Mass flux of 3.6 kg/m^{2}s. B) Mass flux of 7.2 kg/m^{2}s. C) Mass flux of 10.8 kg/m^{2}s.

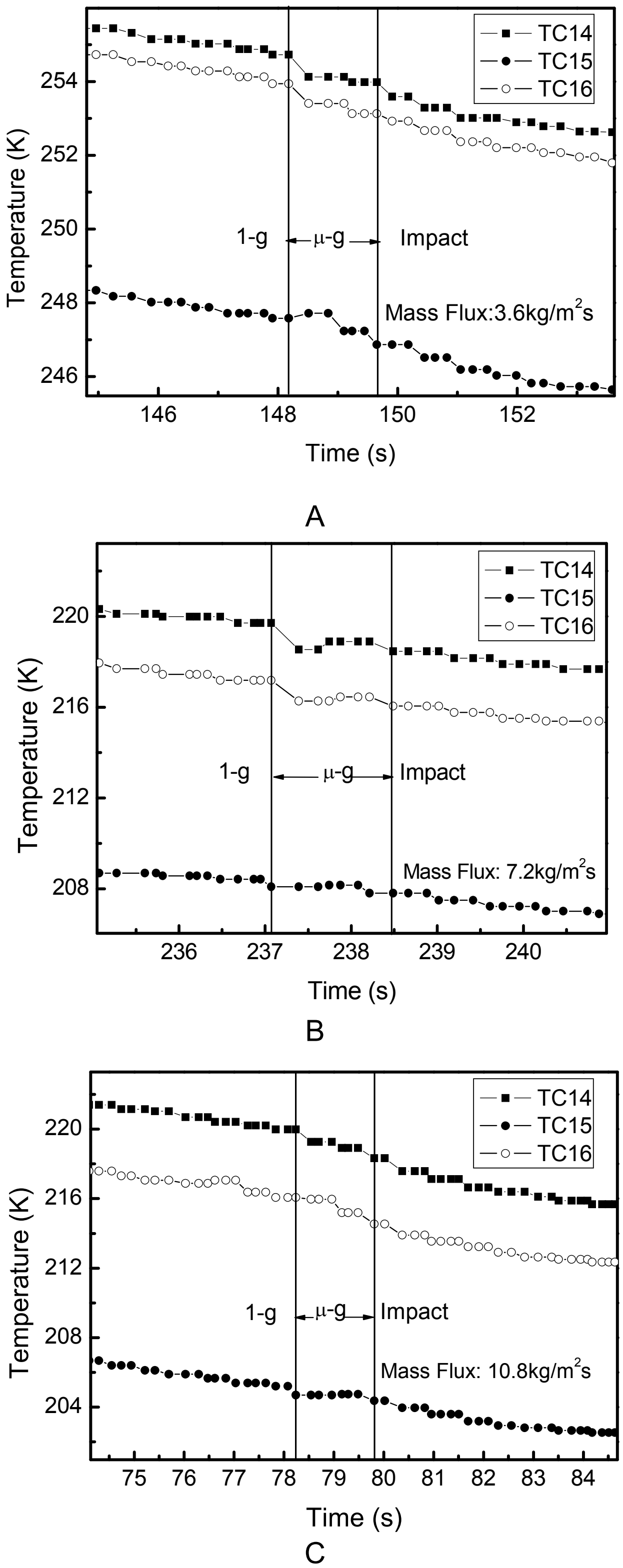

Fig. 16. Wall temperature response to microgravity. A) Mass flux of 3.6 kg/m^{2}s. B) Mass flux of 7.2 kg/m^{2}s. C) Mass flux of 10.8 kg/m^{2}s.

Based on Fig. 15, the general cooling rate of the tube wall is directly proportional to the mass flow rate of the quenching fluid. The circled temperatures in Fig. 15 approximately indicate the time period of microgravity condition during one drop, which includes the release of the drag shield, microgravity time, impact on the air bag, and deceleration period.

To examine the detail of the wall temperature response to sudden removal of the gravity force, the temperature profiles are zoomed in. Figure 16 illustrates the focused results. It is observed that the temperature decreasing rate at the bottom wall is generally slower during the microgravity period, because the removal of the gravitational force will send liquid filaments to the central core and replace them by low thermal conductivity vapor that significantly reduces the heat transfer from the wall. Since the top wall transfers heat mainly by vapor convection, the gravity field is expected to have negligible effects on the heat transfer at the top wall. For the current transient experimental condition, the best way to represent the data is to calculate the averaged heat flux which is given in the following section.

B. Wall Heat Flux

The gravity effect is shown in Fig. 17, in which the ratio of bottom heat flux before drop and during drop is plotted for different flow rates. The heat flux at the bottom of the tube decreases under microgravity condition and the ratio varies from a minimum of about 0.66 to about 0.90. The result does not show a strong dependence on wall temperature and inlet flow rate. Two runs of the quenching test performed by Xu [26] reported similar ratio of 0.7 and 0.8, however, in Westbye et al. [23], this ratio was found to be much less and ranged from 0.15 to 0.6.

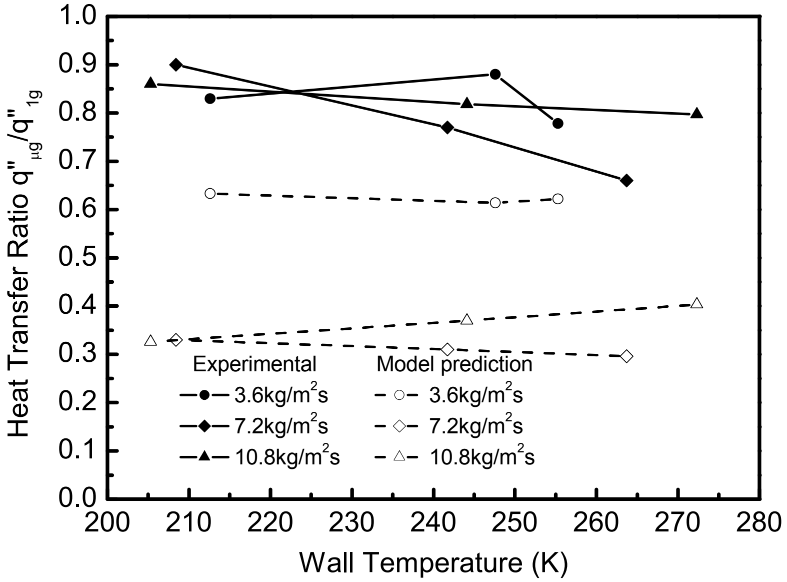

Fig. 17. Ratio of heat flux under microgravity to 1-g condition with different flow rates and comparison with model prediction.

The bottom wall is subjected to film boiling through the liquid filaments near the wall and the convection to the super heated vapor phase. For the film boiling part, the heat flux and the heat transfer coefficient are proportional to $(a/g)^{1/3}$ as suggested by Merte and Clark [27]. Assuming that the convection is not affected by the microgravity condition, the resulted heat flux ratio is shown in the dash line in Fig. 17; the gravity level in this calculation is 10^{-4}g. The calculation results are much scattered and significantly less than the experimental values. This suggests that under microgravity condition, the effect of convection part may raise the heat flux, and therefore the total effect of the microgravity is less prominent than that in the pool boiling experiments.

4.2.2 Two-Phase Flow Dynamics during Quenching

The flow patterns before (terrestrial gravity) and during drop (microgravity) are compared in Fig. 18 for lower flow rates. The images on the left are taken before the drop, while the microgravity images are on the right.

For all the terrestrial cases, they are all stratified flows. For Fig. 17A the mass flow rate is the lowest, so the liquid flow is in the form of chucks on the bottom wall. For higher flow rates in Figs. 17C, 17E, and 17G, the liquid flow on the bottom is in a continuous stream. Different flow behaviors have been recorded during the microgravity period. If the liquid phase before drop is dispersed liquid chunks on the bottom wall, these liquid chunks will enter the central core region still as chunks or stretched ligaments shown in Fig. 17B during the microgravity period. For higher flow rates where continuous liquid filaments are on the bottom in earth gravity, these filaments are lifted up and still maintain their original shapes during the microgravity period (Fig. 17D). In some other cases for even higher flow rates, the larger liquid filaments are broken and dispersed into the central region (Fig. 17F) or has a liquid-vapor core in the center and smaller chunks at both top and bottom (Fig. 17H).

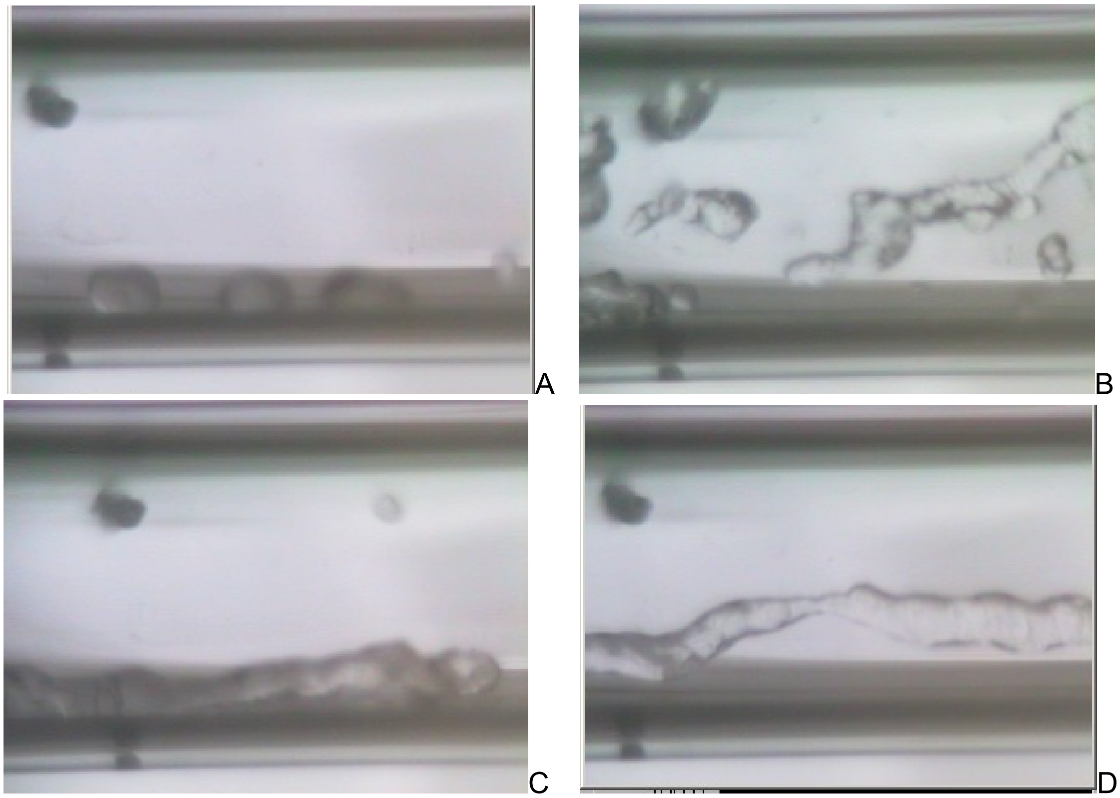

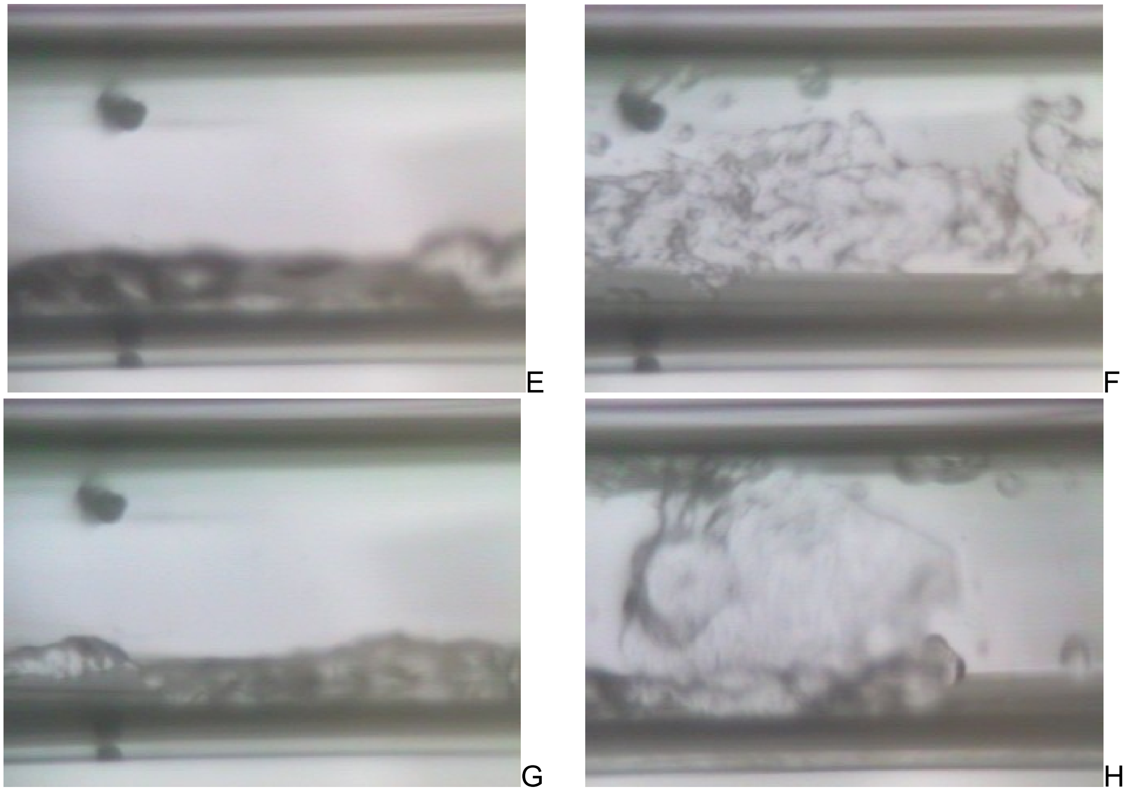

Fig. 18.Two-phase flow images under both 1-g and microgravity conditions. A) 1-g case 1, B) Microgravity case 1, C) 1-g case 2, D) Microgravity case 2, E) 1-g case 3, F) Microgravity case 3, G) 1-g case 4, H) Microgravity case 4

5. Conclusion

This research is aimed at the fundamental understanding of the cryogenic chilldown phenomena inside a pipe in terrestrial gravity and microgravity. An experimental system was designed, built and calibrated. The microgravity environment was simulated in a 1.7-second drop tower. Flow patterns and wall temperature history during the chilldown were obtained for a range of different flow rates. The wall temperature histories were measured at three downstream locations. Primarily we found that the terrestrial chilldown process is divided into three stages based on the temperature of the tube wall. These stages are film boiling, nucleate boiling and single-phase convection that carries a close similarity to the pool boiling mechanisms. In general, the cooling rate of the tube wall is proportional to the mass flow rate of the quenching flow. In microgravity, there is no stratified flow and because the removal of the gravitational force will send liquid filaments to the central core and replace them by low thermal conductivity vapor that significantly reduces the heat transfer from the wall. Thus, the chilldown process is even longer in microgravity.

6. Patents, Publications and Presentations

6.1 Patents

There was no patent application.

6.2 Publications and Presentations

1. J. N. Chung, "Cryogenic Two-Phase Flow and Heat Transfer During Pipe Chilldown" AIAA Paper 2004-2175, an I*nvited key-note paper at the 37th AIAA Thermophysics Conference*, 12 pages, Portland, OR, June 28 - July 1, 2004.

2. Kun Yuan, J. N. Chung, Yan Ji, Cryogenic Two-Phase Flow and Heat Transfer under Terrestrial and MicroGravity, ASME Int. Mech. Eng. Congress (IMECE) paper 82613, pp. 1-8, Orlando, Nov. 2005.

3. Kun Yuan, Yan Ji and J. N. Chung, “Cryogenic Chilldown Process under Low Flow Rates”, *Int. J. Heat and Mass Transfer*, Vol. 50, pp. 4011-4022, (2007).

4. Kun Yuan, Yan, Ji, J. N. Chung and Wei Shyy, “Cryogenic Boiling and Two-Phase Flow During Pipe Chilldown in Earth and Reduced Gravity”, *J. Low Temperature Physics*, Vol. 150, pp. 101-122, (2008).
5.. Yan Ji, Kun Yuan, J. N. Chung, “Numerical Modeling of Cryogenic Quenching Process in Terrestrial Gravity and Microgravity”, In revision for publication, *International Journal of Heat and Fluid Flow*, (2008).

7. Students from Research

Kun Yuan, Ph.D., August, 2006, currently employed by Doty Scientific Inc. in South Carolina.

8. Funding obtained by leveraging NASA Grant

$200k, Office of Naval Research STTR Project entitled Dodecane Reforming for SOFCs, Phase II, August 2006 - March 2008, Funding through InnovaTek Inc. Richland, WA.

9. Collaborations

1. Dr. Jim Klausner, Department of Mechanical and Aerospace Engineering, University of Florida.
2. Dr. Gary Ihas, Department of Physics, University of Florida.

10. Acknowledgments

Partial support by the Andrew H. Hines, Jr./Progress Energy Endowment Fund is also acknowledged.

11. References

[1] V. K. Dhir, R. B. Duffey and I. Catton, *Journal of Heat Transfer* **103**, 293 (1981).
[2] B. D. G. Piggott and D. T. C. Porthouse, *Nuclear Engineering and Design* **32**, 171 (1975).
[3] A. Yamanouchi, *Journal of Nuclear Science Technology* **5**, 547 (1968).
[4] R. B. Duffey and D. T. C. Porthouse, *Nuclear Engineering and Design* **25**, 379 (1973).
[5] T. S. Thompson, *Nuclear Engineering and Design* **31**, 234 (1974).
[6] K. Adham-Khodaparast, J. J. Xu, and M. Kawaji, *J. Int. Heat and Mass Transfer* **38**, 2749 (1995).
[7] Committee on Microgravity Research, Microgravity research in support of technologies for the human exploration and development of space and planetary bodies. National Academy Press, Washington, D.C (2000).

[8] E. G. Brentari, P. J. Giarratano and R. V. Smith, *NBS Technical Note* **317**, National Bureau of Standards (1965).
[9] S. S. Kutateladze, Heat transfer in condensation and boiling. State Sci. and Tech. Pub. Of Lit. on Machinery, Moscow (Atomic Energy Commision Translation 3770, Tech. Info Service, Oak Ridge, Tennessee (1952).
[10] B. P. Breen and J. W. Westwater, *Chem. Engr. Progr.* **58**, 7, 67 (1962).
[11] J. D. Seader, W.S. Miller and L. A. Kalvinskas. Boiling heat transfer for cryogenics. NASA Contractor Report CR-243 (1965).
[12] M. M. Shah, Cryogenics **24**, 231 (1984).
[13] S G. Kandlikar, *ASME J Heat Transfer* **112**, 219 (1990).
[14] K. E. Gungor and R. H. S. Winterton, *Chem. Eg. Res. Des.* **65**, 148 (1987).
[15] N. T.Van Dresar, J. D.Siegwarth and M. M. Hasan, *Cryogenics* **41**, 805 (2002).
[16] B. N. Antar and F. G. Collins, *Int. Journal of Microgravity Science and Technology* **3**, 118 (1997).
[17] K. Yuan, Y. Ji and J. N.Chung, *J. Int. Heat and Mass Transfer* **50**, 4011 (2007).
[18] N. Zuber. Hydrodynamic aspects of boiling heat transfer. Ph.D. dissertation, UCLA (1959).
[19] N. Zuber, *ASME Journal of Heat Transfer* **80**, 711 (1958).
[20] P. J. Berenson, *ASME Journal of Heat Transfer* **83**, 351 (1961).
[21] S. S. Kutateladze, *Kotloturbostroenie* **3**, 10 (1948).
[22] A. E. Bergles and W. G. Thompson, *J.Int. Heat and Mass Transfer* **13**, (1970).
[23] C. J.Westbye, M. Kawaji and B. N. Antar, *AIAA Journal of Thermophysics and Heat Transfer* **9**, 302 (1995).
[24] S. C.Cheng and H. Ragheb, *International Journal of Multiphase Flow* **5**, 281 (1979).
[25] E. N. Ganić and W. M. Rohsenow, *Journal of Heat and Mass Transfer* **20**, 855 (1977).
[26] J. J. Xu . Flow boiling heat transfer in the quenching of a hot surface under reduced gravity conditions. Ph.D. dissertation, University of Toronto (1998).
[27] H. Merte and J. A. Clark, *ASME Journal of Heat Transfer* **86C**, 315 (1964).

6. Development of Nanocrystalline Complex Metal Hydrides for Hydrogen Storage

Task PI: Dr. Fereshteh Ebrahimi, Material Science & Engineering, University of Florida

Graduate Student: Sankara Tatiparti, Material Science & Engineeringm, University of Florida

Research Period: August 3, 2004 to March 31, 2007

Abstract

The objective of this work was to synthesize, via electrodeposition techniques, nanocrystalline Mg and Al alloys which can potentially be used for producing metal hydrides with low hydrogenation/dehydrogenation temperature, fast kinetics and reasonable gravimetric storage capacity. We have been successful in fabricating Al-Mg alloys in the form of porous powder. The composition of the deposits was varied with changing the amount of magnesium ions introduced into the electrolyte by a pre-electrodeposition process. The effects of current density and cathode material (copper versus graphite) were investigated. It was shown that the alloy powders, depending on the magnesium content, consisted of fcc Al-Mg and/or hcp Mg-Al supersaturated solid solutions. No intermetallics were found in the as-deposited powders. The maximum solubility of Mg in Al was found to be approximately 20at%, but supersaturated Mg phase with as high as 40at%Al was observed. TEM studies revealed that the grain size of these powders is ultra-fine. Low temperature heat treatments elucidated that the supersaturated aluminum has a higher thermal stability than the supersaturated magnesium alloy does. We have been able to secure funding from National Science Foundation (DMR-0605406) for continuation of this work.

Accomplishments

1. Electrodeposition set-up

We finished the installation of the glove box and the electrodeposition cell was prepared to fit our needs. Figure 1 presents the electrodeposition set-up. Since Al and Mg cannot be deposited from aqueous solutions, we have to use organometallic-based electrolytes. These materials are highly sensitive to the oxygen and moisture, and therefore, an atmosphere of less than 5 ppm moisture and 1 ppm of oxygen has to be maintained during mixing of chemical and electrodeposition using the glove box.

We employed a rotating cylinder cell design with pure copper as the substrate. The potential or current was controlled using a PAR 273 Potentiostat/Galvanostat, which was interfaced with a computer. For the reason of moisture and oxygen sensitivity of the electrolyte a non-aqueous Ag/AgCl reference electrode in a 1 molar LiCl in ethylene glycol monobutyl ether solution was used. The copper electrode was electropolished outside the glove box using a 82.5% phosphoric acid + 17.5% de-ionized water solution at a potential of 0.6V (SCE) at room temperature using a stainless steel cathode and then it was transferred inside.

2. Electrodeposition of pure aluminum

Prior to the deposition of Al-Mg alloys, the electrodeposition of the aluminum was attempted to serve as trial run on the organometallic chemical to be used as the main component of the electrolyte. The electrolyte used was made of NaF, $AlEt_3$, Toluene as suggested by Lehmkuhl et al. [1]. Electrolyte compositions with two different compositions, namely NaF+(2 or 4mol) $AlEt_3$ (where Et = $-C_2H_5$) +(3 or 6mol) Toluene were studied. Toluene a solvent and NaF + $AlEt_3$ form a complex according to the equation 1.

$$NaF + 2Al(Et)_3 \rightarrow Na[Et_3Al\text{-}F\text{-}AlEt_3] \quad (1)$$

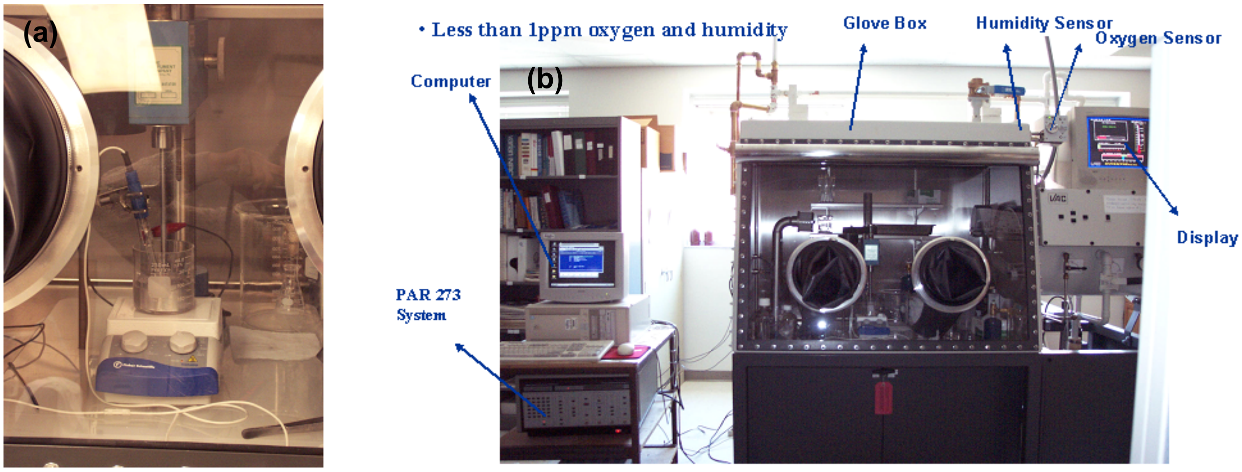

Figure 1. Pictures of deposition set-up (a) and the glove box (b) used for the deposition of pure Al.

Prior to electrodeposition, cyclic voltammetry was conducted in order to select the suitable potential for the deposition of aluminum powders. The cyclic voltammetry curve is shown in Figure 2. The fluctuations in the curve are due to the rotation of the copper cathode at 400 rpm.

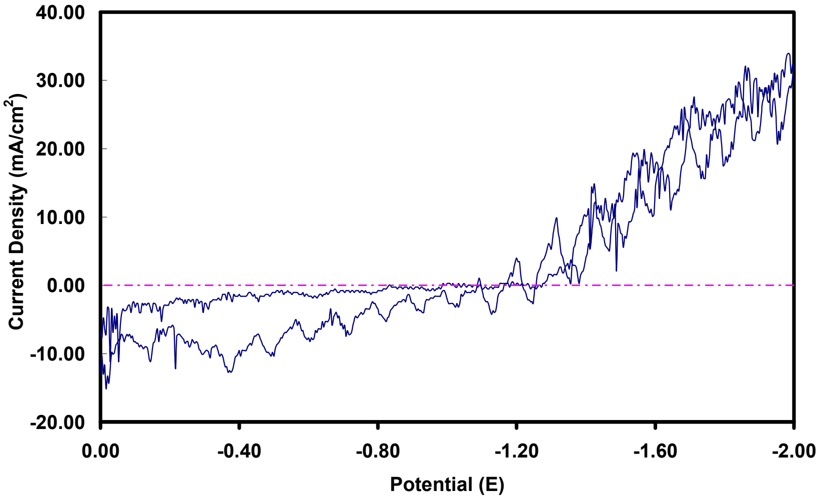

Figure 2. Cyclic voltametery results with a scan rate of 3.33 V/s at 75°C and rotation speed of 400 rpm. Potential is measured versus Ag/AgCl reference electrode.

A potential of -1.5 V was selected for the electrodeposition of aluminum based on the voltametery results. The deposition was conducted potentiostatically at 75 °C for 15 minutes with cathode rotation of 400 rpm. Figure 3(a) presents the current density versus time curves for the two electrolyte compositions. Since only complexes liberate the Al^{+3} ions to be deposited, according to equation (1), the electrolyte containing the 1:2 ratio of Na:$Al(Et)_3$ will have a higher concentration of complexes than the electrolyte with 1:4 ratio. The higher current density observed using the former electrolyte can be attributed to the higher concentration of the available Al^{+3} ions. Figure 3(b) shows a low magnification picture of the copper electrode with the aluminum deposit on it.

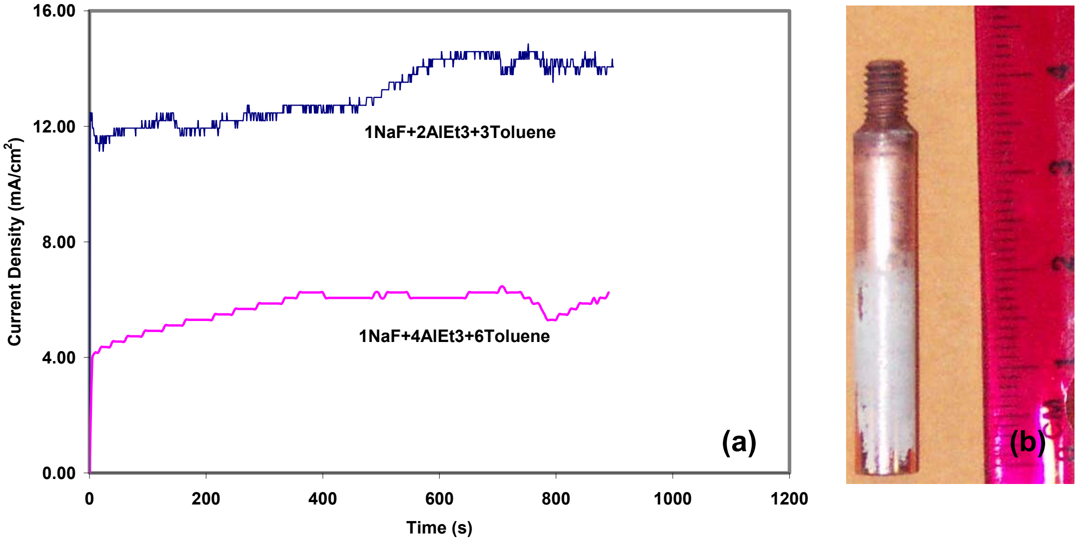

Figure 3. (a) Current density as a function of time for potentiostatic deposition of pure Al using two different electrolyte compositions. (b) Copper electrode with deposited aluminum.

The SEM (scanning electron microscope) images of the deposits of pure Al are shown in Figure 4. It can be observed that the morphology and the size of powders depend on the electrolyte composition. A higher concentration of available Al^{+3} (NaF: $Al(Et)_3$ ratio of 2) and the resultant higher current density led to a deposit with a much smaller powder size (Figure 4a). This observation is consistent with the theoretical prediction that the nucleation rate should increase with increasing the current density.

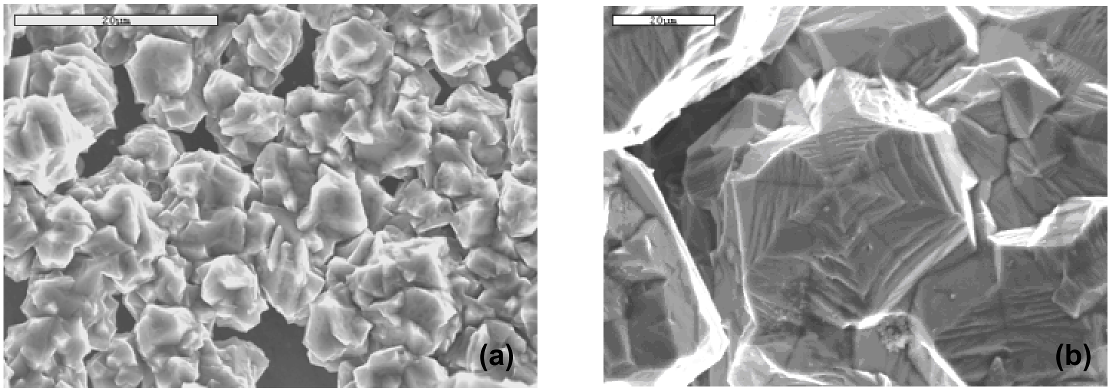

Figure 4. SEM pictures of deposits made with (a) NaF: $Al(Et)_3$ ratio of 2, and (b) NaF: $Al(Et)_3$ ratio of 4.

Figure 5 presents the energy dispersive spectra (EDS) showing that the deposit consisted of pure aluminum. The x-ray diffraction (XRD) profile of the pure aluminum powder is shown in Figure 6.

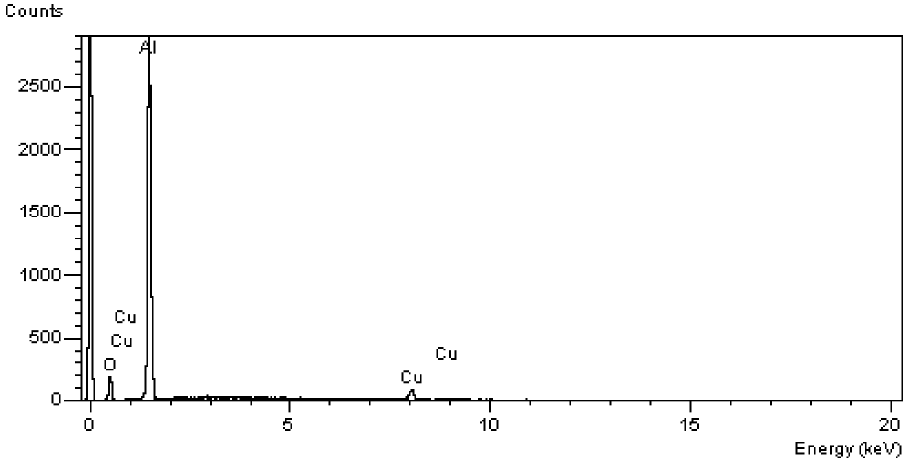

Figure 5. EDS spectra of an Al deposit. The Cu peak is due to the residue from the substrate.

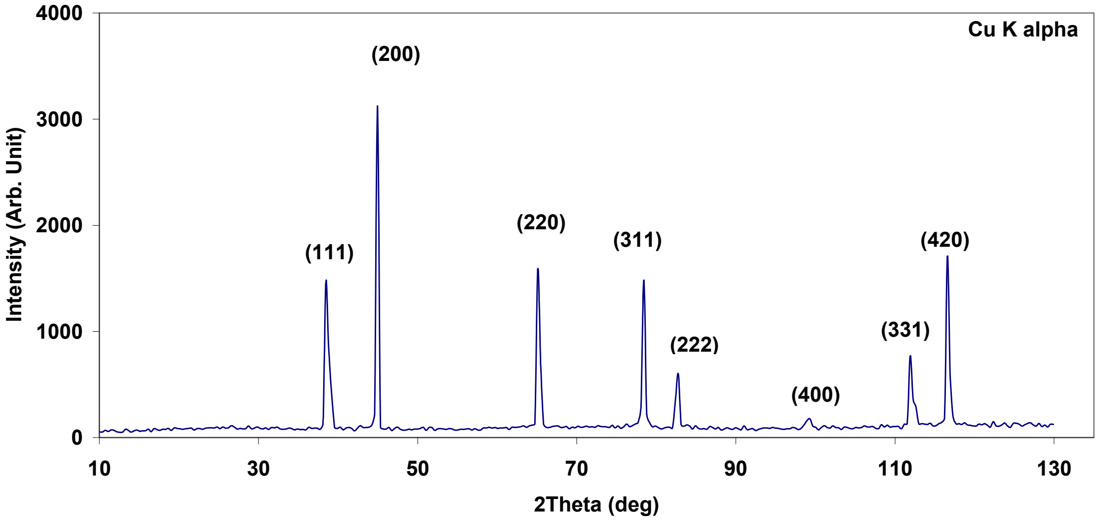

Figure 6. XRD profile for pure aluminum deposits.

3. Electrodeposition of aluminum-magnesium alloys

For making Al-Mg alloys, magnesium can be introduced as diethyl- or dimethyl-magnesium into the electrolyte [2], however, the transportation of these materials is not allowed in the US. An alternative method to introduce Mg is to use a magnesium anode, which dissolves during the deposition and provides the necessary Mg for forming complexes. It has been demonstrated that an electrolyte with $Na[AlEt_4]/2Na[Et_3Al\text{-}H\text{-}AlEt_3]/2AlEt_3/6$ toluene will allow the dissolution of Mg at anode [3,4]. The $Na[AlEt_4]$ can be produced by reaction of 3Na with $4AlEt_3$ or by reaction of NaH with $AlEt_3$ in the presence of ethylene [4]. In this case a pre-electrolysis should be carried out to increase the Mg content in the electrolyte before the actual deposition.

We attempted to prepare several electrolytes using different procedures. After many trials we were successful in establishing the correct procedures for preparing the electrolyte and pre-electrolysis. We reduced the electrolytic cell size from 100 ml to 30 ml to decrease the chemical waste. Based on our studies, we improved our technique for producing $Na[AlEt_4]$ and selected galvanostatic pre-electrolysis at a current density of 60 mA/cm^2 and temperature of 90 ^oC with a cathode rotation speed at 200 rpm.

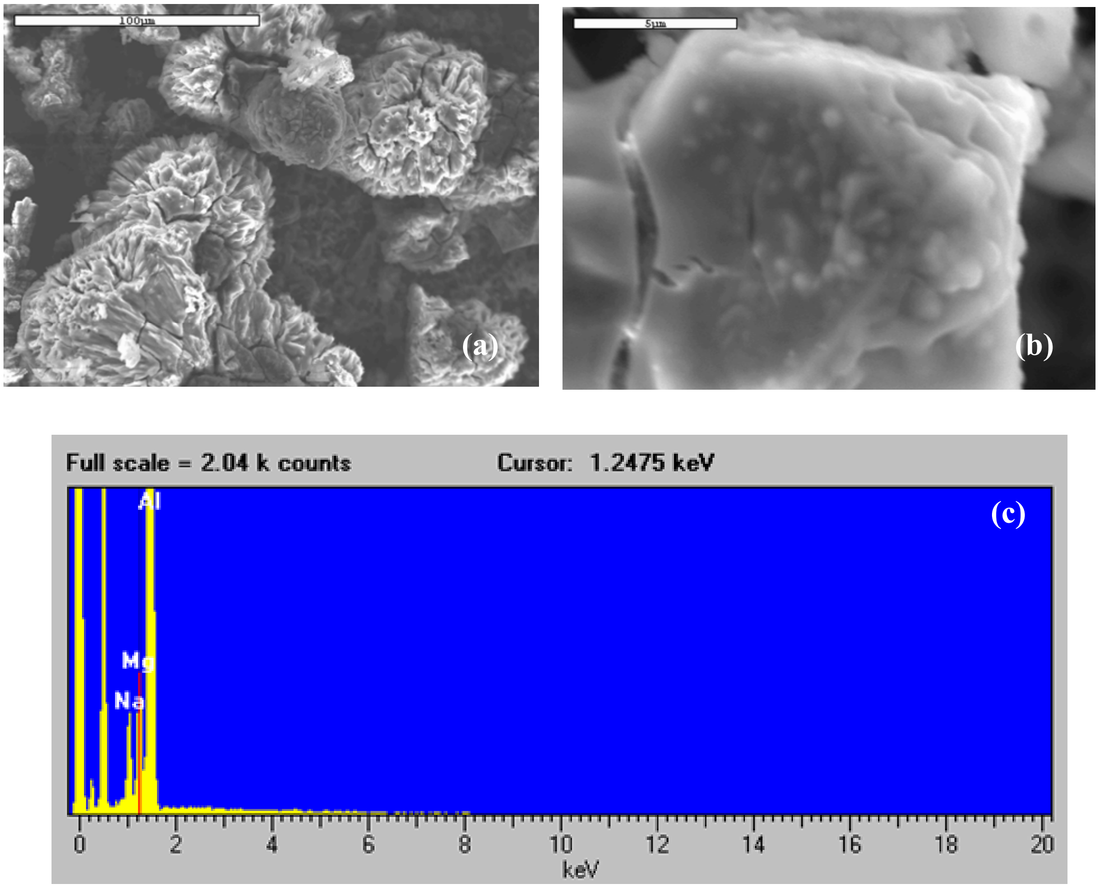

Figure 7. (a) Low and (b) high magnification SEM pictures of the deposit with 5.5 at.%Mg. (c) EDS profile.

In order to minimize the deposition of sodium we added an excess of 0.5 M of $AlEt_3$ to our electrolyte containing $Na[AlEt_4]$, 2M $Na[Et_3Al\text{-}H\text{-}AlEt_3]$, 2M $AlEt_3$ and 6M toluene. We varied the duration of the pre-deposition from 30 min to 4 hours 25 min to establish the composition of the deposits as a function of the pre-electrolysis time. The composition as a function of the time is shown in Figure 7. It should be noted that this concentrations of Mg and Na were evaluated using EDS in SEM and therefore, they represent approximate values. The curve has a parabolic shape suggesting that a steady state can be reached at long times (or high Mg concentrations) where the amount of Mg dissolved from the anode becomes equal to the amount of Mg deposited, which results in a constant deposit composition. It is expected that this saturation concentration can be modified using anodes made of Al as well as Mg. The amount Na was reduced but it was not completely eliminated.

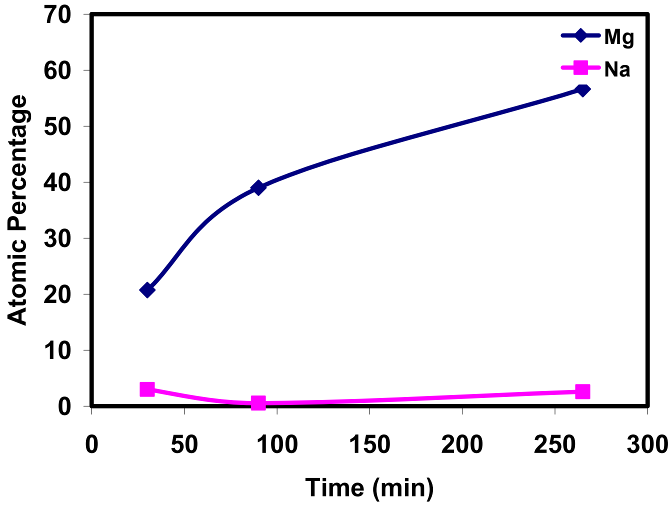

Figure 8. The approximate composition of the Al-Mg alloys as a function of the duration of electrodeposition.

All three deposits whose compositions are given in Figure 8 exhibited dendritic growth as shown in Figure 9. The size of the dendrite arms became smaller and more directional as the amount of Mg in the alloy was increased.

The XRD results for the Al-Mg deposits are presented in Figures 10 through 12. These results indicated that the 20 at.% Mg deposits was in a supersaturated condition containing only the solid solution of magnesium in aluminum. The 40 at.% Mg deposit consisted of supersaturated solid solution of magnesium in aluminum along with Al_3Mg_2 intermetallic. The 60 at.% Mg deposit contained both Al_3Mg_2 and $Al_{12}Mg_{17}$ intermetallics. Again, the presence of Cu is due fact that some copper was scraped from the substrate during the removal of the deposited alloys.

Our objective is to fabricate supersaturated nanocrystalline Al-Mg alloys with approximately of 25-35 at.% Mg. A recent study of sputtered Al-Mg alloys indicate that this range of composition may result in the formation of magnesium alanate, $Mg(AlH_4)_2$ upon hydrogenation [5]. We have been successful in preparing supersaturated solid solution of Al-Mg. The next step is to design deposition schemes that result in more precise composition control with least variation as well as smaller powders with minimum grain size.

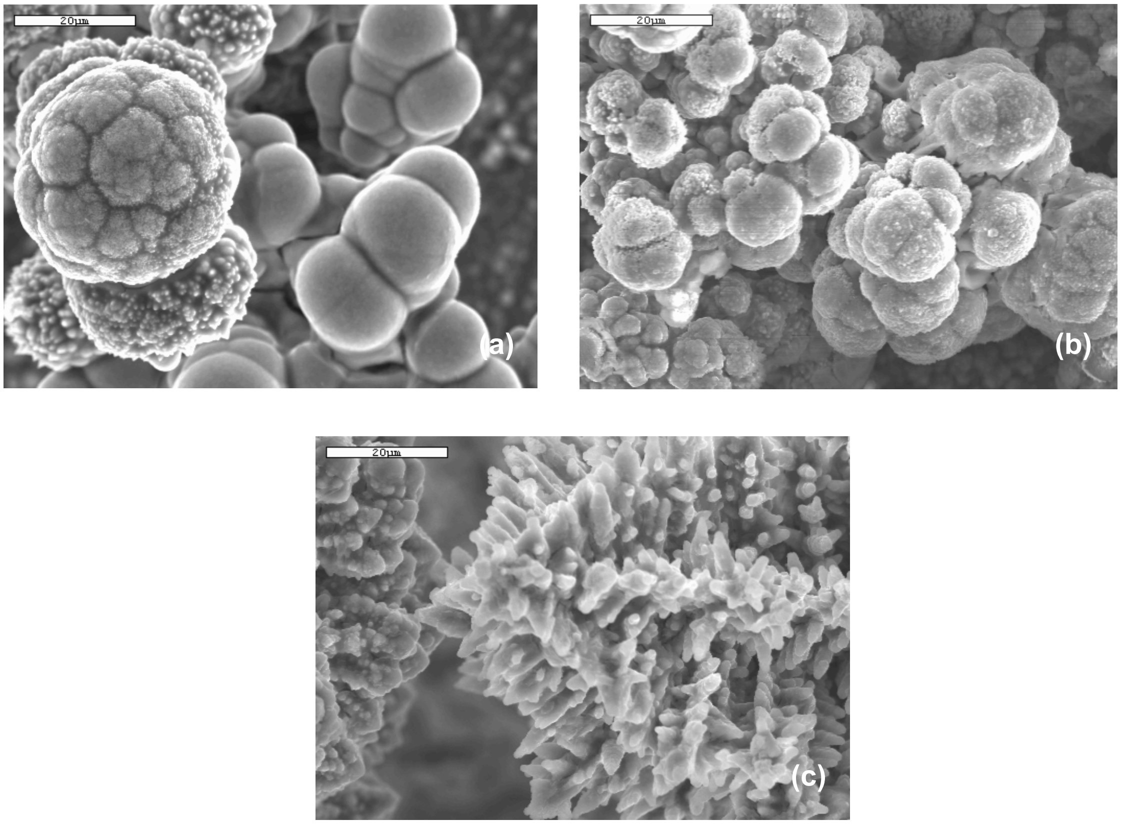

Figure 9. SEM pictures showing the morphology of the deposits with nominal compositions of (a) 20 at.%Mg, (b) 40 at.%Mg, and (c) 60 at.%Mg.

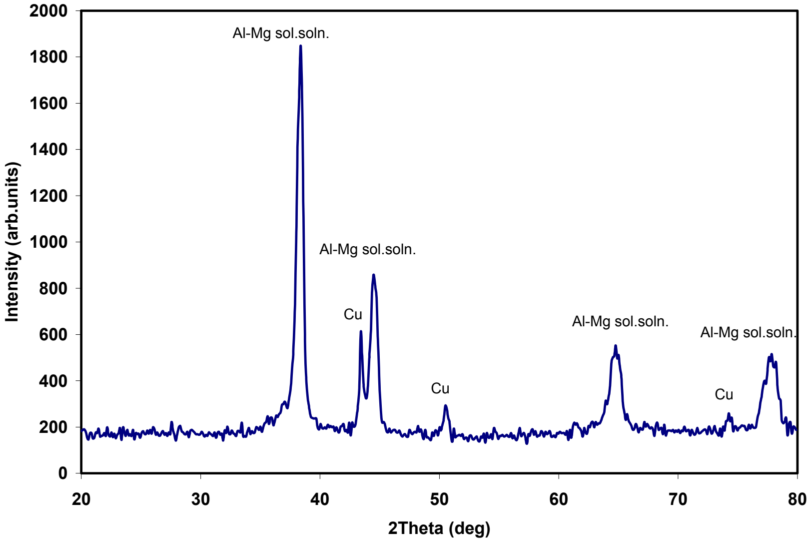

Figure 10. The XRD profile for powders with an average composition of approximately 20 at.% Mg in Al.

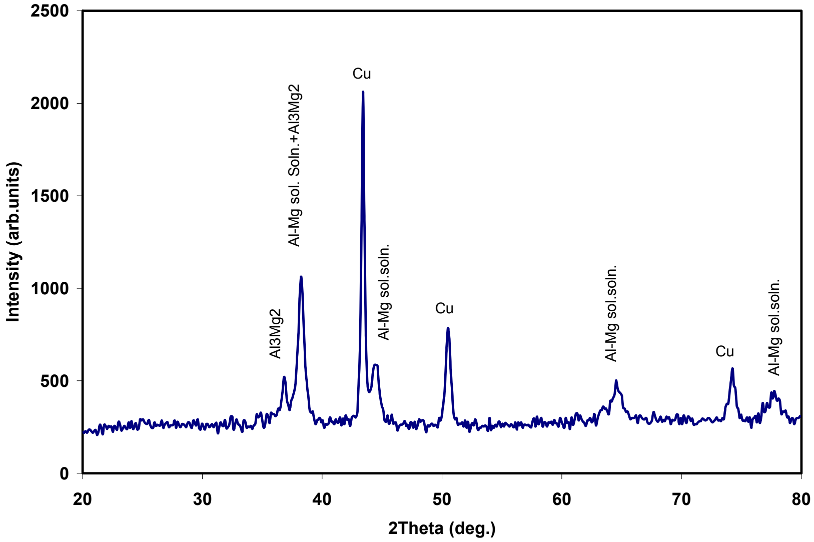

Figure 11. The XRD profile for powders with an average composition of approximately 40 at.% Mg in Al.

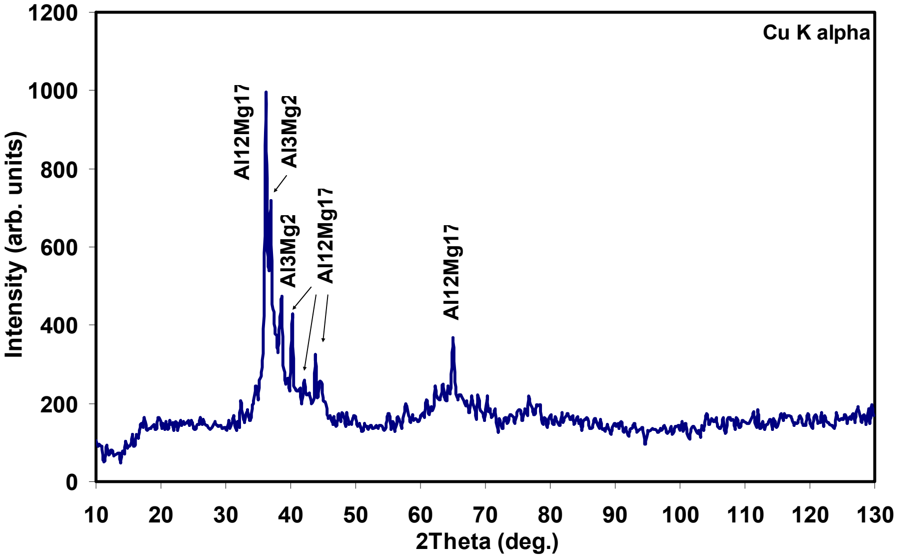

Figure 12. The XRD profile for powders with an average composition of approximately 60 at.% Mg in Al.

Milestones

1st - Research and design the electrodeposition set-up.

2nd - Order and prepare components.

3rd - Initial attempt for depositing Mg-Al alloys. Microstructural characterization of the deposits.

4th - Establish the relevant electrodeposition parameters for obtaining the desired nanocrystalline Mg-Al alloys. Characterize the properties of the alloys.

Products and Deliverables

1st - Glove box delivered and installed, interim report.

2nd -. Electrodeposition set-up completed, interim report.

3rd - Nanocrystalline Mg-Al material fabricated, interim report.

4th- - Properties of the Mg-Al alloy characterized and the electrodeposition parameters adjusted for improved properties, final report.

References

1. H. Lehmkuhl, K. Mehler, U. Landau, *“The principles and techniques of electrolytic aluminum deposition and dissolution in organoaluminum electrolytes”,* H.Gerischer, C. Tobias, *“Advances in electrochemical science and engineering”,* 3, VCH, p. 163.
2. Mayer A, “Electrodeposition of aluminum, aluminum/magnesium alloys, and magnesium from organometallic electrolytes”, Electro Chem. Soc. 137: 2806-2809 (1990).
3. Lehmkuhl H, Mehler K, Reinhold B, Bongard H, Tesche B “Deposition of aluminum-magnesium alloys from electrolytes containing organo-aluminum complexes“ Adv. Engg. Mater. 3: 412-417 (2001).
4. Lehmkuhl H, Mehler K, Reinhold B, Bongard H, Tesche B “Deposition of aluminum-magnesium alloys from electrolytes containing organo-aluminum complexes” Materialwissenschaft und Werkstoffechnik 31:889-898 (2000).
5. R. Gremaud, A. Borgschulte, W. Lohstroh, H. Schreuders, A. Z¨uttel, B. Dam, R. Griessen, Journal of Alloys and Compounds 2005, 404-406 (2005), pp. 775-778.

7. Lithium Borohydride for Hydrogen Propellant Storage

Task PI: Dr. Samim Anghaie, Nuclear & Radiological Engineering Department

Graduate Student: Anne Charmeau, Nuclear & Radiological Engineering Department

Undergraduate Student: Laura Padilla, Nuclear & Radiological Engineering Department

The final report was submitted for this project. It is given again.

Research Period: August 3, 2004 to April 1, 2006

Projects Goals

The proposed research task will be focused on the development and characterization of lithium borohydride for the dual hydrogen propellant storage and neutron shielding applications. Lithium borohydride uniquely combines two important properties that are pivotal to the operation of space propulsion systems; it has the highest hydrogen storage density and the highest neutron absorption cross section when fully enriched ^{6}Li and ^{10}B are used.

Abstract

Lithium borohydride features unique properties for hydrogen storage and radiation shielding. Room temperature properties of lithium borohydride are measured and compared with data available in open literature. Measurement of high temperature properties of lithium borohydride requires additional safety measures and operation under inert gas environment. Radiation shielding properties of lithium borohydride with and without the use of enriched lithium and boron isotopes were quantified and analyzed. Results indicated that significant improvement in neutron shielding effectiveness can be achieved by replacing natural lithium borohydride with fully enriched ^{6}Li^{10}BH$_{4}$. This is especially true at lower neutron energies where the neutron absorption cross-sections for ^{6}Li and ^{10}B are much higher than their naturally occurring isotopic forms.

Introduction

Storage of a gram of hydrogen gas at atmospheric pressure would require about 11 liter of space. So for convenience the hydrogen gas must be intensely pressurized to several hundred atmospheres or it must be stored in liquid form under cryogenic temperatures. These options are not practical for long duration space missions. A viable solution to these difficulties is storage of hydrogen in hydride form. Among all hydride materials, lithium borohydride ($LiBH_4$) has the highest hydrogen density and the lowest mass density in solid phase (0.82 g/cm^3). In addition, the unique nuclear properties of basic elements of the $LiBH_4$ would make it the most effective shielding materials for neutrons. Hydrogen is one of the best material for moderation and shielding of neutrons. Lithium and boron in their low isotopic forms, ^{6}Li and ^{10}B, are among the best neutron absorbing materials. The relative aboundance of ^{6}Li and ^{10}B are 7.5% and 19.9%, respectively. The application of ^{6}Li^{10}BH$_4$ could potentially bring about a revolutionary reduction in the size, weight, and the cost of future space propulsion systems for long duration manned missions to the solar system.

The focus and specific tasks of the research included:

- Research Focus
  - Development and characterization of lithium borohydride for the dual hydrogen propellant storage and neutron shielding applications
- Research Tasks
  - Measure and compile physical and thermodynamic property data for lithium borohydride at room temperature.
  - Perform thermal stability analysis of lithium borohydride at temperatures up to the total dissociation point (~700K) for the compound.
  - Performance and microstructural characterization of lithium borohydride under intense radiation field.

Experimental Facility

Due to high combustibility of lithium borohydride in presence of air and moisture, all testing and preliminary characterizations were conducted in the Innovative Nuclear Space Power & Propulsion (INSPI) see-through low vacuum chamber. X-ray Diffraction (XRD – Philips APD 3720) technique was used for identification of chemical compound. This device uses powder diffraction standards files of d-spacings and intensities of known compounds to determine crystallographic information such as crystal structure, reflections and lattice parameters.

Accomplishments

An extensive literature search was conducted to update the existing database on lithium borohydride. The crystalline structure of $LiBH_4$ has been studied using synchrotron soft x-ray diffraction (J-P Soulie et.al. J. Alloys Compnd., 346, 200 (2002)). At ambient conditions $LiBH_4$ has orthorhombic symmetry. At higher temperatures (T > 100C), $LiBH_4$ undergoes phase transition to hexagonal structure. In both structures, four hydrogen atoms are arranged around boron in a tetrahedral configuration.

First principal calculations for prediction of fundamental properties of LiBH4 have been performed by K. Miwa et. al. (Phys. Rev. B, 69, 245120 (2004)) using the ultrasoft psedopotential method based on density function theory. The generalized gradient approximation approach has been used for the exchange-correlation energy and prediction of $LiBH_4$ fundamental properties such as the structural properties, electronic properties, dielectric properties, vibrational properties, and heat of formation. The calculation and analysis suggested a nearly ideal tetrahedral configuration of BH_4, which is in contrast to recently measured structural properties that suggest strongly distorted configuration. Calculation of electronic structure indicated that Li atoms are ionized as Li+ cations.

Known properties of lithium Borohydride pertinent to hydrogen storage include:

– 19.6% H content	
– Molecular weight	21.78 g/mol ($LiBH_4$) 20.22 g/mol ($6Li10BH_4$)
– Density	0.66 g/cm^3
– Melting point @ 0.1 MPa	541 K
– Boiling point @ 0.1 MPa	551 K
– Decomposition point @0.1 MPa	473 K
– White crystalline solid	

– X-ray power diffraction:	Orthorombic symmetry
– Stable in dry air or vacuum	(T < 473 K)
– Transition to hexagonal structure	~381K
– Hydrogen desorption peak	700K
– Primary solvent	Tetrahydrofuran (THF)

The primary methods of preparing high purity LiBH4 is through the following chemical reactions:

$NaBH_4 + LiB\ LiBH_4 + NaB \longrightarrow$
(Under nitrogen environment, 18 h at 298 K and .5 h at 308 K)

$Li + B + 2H_2\ LiBH_4 \longrightarrow$
(Heat of formation ~ - 194 KJ/mol)

The hydrogen desorption reaction proceeds at temperatures above 573 K with SiO_2 as catalyst:

$LiBH_4\ LiH + B + 3/2\ H_2 \longrightarrow$

For the purpose of this project, the destabilization of $LiBH_4$ to decrease the dehydriding temperature is a primary focus of research. Based on the published data, it is suggested that the charge compensation by Li+ cations play a pivotal role in the stability of the internal bonding of [BH4]- anions. It is also expected that the suppression of the charge transfer by the partial substitution of Li by other elements will be effective to lower the dehydriding temperature.

Thermal stability experiment was conducted to measure the melting point and stability of natural $LiBH_4$ at temperatures ranging from 300 K to 800 K. 500 g of ultrahigh pure natural $LiBH_4$ in powder form was acquired. Due to high flammability of $LiBH_4$, small packs of 2 g powder were prepared to minimize potential damage to the inert environment furnace system. During the preparation of test samples, it was observed that even at very low humidity the rate of moisture absorption is too high. $LiBH_4$ is soluble in water at room temperature. During weighting of $LiBH_4$ under normal atmospheric conditions, the air moisture dissolved $LiBH_4$ particles to form small droplets. The process was moved to an inert gas chamber to minimize reaction with moisture. X-ray analysis was performed to obtain diffraction pattern for both pure and dissolved $LiBH_4$ samples. Figure 1 shows the x-ray diffraction pattern for $LiBH_4$ samples prepared under inert gas atmosphere and at room temperature (~20 °C).

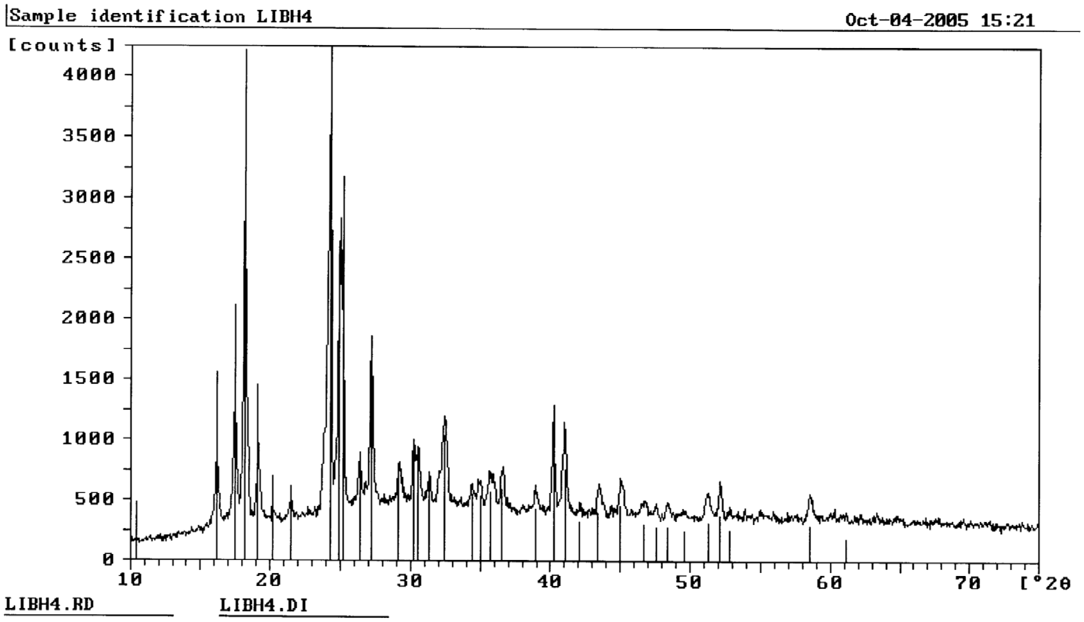

Figure 1. LiBH4 x-ray diffraction pattern.

High temperature measurement of the $LiBH_4$ properties was hindered by the safety concern associated with high combustibility in presence of air and moisture. In two occasions during handling of small $LiBH_4$ samples from the inert gas chamber to the analytical lab and vacuum furnace, spontaneous combustion resulted in small and limited lab fire. Though none of the lab fires resulted in any property damage or personal injury, the high temperature experiment with $LiBH_4$ was suspended pending the review of safety procedures. Further analysis of the experimental procedure and properties of $LiBH_4$ yielded the conclusion that high temperature testing only should be performed under inert gas environment. This change would have necessitated moving the furnace and basic analytical instruments under the controlled environment of an inert gas chamber. Due to significantly additional costs, continuation of this task was postponed to the nest funding cycle of this project.

In addition to hydrogen storage, $LiBH_4$ could be used for shielding of space nuclear reactors. To assess and evaluate the shielding capability of $LiBH_4$, a computational study was conducted using the industry standard MCNP-5 computer code system[3]. In particular, cross-sections for natural lithium and boron in $LiBH_4$ were replaced with highly enriched ^6Li and ^{10}B, respectively. The neutron absorption cross-sections for these isotopes are much higher than the other naturally occurring isotopes of these elements. This is a key factor in reducing the overall weight of shielding materials that are needed for protection against radiation originated from external or internal sources.

A cylindrical model with a neutron emitting line at the center was developed to evaluate and compare shielding properties of $LiBH_4$ with and without isotopic enrichment. Two different set of runs were conducted using this geometry, one for natural $LiBH_4$ and one for $^6Li^{10}BH_4$. Both materials were modeled under the same conditions. In order to check the effect of the neutron energy and depth of the material on its performance as a shield, values of both the cylindrical model radius and the neutron source energy were varied. The radius of the cylinder varied from 10 to 50 cm that covers a broad range of proposed space nuclear reactor designs. The energy of the linear neutron source was set at four different points, 0.010, 0.100, 0.500 and 1 MeV, which in the lower end of the fission spectrum that is shown in Figure 2. The height of the cylinder was maintained constant at 20 cm. Results of the analysis indicated that though both natural and enriched lithium borohydride materials have excellent shielding capabilities, $^{6}Li^{10}BH_4$, has significantly higher shielding capability for low energy neutrons.

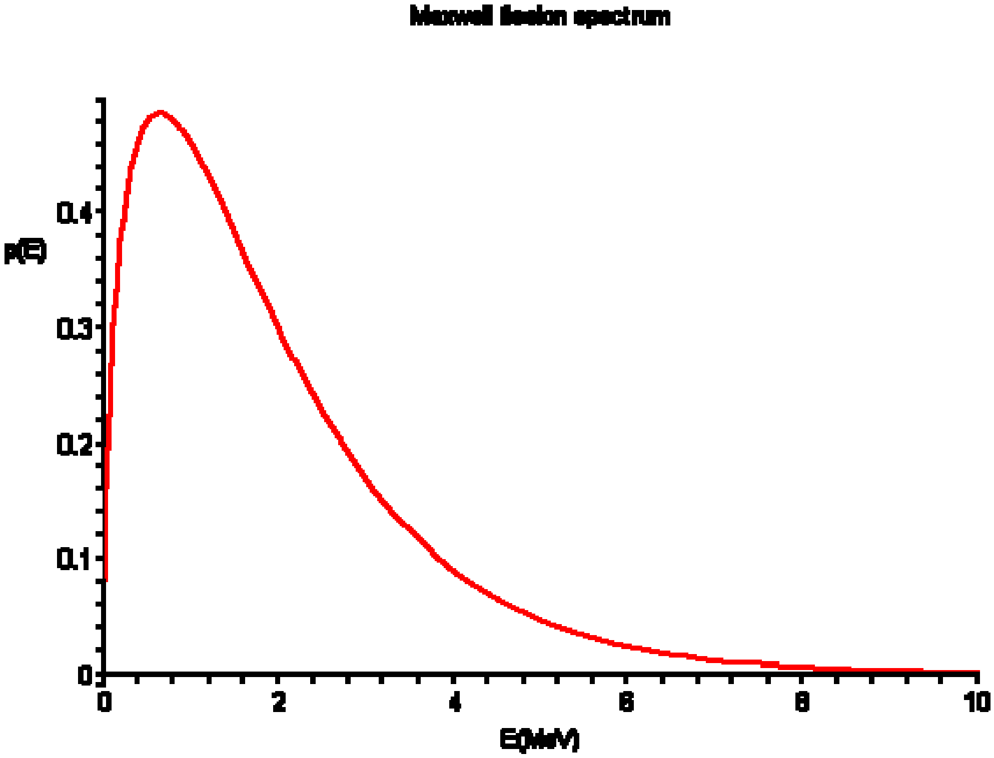

Figure 2. Maxwellian distribution of fission neutron energy (fission spectrum)

Results of the analysis indicated that though both natural and enriched lithium borohydride materials have excellent shielding capabilities, $Li^{6}B^{10}H_4$, has significantly higher shielding capability for low energy neutrons.This is expected because Li and B neutron absorption cross-sections increase with decreasing neutron energy (especially for Li^{6} and B^{10}). However, the shield still proves to be highly effective in higher energies. At 1 MeV, according to our calculations, only 0.152 % of the neutrons make it through a 10 cm shield of natural $LiBH_4$. This is impressive since 10 cm is the thinnest shield we modeled (therefore the most ineffective one) and natural $LiBH_4$ is not as good a shield as $Li^{6}B^{10}H_4$. This value drops to 0.109% when using $Li^{6}B^{10}H_4$.

Figure 3 shows the calculated value of neutron flux penetrated through 40 cm of lithium borohydride with and without isotopic enrichment at different energies. The energy integrated values of the neutron flux penetrated through 10 cm of lithium borohydride is shown in Figure 4.

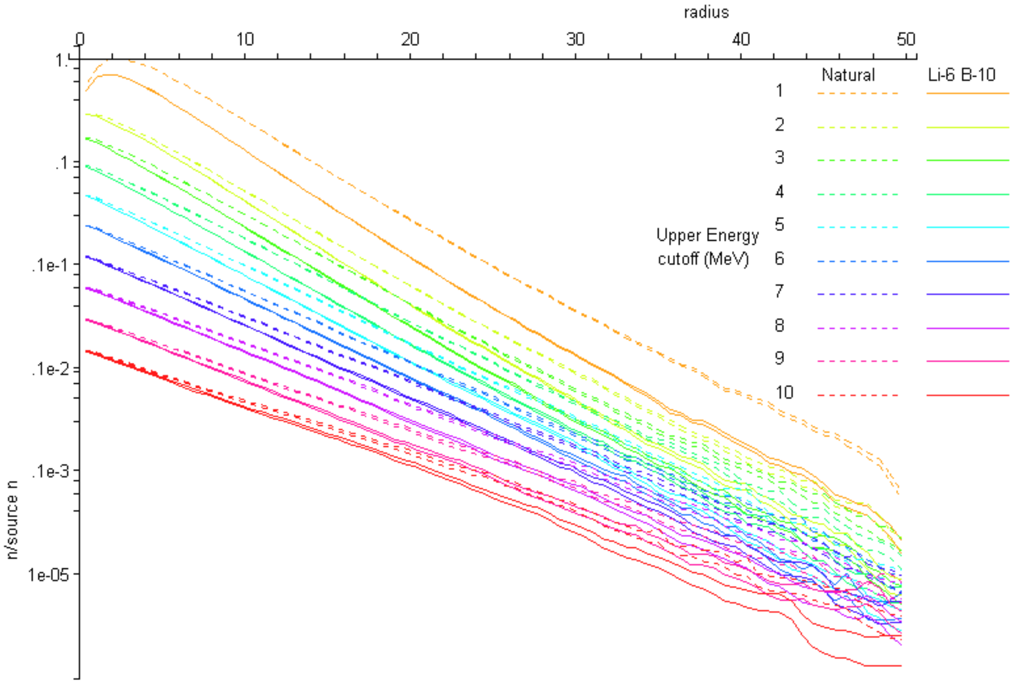

Figure 3. Neutron flux and energy penetrated through 40 cm of lithium borohydride with and without isotopic enrichment.

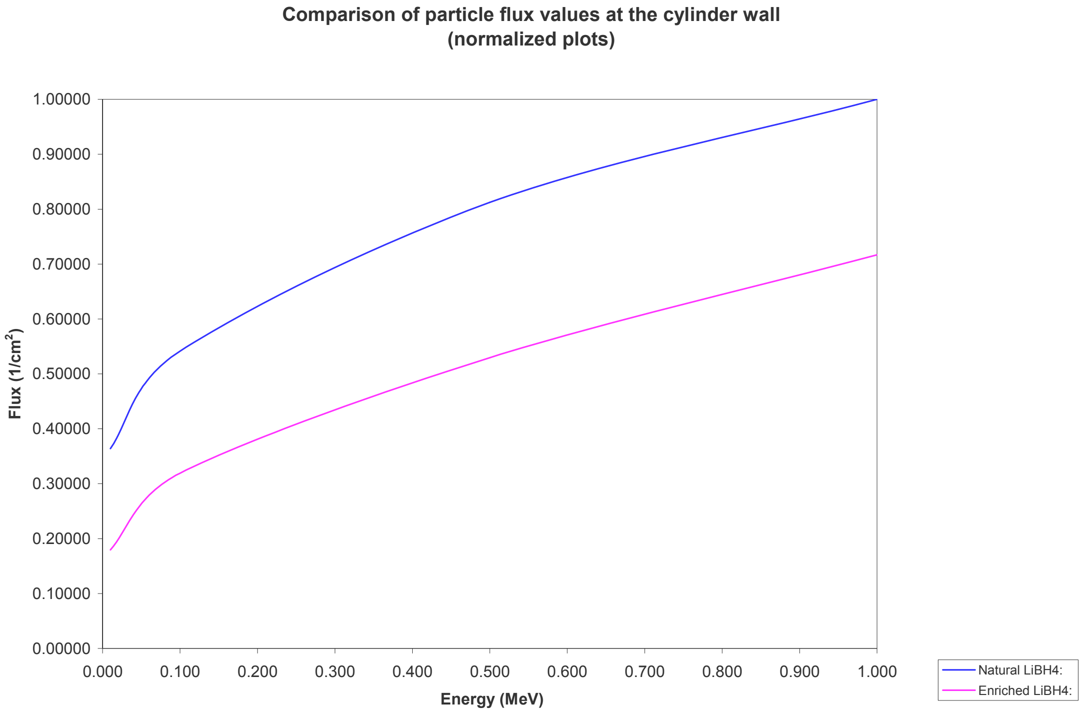

Figure 4. Neutron flux penetrating through 10 cm of lithium borohydride as a function of source neutron energy.

Further analysis of results indicated that as the radius of the cylinder increases the relative effectiveness of the shield will also increase. The amount of neutrons transmitted through a 20 cm shield is 25% of what is transmitted through a 10 cm shield. The amount of neutrons transmitted through a 50 cm shield is 16% of that transmitted through a 20 cm shield. These percentages remain fairly constant with increasing energy and they practically remain unchanged going from natural to enriched $LiBH_4$. Another trend shown in these results is the significant improvement in shielding effectiveness by replacing natural lithium borohydride with fully enriched $^6Li^{10}BH_4$. This is especially true at lower energies where the neutron absorption cross-sections for fully enriched ^6Li and ^{10}B are much higher than their naturally occurring isotopic forms. For 100 keV source neutrons, 50% fewer neutrons penetrate through the shield when natural $LiBH_4$ is replaced with fully enriched $^6Li^{10}BH_4$. For 1 MeV source neutrons, the percentage reduction in penetrated flux ix approximately 30%.

In summary, results of this study on hydrogen storage and shielding capabilities of lithium hydroboride have yielded the following conclusions;

1. Lithium Borohydride for Hydrogen Propellant Storage:
    - Lithium Borohydride features superior properties for hydrogen storage, in particular, for once use and non-recycled application of hydrogen.
    - Chemical stability and high energy reaction with water and air limits high temperature and terrestrial applications of Lithium Borohydride.
    - Measured properties at room temperature agreed with reported data.
    - X-ray analysis was performed to measure the moisture absorption and reaction.
    - White, odorless powder, water-reactive and is corrosive in the presence of moisture.
    - Reaction with water generates flammable hydrogen gas, causing ignition or explosion.
    - Thermal decomposition of Lithium Borohydride produces hydrogen gas, lithium and boron oxides, and borane.
    - Lithium Borohydride will react with water, carbon dioxide, and oxygen in air to form other inorganic compounds.
    - High combustibility of Lithium Borohydride in presence of air and moisture necessitates additional safety measures and procurement of new equipments that have not been foreseen at the outset of this project.
2. Unique radiation Shielding Features of Lithium Borohydride
    - $LiBH_4$ with natural isotopic constituents is an excellent neutron shielding material.
    - Enrichment of natural B and Li to ^{10}B and ^6Li, respectively, further enhances neutron shielding property of $LiBH_4$
    - Monte Carlo analysis is performed to quantify the enhanced neutron shielding behavior of $^6Li^{10}BH_4$.

- Work in progress includes effect of radiation – neutron and gamma-rays – on properties of Lithium Borohydride

3. Potential Applications of Lithium Borohydride:

   - Compact hydrogen storage.

   - Light weight & compact radiation shielding for space reactors.

   - Dual use as propellant storage for Nuclear Thermal Rocket (NTR) and rocket fuel for lift up from Moon or Mars surface.

References

1. J-Ph. Soulié, G. Renaudin, R.Cerny, K. Yvon., “Lithium boro-hydride $LiBH_4$: I. Crystal structure,” *J. Alloys and Compounds*, **346**, 200-205 (2002).

2. Kazutoshi Miwa, Nobuko Ohba, and Shin-ichi Towata, ”First Principle Studies on Lithium Borohydride LiBH4,” Phys. Rev. B **69**, 245120 (2004).

3. MCNP - A General Monte Carlo N-Particle Transport Code - Version 5, 2005, <http://mcnp-green.lanl.gov/index.html>

REPORT DOCUMENTATION PAGE

Form Approved
OMB No. 0704-0188

1. REPORT DATE *(DD-MM-YYYY)* 01-11-2008	**2. REPORT TYPE** Final Contractor Report	**3. DATES COVERED** *(From - To)*

4. TITLE AND SUBTITLE
Hydrogen Research for Spaceport and Space-Based Applications
Hydrogen Production, Storage, and Transport

5a. CONTRACT NUMBER

5b. GRANT NUMBER
NAG3-2930

5c. PROGRAM ELEMENT NUMBER

6. AUTHOR(S)
Anderson, Tim; Balaban, Canan

5d. PROJECT NUMBER

5e. TASK NUMBER

5f. WORK UNIT NUMBER
WBS 561581.02.08.03.11

7. PERFORMING ORGANIZATION NAME(S) AND ADDRESS(ES)
University of Florida
1 Univ of Florida
Gainesville, Florida 32611

8. PERFORMING ORGANIZATION REPORT NUMBER
E-16612-3

9. SPONSORING/MONITORING AGENCY NAME(S) AND ADDRESS(ES)
National Aeronautics and Space Administration
Washington, DC 20546-0001

10. SPONSORING/MONITORS ACRONYM(S)
NASA

11. SPONSORING/MONITORING REPORT NUMBER
NASA/CR-2008-215440-PART3

12. DISTRIBUTION/AVAILABILITY STATEMENT
Unclassified-Unlimited
Subject Categories: 25, 28, 33, and 34
Available electronically at http://gltrs.grc.nasa.gov
This publication is available from the NASA Center for AeroSpace Information, 301-621-0390

13. SUPPLEMENTARY NOTES
Faculty Coordinator: Dr. James Klausner, Professor, Mechanical & Aerospace Engineering

14. ABSTRACT

The activities presented are a broad based approach to advancing key hydrogen related technologies in areas such as fuel cells, hydrogen production, and distributed sensors for hydrogen-leak detection, laser instrumentation for hydrogen-leak detection, and cryogenic transport and storage. Presented are the results from research projects, education and outreach activities, system and trade studies. The work will aid in advancing the state-of-the-art for several critical technologies related to the implementation of a hydrogen infrastructure. Activities conducted are relevant to a number of propulsion and power systems for terrestrial, aeronautics and aerospace applications. Hydrogen storage and in-space hydrogen transport research focused on developing and verifying design concepts for efficient, safe, lightweight liquid hydrogen cryogenic storage systems. Research into hydrogen production had a specific goal of further advancing proton conducting membrane technology in the laboratory at a larger scale. System and process trade studies evaluated the proton conducting membrane technology, specifically, scale-up issues.

15. SUBJECT TERMS
Hydrogen; Cryogenic fluids; Cryogenic storage; Thermodynamics; Sensors; Hydrogen production; Fuel cells

16. SECURITY CLASSIFICATION OF:			**17. LIMITATION OF ABSTRACT**	**18. NUMBER OF PAGES**	**19a. NAME OF RESPONSIBLE PERSON**
a. REPORT	**b. ABSTRACT**	**c. THIS PAGE**			STI Help Desk (email:help@sti.nasa.gov)
U	U	U	UU	209	**19b. TELEPHONE NUMBER** *(include area code)* 301-621-0390